POLITECNICO DI MILANO
DEPARTMENT OF ENERGY
DOCTORAL PROGRAMME IN
ENERGY AND NUCLEAR SCIENCE AND TECHNOLOGY

CFD MODELLING OF TURBULENT PREMIXED COMBUSTION IN SPARK-IGNITION ENGINES

Doctoral Dissertation of:
Luca Cornolti

Supervisor:
Dr. Tommaso Lucchini

Tutor:
Prof. Angelo Onorati

The Chair of the Doctoral Program:
Prof. Carlo Bottani

2015 – XXVII Cycle STEN

Acknowledgements

I would like to express my gratitude to my supervisor Dr. Tommaso Lucchini and my tutor Prof. Angelo Onorati for giving me the opportunity to join the ICE group and for what I learned in the last three years.
I also thank Prof. Boulochous for hosting me in his research group at ETH, where I experienced the feeling of belonging to a worldwide community.
I'm also very grateful to all my colleagues, which helped me in these years with their friendship and their ideas. Specifically: the divine Augustus, a real example of assertiveness and determination. Roberto with whom I shared my experience. Andrea and Marco for our interesting discussion. Tarcisio, the kindness personification and all the other members of ICE group. I also thank Michele, Martin, Mahdi, Sushant and Andrea from ETH group.
Finally I want to thank all my friends and my family for supporting me in these years of heavy involvement in research activity, which sometimes prevented me from spending with them the time they deserved.

Abstract

The present work focuses on the development of computational tools to model turbulent premixed combustion for spark-ignition engine applications in the context of RANS simulations. The model covers all the stages of combustion process, starting from early flame kernel development to its fully developed phase. After a brief general introduction to the problem, through asymptotic theory, the behaviour of laminar flames is analyzed to underline its fundamental physical properties. This is considered a basic step to understand the more complex behaviour of turbulent flames, which, otherwise, would be very difficult to be interpreted. Afterwards, three of the most employed models in literature (Flame Surface Density, Flame Speed Closure and G-Equation approach) to simulate turbulent premixed flames are described and compared. At the conclusion of this analysis, the G-Equation model is selected for the further developments which led to implement a new solver. This exploits a Lagrangian approach to describe the initial stages of flame development; then it shifts to a more canonical Eulerian approach, when the advanced phase of combustion is described. Afterwards, to check its predictive capabilities, the model is tested against the experimental data provided by a laboratory engine with optical access. All the models used in this work were implemented within the OpenFOAM framework, as a contribution to the library "LibICE", developed by the Internal Combustion Engine group of the Energy Department of Politecnico di Milano.

Publications

List of publications related to the discussed topic with author's contributions:

- L. Cornolti, T. Lucchini, G. Montenegro, G. D'Errico "A comprehensive Lagrangian flame kernel model to predict ignition in SI engines", International journal of computer mathematics, volume 91 Issue 1, January 2014.
- T. Lucchini, L. Cornolti, G. Montenegro, G. D'Errico "A comprehensive model to predict the initial stage of combustion in SI engines", SAE Technical paper, 2013-01-1087, 2013.

Contents

1 Introduction **1**
1.1 Thesis outline 2

2 Introduction to turbulent combustion modelling **5**
2.1 Governing equation of reacting flows 5
2.2 The purposes of models 7
2.3 Combustion models classification 8
2.4 Logical structure of this work 9
2.5 Experiment and modelling issues 10

3 Laminar flame modelling **13**
3.1 The Planar laminar flame 13
3.2 Asymptotic analysis of unstretched laminar flame 16
3.2.1 Asymptotic theory assumptions 17
3.2.2 Asymptotic theory: governing equations 18
3.2.3 Asymptotic theory: laminar flame speed computation 19
3.3 Asymptotic analysis of stretched laminar flame 22
3.4 Instabilities of laminar flame 27
3.5 Concluding remarks 30

4 Turbulent combustion modelling **33**
4.1 Turbulence: characteristic scales and models 33
4.1.1 Turbulent scales 34
4.1.2 Turbulence models 36
4.2 Turbulent combustion diagram 38
4.3 The hydrodynamic model 40
4.4 RANS/LES turbulent combustion models 41
4.4.1 Preliminary definitions 41
4.4.2 G-Equation model 44
4.4.3 Flame surface density model 44
4.4.4 Flame speed closure model 46

4.5 Comparison of RANS turbulent combustion models 50
4.5.1 Planar configuration 51
4.5.2 2D test case 57
4.5.3 Summary of the comparison 62
4.6 The turbulent flame speed 65
4.6.1 Turbulent planar flames 65
4.6.2 Turbulent spherical expanding flames 69
4.7 Concluding remarks 73

5 modelling ignition process 75
5.1 Spark discharge 76
5.1.1 Dark discharge and breakdown regimes 76
5.1.2 Arc and glow discharge regimes 81
5.1.3 Ignition devices 84
5.2 Models for spark discharge 86
5.2.1 Simplified models to describe spark discharge process 87
5.3 Early flame kernel development 95
5.4 Concluding remarks 99

6 A comprehensive combustion model for spark-ignition engines 101
6.1 Equations solved in the Eulerian domain 102
6.2 Numerical solution of Eulerian equations 104
6.3 Sub-models which describe initial stages of flame kernel 107
6.3.1 Electrical circuit and spark energy deposition model 108
6.3.2 Flame kernel growth model 110
6.4 Coupling the Lagrangian model with the mesh domain 112

7 Combustion model validation 115
7.1 Experimental configuration and test conditions 116
7.2 Case set-up 116
7.3 Results at non combusting conditions 120
7.4 Combustion data analysis 123
7.5 Combustion model results 127
7.6 Summary 135

8 Summary and conclusions 137

Bibliography 141

List of Figures

2.1 Historical measurements of the maximum laminar flame speed for methane/air mixture at ambient temperature and pressure. 10
2.2 Relation between measured planar turbulent burning velocity and Damkohler number. 11

3.1 Temperature and heat release profiles of a stoichiometric methane/air mixture at 300 K and 1 bar. 14
3.2 Mass fraction profile of methane, water and carbon dioxide for a stoichiometric methane/air mixture at 300 K and 1 bar. 14
3.3 Laminar flame thickness for different equivalence ratio of methane-air mixture at $1atm$ and $25°C$. 16
3.4 Example of non-dimensional temperature (T/T_u) and non-dimensional heat release profile (ω/ω_{max}) for a one step global reaction mechanism. 18
3.5 Unconfined flame speed as a function of flame radius as determined by 3.62, for $Le_{eff} < 1$. 26
3.6 Onset of cellular instabilities of the same hydrogen/propane mixture at different pressure. 28
3.7 The growth rate for propane/air mixture at different equivalence ratio calculated for increasing radii. 30
3.8 Neutral stability curves for propane/air mixture at different equivalence ratio. 30

4.1 Non-dimensional Power spectra density for increasing Taylor Reynolds numbers. 36
4.2 Regime diagram for turbulent premixed combustion. 39
4.3 Comparison of progress variable profile given by 4.74 with experimental data obtained by various authors for different configuration. 50
4.4 1D configuration test case 52

4.5 Evolution of a planar turbulent flame for the constant density case. Figure (a) shows the non-dimensional turbulent flame speed. Figure (b) shows the turbulent flame brush thickness evolution. The parameters used to initialize the problem and to make the reported quantities non-dimensional are given in Figure 4.4. 53
4.6 Evolution of a planar turbulent flame for the constant density case. Figure (a) shows the Progress variable profile. Figure (b) shows the Dependence of Σ source term on the progress variable $\overline{c}$. The parameters used to initialize the problem are given in Figure 4.4. 53
4.7 Turbulent Flame speed development for different initialization of the progress variable 54
4.8 Evolution of a planar turbulent flame for variable density cases. $\sigma = \rho_u/\rho_b$. Figure (a) shows the non-dimensional turbulent flame speed. Figure (b) shows the turbulent flame brush thickness evolution. The parameters used to initialize the problem and make the reported quantities non-dimensional are given in Figure 4.4. 55
4.9 Evolution of a planar turbulent flame for variable density cases. $\sigma = \rho_u/\rho_b$. Figure (a) shows the Progress variable profile. Figure (b) shows the Dependence of Σ source term on the progress variable $\overline{c}$. The parameters used to initialize the problem are given in Figure 4.4. 56
4.10 Flame brush thickness after introduction of the term $a\ u_{rms}(2\tilde{c}-1)|\nabla\tilde{c}|$ in the progress variable equation. 56
4.11 2D configuration test case. 57
4.12 Comparison of models results for the 1D planar and 2D cylindrical configurations with $\sigma = 4$. Turbulence properties can be found in Figure 4.11. Strain lines represent the planar case, dashed lines the cylindrical case. Figure (a) displays the turbulent flame speed. Figure (a) depicts the development of the flame brush thickness 58
4.13 Stretch effect on turbulent Flame speed evolution for different planar flame brush thickness Δ_t 59
4.16 Pancake engine configuration. 60
4.17 Comparison between experiments and numerical results of G-Equation model of cylinder pressure and burnt mass fraction. 61
4.18 Comparison between experiments and numerical results of FSD-CFM2-a model of cylinder pressure and burnt mass fraction. 61
4.22 Comparison between experiments and numerical results of G-Equation model of cylinder pressure and burnt mass fraction. 63
4.23 Comparison between experiments and numerical results of FSD-CFM2-a model of cylinder pressure and burnt mass fraction. 63
4.24 Comparison between experiments and numerical results of G-Equation model of cylinder pressure and burnt mass fraction. 64
4.25 Comparison between experiments and numerical results of FSD-CFM2-a model of cylinder pressure and burnt mass fraction. 64
4.26 Methane-air mixture, ϕ = 0.9, p = 5 atm, δ_L = 0.16 mm, $Ma_b\delta_L$ = 0.12 mm, $\bar{R}$ = 21.87 mm, l_t = 4 mm, Re_t = 210. 68

4.27 hydrogen-air mixture, ϕ = 4.0, p = 5 atm, δ_L = 0.09 mm , $Ma_b\delta_L$ = 0.35 , $\bar{R}$ = 21.41 mm, l_t = 4, Re_t = 221. 68
4.28 Turbulence intensity ratio 71
4.29 Comparison of the transient behaviour of turbulent flame speed models proposed in [117], [63] and [65] 72

5.1 Direct current discharge regimes. 77
5.2 Mechanism of formation of the streamers 80
5.3 Time dependence of pulse breakdown voltage in gases 81
5.4 Variation of rotational temperature with discharge current for normal glow discharge in air at atmospheric conditions with 100 and 300 μm electrode spacing 82
5.5 CDI ignition system voltage evolution in time 84
5.6 CDI ignition system voltage evolution in time 84
5.7 Essential features of a transistor controlled ignition (TCI) circuit scheme 85
5.8 Essential features of a capacitor discharge ignition (CDI) circuit scheme 85
5.9 Current profile of the primary circuit of a TCI ignition system 85
5.10 Current profile of the secondary circuit of a TCI ignition system 85
5.11 Properties of a thermal air plasma 87
5.12 Molar fraction of N_2 and O_2 species in air at atmospheric pressure, for increasing temperature 88
5.13 Axis temperature and pressure evolution in the very fist stages after breakdown. 89
5.14 Temperature profile evolution after breakdown. 90
5.15 Example of Application of non-thermal plasma for combustion. 91
5.16 Measured high temperature kernel radii for different discharge energies 91
5.17 Discharged current profile with different charge levels of the CDI system capacitor 91
5.18 Comparison of experimental and computed spark radii after breakdown 92
5.19 High temperature sphere radius predicted by 0D model with and without radiation losses 93
5.20 Radiation heat losses obtained by the computed radii shown in [33] . . 94
5.21 Temperature profile evolution throughout glow phase. 94
5.22 Comparison of analytical results and numerical solutions of asymptotic equations 5.26 and 5.27 for various power sources 97
5.23 Effect of Lewis number on flame kernel development 97
5.24 Flame kernel grow of propane-air mixture at different equivalence ratio 99

6.1 Reinitialization procedure applied to G-Field 105
6.2 G-Equation: comparison of computed and theoretical radius for a moving spherical expanding geometry 107
6.4 Lagrangian approach concept 109
6.5 Simplified scheme of a TCI system modelled in the solver 109
6.6 Restrike phenomenology: on the top voltage and current profiles in time; on the bottom images of the spark during a restrike 110
6.7 Voltage evolution in time across the spark gap for different flow velocities at ambient pressure and temperature. 110

6.8 1D thermal channel model 111
6.9 Example of computed flame kernel velocity 113
6.10 Flow char of the proposed model: interaction between sub-models, lagrangian particles and Eulerian mesh 114

7.1 Experimental engine configuration 117
7.2 Data needed to create a mesh with snappyHexMesh utility 118
7.3 The three stages to build a mesh with snappyHexMesh 118
7.4 Example of finite volume discretization domain used for computations . 119
7.5 Pressure development in compression phase 120
7.6 Comparison between profile obtained by the simplified electrical system and experimental data extrapolated from [71] 120
7.7 Swirl motion inside the side chamber at 335 and 345 CAD 121
7.8 Radial profile of non-dimensional velocity and turbulent intensities within the side chamber 122
7.9 Comparison of computed and LDV measurements at peripheral spark position for three engine speeds 122
7.11 Radial profile of integral length scale within the side chamber 123
7.12 Burnt volume as function of time after ignition for central spark position cases 124
7.13 Burnt volume as function of time after ignition for peripheral spark position cases 125
7.14 Position in Borghi diagram of test points for different engine speed at stoichiometric condition 126
7.15 Position in Borghi diagram of test points at 1250 rpm for different air-fuel equivalence ratios 127
7.16 Comparison of experimental and computed burnt volume for different engine speeds 129
7.17 Central spark location: comparison of experimental and computed burnt volume for different mixture compositions. 129
7.18 Comparison of experimental and computed laminar flame speed for the mechanism proposed in [99] 130
7.19 Average flame position ($G = 0$) for the 1000 rpm case at stoichiometric condition with electrodes located in the centre of the chamber 130
7.20 Favre progress variable fields for the 1000 rpm case at stoichiometric condition with electrodes located in the centre of the chamber 131
7.21 Comparison of the computed spark voltage between the electrodes for central and peripheral spark positions at 1000 rpm. 131
7.22 Peripheral spark location: Comparison of experimental and computed burnt volume for different engine speeds 132
7.23 Average flame position ($G = 0$) for the 1000 rpm case at stoichiometric condition with electrodes located in the peripheral zone 132
7.24 Favre progress variable fields for the 1000 rpm case at stoichiometric condition with electrodes located in the peripheral zone 133
7.25 Peripheral spark location: comparison of experimental and computed burnt volume for different mixture compositions 134
7.27 Effect of different discharged powers. 135

7.28 Differences between a long and short discharge for the peripheral spark case. 135

List of Tables

4.1 Source terms for Flame Surface Density models and corresponding turbulent flame consumption speeds 52

6.1 Constants value for Peters turbulent flame speed relation 104

7.1 Geometric data of the simulated side-chamber engine 117
7.2 Operating conditions tested in experiments 117
7.3 Properties of mixture at different air-fuel equivalence ratio 120
7.5 Experimental time delay of the peripheral spark position cases with respects to the corresponding stoichiometric mixture case with electrodes placed in the centre of the chamber. 125
7.6 Properties of mixture at different air-fuel equivalence ratio 126
7.7 Computed Herweg et al. test cases conditions. 128
7.8 Computed time after ignition needed to burn a volume of 1 cm^3. 134

Nomenclature

Latin letters

$\dot{Q}$	external energy source [j/m^3]
κ	Curvature of a surface[1/m]
$\mathbf{g}$	gravitational acceleration [m/s^2]
$\mathbf{U}$	velocity [m/s]
$\mathbf{V_c}$	correction velocity [m/s]
c_p	specific heat capacity at constant pressure [j/(kg K)]
d_{gap}	minimum distance between two electrodes [m]
D_k	equivalent diffusion coefficient of species k [m^2/s]
D_{th}	thermal diffusivity [m^2/s]
Da	Damkohler number [-]
h_t	total specific enthalpy [j/kg]
I	unity tensor
K	Stretch rate [1/s]
k	Specific total turbulent kinetic energy [m^2/s^2]
l_k	Kolmogorov scale [m]
l_n	turbulent scale for wavenumber n [m]
l_t	Integral scale [m]
Le_{eff}	Effective Lewis number [-]
Le_k	Lewis number of species k [-]

Ma Markstein number [-]

p pressure [Pa]

Pr Prandtl number [-]

q heat release parameter [-]

Re Reynolds number [-]

Re_λ Taylor Reynolds number [-]

Re_t Turbulent Reynolds number [-]

S_L laminar flame speed [m/s]

S_L^0 unstretched laminar flame speed [m/s]

S_L^0 unstretched laminar flame speed [m/s]

S_t Turbulent flame speed [m/s]

T_{ad} adiabatic flame temperature [K]

u_{rms} Turbulent characteristic velocity at integral scale $[m/s]$

W mean molecular weight of a mixture [kg/kmol]

W_k molecular weight of species k [kg/kmol]

Y_k species mass fraction [-]

Ze Zel'dovic number [-]

Greek letters

δ_L laminar flame thickness [m]

Δ_t Flame brush thickness [m]

$\dot{\omega}_k$ species reaction rate [[kg/m^3]

γ Heat capacity ratio k [-]

λ Taylor microscale $[m]$

λ heat diffusion coefficient [j/(K m^2)]

μ dynamic viscosity [Pa·s]

ν kinematic viscosity [m^2/s]

$\nu_{k,j}$ molar stoichiometric coefficient of species k in reaction j [-]

ν_t Turbulent viscosity $[kg/(m \cdot s)]$

ρ density [kg/m^3]

Σ Flame surface density $[1/m]$

σ Heat release ratio T_{ad}/T_u [-]

τ_k Kolmogorov turnover time $[s]$

τ_n turbulent turnover time for wavenumber n $[s]$

τ_t Integral scale turnover time $[s]$

ε Turbulent dissipation $[m^2/s^3]$

Ξ Wrinkling factor [-]

Subscripts

ϕ_b property defined in burnt gas region

ϕ_D property of deficient reactant

ϕ_E property of excess reactant

ϕ_u property defined in unburnt gas region

Superscripts

$\bar{\phi}$ Reynolds-averaged quantity

$\tilde{\phi}$ Favre-averaged quantity

CHAPTER 1

Introduction

Combustion has been the key technology for domestic heating, transportation and power generation during the last century: about 85% of the world's energy comes from combustion. The success of this technology is linked to the availability of fossil fuels at low-price, the controllability of combustion process and the low installation costs compared to other alternatives (e.g. nuclear power plants). On the other hand, some problems have recently arisen: first, the growing awareness of the limited availability of fossil fuels, accelerated by the increasing energy demand of countries like China, India and Brazil. Second, the greater attention dealt to the health effects and environmental implications of combustion products. It is well known that combustion of fossil fuels produces emissions of carbon dioxides (CO_2) and pollutants such as nitrogen oxides (NO_x), soot, unburnt hydrocarbons (UHC) and carbon monoxides (CO). While the last products directly affect human health, but can also be reduced with proper after-treatment devices, the first one is unavoidable and it is believed to significantly contribute to global warming. Concerning passenger cars, electric propulsion systems are currently considered as a possible future alternative to IC engines. Anyway, in the near future the ICE will still provide the key technology for vehicle propulsion. In particular two different combustion processes characterize most of the engines currently employed in automotive sector: non premixed combustion in Diesel engine and premixed combustion in spark ignition (SI) engines. Given the prospect of easy improvements in terms of efficiency, Diesel engine has been developed a lot in the last twenty years. Its prevalence has increased over the time, going from an almost exclusive use for commercial vehicles, like tracks, to cover half of total vehicle fleet. Nowadays SI engine is starting to regain attention for different reasons: first, the amount diesel fuel and gasoline that can be produced from fractional distillation of oil is roughly the same and vehicle fleet should be balanced in order to burn both of them. Second, Diesel engine

has reached a mature level of development and further improvements are harder to be achieved than before. Third, SI engine is quite flexible in terms of use of different fuels (methane, LPG, hydrogen) and it seems to be the favored choice for hybrid engine concepts, due to their reduced weight/power ratio. One of the possible strategies that can be used in order to improve SI engine efficiency is to replace throttling at partial loads with lean or diluted (with exhaust gas recirculation) mixtures. Another one is to exploit the capability of direct injection spark-ignition engine in order to create stratified mixture. Both of these strategies are still actually not fully exploited because of resulting important operational instabilities of the engine (i.e. cyclic dispersion). In order to overcome these difficulties, a deeper understanding of ignition and flame propagation processes is required. Considering the limitation of actually available experimental techniques to study combustion, theory and computational fluid dynamics (CFD) are becoming very important support tools. Moreover, because of the increasingly development costs of ICE, the concept of virtual development supported by computational fluid dynamics is becoming more and more important.

1.1 Thesis outline

The description of the combustion process requires the solution of the well know Navier-Stokes equations with the addition of the transport equations for hundreds of species (fuel, oxidizer and radicals) and a non-linear system of even more reactions. The solution of such equations (direct numerical simulation, DNS) for industrial scale problems is currently and will remain in the next future prohibitive. Within this context, the development of simplified models and numerical tools which deal with turbulent combustion is important for three reasons: first, they are useful to understand the physical mechanisms which govern the phenomenon, since they make explicit those parameters which are hidden in the many equations solved in DNS (synthesis process). Second, they provide a way to process the experimental data and obtain some physical quantities which cannot be directly measured (analysis process). Finally, due to their lower computational time, they serve as an useful tool to speed up the engine design phase, reducing the time and costs which are necessary for experimental investigations. Following these three aims, this work will first provide a review of the known physical processes occurring in premixed combustion and the different available modelling strategies. This is an important step, since turbulent combustion has been studied over the past 60 years and the amount of literature on the topic is impressive, dispersive and sometimes contradictory. After a general introduction on combustion modelling problem, it will be illustrated how to turn a reaction based problem into a simpler one, where no more reaction description is needed. This will be done with the help of asymptotic theory which exploits the multiscale nature of premixed combustion to decompose the process into large and small-scale interacting phenomena. If only large scale effects are to be described, small scale processes can be taken into account limiting the description to only their connections with large scales. These relations require the definition of summary parameters which identify the global mechanism of the phenomenon. The details of small scales are lost, but the computational time is also reduced. This description will be applied to laminar flames, which are the basic brick on which turbulent combustion modelling is built. Then turbulence related aspects will be briefly discussed

and it will be shown that, contrary to combustion, this is not a multiscale process, as the scales involved create a limited continuous spectrum. Afterwards, some modelling approaches to connect turbulence with premixed flame will be reviewed. As turbulence can be described with three different degrees of accuracy, three modelling strategies are necessary. In particular, the more accurate the turbulence model is, the more effects will be implicitly described by Navier-Stokes equations. For higher modelling levels, these effects need to be described explicitly by means of additional relations. After a short section related to models for direct numerical simulation, which just provide a logical step for what comes next, models from RANS/LES approaches will be discussed. In particular the most employed models in literature (flame surface density, flame speed closure model and G-Eqaution approach) will be compared in order to understand which one is best suited for the description of combustion process in spark-ignition engines, in the context of RANS approach. Then a chapter will be dedicated to spark discharge, initial flame kernel development and modelling approaches. Finally all the previous descriptions will contribute to define a combustion model for RANS applications, which has been implemented within the OpenFOAM framework. After the description of the main features of the model, a preliminary test to understand its potentiality will be proposed. The thesis is structured as follows:

- In chapter 2, a general introduction to combustion modelling problem is given. The basic reacting flows equations are briefly introduced; it is discussed the need of providing simplified models which allow to get a solution without solving these equations, as they are too computationally expensive. A model classification is proposed to underline their domain of validity. Finally some issues related to model validation are presented.
- In Chapter 3 an overview of laminar premixed flames, seen as the base for understanding turbulent premixed combustion is given. In particular, a set of global parameters and equations to describe the physics of laminar flames, is presented. Their aim is to replace the reaction mechanisms which characterize the combustion behaviour of a mixture.
- In Chapter 4 the physics of turbulence and its interaction with premixed flame are discussed. The main premixed turbulent combustion models available in literature are presented and compared with respect to their ability to simulate the flame development. Comparison is achieved through basic test cases which underline the essential properties of each model, removing all the unnecessary effects. The end of the chapter is addressed to the relations which describe developing and fully developed turbulent propagation speed.
- In Chapter 5 an overview of ignition process, including spark channel formation, ignition devices and early flame kernel development is given. Empirical correlations and simplified models are used to further analyze these phases.
- In Chapter 6 a comprehensive model which has been implemented in OpenFOAM to simulate combustion for SI engines is presented. The model is designed to describe the flame development since its very first stage.
- In Chapter 7 the previous comprehensive model is tested against the data related to flame propagation in an engine-like geometry with optical access.

- In Chapter 8 the thesis closes with a discussion of the results and an outlook for future developments

CHAPTER 2

Introduction to turbulent combustion modelling

This chapter is a general introduction to combustion modelling. First, the reacting flows equations are presented, as they can describe any kind of combustion problem. Afterwards a brief discussion about the significance of models is proposed. Then combustion processes will be classified in order to better define the physical problem which is described in the rest of thesis. Finally, after a brief discussion about the logical steps followed in this work, some issues related to models validation will be discussed.

2.1 Governing equation of reacting flows

The most general way to describe any kind of combustion process of gases is to solve the conservation equations of reacting flows. These differ from standard Navier-Stokes equations as the reacting gas is a mixture of multiple species which must be tracked individually and that change in times due to chemical reactions whose rate requires specific modelling. The reacting flows conservation equations are:

- Conservation of mass:

$$\frac{\partial \rho}{\partial t} + \nabla \cdot (\rho \mathbf{U}) = 0 \tag{2.1}$$

- Conservation of species k:

$$\frac{\partial \rho Y_k}{\partial t} + \nabla \cdot (\rho(\mathbf{U} + \mathbf{V_c})Y_k) - \nabla \cdot \left(\rho D_k \frac{W_k}{W} \nabla X_k \right) = \dot{\omega}_k \tag{2.2}$$

- Conservation of momentum:

$$\begin{aligned}\frac{\partial \rho \mathbf{U}}{\partial t} + \nabla \cdot (\rho \mathbf{U}\mathbf{U}) &= \rho \mathbf{g} - \nabla \left(p + \frac{2}{3}\mu \nabla \cdot \mathbf{U} \right) + \\ &+ \nabla \cdot \left[\mu \left(\nabla \mathbf{U} + \nabla \mathbf{U}^T \right) \right] \end{aligned} \tag{2.3}$$

- Conservation of total enthalpy:

$$\begin{aligned}\frac{\partial \rho h_t}{\partial t} + \nabla \cdot (\rho \mathbf{U} h_t) &= \frac{\partial p}{\partial t} + \rho \mathbf{g} \mathbf{U} - \nabla \cdot \left[\frac{2}{3}\mu \left(\nabla \cdot \mathbf{U} \right) \mathbf{U} \right] + \\ &+ \nabla \cdot \left[\mu \left(\nabla \mathbf{U} + \nabla \mathbf{U}^T \right) \mathbf{U} \right] + \dot{Q} + \\ &+ \nabla \cdot (\lambda \nabla T) + \rho \sum_{k=1}^{N} h_k D_k \frac{W_k}{W} \nabla X_k \end{aligned} \tag{2.4}$$

The only unknown terms of the previous system are the mass reaction rates $\dot{\omega}_k$ which appears in the conservation of species equations. Without reactions ($\dot{\omega}_k$ = 0), these N + 5 equations together with the equation of state of the mixture constitute a closed system of partial differential equations. Given a chemical system of N species reacting through M reactions:

$$\sum_{k=1}^{N} \nu'_{k,j} M_k \Longleftrightarrow \sum_{k=1}^{N} \nu''_{k,j} M_k, \ for \ j = 1, M \tag{2.5}$$

Where M_k is a symbol for species k, and the progress rate of reaction j Q_j:

$$Q_j = K_{f,j} \prod_{k=1}^{N} X_k^{\nu'_{k,j}} - K_{r,j} \prod_{k=1}^{N} X_k^{\nu''_{k,j}} \tag{2.6}$$

Where $K_{f,j}$ and $K_{r,j}$ are respectively the forward and reverse rates of reaction j and are related through an equilibrium constant which only depends on the species of reaction j and temperature. Given the Arrhenius equation:

$$K_{f,j} = A_{f,j} (T)^{\beta_j} exp \left(\frac{E_j}{RT} \right) \tag{2.7}$$

where E_j is the activation energy of the reaction, $\dot{\omega}_k$ can be finally computed as:

$$\dot{\omega}_k = W_k \sum_{j=1}^{M} (\nu''_{k,j} - \nu'_{k,j}) Q_j \tag{2.8}$$

With these relations, the reacting flows equations are closed and can be solved if the mesh size and time step resolution are small enough to solve all the scales which characterize the problem (see section 4.1.2 for more details). The non-reacting part ($\dot{\omega}_k$ = 0) can be directly derived from first principles (for more details see [96] or [123]) and, even if some simplifications have been adopted in the proposed version (like the

Hirschfelderand-Curtiss approximation), these involve negligible errors. The chemical kinetic part can be theoretically derived from statistical mechanics and non-equilibrium thermodynamic theory. The selection of the chemical mechanism (species, reaction and constants $A_{f,j}$, β_j and E_j) is more critical as, for many fuel (except perhaps hydrogen and methane), reduced mechanisms which are able to reproduce the combustion behaviour of the mixture for different temperatures, pressures and compositions, are not available, while detailed mechanisms are too complex to be used in multidimensional domains. Even with simplified mechanisms, the correct resolution of such equations requires an enormous amount of computational power, as the reactions have a large variety of time and length scales which have to be solved. The smallest scales determine the total computational time (for example if the mesh is very fine because of one stiff reaction of one specie, then also the other equations will be solved on the same mesh while it shouldn't be necessary). Up to now, not many 3D DNS cases have been computed [37], [54] and all of them are limited to academic problems. Even accounting for the significant increase of the available computational power during the last decade, the prediction of industrial-relevant applications using the method of Direct Numerical Simulation remains impossible in the foreseeable future. Moreover, unless of a technology revolution, it cannot be even expected that computational power will increase in the near future at the same rate of the last decades [79]. As a consequence, developing simplified models is still of great importance.

2.2 The purposes of models

In the previous section, the need of simplified models was introduced as a way to reduce the computational power and make the study of combustion in industrial configurations possible; so models are seen as design tools. In the next lines, other points of view to see modelling purposes will be given. Direct numerical simulations can be seen as experiments (they are sometimes called experiments) providing some advantages, like the complete control of the set-up and the availability of many accurate information which cannot be provided by modern measurement instruments, and some disadvantages, like long computational time, which limits the number of tests and the size of the domain. Moreover there can be some errors related mainly to the selected chemical reaction mechanism and physical properties. From a gnoseologic point of view, simplified models can be seen as the result of a synthesis process as they describe the main mechanisms that govern the phenomenon hidden in the many equations which are solved within DNS context. Indeed, in many of these models, quantities and parameters which are not present in reacting flows equations are introduced. These parameters are fewer than the variables of reacting flows equations and allow a faster and direct description of the problem. Moreover the comparison of different systems (in terms of composition, fuel, environment) becomes much more intelligible. Finally, because of the complexity of the problem, in many contexts, the accuracy of the models is not enough to describe the whole combustion process, but can anyway provide some useful information. In these cases, models require the aid of experimental data to compensate their lack of accuracy. Numerical parametric studies of quantities, which cannot be controlled in experiments, and computed values of quantities, which cannot be measured, provide a deeper physical insight of the problem and a more comprehensive way

to post-process experimental data.

2.3 Combustion models classification

This section intends to classify the combustion models depending on their level of detail, governing mechanism, problem scale ratio or strategy. modelling of turbulent combustion mainly concerns three aspects: turbulence, chemical reactions and the interaction between flow field and chemistry. Each of these fields includes very challenging problem: for example, turbulence has a hundred years research tradition and, even if many progresses have been done, it is still not considered solved. Combustion models are usually focused on the third aspect, while for the first two, their "stand alone" description is usually employed, even if this is not completely correct, especially for turbulence models. Models can be classified based on:

- The level of details with which turbulence is described. Specifically, three families can be identified: Reynolds Averaged Navier-Stokes (RANS) equations models, Large Eddy Simulations (LES) and Direct Numerical Simulation (DNS) [98]. The first family solves a set of equations whose variables are the time (for statistically steady flows) or ensemble averaged (for statistically unsteady flows) quantities of the flow; all the scales related to turbulence are modelled. The second family solves a set of equations whose variables are the filtered quantities of the flow; the filter size is usually linked to the mesh size and sub-filter turbulence scales are modelled. DNS solves the instantaneous quantities and all the turbulence scales. In this work only RANS approaches will be addressed, even if much of these approaches can be directly applied to LES computations. More details will be given in chapter 4.

- The state of the mixture before the reactions activation, which leads to two very different types of combustion: non premixed combustion (fuel and oxidizer are separated before combustion occurs) and premixed combustion (fuel and oxidizer are already mixed before combustion occurs). The key mechanisms governing these two processes are respectively mixing (turbulent diffusion effect at large scales) and propagation (reaction-diffusion at small scales). As a consequence, models which describe these two configurations are very different (based on somehow opposite assumptions) and are not interchangeable. A third situation is partially premixed flame whose models actually employ a bit of both the previous approaches (depending on the level of incomplete mixing state before combustion). In this work only premixed combustion will be covered.

- Scale ratio analysis, which leads to the characterization of different regimes. In particular, for premixed combustion, according to Peters [92], four regimes can be identified: the wrinkled flamelets regime, the corrugated flamelets regime, the thin reaction regime and the broken reaction regime. In the first two regimes the smallest turbulent scale is bigger than the thicker combustion scale. As a consequence, chemical reactions are confined into a thin layer, the flame structure remains the same of the laminar case and the flame can be considered as an hydrodynamic discontinuity which separates burnt from unburnt gas. In the last regime, turbulence

completely changes the structure of the flame, leading to quenching, while in the third regime stands in the middle. More details will be given in chapter 4.

- The strategy employed to obtain models are essentially two. The first one takes into advantage of the relative magnitude of different controlling parameters and/or the disparate scales. Specifically, reacting flows equations are rewritten in order to outline some terms depending on the previous parameters/scales, which are known to be small from experimental evidence; then the equations are expanded in Taylor series with respect to these variables and higher order terms are neglected. The obtained simplified relations are correct in the limit of the assumed smallness of the considered scale ratio. Accuracy improvements can be achieved retaining higher order terms. The second strategy implies the manipulation of reacting flows equations to change the variables of the problem (for instance from instantaneous to averaged/filtered variables) with more suitable ones. After this process, in the derived equations some terms, which are not written as function of the new variables, appear. They can be added to the set of the variables of the problem together with new transport equations (higher momentum equations) or they can be directly rewritten as functions of the already known variables by means of theoretical or empirical considerations. The merits of the model resulting from this second strategy rely on whenever it reproduces sensible results that compare favorably with experiments. Following Van Dike definition [31] the models obtained with the first strategy are called rational, as they derive from expansion process, and describe the asymptotic behaviour of the equations. In contrast the second strategy is called irrational or phenomenological and relies on physical intuitions of the author. Examples of rational models will be described manly in chapter 3; examples of irrational models will be found in chapter 4.

2.4 Logical structure of this work

The objective of this work is not only to describe the development of a premixed combustion model implemented in OpenFOAM, but it tries to define, according to literature, a series of logical steps which should be followed to achieve the final model. This sequence is the result of the decomposition of the global phenomenon into an ordered series of interconnected elementary mechanisms. Actually, the description of some of these steps has not yet exhaustively covered, because of their complexity and the difficulties in carrying out experimental measures. In addition, this split helps to delineate strengths and weaknesses of models and the aspects which require further investigations. Engine environment is commonly associated with the corrugated flamelets regime. The paradigm which characterizes this regime is that the flame retains a laminar like structure and the interaction between turbulence scales and flame front is purely kinematic. As a consequence, the description of the flame dynamic does not require the solution of chemical reactions, but the flame can be regarded as a propagating surface which is wrinkled by turbulent eddies. The logical sequence to build a model based on these assumptions should involve the following steps:

1. Characterize the mixture and the chemical reaction scheme with some global parameters and relations describing the kinematic behaviour of the corresponding laminar flame.

2. Identify turbulence scales affecting the flames and the global parameters which describe these scales.
3. Model the interaction between turbulent scales and the flame with some relations which rely on the previously defined global parameters.

The structure of the following chapters will try to follow this outline and information available in the literature will be organized according to this logic. The author hopes that this structure will make it easier to understand the state of the art of the topic, modelling issues and limits of the proposed approach and some ideas of future developments.

2.5 Experiment and modelling issues

The problem of turbulent combustion is very complex as it involves the interaction of strongly non linear processes. In order to make the problem mathematically handy, rational models usually introduce simplifications (for example constant density combustion) that make their results appear quite dubious a priori. Irrational models are usually developed under less restrictive assumptions, but are based on physical intuitions and lack of the rigor guaranteed by mathematical derivation. As a consequence, their solution must be compared with more reliable results of the problem. These results can be obtained by the DNS or by experiments. As already stated, DNS have some minor modelling issues, but their greater problem is related to computational time and memory storage, as many simulations are required in order to compute the quantities which are predicted by simplified models (such as the ensemble average) or to estimate the response to the variation of some parameters. Moreover, for many situations (like high pressure environments), DNS are so expensive that no computation have been actually carried out. As a consequence, nowadays only experiments are suitable for models validation. The problem is how to design an experiment in order to obtain reliable and useful data. In order to explain some issues related to this topic, a simple historical example is described.

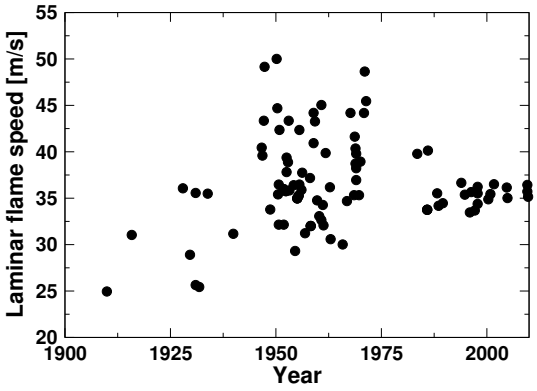

Figure 2.1: *Historical measurements of the maximum laminar flame speed for methane/air mixtures at ambient temperature and pressure. Old data obtained from [5] and [58] with recent measurements taken from [44] and [87].*

Figure 2.1 shows the measurement of the maximum laminar flame propagation speed (a fundamental parameter for premixed combustion theory) for methane/air mix-

tures at the same environment conditions over the past 60 years from different authors. Among the quantities which characterize turbulent combustion, laminar flame propagation speed is one of the less complicated to be measured. From the picture, it can be noticed that before the half of the eighties, the measurements show a large scatter, which has been considerably reduced in the last twenty years. This reduction was not due to the development of new measuring techniques, but to the finds of asymptotic theory described in [20], [75] which introduced a physical relation between laminar flame speed and another parameter known as stretch. Then the new experiments were designed in order to take into account this new parameter. Experimental data were corrected and the scatter reduced to much lower values. Reminding that this problem is not considered completely solved, as new corrections and experimental procedures are still proposed [127], this case is a powerful example which represents a successful application of a model to analyze experimental data. In particular it shows how a simplified model was able to make explicit a physical mechanism which was included in the reacting flows equations, which were already well known at the time. Moreover it shows one of the few examples where the results of a model were used to correct experimental data and not the reversal. For turbulent cases the problems are more complicated: models quantities, like ensemble Favre averages, are difficult to be measured directly and usually some correlations and assumptions (not always completely justified, see for example section 4.6.2) are used in order to obtain values for the comparison. Moreover, some of the statistical quantities which characterize turbulence flows, like the integral length scale, are harder to be accurately measured, also because their definition is not easy to be converted into a measuring technique. Finally, various definition of quantities which represent the same parameter, for example the laminar flame thickness, can be found in literature. In many works the results are shown in terms of non-dimensional numbers, and, even if the formulas employed to obtain these numbers are clearly stated, it is not always clarified which definition has been used to define the quantities which enter in these formulas.

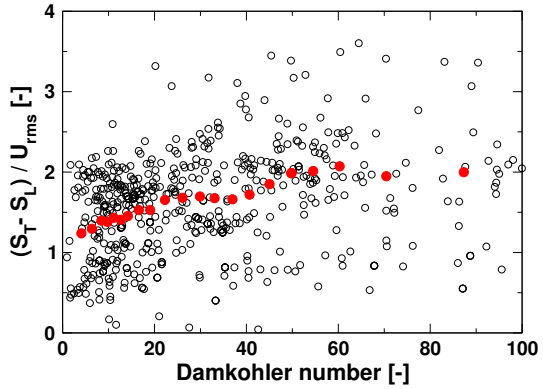

Figure 2.2: *Measured planar turbulent burning velocity S_t reduced by the laminar flame speed S_L and normalized with the mean square root of velocity u_{rms} for different Damkohler numbers: black dots values are the data reported by different authors, red dots are their sector average.*

As a second example, Figure 2.2 shows the experimental results taken from the quite well known Leeds group's data collection [13]. The values have been rearranged in order to underline the relation between some non-dimensional parameters. These

parameters are the Damkohler number, the root mean square of flow velocity, the laminar flame speed and the turbulent burning speed. The figure shows a large scatter of values; their local average (red dots) shows a trend, but the standard deviation is close to the average value. Because of the problems previously reported, it is not clear if this scatter is due to lack of well defined correlation between the chosen parameters or to the incompatibility of the different experimental configurations or to the uncertainties of the measurements or if the turbulent burning velocity is a very unstable parameter. If the last case is true, even the existence of this parameter could be questioned. The author thinks that a further development of turbulent combustion theory and models, in conjunction with more accurate experimental techniques, can resolve these issues and can provide a deeper understanding of the governing mechanisms, increasing at the same time the accuracy of the results predicted by numerical simulations. The example reported in Figure 2.1 supports this encouraging prospect.

CHAPTER 3

Laminar flame modelling

Premixed combustion requires complete mixing of fuel and oxidizer at molecular level. Chemical reactions are initiated by a local temperature increase above the cross-over temperature of the mixture. Beyond this value, chain-breaking reactions dominate over chain-branching reactions. The balance between heat release and heat diffusion results in the propagation of a thin layer where the all reactions are confined. Because of the large range of spacial and time scales involved, for many applications the resolution of chemical reactions is the most computationally demanding part of premixed combustion. As a consequence, the first important stage is to build up a simplified model to replace this complex chemical mechanism with something which is able to describe only a part of its physics in an efficient way. The main interest of this work is directed towards the prediction of heat release, which requires only the kinematic description of this thin layer. In this chapter, aspects of laminar flame propagation are analyzed in order to find a set of parameters and relations to describe their kinematic behaviour.

3.1 The Planar laminar flame

The solution of reacting flows equations presented in section 2.1 involves many time and space scales, which are strictly related to the value of activation energy of the many reactions which compose the chemical mechanism. The simplest combustion problem that can be solved is the laminar planar steady state configuration which can be considered one dimensional and, thanks to local refining strategies, can be solved quite quickly. Many optimized solvers have been developed for this task [40], [47]. In this work the opensource code FlameMaster by Pitsch Group [1] is used.

Figure 3.1 shows an example of temperature profile and heat release rate of a stoichiometric methane mixture. The balance between heat release related to reaction

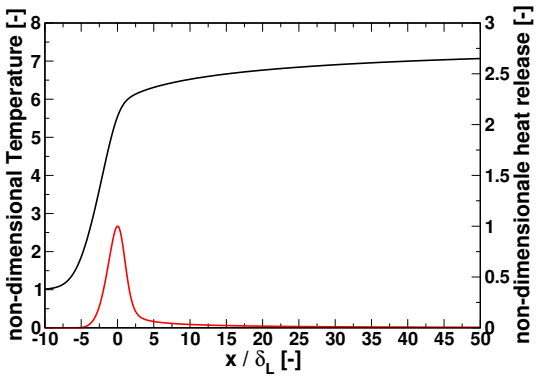

Figure 3.1: *Temperature and heat release profiles of a stoichiometric methane/air mixture at 300 K and 1 bar. Temperature is made non-dimensional by means of the unburnt value, while the heat release is scaled on its maximum value.*

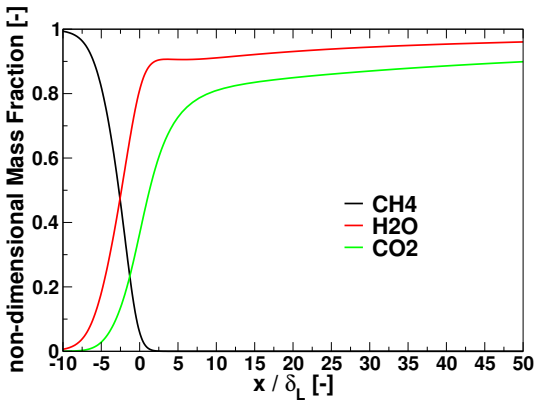

Figure 3.2: *Mass fraction profile of methane, water and carbon dioxide for a stoichiometric methane/air mixture at 300 K and 1 bar. The values are scales on their corresponding maximum value.*

progress and heat diffusion results in the propagation of a thin layer, where the temperature of the mixture increases from the unburnt value to the adiabatic flame temperature and the mixture composition changes from reactants to products. Looking at the temperature and heat release profiles, three zones can be identified:

- the preheat zone, which is characterized by a change of temperature and species concentrations which is essentially due to diffusion and is chemical inert.
- the inner reaction zone, in which the fuel is consumed to form intermediate species (like CO).
- the oxidation layer, where the intermediate species are oxidized (see figure 3.1) and temperature rises to the adiabatic flame value.

The flame propagates normal to itself towards the unburnt gas with a speed known as laminar flame speed S_L. This quantity is a thermo-chemical property of the mixture and is an eigenvalue of the system of the reacting flows equations. In order to make the flame steady in 1D computation, the mixture at the inlet is introduced with a velocity equal to the laminar flame speed. This set-up is also used in experiments. In particular,

due to heat release and mass conservation, the velocity at the outlet is equal to the velocity at the inlet multiplied by the ratio between the adiabatic flame temperature and inlet/unburnt gas temperature. In the preheat zone, chemical reactions are negligible and a balance between convection and diffusion exists. In this zone, the mixture temperature rises towards the reaction zone until the thermal energy reaches the activation energy of chain-breaking reactions. In the inner reaction zone, diffusion-reaction balance exists and most of the heat is released. Finally, intermediate species are oxidized to combustion products, primarily formed by CO_2 and H_2O, in the oxidation zone. While the fuel is completely consumed in the reaction zone, formation of CO_2 and H_2O requires a more time. Due to the higher velocity at outlet, this time corresponds to a long tail of the flame after the reaction zone which is observed in Figure 3.2. Various relations have been proposed to identify a length scale which characterizes the zone in which the reaction-diffusion process is confined. The first relation is derived by a convection-diffusion balance in the preheat zone, which gives:

$$\delta_L = \frac{\lambda}{\rho c_p S_L} \tag{3.1}$$

While S_L is always associated with the inlet velocity and it is uniquely defined for the mixture, λ, ρ and c_p should be computed at the interface between preheat zone and inner layer reaction zone. Usually the properties of that interface are not known a priori and are hard to be identified. A possible approach to estimate them is to compute the properties at the unburnt gas conditions and then to correct them with respect of the adiabatic flame temperature using the formula proposed in [96]:

$$\delta_L = 2\frac{\lambda_u}{\rho_u c_{p,u} S_L}\left(\frac{T_{ad}}{T_u}\right)^{0.7} \tag{3.2}$$

Where the subscript "u" means that the quantity is computed at unburnt mixture conditions. On the contrary, in many experimental works relation 3.1 is computed with the properties at unburnt condition as they can be easily measured. In this case, the obtained thickness is commonly known as diffusion length. The second relation is based on the spatial increase of temperature:

$$\delta_L = \frac{T_{ad} - T_u}{max \mid \frac{\partial T}{\partial x} \mid} \tag{3.3}$$

This relation better represents the physical meaning of this parameter, but requires the 1D temperature profile, which depends on the chemical mechanism selected for the considered fuel. Figure 3.3 shows a comparison of the laminar flame thickness computed with these three different expressions. As can be noted, δ_L obtained by 3.1 at unburnt conditions and 3.3 are of the same order of magnitude, but quantitatively the second value is 5-6 times bigger than the first. Relation 3.2 gives results which are much closed to the value obtained with 3.3. In literature both 3.1 and 3.3 are commonly employed and some problems can arise when comparing the results depending on non-dimensional numbers which require δ_L. Equation 3.2 can be used to estimate δ_L referred to the temperature gradient definition, when only few are available. In general the flame thickness of common fuel at ambient pressure is a fraction of millimeter. At

higher temperatures and pressures, which are typical engine environment, this value decreases even further.

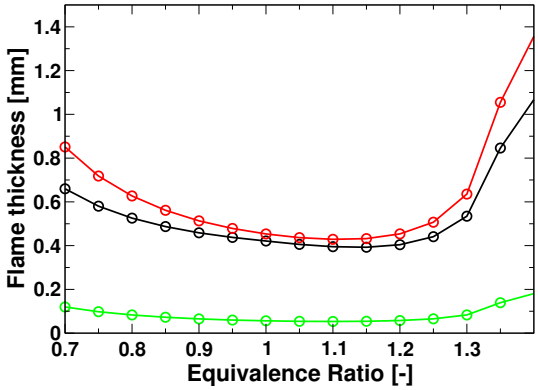

Figure 3.3: *Laminar flame thickness for different equivalence ratio of methane-air mixture at* $1atm$ *and* $25°C$*. The black line correspond to the maximum temperature gradient definition (Eqn. 3.3), the red line with Eqn. 3.2 and the green line with the diffusion length (Eqn. 3.1 with unburnt gas properties).*

From the computation of 1D laminar flames many important parameters can be estimated. Some of them have been already introduced like the laminar flame speed and thickness, others will be presented in the following sections. Before proceeding with the discussion, some kinematic definitions related to laminar flames will be given:

- Absolute flame speed: flame front speed relative to a fixed reference frame, it will be indicated with V.
- Displacement flame speed: flame front speed relative to the flow, it will be indicated with S.
- Consumption speed: speed at which reactants are consumed, it will be indicated with C.

For example, in the planar case, the flame propagation speed changes in space and it increases towards the burnt gas zone, while the absolute velocity is constant and equal to zero. The consumption speed is only one for every mixture composition as it is defined as the volume integral across the whole flame thickness. In the planar case it is equal to the inlet velocity.

3.2 Asymptotic analysis of unstretched laminar flame

In this section some concepts related to asymptotic theory applied to laminar flame studies are introduced. This is done in order to clarify the limits and potentiality of this approach to study the physical mechanisms which are the objects of the present work. First the common hypothesis used to simplified the reacting flows equations are presented and their validity is discussed; then the resulting non-dimensional system of equations will be presented and finally an example of asymptotic result will be given.

3.2.1 Asymptotic theory assumptions

Asymptotic methods take advantage of the relative magnitude of the different controlling parameters and/or the disparate scales to replace a complicated problem by a simpler one. In order to identify these parameters for laminar flame studies, the following assumptions are usually employed:

- The reaction mechanism, at least for the description of the dynamic of the flame, can be replaced by a single irreversible global reaction:

$$\nu_E M_E + \nu_D M_D \Longrightarrow Products \tag{3.4}$$

$$\nu = \frac{\nu_E W_E}{\nu_D W_D} \tag{3.5}$$

$$\Phi = \frac{Y_{E,u}}{\nu Y_{D,u}} \tag{3.6}$$

$$\dot{\omega} = A\left(\rho X_D\right)^{n_D}\left(\rho X_E\right)^{n_E} exp\left(\frac{E_a}{RT}\right) \tag{3.7}$$

  Where the subscripts D and E indicate respectively deficient and excess reactants, ν is the mass weighted stoichiometric coefficient ratio and $\Phi \geq 1$ corresponds to the equivalence ratio for rich mixtures and the air excess index for lean mixtures. Even if some analyses have been conducted with simplified chemical mechanisms up to four reaction [93], [105], the results with a single global reaction are more significant and can be generalized to any fuel; so only this case is considered here. With a single global reaction mechanism, there is no oxidation layer, but only preheat and inner reaction zone. An example of resulting temperature profile is given in figure 3.4. The parameters of the global reaction (the constants in equation 3.7) change with the mixture composition. They can be computed starting from the planar solution with the detailed chemical mechanism and exploiting some relations derived from asymptotic theory, as proposed in [113]. Between them, the most important parameter is the activation energy E_a which is usually represented by means of the non-dimensional number dedicated to Zel'dovic:

$$Ze = \frac{E_a(T_{ad} - T_u)}{RT_{ad}^2} \tag{3.8}$$

  and represents the sensitivity of the flame to temperature changes.

- The activation energy of the global reaction, i.e. the Zel'dovic number, is very large. The value of Ze is typically in range between 5 and 15. The lower this value, the higher will be the error associated with the neglected higher order terms which arises when asymptotic analysis is carried out.

- The properties of the mixture λ, μ, D_k can change with temperature and pressure, but the Lewis and Prandtl numbers are constant. Effects of the change of mixture composition across the flame on the previous properties are not considered.

$$Le_k = \frac{\lambda}{\rho c_p D_k} = \frac{D_{th}}{D_k} \tag{3.9}$$

$$Pr = \frac{\mu c_p}{\lambda} = \frac{\nu}{D_{th}} \tag{3.10}$$

Where D_k is the binary diffusion coefficient with respect to nitrogen of species k, which is realistic if the oxidizer is air. Because thermal diffusivity D_{th}, binary diffusion coefficient D_k and the kinematic viscosity ν have essentially the same temperature and pressure dependence, this assumption is realistic.

- The product $Ze(Le - 1) = \mathcal{O}(1)$. This means that the Lewis number of the species which form the mixture should be close to one. This is generally not true, but the fact that Ze is not very high can compensate the error introduced by this approximation.
- Low Mach number approximation. This assumption is valid for many industrial applications and even for spark-ignition engines if only the combustion process is studied.

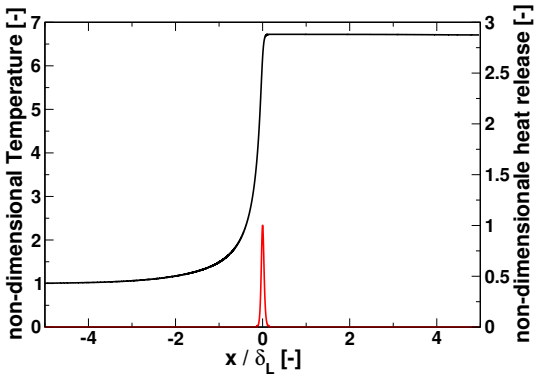

Figure 3.4: *Example of non-dimensional temperature (T/T_u) and non-dimensional heat release profile (ω/ω_{max}) for a 1 step global reaction mechanism with Ze = 10. The preheat zone is about five times δ_L, while the reaction zone ($\omega \neq 0$) is about δ_L/Ze.*

3.2.2 Asymptotic theory: governing equations

In order to write the reacting flows equations in non-dimensional form and to underline the scales which will be exploited for the analysis, scaling quantities must be defined. Specifically velocity is scaled on the planar (unstretched) laminar flame speed (from now named S_L^0). A generic hydrodynamic length scale L which characterizes the problem is used as length scaling quantity. $\delta = \delta_L/L$ defines the ratio between diffusion thickness (Eqn. 3.1 using unburnt gas properties) and the hydrodynamic length. $\theta = (T - T_u)/(T_{ad} - T_u)$ is used as non-dimensional temperature. All the other quantities are scaled with their value in the unburnt gas zone. The resulting non-dimensional low Mach number reacting flows equations are:

$$\frac{\partial \rho}{\partial t} + \nabla \cdot (\rho \mathbf{U}) = 0 \tag{3.11}$$

$$\frac{\partial \rho \mathbf{U}}{\partial t} + \nabla \cdot (\rho \mathbf{U}\mathbf{U}) = -\nabla (p) + \delta Pr \nabla (\lambda \Sigma) \tag{3.12}$$

$$\frac{\partial \theta}{\partial t} + \nabla \cdot (\rho \mathbf{U} \theta) - \delta \nabla (\lambda \nabla \cdot \theta) = \frac{\gamma - 1}{\gamma} \delta^{-1} \omega \tag{3.13}$$

$$\frac{\partial Y_D}{\partial t} + \nabla \cdot (\rho \mathbf{U} Y_D) - \delta L e_D^{-1} \nabla (\lambda \nabla \cdot Y_D) = -\delta^{-1} Y_{D,u} \omega \tag{3.14}$$

$$\frac{\partial Y_E}{\partial t} + \nabla \cdot (\rho \mathbf{U} Y_E) - \delta L e_E^{-1} \nabla (\lambda \nabla \cdot Y_E) = -\delta^{-1} \nu Y_{D,u} \omega \tag{3.15}$$

$$\rho[1 + (\sigma - 1)/\sigma] = P(t) \tag{3.16}$$

$$\frac{\partial P}{\partial t} = \frac{\gamma q}{V} \int_V \omega \, \mathrm{d}V \tag{3.17}$$

$$\omega = Da \rho^{n_D + n_E} Y_D^{n_D} Y_E^{n_E} exp\left(\frac{Ze\sigma(\theta - 1)}{1 + (\sigma - 1)\theta}\right) \tag{3.18}$$

$$Da = \frac{\lambda}{\rho_u c_p S_L^2} A \rho_u^{n-1} W_D \frac{\nu_D}{Y_{D,u}} exp\left(\frac{E_a}{RT}\right) \tag{3.19}$$

Where Σ is the viscous stress tensor, γ is the heat capacity ratio, Da is the Damkohler number (defined as the ratio of flow time on reaction time), σ is the ratio of unburnt on burnt gas densities and q is the heat release parameter. $P(t)$ is the average pressure of the system which can be computed from the integral of heat release in the whole volume V of the system 3.17, while p is the hydrodynamic pressure. In open systems $P(t) = 1$.

3.2.3 Asymptotic theory: laminar flame speed computation

As a simple example of application of asymptotic process, the derivation of an expression to compute the laminar flame speed for mixture far from stoichiometry is proposed. The following analysis will clarify some of the concepts which were introduced in the previous sections about the structure of a laminar flame. The problem to be solved is a planar flame which propagates against a flow whose velocity is constant and equal to the opposite of the propagation speed. This property implies that the absolute velocity of the flame is zero and the problem is steady. The hydrodynamic length is equal to the diffusion length δ_L, time derivatives are zero and spatial derivatives are different from zero only in one direction (x direction). $x = 0$ is the position of the reaction zone, whose thickness is proportional to δ_L / Ze and tends to zero for large activation energy. The unburnt side is located in the negative region of x. Being the mixture far from stoichiometry, only the deficient mass fraction equation is needed. For positions sufficiently remote from $x = 0$ (preheat zone and burnt zone) ω is negligible and the resulting equations are:

$$\rho \left(1 + \frac{\sigma - 1}{\sigma}\right) = 1 \tag{3.20}$$

$$\rho \mathbf{U} = 1 \tag{3.21}$$

$$\frac{\partial \theta}{\partial x} - \frac{\partial^2 \theta}{\partial x^2} \sim 0 \tag{3.22}$$

$$\frac{\partial Y_D}{\partial x} - Le_D^{-1}\frac{\partial^2 Y_D}{\partial x^2} \sim 0 \tag{3.23}$$

$$\omega = Da\rho^{n_D}Y_D^{n_D}exp\left(\frac{Ze\sigma\left(\theta-1\right)}{1+\left(\sigma-1\right)\theta}\right) \tag{3.24}$$

The solutions of equations 3.22 and 3.23 with the corresponding boundary conditions are:

$$\theta = \begin{cases} exp(x), & \text{if } x < 0 \\ 1, & \text{if } x > 0 \end{cases} \tag{3.25}$$

$$Y_D = \begin{cases} Y_{D,u}(1-exp(Lex)), & \text{if } x < 0 \\ 0, & \text{if } x > 0 \end{cases} \tag{3.26}$$

These solutions are not valid near $x = 0$, which is the reaction zone position, where ω is no more negligible. In this region the sum of equations 3.22 and 3.23 is:

$$\frac{\partial(\theta + Y_D)}{\partial x} - \frac{\partial^2(\theta + Le^{-1}Y_D)}{\partial x^2} = 0 \tag{3.27}$$

Integration of 3.27 across the reaction zone (from $x = 0^-$ to $x = 0^+$) and the continuity of variables at $x = 0$ give the following jump relations (namely the value on the burnt side minus that on the unburnt side):

$$[[\theta]] = [[Y_D]] = 0 \tag{3.28}$$

$$[[\frac{\partial\theta}{\partial x}]] + Le^{-1}[[\frac{\partial Y_D}{\partial x}]] = 0 \tag{3.29}$$

Introducing a stretching coordinate transformation $x = Ze^{-1}\xi$ in the governing equations and looking for solutions in the form:

$$\theta = 1 + Ze^{-1}\phi(\xi) + ... \tag{3.30}$$

$$Y_D = Ze^{-1}\psi(\xi) + ... \tag{3.31}$$

$$Da = Ze^{n+1}(\Lambda + Ze^{-1}\Lambda_2 + ...) \tag{3.32}$$

The following equations are obtained:

$$Ze^{-1}\frac{\partial\phi}{\partial\xi} - \frac{\partial^2\phi}{\partial\xi^2} = \Lambda\sigma^{-n_D}\psi^{n_D}exp(\phi) \tag{3.33}$$

$$Ze^{-1}\frac{\partial\psi}{\partial\xi} - Le_D^{-1}\frac{\partial^2\psi}{\partial\xi^2} = -\Lambda\sigma^{-n_D}\psi^{n_D}exp(\phi) \tag{3.34}$$

It can be noted, that in the reaction zone, the convective term is a higher order term with respect to the conductive and reaction terms. Summing as before 3.33 and 3.34, the following relation is obtained:

$$Le_D\frac{\partial^2\phi}{\partial\xi^2} + \frac{\partial^2\psi}{\partial\xi^2} = 0 \tag{3.35}$$

Whose solution is:

$$Le_D\phi + \psi = 0 \tag{3.36}$$

The solution of 3.33 and 3.34 must match θ and Y_D as $\xi \to \pm\infty$. Expanding 3.25 and 3.26 near $x = 0^{\pm}$, the matching relations are:

$$\phi = \begin{cases} 1+\xi, & \text{if } \xi \to -\infty \\ 0, & \text{if } \xi \to +\infty \end{cases} \tag{3.37}$$

$$\psi = \begin{cases} -Y_{D,u} Le_D \xi, & \text{if } \xi \to -\infty \\ 0, & \text{if } \xi \to +\infty \end{cases} \tag{3.38}$$

Neglecting the convective term, multiplying 3.34 by $\frac{\partial\psi}{\partial\xi}$ and integrating from $\xi \to -\infty$ to $+\infty$ and from $\psi = \infty$ to 0, the following relation is obtained:

$$\frac{1}{2}\left(\frac{\partial\psi}{\partial\xi}\,|_{-\infty}^{+\infty}\right)^2 = -\Lambda Le_D \sigma^{-n_D}\int_{\infty}^{0}\psi^{n_D} exp\left(-\frac{\psi}{Le}\right)d\psi \tag{3.39}$$

which, for the matching relations 3.38, is equal to:

$$\frac{1}{2}Y_{D,u}^2 Le^2 = \Lambda Le_D^{n_D+2}\sigma^{-n_D}\Gamma(n_D+1) \tag{3.40}$$

Remembering relations 3.32 and 3.19, the dimensional laminar flame speed is:

$$S_L^2 = \frac{\rho_b^{n_D}}{\rho_u}\frac{\nu_D W_D}{Y_{D,u}^3}\frac{2A\Gamma(n+1)(\lambda/cp)}{Le_D^{-n_D} Ze^{n_D+1}} exp\left(\frac{E_a}{RT_{ad}}\right) \tag{3.41}$$

A more comprehensive formulation of the laminar flame speed, which includes variation of the properties with temperature and for general mixture composition, can be derived with the same (but more tedious) procedure and it is:

$$\begin{aligned} S_L^2 = {} & \frac{2Ag(n_D, n_E; Ze(\Phi-1)/Le_E)(\lambda_b/cp)}{\rho_u^2 Ze^{n_D+n_E+1}} Le_D^{n_D} Le_E^{n_E} \cdot \\ & \cdot \frac{\nu_E^{n_E} Y_{D,u}^{n_D+n_E-1}\rho_b^{n_D+n_E}}{\nu_D^{n_E-1} W_D^{n_D+n_E-1}} exp\left(\frac{E_a}{RT_{ad}}\right) \end{aligned} \tag{3.42}$$

with:

$$g(a,b;Z) = \int_0^{\infty} \varsigma^a(\varsigma+Z)^b exp(-\varsigma)\,\mathrm{d}\varsigma \tag{3.43}$$

Equation 3.42 is able to explain many trends which are well documented by experimental data. For example, at higher adiabatic flame temperature correspond higher propagation speed value and thinner flame structure. It also explains why the maximum propagation speed is close but not at stoichiometric conditions for which T_{ad} is the highest. In fact, the product $Le_D^{n_D} Le_E^{n_E}$ moves the flame speed peak a little to the lean side for light fuel, like hydrogen, and to the rich side for heavier fuel like isooctane. Moreover asymptotic process also shows how to increase the accuracy of the prediction. For example if higher order terms of equation 3.32 are kept, the accuracy of the predicted flame speed can be improved for realistic activation energy values.

3.3 Asymptotic analysis of stretched laminar flame

In this section, the discussion is focused on possible modifications of laminar flame speed due to the interaction of the flame with the flow field. In particular different relations between flame speed and stretch rate which has been developed in the years are reviewed. Moreover some equations and experimental techniques to estimate the governing global parameters are presented. The effect of flow field and shape of the flame are considered with one parameter known as stretch rate K. Its definition for a surface is:

$$K = \frac{1}{A}\frac{dA}{dt} = S_L \nabla \cdot n - n \cdot E \cdot n = S_L \kappa + K_s \tag{3.44}$$

Where A is the area of the surface, n is the direction normal to the flame front pointing to the burnt side, E is the rate of strain tensor $1/2(\nabla \mathbf{U} + (\nabla \mathbf{U})^T)$, κ is the curvature of the surface, K_s the strain rate and V_f is the absolute velocity of the flame $\mathbf{U} - S_L n$. Equation 3.44 is the most commonly adopted formulation to define stretch rate in large activation energy asymptotic theory context, which implicitly considers the flame as a surface with negligible thickness. Another approach employed to take into account also the thickness of the flame is the integral analysis derivation [19]. These two approaches give different results, but, even if the second one seems to be more comprehensive, it requires some ad hoc assumptions. It has been recently completely proved in [38] that the first approach, once extended and correctly applied, can be used also inside the flame (preheat zone) and gives results which agree very well with numerical simulations. For this reason only this second approach is discussed.

Even if Markstein presented in [72] an empirical formulation which connects stretch rate with flame speed, only after the theoretical works of Clavin and Matalon [20], [75] the scientific community recognized that the laminar flame speed they were measuring was affected by the geometric configuration employed in the experiments. In order to evaluate a propagation speed which only depends on mixture composition and thermodynamic conditions (pressure and temperature), known as unstretched laminar flame speed (S_L^0), a perfect planar flame configuration should be employed. Because such configuration is quite hard to be faithfully reproduced, extrapolation from stretched data to zero stretch value is commonly employed [127]; such approach requires the knowledge of a relation between stretch and flame speed. For weakly stretched flames, asymptotic analysis is able to derive the value of laminar flame speed subject to stretch, applying the same methodology shown in the previous section, but with two additional steps: first, a curvilinear coordinate system (χ_1, χ_2, n) is introduced in order to generalize the equations to every flame shape. n is the direction normal to the flame and χ_1, χ_2 are two directions tangential to the flame in the point. Second, the considered hydrodynamic length L is no more equal to δ_L, but it is much bigger ($L >> \delta_L$). Second, the stretching process, which was previously applied only to the reaction zone, is also employed to describe the rest of flame structure. As a consequence, two stretching coordinates are introduced: $\eta = \delta^{-1} n$ for preheat zone and $\xi = Ze^{-1}\eta$ for the reaction zone. From the analysis of the flame structure (see [74]), the jumping conditions across the whole flame and the corrected flame propagation speed with respect to the unstretched value are:

- jumping conditions:

$$[[\rho(\mathbf{U} - V_f)]] = \delta\frac{\sigma - 1}{\sigma}\gamma_1 K \tag{3.45}$$

$$[[n \times (\mathbf{U} \times n)]] = \delta\{-(\lambda_b Pr + \gamma_1)(n \times (\nabla \times n)) + \\ +2Pr(\lambda_b - 1)(n \times (E \cdot n) \times n)\} \tag{3.46}$$

$$[[p + \rho(\mathbf{U} \cdot n)(\mathbf{U} \cdot n - V_f)]] = \delta\{\gamma_1[[n \cdot \nabla p]] + \\ +\frac{\sigma - 1}{\sigma}\gamma_1 V_f K + \Gamma\kappa + 2Pr(\lambda_b - 1)(n \cdot E \cdot n)\} \tag{3.47}$$

- Propagation speed with respect to unburnt side:

$$S_{L,u} = S_L^0 - \alpha\delta_L K \tag{3.48}$$

- Propagation speed with respect to burnt side:

$$S_{L,b} = \sigma(S_L^0 - (\alpha + \frac{\sigma - 1}{\sigma}\gamma_1)\delta_L K) \tag{3.49}$$

Where:

$$\alpha = \gamma_1 + \frac{Ze(Le_{eff} - 1)}{2}\gamma_2 \tag{3.50}$$

$$Le_{eff} = Le_D + (Le_E - Le_D)\frac{n_D g(n_E, n_D - 1; Ze(\Phi - 1)/Le_E)}{g(n_D, n_E; Ze(\Phi - 1)/Le_E)} \tag{3.51}$$

$$\Gamma = (\sigma - 1)\gamma_1 + (2Pr - 1)\gamma_3 + 2Pr(\sigma - 1)\lambda_b \tag{3.52}$$

$$\gamma_1 = \frac{\sigma}{\sigma - 1}\int_1^\sigma \frac{\lambda(x)}{x}\,dx \tag{3.53}$$

$$\gamma_2 = \frac{1}{\sigma - 1}\int_1^\sigma \frac{\lambda(x)}{x} ln\left(\frac{\sigma - 1}{x - 1}\right)\,dx \tag{3.54}$$

$$\gamma_3 = \int_1^\sigma \lambda(x)\,dx \tag{3.55}$$

The product $\alpha\delta_L$ is known as Markstein length and α as Markstein number. The term γ_1 is associated with thermal diffusion, while $Ze(Le_{eff} - 1)$ is associated with the contribution due to inequality of thermal-mass diffusion. It can be noted that, due to the jumping conditions across the flame, two different Markstein numbers can be defined: one with respect to unburnt gas Ma_u and the other with respect to the burnt gas Ma_b. While both relations 3.48 and 3.49 can be used to describe the motion of the flame, only Ma_b has a corresponding physical quantity which can be measured. In literature other Markstein numbers have been identified [10], one associated with the stretch rate Ma_K and another one associated only to curvature Ma_c. As all these definitions can generate confusion, in order to clarify the meaning of all these quantities, the extended relation [7] which is valid inside the flame is presented:

$$S_L = S_L^0 - \delta_L\{K\left[\alpha - \int_\theta^\sigma \frac{\lambda(x)}{x(x-1)}\,dx\right] - \left[\int_1^\sigma \frac{\lambda(x)}{x}\,dx.\right] + \\ +\kappa S_L\left[\int_\theta^\sigma \frac{\lambda(x)}{x-1}\,dx.\right]\} \tag{3.56}$$

where:

$$\theta = 1 + (\sigma - 1)exp(\eta) \tag{3.57}$$

η is the stretched coordinate inside the preheat zone and after the reaction zone. In particular $\eta \to -\infty$ corresponds to the leading edge of preheat zone; the reaction zone starts at $\eta \to 0^-$ and ends at $\eta \to 0^+$. The region after the reaction zone ends at $\eta \to +\infty$. Equation 3.56 shows that the laminar flame speed is linearly dependent on both stretch rate K and curvature κ and can be rewritten as:

$$S_L = S_L^0 - Ma_K\delta_L K - Ma_c\delta_L\kappa \tag{3.58}$$

Which shows the existence of the two Markstein numbers identified in [10]. If equation 3.56 is computed on the burnt side ($\eta \to +\infty$), Ma_c becomes zero and Eqn. 3.56 reduces to the relation 3.49, which represents the motion of the iso-surface $T = T_b$. On the un burnt side ($\eta \to -\infty$), equation 3.56 does not become relation 3.48. This is because Ma_u is a parameter which describes the motion of the whole flame seen as a surface and takes into account the variation of temperature along the preheat zone; hence it does not characterize the motion of the leading edge of the preheat zone. Moreover, distinction of curvature and stretch Markstein number is meaningful only inside the flame, but it is not required to define the motion of the flame. In summary, among the all parameters, Ma_b is the most significant one because it can be measured [50], [87] and it can describe the motion of the flame. Ma_u can be derived from the value of Ma_b by means of equation 3.49. Their meaning is the same and their different values are due to the jumping relation which abruptly changes the velocity across the flame, which is seen as a discontinuity surface. These two Markstein numbers must be used together with their coherent value of flame propagation speed and flow velocity. The physical mechanism which governs the process is related to the change of temperature of the reaction zone induced by stretching effect. In particular, looking at the definition of α, it can be noted that this value is the summation of two contributions: the first one γ_1 is due to thermal diffusion and it is always positive (reduction of reaction zone temperature with positive stretch), while the second term is proportional to $Ze(Le_{eff} - 1)$, which can be positive or negative depending on Le_{eff}, and it is magnified by the positive term γ_2, whose value is close to γ_1. This second term is connected with non equality of mass-thermal diffusion which can change the local total enthalpy of the mixture in the reaction zone and the related flame temperature. In particular Le_{eff} depends on the diffusivity of the deficient and excess reactants, weighted with a term which increases the importance of the deficient reactant as the mixture gets far from stoichiometric air/fuel ratio. For Le_{eff} > 1 the second term is always positive, while if Le_{eff} a bit less than one the whole Markstein number becomes negative. The introduction of this linear relation to extrapolate the unstretched laminar flame speed has considerably reduced the scattering previously reported in literature. Still, the measurements of the unstretched laminar flame speed have uncertainties around 10% which is considered too much for

such a fundamental parameter. For this reason new relations to correlate laminar flame speed with stretch have been proposed and applied in particular for spherical expanding flames. Because the initial stages of the flame development in spark-ignition engine is connected with this configuration, in the following some details about this problem will be given even if it is usually regarded as an experimental issue. For spherical expanding flames in initial quiescent velocity field, geometry considerations lead to the following expression for the stretch rate:

$$K = \frac{2}{r}\frac{dr}{dt} \tag{3.59}$$

The experimental quantity which is usually measured is the radius of flame. Its time evolution is used to numerically evaluate its time derivative. The problem is how to relate the radius and its time derivative with the unstretched laminar flame speed and the Markstein number and how to select the range of measured radius to increase the accuracy of extrapolation to zero stretch rate. Starting from 3.49 and defining S_L as the ratio of actual propagation speed with the unstretched value, different correlations have been proposed:

$$S_L\left(1 + \frac{2Ma_b\delta_L}{r}\right) = 1 \tag{3.60}$$

$$S_L = \left(1 - \frac{2Ma_b\delta_L}{r}\right) \tag{3.61}$$

The first expression is derived from asymptotic results. The second one, which was originally proposed by Markstein in 1964, correlates dR/dt with S_L^0 instead of the actual value S_L. Another non linear relation can be found in literature [73], [104] and has been derived without the assumption of $Ze(Le-1) \sim \mathcal{O}(1)$. For off-stoichiometric mixture it is:

$$S_L^2 ln(S_L^2) = \left(\frac{1}{Su}\frac{dSu}{dt} - \frac{2\sigma\delta_L}{r}\right) I_D \tag{3.62}$$

Where

$$I_D = \int_1^\sigma \frac{\lambda(x)}{x}\left(1 - \frac{x-1}{\sigma-1}\right)^{Le_D-1} dx \tag{3.63}$$

Corresponding equations for near stoichiometric mixture can be found in [49]. This last expression should be valid for higher stretch rate than equation 3.60, as proved in [48]. In literature also the quasi-steady version ($dSu/dt = 0$) of 3.62 is commonly used to extrapolate the unstretched laminar flame speed [119]. It can be easily shown that for $S_L \to 1$ the unsteady term decreases much faster than the stretch term and it is negligible. The expansion of Eqn. 3.62 leads to Eqn. 3.60 with $Ma_b = \sigma I_D/2$, which is different from the expression 3.49. The numerical solution of 3.62 gives results which depends on initial conditions, but they all converge to the same line, which is the part of the solution with a physical meaning (see Figure 3.5). For extrapolation purpose, some kind of expansion must be applied to this relation.

With the definition of a non-dimensional radius $R = r/(2Ma_b\delta_L)$, equations 3.60, 3.61 and 3.62 together with its quasi-steady version, can be rewritten as expansion in power of R^{-1}:

$$S_L\left(1 + \frac{1}{R}\right) = 1 \tag{3.64}$$

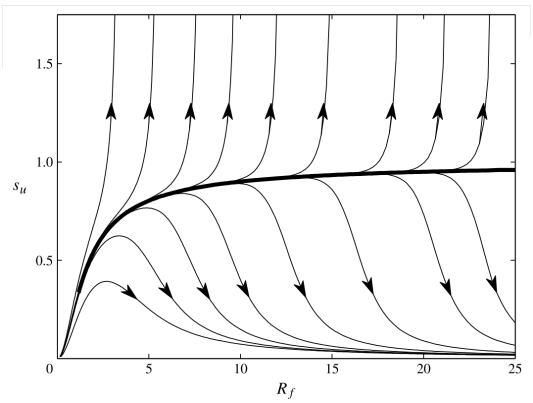

Figure 3.5: *Unconfined flame speed as a function of flame radius as determined by 3.62, for $Le_{eff} < 1$. The parameter on the axis are $su = S_L/S_L^0$ and $R_f = r/(2Ma_b\delta_L)$. Different curves correspond to different solutions of 3.62 depending on the initial conditions supplied. Arrows indicate temporal variation of the flame position. The separatrix solution, corresponding to the physical realistic solution, is shown in bold line. Figure is taken from [49].*

$$S_L\left(1+\frac{1}{R}+\frac{1}{R^2}+\frac{1}{R^3}+\mathcal{O}(\frac{1}{R^4})\right)=1 \tag{3.65}$$

$$S_L\left(1+\frac{1}{R}+\frac{1}{R^2}+\frac{2}{3}\frac{1}{R^3}+\mathcal{O}(\frac{1}{R^4})\right)=1 \tag{3.66}$$

$$S_L\left(1+\frac{1}{R}+\frac{3}{2}R^2+\frac{8}{3}\frac{1}{R^3}+\mathcal{O}(\frac{1}{R^4})\right)=1 \tag{3.67}$$

As can be noted, Markstein formulation 3.65 agrees up to the third term with the most comprehensive relation 3.66. Its agreement is even better than the quasi-steady version of 3.67. All these relations have been used in order to compute the unstretched laminar flame speed and Markstein number, in particular 3.65 and 3.66 should be preferred because they are valid for high value of stretch rate (smaller radius) both for extrapolation and modelling purpose. Anyway some issues on this topic still exist; in fact Kelley in [48] applied the same extrapolation procedure to his data and the ones taken from the Leeds group [12] for the same iso-octane mixtures and observed clear discrepancy in data and extrapolated values. While these discrepancies generate a difference of no more then 10% for the extrapolated value of unstretched laminar flame speed, they can generate differences up to 100% for the Markstein length for lean mixtures. In [119] it is suggested that a possible source of error could be related to the estimated value of burnt density, which is used to compute σ, because the adiabatic temperature usually adopted is not always reached. As an example, in [119], it is shown that for ethanol, the oxidation layer computed with detailed mechanism can be long up to 1 cm, so that, for smaller radii, also σ could change with the radius. Instead, in [127], it is underlined that the problems are connected with extrapolation procedure and data acquisition, as none of the previous equations can describe the relation between flame speed and stretch for high of this quantity.

To close this topic, two other aspects will be briefly mentioned: flame extinction and response of the laminar premixed flame to unsteady stretch. As pointed out, stretch changes laminar flame speed because it modifies the temperature of reaction zone with

respect to its planar flame value. Little variations of this temperature produce significant variation of the propagation speed because of the exponential dependence. When the effective Lewis number is greater than one, increasing stretch rate decreases temperature. When temperature becomes lower than a critical value for which reaction is too slow to balance heat diffusion, the flame stops to propagate and usually quenches. The parameters characterizing the phenomenon explained before can be used to correctly predict trends (mixtures characterized by high Markstein number are easier to be quenched than mixtures with lower value), but the previous relations cannot be used to predict quenching. This is because they were derived for weakly stretch rate, while flame quenching is associated with high stretch values, radiation losses and other issues related to chemistry (radical production/diffusion) which are not incorporated in the one step overall reaction mechanism. Counterflow laminar flames can be employed to estimate the extinction stretch rate of a premixed mixture, but the value could be dependent on the experimental configuration, as radiation losses are geometry dependent. Up to now, steady or quasi-steady stretch effect has been considered. The response to sinusoidal stretch rate with different average values has been investigated numerically in [114]. A premixed flame can move and adjust its position in response to the changes of flow field; in particular, in [114] it is found that the response of premixed flames depends on the product of frequency of induced stretch with the characteristic flame time δ_L/S_L^0. If this product is close to zero the flame moves like the steady state condition, while, if it is more than one, the flame has no time to relocate itself and does not respond anymore to stretch changes. Consumption speed C_L for high frequency is much less influenced by stretch effect: this is associated with inhibition of thermo-diffusion imbalance mechanism, like if the effective Lewis number becomes close to one. Moreover it was shown that increasing frequencies cause the extinction stretch rate (corresponding to the peak of sinusoidal signal) to become greater and in particular that this increase was stronger for mixtures with $Le > 1$.

3.4 Instabilities of laminar flame

In this section the response of a laminar flame to perturbation is investigated. This analysis can provide some insight to the interaction between turbulence eddies and premixed flames. Since the seminal works of Darrieus and Landau [27], [57], it is known that premixed flames tend to become unstable. Specifically three kinds of instability have been identified: Darrieus-Landau, thermo-diffusion and Rayleigh-Taylor. The first kind of instability is due to the change of flow field ahead of the flame induced by the density drop across the flame. The second one is due to thermo-diffusion imbalance and the last one is related to gravity effect on interface between fluids with different densities. Only the first two kinds of instability are considered in the following.

Experiments of spherical expanding laminar flames [23], [59] show that after a certain amount of time the initial spherical like flame starts to be corrugated and to assume a cellular like shape (see Figure 3.6).

Asymptotic instability analysis starts from the basic state solutions of spherically growing flames discussed in the previous section. The logic is to begin with a steady basic state; disturbances are then introduced at the time $t = 0$ and their following development is observed. Because a spherical expanding flame is not a steady phenomenon,

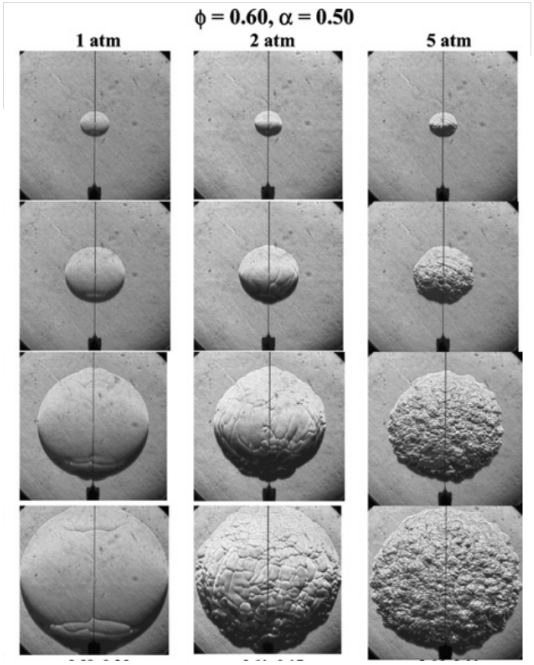

Figure 3.6: *Onset of cellular instabilities of the same hydrogen/propane mixture at different pressure. Image taken from [59].*

this description regards the propensity toward stability or instability at a given moment, reflecting the tendency of the spherical flame front to become more or less distorted. For example, if a disturbance increases, but the flame grows more rapidly, than the induced perturbation is reabsorbed by the flame, implying stability (in turbulence context, Peters in [92] refers to this effect as kinematic restoration). Instability results only when the disturbance grows at a faster rate than the flame. The perturbed flame front is expressed in the form $r = R(t)(1 + A(t)S_n(\theta, \phi))$, where S_n are the spherical surface harmonics, n is a integer and A is the amplitude of the disturbance. It is the growth or decay of A that determines instability. After solving the perturbed flow field ahead and behind the flame with the correct boundary conditions across the flame front [4], the following relations can be found:

$$A = A_0 \frac{R}{R_0}^{\theta(R)} \tag{3.68}$$

$$\theta(R) = \omega + \frac{\delta_L/R}{ln(R/R_0)}\Omega \tag{3.69}$$

$$\Omega = \left(Q_1 + Ze(Le_{eff} - 1)\frac{Q_2}{\sigma - 1} + PrQ_3 \right) \tag{3.70}$$

Where ω, Q_1, Q_2, Q_3 depend only on the density ratio of the mixture and the wavenumber n. In particular ω is always positive and is connected with the Darrieus-Landau instability and, taken alone, always indicates that a flame is unstable. The terms Q_1, Q_2, Q_3 are connected respectively with thermal diffusion, species-diffusion and viscous effect. The relation of ω, Q_1, Q_2, Q_3 with density ratio and n can be found

in [4]. The growing rate of a disturbance of wavenumber n can be determined from 3.68 as:

$$\frac{1}{A}\frac{dA}{dt} = \frac{\dot{R}}{R}\left(\omega - \frac{\delta_L}{R}\Omega\right) \tag{3.71}$$

Figure 3.7 shows the growth rate (equation 3.71) for different flame radii and mixtures; $\dot{R}$ is estimated as:

$$\dot{R} = \sigma S_L^0\left(1 - 2Ma_b\frac{\delta_L}{R}\right) \tag{3.72}$$

The values of S_L^0, σ, δ_L (diffusion thickness) and Ma_b are reported in table 7.6. It can be seen that for small enough radii, the growth rates of disturbances are all negative, which means that the flame is stable. As the radius increases, disturbances in a wider and wider range of wavenumber induce instability. This range increase indicates that the stretch rate, which is inversely proportional to the radius, is a stabilizing mechanism. Moreover it can be seen that the growth rate is a non-monotonic function and has a maximum (whose corresponding wavelength is n_{max}) which moves towards lower wavelengths as the radius increases. This function is not symmetric with respect to the maximum, but for $n < n_{max}$ the growth rate decreases much faster than for $n > n_{max}$. Setting to zero the right hand side of equation 3.71, neutral stability curves are obtained. Defining the Peclet number (Pe)as the ratio of convection on diffusion terms $(S_L R)/(D_{th}) = R/\delta_L$, the neutral stability curves are $Pe = \Omega$. Figure 3.8 shows the regions of stability/instability for various wavelengths as function of the Peclet number. It can be seen that for low Peclet numbers (small radii) there is no unstable region, while the range of the wavelengths for which the growth rate is positive starts to exist and gets wider as Pe increases, after it has reached a critical value. In particular the lower branch of the neutral stability approaches a constant line $n = n_{min}$, which is function of σ alone, and determines the expected biggest cell size observed in experiments (see Figure 3.6) $\Lambda_{max} = (2\pi R)/n_{nim}$, which increases with the radius. On the contrary, the upper branch increases indefinitely and asymptotically tends to a line $Pe/n = \Gamma = const$. As a consequence, the smallest cell size observed in experiments approaches a constant value proportional to the diffusion thickness $\Lambda_{min} = 2\pi\Gamma\delta_L$. For realistic values of σ, Q_1 and Q_2 are positive for all the wavenumber, while Q_3 is positive for all but the first few n, implying that viscosity has a stabilizing influence as thermal diffusion term. Analyzing equation 3.70, it can be noted that for $Le_{eff} > 1$ the second term is positive and contributes to increase Pe_{cr} and stability, while for $Le_{eff} < 1$ this term is negative and can overcome the other two terms, making the flame unstable for much lower radii. This second case is known in literature as thermal-diffusion instability effect and it is typical of lean hydrogen flames for which Le is much less than unity. Finally as δ_L decreases, smaller radii are required to reach the critical Peclet.

All the considerations written before have been verified experimentally [23], [59]. In particular lean hydrogen flames ($Le_{eff} < 1$) have always shown the onset of cellular instability for very small radii, while, for lean mixture, heavy fuels do not show instabilities until very big radii are reached. Anyway, if the pressure is increased, δ_L decreases, while σ, Le, Pr remain almost constant and Ze tends to increase much less than proportionally. As a consequence, the critical Peclet number does not change significantly

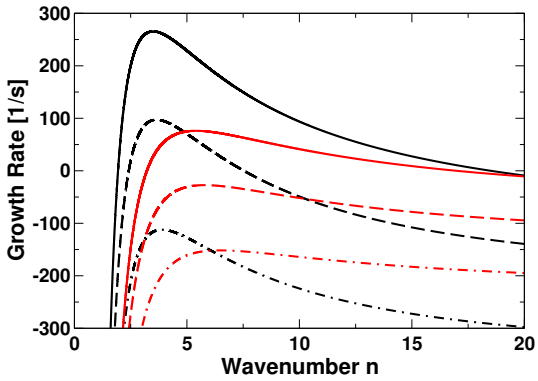

Figure 3.7: *The growth rate for propane/air mixture at different equivalence ratio calculated for increasing radii. Red line $\phi = 1.3$, black line $\phi = 1.5$. Selected radius: R1 = 6 mm (lower curves), R2 = 10 mm (broken lines), R3 = 20 mm (full lines).*

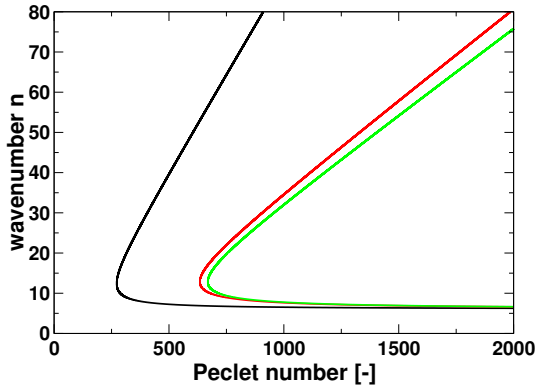

Figure 3.8: *Neutral stability curves for propane/air mixture at different equivalence ratio. Black line $\phi = 1.0$, red line $\phi = 1.3$, green line $\phi = 1.5$.*

and the corresponding radius scales proportionally to the inverse of pressure. For this reason also lean mixtures of heavy fuels show cellular instability at high pressure.

3.5 Concluding remarks

In this chapter laminar flame theory has been reviewed, as it is considered the foundation on which to build models for turbulent premixed flames. Thank to asymptotic approach, the main mechanisms characterizing laminar flame kinematics with the corresponding governing parameters have been underlined. To summarize the results of this discussion:

- assuming that a global reaction can represent the kinematic behaviour of a mixture with large activation energy, a planar laminar flame can be represented by its propagation speed S_L^0 , heat release parameter $\sigma = T_{ad}/Tu$, laminar flame thickness δ_L, the Zel'dovic number Ze and the effective Lewis number Le_{eff}. These parameters can be extracted by 1D steady state computations employing detailed kinetics and using asymptotic relations [113]. S_L^0 and σ can be also directly measured.

- Stretch rate changes the structure of the flame. In particular it modifies the temperature of the reaction zone with respect to the unstretched value. For weak stretched flame the departure from this value is small, but it produces a finite change of flame speed. The parameter which governs this process is the Markstein Number Ma. Various relations (equations 3.56, 3.62) between flame speed and stretch rate were proposed. The difference among them is related to the range of stretch rate for which they are valid. Anyway, as all these expressions were derived for weakly stretch flame, they cannot be use to predict the extinction of the flame. The Markstein number can be measured together with the S_L^0, but there are still some difficulties in the experimental procedures, which lead to values which can differ by 100%. For this reason, the asymptotic relations 3.56, which were validated against numerical simulations, are actually more reliable, even if their accuracy depends on the detailed chemical mechanism adopted to find the global reaction characteristics.
- The response of a flame with respect to a perturbation depends on the properties of the mixture and the wavelength of the disturbance in a complex manner. The critical Peclet number Pe_{cr}, n_{min} and Γ can be used to understand the range of wavelength for which these instabilities influence the flame growth/average speed. Thees disturbances could be related to the eddies which characterized turbulence.

It must be empathized that all the relations and mechanisms previously described are experimentally verified in term of trends. Quantitatively, the validity of some asymptotic relations, like the Markstein number, has not been completely achieved because experimental data are too scattered. Recent numerical experiments [38] have proven the accuracy of the description provided by asymptotic theory. For high pressures (typical of SI engine environment), instabilities can develop for small radii even with heavy fuels. As a consequence, experimental techniques are not able to measure accurately the unstretched laminar flame speed for these conditions. 1D laminar computation with complex chemistry could replace experiments in these situations. Anyway the detailed mechanisms of some fuels are still discussed and their use in conditions for which experimental comparison is not possible does not guarantee the accuracy of the results. The relations presented in this chapter provide information about the combustion behaviour of a mixture in a specific environment. In particular they help to identify the mechanisms which contribute to the flame development. For example, if the radius associated with the critical Peclet number is bigger that the hydrodynamic length scale characterizing the problem, instabilities will not play a role. As a consequence, they give information about the applicability of models which were developed without taking into account some of these mechanisms and they provide some suggestions to correct these models. In the following chapters these concepts will contribute to analyze some models proposed in literature and their results.

CHAPTER 4

Turbulent combustion modelling

In this chapter turbulence modelling concept related to premixed combustion will be reviewed. First, the main aspects of turbulence and its modelling will be briefly described, with particular emphasis on characteristic turbulence scales. Then a section will deal with combustion models with a complete description of turbulence, focusing on which are the information that can be obtained by such models. Then the main part of the chapter will cover RANS/LES models. In particular the three most employed models proposed in literature will be described. A comparison of their results on simple test cases will be discussed in order to understand which of them is more suitable for the description of combustion in spark-ignition engine. The final part of the chapter will be focused on the turbulent flame speed, which is the most important parameter characterizing the selected combustion model.

4.1 Turbulence: characteristic scales and models

The previous chapter was dedicated to the description of the physics and asymptotic models related to laminar premixed flames. In particular, the author tried to collect and organize the results scattered in many articles written in the last twenty years to give a comprehensive idea about the mechanisms which govern laminar premixed combustion, as, in the author knowledge, there is not a single text that covers all these aspects. On the contrary, turbulence and its modelling, being a more general argument, have been the subject of many detailed textbooks, such as [98]. As a consequence, in the following only the main concepts and properties which are important to understand turbulence combustion modelling are reviewed.

4.1.1 Turbulent scales

Turbulence is the result of the amplification of the perturbations which affect a flow characterized by a high Reynolds numbers ($Re = (\rho U d)/\mu$, where d is a characteristic geometrical dimension of the flow domain). Theoretically speaking, the non linear transport term in momentum equation 2.3 is able to describe this phenomenon if appropriate boundary conditions are provided. As the overall motion of the molecules which constitute a fluid can be described by means of some statistical quantities, like velocity and temperature provided by the Navier-Stokes equations, also the behaviour of turbulence can be explained through probabilistic approaches and statistical quantities. The most prolific paradigm which was proposed to describe this phenomenon is the Richardson's energy cascade concept [102] together with the statistical description due to Kolmogorov [55], based on similarity analysis, which was proposed for homogeneous turbulence at very high Reynolds numbers. For the cascade concept, turbulence is seen as ensemble of eddies of different size through which the energy of the fluid flows from the largest scales to the smallest ones. Energy transport is connected to the break up of unstable large eddies into smaller ones; this is a kinematic process and, at this level, viscous losses are negligible. At the smallest scales, viscous effects are no longer negligible and the energy transferred is converted into heat. The largest turbulent structures, known as integral scales, are of the same order of the characteristic geometrical dimensions of the flow domain. The smallest turbulent structures, known as Kolmogorov or dissipative scales, are bounded by the molecular mixture properties. Defining $E(n)$ the distribution of turbulent kinetic energy in the wavelength space ($n = 2\pi/l_n$), the total turbulent kinetic energy k can be found though integration:

$$k = \int_0^\infty E(n), dn \tag{4.1}$$

The total turbulent kinetic energy is also defined as:

$$k = \frac{1}{2}\langle u_i' u_i' \rangle \tag{4.2}$$

where u_i' are the fluctuating components of the velocity vector. In this model only two parameters are needed in order to describe the energy transfer process; all the others are related to them. In particular the smallest scales can be described by turbulent dissipation rate ε, defined in Eqn. 4.3, and the kinematic viscosity ν.

$$\epsilon = 2\nu\langle S_{i,j} S_{i,j} \rangle \tag{4.3}$$

$$S_{i,j} = \frac{1}{2}\left(\frac{\partial u_i}{\partial x_j} + \frac{\partial u_j}{\partial x_i}\right) \tag{4.4}$$

From dimensional analysis, the characteristic length (l_k), turnover time (τ_k) and velocity (u_k) of Kolmogorov scales are:

$$l_k \propto \left(\frac{\nu^3}{\epsilon}\right)^{0.25} \tag{4.5}$$

$$\tau_k \propto \sqrt{\nu/\epsilon} \tag{4.6}$$

$$u_k \propto (\nu\epsilon)^{0.25} \tag{4.7}$$

Considering Eqn. 4.7, the Reynolds number for Kolmogorov scales is $Re_\eta \propto 1$. The range of scales (or wavenumber) of the order of Kolmogorov scale ($l_k < l < 60l_k$), where viscous effects are important, is called dissipative range. The range of larger scales up to the integral scale is known as inertial range; for them energy dissipation is negligible and viscosity does not play a role anymore. Assuming the steadiness of the process, the energy given to lower scale must be equal to the one taken by larger scales. As a consequence, turbulent dissipation rate ε is equal for all these scales and, in particular, it is equal to the one at Kolmogorov scale; so only another parameter is needed to characterize this range. For example, if the characteristic velocity of the eddies u_n is selected, characteristic length and turnover time are:

$$l_n \propto u_n^3/\epsilon \tag{4.8}$$

$$\tau_n \propto u_n^2/\epsilon \tag{4.9}$$

At the upper bound of inertial range, the energy-containing range is found. In this range, the scales around the integral length scale ($(1/6)l_t < l < 6l_t$) contain most (about 80%) of the total turbulent kinetic energy which is received directly from the mean flow by turbulent production due to mean velocity gradient. Because of that and isotropy condition, from 4.2 the characteristic velocity at integral scale u_t can be estimated as:

$$u_t = \sqrt{(2/3)k} = u_{rms} \tag{4.10}$$

and directly from that:

$$l_t \propto u_t^3/\epsilon \propto k^{2/3}/\epsilon \tag{4.11}$$

$$\tau_t \propto u_n^2/\epsilon \propto k/\epsilon \tag{4.12}$$

Applying the definition of Reynolds number to the integral scale $Re_t = (u_t l_t)/\nu$, using 4.11 and 4.5:

$$l_k/l_t \propto Re_t^{-3/4} \tag{4.13}$$

$$u_k/u_t \propto Re_t^{-1/4} \tag{4.14}$$

Because of the constant dissipation rate, in the inertial range:

$$u_n \propto u_t(l_n/l_t)^{1/3} \tag{4.15}$$

$$\tau_n \propto \tau_t(l_n/l_t)^{2/3} \tag{4.16}$$

Moreover from dimensional analysis:

$$E(n) \propto \epsilon^{2/3} n^{-5/3} \tag{4.17}$$

The remaining range contains the scales associated with the mean flow up to the maximum dimension of the domain. There energy transfer relation is no more valid. Another characteristic scale which is found in literature is the Taylor microscale λ, which is included in the inertial range. It is defined as:

$$\lambda \propto \sqrt{15\nu u_t^2/\epsilon} \tag{4.18}$$

The corresponding Reynolds number is $Re_\lambda = (u_t\lambda)/\nu$ and it is usually employed to derive semi-empirical formulations of energy spectrum. For example, figure 4.1 shows turbulent spectra as function of the Taylor Reynolds number derived from experimental data [14].

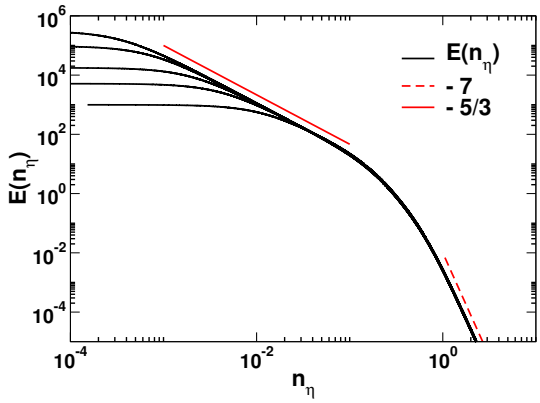

Figure 4.1: *Non-dimensional Power spectra density for increasing Taylor Reynolds numbers.* $n_\eta = 2\pi l_k/\tau_n$ *is the non-dimensional wavenumber scaled with the Kolmogorov scale. The two red lines show the power law dependence of dissipative and inertial ranges.*

In order to find the previous relationship, Kolmogorov theory assumes that the turbulent motions with length scales much smaller than the integral scale are statistically independent from the motion components of the mean flow. As a consequence, for inertial and dissipation ranges, a universal scaling law exists. On the contrary, the scales in the energy-containing range of the motion may be inhomogeneous and anisotropic and are subject to the domain geometry influence, however this information is lost in the cascade process, so that motion at smaller scale level is homogeneous and isotropic. This assumption has been widely confirmed for high Reynolds numbers. For intermediate Reynolds numbers the information from large scales is no more completely lost in cascade process; as a consequence the shape of the spectra is no more universal as the exponent p of $E(k) \sim k^{-p}$ changes with the Reynolds number. Moreover Kolmogorov theory assumes that the energy cascade is one way process from large to small eddies, while experimental studies shown that energy is also transferred from smaller to larger scales (a process called backscatter), albeit at a much lower rate, so the dominant energy transfer is indeed the one assumed by Kolmogorov theory.

4.1.2 Turbulence models

The different strategies employed to model turbulence can be described referring to the energy cascade concept. Direct Numerical Simulation (DNS) resolves all the scales involved in the cascade process. As such it requires mesh size of the order of the Kolmogorov scale (Eqn. 4.13) and no simplification due to geometric symmetry is allowed. Moreover high order schemes are required to avoid the introduction of a numerical dissipation which could be as high as the viscous dissipation of the fluid. Furthermore

detailed information at boundaries are required in order to correctly simulate the development of turbulent perturbations. Large Eddies Simulation (LES) solves only the largest scales up to the inertial range, for which the relation that describes the cascade process should be self-similar and the related models should be universal. In order to do that, explicit or implicit filtering techniques are applied to the flow; the mesh size itself is an implicit filter which cuts all the scales lower than its dimension. As a consequence, LES requires mesh resolutions which are fine enough to simulate all the energy-containing range. In particular near the walls the integral scale becomes very small and the mesh is close to that of a DNS. Also in these simulations high order schemes should be employed and mesh quality is a very important issue, so that such simulations become quite difficult for complex geometries, like the ones encountered in spark-ignition engines. Actually different sub-models have been proposed to describe the energy transfer at lower scales. Usually the energy drained from the flow by turbulence and the higher mixing rate are mimicked by means of an increased viscosity (Boussinesq assumption), known as turbulent viscosity ν_t, which is obtained by the models. More information can be found in [98]. Finally the last way to deal with turbulence is to solve the Reynolds Average Navier-Stokes equations (RANS). In this case, time or ensemble average is applied to the flow field equations in order to filter all the scales related to turbulence; only the largest scales (bigger than the integral scale) connected with the mean flow motion are kept. Neglecting the effect of density variations due to pressure fluctuations, the averaged momentum equation presents one unclosed term, known as Reynolds stress tensor, which is composed by six unclosed scalars. Six second momentum closure equations can be derived and solved in order to find these unknowns (Reynolds stress models); however, for every new equation, the number of unclosed terms increases and so the related modelling issues which require more physical insight. Because of that and the higher computational time, the most used approach is to compute two quantities which characterize energy cascade process, usually the dissipation rate ε and the total turbulent kinetic energy k. A transport equation for both of these parameters is usually employed (two-equations models) and an effective turbulent viscosity is directly derived from these parameters. More information about these models can be found in [98]. For many applications, RANS and LES conservation equations are formally the same, but the computed quantities have a different meaning. Their main difference is related to the sub-models employed to estimate the quantity ν_t. Considering Kolmogorov theory, the scales in the energy-containing range are geometry/flux dependent, so that the general validity of RANS sub-models is less justified than for LES. On the other hand, RANS approaches are more developed and the quantities that they compute (ε, k) represent only the global characteristic of turbulence for a selected flow configuration. Instead, the corresponding filtered quantities in LES are also determined by the mesh size employed to solve the problem. Moreover experimental correlations usually employ the global parameters which are directly obtained by RANS sub-models, while some modifications have to be considered when the available quantities are the filtered ones.

4.2 Turbulent combustion diagram

In the previous chapter it was shown how to characterize a premixed flame as a moving surface of discontinuity. In particular, the multi-scale structure of premixed flames was exploited in order to substitute a complex reacting flow problem with a set of relations between parameters which can be extrapolated from detailed chemical mechanisms. Moreover temporal/spatial scales which characterize premixed flames and turbulence were previously presented. In this section, comparison of these scales will be used to define different combustion regimes. The classic order of magnitude analysis proposed by Borghi [8] and resumed/expanded by other authors in [91], [115] is reviewed as a preliminary way to understand the interaction between flame and turbulence scales and to identify the regions where different modelling concepts are required. Some of the non-dimensional numbers which have been already introduced will be applied now to turbulent characteristic scales. In particular, using the definition of flame thickness as a diffusion length and assuming that Lewis and Prandtl numbers are equal to one, the turbulent Reynolds number can be rewritten as:

$$Re_t = \frac{u_t l_t}{S_L \delta_L} \tag{4.19}$$

Identifying the hydrodynamic scale with the integral length, the turbulent Damkohler number is:

$$Da = \frac{S_L l_t}{u_t \delta_L} \tag{4.20}$$

Finally the turbulent Karlovitz number, defined as the ratio of the chemical time scale $\tau_L = \delta_L / S_L$ on the Kolmogorov time, is:

$$Ka = \frac{\tau_L}{\tau_k} = \frac{\delta_L^2}{\eta_k^2} \tag{4.21}$$

From relation 4.11 it can be shown that:

$$Re_t = Da^2 Ka^2 \tag{4.22}$$

Defining the Karlovitz number with respect to the reaction zone thickness, the following relation is obtained:

$$Ka_\delta = \frac{Ka}{Ze^2} \tag{4.23}$$

With these quantities, the turbulent combustion diagram can be constructed (Figure 4.2). This diagram is referred to statistical planar turbulent flames. The abscissa is denoted by the normalized turbulent length scale l_t/δ_L , whereas the ordinate depicts the normalized turbulence intensity u_t/S_L. Usually turbulent flow characteristics are taken in the unburnt gas region. Different regions can be identified:

- *laminar regime*: for $Re_t < 1$ the flow is laminar and only instabilities related to flame dynamic are able to develop.
- *Flamelets regime*: region for which $Re_t > 1$, $Ka < 1$, all turbulent scales are smaller than the laminar flame thickness. The flame preserves its steady laminar structure and is wrinkled and stretched by turbulent eddies. Two sub-regimes

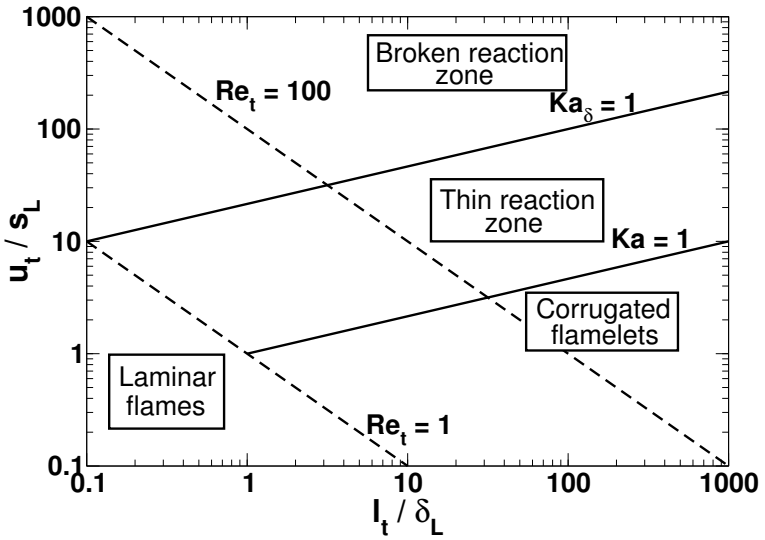

Figure 4.2: *Regime diagram for turbulent premixed combustion as proposed in [92].*

have been defined: the corrugate and wrinkled flamelets. The bounding of the two zones is identified by the line $u_t = S_L$. The border line underlines the idea that, if the higher velocity associated with turbulence is lower than the laminar propagation speed (wrinkled flamelets), the effect of turbulence is dumped out by kinematic restoration effect (flame propagation cancels out any wrinkle). Instead, for higher turbulence intensities, the eddies have enough time to effectively wrinkle the flame. Based on a similar concept, in [115], another subdivision of this regime based on onset of Darrieus-Landau instability is underlined. In particular, as shown in section 3.4, the onset of instability is associated with a particular wavenumber which depends on laminar flame properties. Large scale coherent structures could prevent the onset of this instability through wrinkling because corrugation does not allow the surface to reach the critical length scale, after which perturbations are enhanced. On the other hand, if this is not the case, the "laminar flame speed" increases by a factor of about 1.75, so the border line between wrinkled and corrugated flamelets regimes has to be updated to this value.

- *Thin reaction zone*: it is the zone where $Re_t > 1$, $Ka > 1$, $Ka_\delta < 1$. Large scale eddies wrinkle the flame, while some of the small scale eddies are able to penetrate into the preheat zone and to change the structure of the flame enhancing, for example, heat exchange. No eddy is able to penetrate into the reaction zone ($Ka_\delta < 1$), which should remain close to the laminar case.

- *Broken reaction zone*: it is the zone where $Re_t > 1$, $Ka_\delta > 1$. In this zone small eddies are able to penetrate into the reaction zone, to disperse the radicals which are reacting and also to reduce the gradient of temperature. These two effects, in combination with the high level of stretch induced by large scale eddies, are thought to be the cause of the local extinction of the flame. If a characteristic value of Zel'dovich number equal to 10 is taken, then, because of Eqn. 4.23, the boundary line between thin and broken reaction zone become $Ka = 100$ (which is the value reported in Figure 4.2).

This order of magnitude analysis is useful in order to underline some concepts related to turbulence/flame interaction, but it is hard to clearly define the different zones. For example, it was shown that the preheat zone is about 5 times the diffusion length and that the flame thickness computed with the gradient of temperature Eqn. 3.3 can be also 6-7 time this length, which, for the same Kolmogorov scale, can give (see equation 4.21) a Karlovitz number which is 36-49 times greater (the Karlovitz ratio of the two lines which delimit the thin reaction zone regime is just 100). Moreover at the end of section 3.3, it was underlined that laminar flame has a different response to unsteady perturbation; in particular it seems to be less affected by high frequency perturbation. Finally small eddies life time could be considerably reduced because of the strong increase of viscosity inside the preheat zone ($\mu \sim T^{1.7}$), so that their effect is probably completely dumped out. Clarified all of these uncertainties problems, because of the high pressure environment, flames in SI engines should be in the corrugate flamelets and, sometimes, in the thin reaction zone regimes. The first of these two regimes is the one for which the description of the flame as a surface of discontinuity is a meaningful approximation.

4.3 The hydrodynamic model

Now that the concept of flamelets regime has been introduced to theoretically justify the approximation of considering the flame as a surface of density discontinuity, the best way to describe this regime without introducing more approximations is to solve the hydrodynamic model equations [74]. The problem simplifies the low Mach number reacting flows equations, which were presented in section 3.2.2, to an hydrodynamic free-boundary problem. On the either side of the flame sheet identified by the scalar field $F(x,t) = 0$, the incompressible Navier-Stokes equation must be satisfied, but with different density and viscosities:

$$\nabla \cdot (\mathbf{U}) = 0 \tag{4.24}$$

$$\begin{aligned} \frac{\partial \rho \mathbf{U}}{\partial t} + \nabla \cdot (\rho \mathbf{U}\mathbf{U}) &= -\nabla (p) + \\ &+ \nabla \cdot \mu \left[\left(\nabla \mathbf{U} + \nabla \mathbf{U}^T \right) \right] \end{aligned} \tag{4.25}$$

with

$$\rho = \begin{cases} \rho_u & : F < 0 \\ \rho_b & : F > 0 \end{cases} \tag{4.26}$$

and

$$\lambda = \begin{cases} \mu_u & : F < 0 \\ \mu_b & : F > 0 \end{cases} \tag{4.27}$$

The problem is closed with the jumping conditions given by Equations 3.45, 3.46 and 3.47 and the surface tracking equation:

$$\frac{\partial F}{\partial t} + \mathbf{U} \nabla \cdot (F) = S_f |\nabla (F)| \tag{4.28}$$

Where S_f can be computed by means of one of the relations derived in the previous chapter like equation 3.48. Theoretically speaking, because of the low stretch rate assumption made to derive 3.48, only low value of turbulent intensities should be used. The advantages of this approach with respect to the standard DNS with one step reaction mechanisms are the lower computational time, the clear definition of some parameters, which makes parametric studies easier, and finally that the interaction between turbulent scales and the flame is only of advection/kinematic nature. Low computational cost and clear definition of flame position give also a way to extract filter or ensemble average quantities which can be used to quantify closure terms needed in LES/RANS models. This approach can be used as in [22], to describe non linear effects of turbulence/flame interaction for weakly stretched flames. To extend this model to higher level of stretch rate, the relation which gives S_f can be substituted with flamelets libraries. These can be created by means of the 1D solution of laminar flame in a stretched coordinate system for different imposed stretch rates. The jumping relations 3.45, 3.46 and 3.47 should be updated accordingly. In order to describe the thin reaction zone, the preheat zone should be resolved, but the inner reaction zone can still be described by means of appropriate jumping relations, avoiding the solution of detailed chemistry. Comparison of the results obtained with this last approach and the previous one, with the same turbulent field, could clearly underline the difference between thin reaction zone and corrugated flamelets regime.

4.4 RANS/LES turbulent combustion models

In this section the main models known in literature which have been developed in the context of RANS simulations will be presented. Most of the equations and models which will be discussed are formally the same for LES simulation; the main difference is that the computed quantities are filtered instead of averaged. Before introducing these models, the definition of some quantities which are used to characterize combustion in these approaches will be given and some related modelling problems will be underlined.

4.4.1 Preliminary definitions

While for constant density flows the filtering/average operation is uniquely defined, for combustion problems there are two different operators which can be defined:

- The Reynolds-average operator is the time-average for statistically steady problems or the ensemble-average for unsteady problems:

$$\bar{\phi} = \frac{1}{T}\int_0^T \phi(t)\,\mathrm{d}t$$
$$\bar{\phi} = 1/N \sum_{n=1}^{N} \phi_n \tag{4.29}$$

- The Favre-average operator is the density weighted Reynolds-average of a quantity:

$$\tilde{\phi} = \frac{\overline{\rho\phi}}{\bar{\rho}} \tag{4.30}$$

- The conditioned-average operator, which is obtained using one of the previous ensemble average operator multiplied by an indicator function $I(x,t)$ (see section 4.4.4 for more information).

In combustion problems a point can belong to three different zones: the unburnt gas zone, the burnt gas zone and inside the flame. The probability that this point belongs to these three zones is respectively $\alpha(t)$, $\beta(t)$, $\gamma(t)$. By definition of probability, $\alpha(t) + \beta(t) + \gamma(t) = 1$. If the flame thickness is infinitely small or if the Damkohler number is high enough (for example in [17] it is shown that $Da > 7$ seems to be high enough), the probability $\gamma(t)$ is close to zero. Then $\alpha(t) + \beta(t) = 1$ and $\alpha(t) = 1 - \beta(t)$. The progress variable $\bar{c}$ is defined as the probability that a point belongs to the burnt gas region $\bar{c}(x,t) = \beta(x,t)$. As a consequence, after an averaging process applied to a physical domain, three zones can be identified by means of $\bar{c}(x,t)$. The two regions where the gas is always burnt or unburnt identified respectively by the value $\bar{c}(x,t) = 1$ and $\bar{c}(x,t) = 0$, and a region subject to intermittency between fresh and fully burnt gases where $0 < \bar{c}(x,t) < 1$. This last region is known as flame brush and its thickness will be indicated as Δ_t. With this assumption, any Reynolds-averaged quantity can be related to the corresponding conditioned averages in fresh and burnt gases by means of the following relation:

$$\bar{\phi} = (1 - \bar{c})\bar{\phi}^u + \bar{c}\bar{\phi}^b \tag{4.31}$$

Moreover relations between Reynolds and Favre average can be derived:

$$\overline{\rho c} = \bar{\rho}\tilde{c} = \rho_b \bar{c} \tag{4.32}$$

$$\bar{c} = \frac{\sigma \cdot \tilde{c}}{1 + (\sigma - 1)\tilde{c}} \tag{4.33}$$

where $\sigma = \rho_u / \rho_b$. As a consequence:

$$\tilde{\phi} = (1 - \tilde{c})\bar{\phi}^u + \tilde{c}\bar{\phi}^b \tag{4.34}$$

In particular the turbulent fluxes, which are generated as results of the average, can be expressed as:

$$\widetilde{\rho u' c'} = \bar{\rho}\tilde{c}(1 - \tilde{c})(\overline{\mathbf{U}}^b - \overline{\mathbf{U}}^u) \tag{4.35}$$

The Reynolds stress tensor components are also expressed as:

$$\widetilde{u'_{i,j} u'_{i,j}} = (1 - \tilde{c})\overline{u'_{i,j} u'_{i,j}}^u + \tilde{c}\overline{u'_{i,j} u'_{i,j}}^b + \tilde{c}(1 - \tilde{c})(u_i^b - u_i^u)(u_j^b - u_j^u) \tag{4.36}$$

And the turbulent kinetic energy is:

$$\widetilde{k} = (1 - \tilde{c})\bar{k}^u + \tilde{c}\bar{k}^b + \frac{1}{2}\tilde{c}(1 - \tilde{c})[\sum_i (u_i^b - u_i^u)^2] \tag{4.37}$$

This set of relations is known in literature as the results of Bray-Moss-Libby analysis (BML) [16]. Usually, in non-reacting flows, local variations of density are quite small and the associated non linear fluctuation term resulting from averaging process $\overline{\rho' \mathbf{U}'}$ can be neglected. In combustion problems, the sharp change of density across the flame does not allow such assumption. In order to deal with this issue, two approaches have been used to model turbulent premixed combustion. The first and most used one

is to derive RANS equation applying Favre-average operator. In this case the resulting set of equations [96] is formally the same of Reynolds-average applied to non reacting flows and no term related to density fluctuations appears in the final equations. As a consequence, formally, the same unclosed terms remain and usually the same closing strategies are applied. Of course this procedure is quite questionable. The second method is to apply conditioned average technique [28] and to derive two sets of equations, one set for the conditioned variables on the burnt side of the flame and the other one for the unburnt side [60], and an interface transport equation (see Eqn. 4.52). In these two sets of equations the problem of density fluctuation disappears because the conditioned density of the two zones behaves like the one in non reacting flows; for this reason Favre-average in the context of conditioned average is practically unnecessary, being its value very close to the Reynolds-average. The previous equations show how to correlate the quantities obtained with the two procedures. These relations underline some problems which can come out in modelling phase. For example, Eqn. 4.35 shows that the sign of the turbulent flux of the progress variable depends on the difference between the conditioned velocity of the two regions. This relation can describe the well known transition from gradient to counter-gradient transport (the product $\overline{\rho u' c'} \nabla c$ can become positive in some points of the domain), which has been extensively reported in literature [107], while the classic gradient assumption used with Favre-averaged equation cannot. Moreover equation 4.37 shows that the Favre turbulent kinetic energy is not just the sum of the weighted average of the conditioned value on both side of the flame, but that another terms related to intermittency phenomenon appears. This term is not related to the physical turbulent motion, but to the definition of Favre-average. This last observation underlines another problem related to turbulent combustion modelling with Favre-averaged quantities: most of experiments and theoretical derivation does not account of the effect of flame on turbulence and implicitly correlates the unclosed terms with the turbulence properties of the unburnt side ($u'^u_{i,j}$, l^u_t), while the variables obtained with Favre-average equations are not correlated only to these quantities, as shown in Eqn. 4.37. For these reasons the second modelling approach should be preferred to the first as it can better describe the interaction between flame and turbulence and is more consistent with the relations provided by experiments. On the other hand, this approach is computationally expensive (it doubles the number of equations to be solved), and actually no formulation for modelling Reynolds stress tensor terms has been proposed yet, but some attempts to find closure relations are in progress [17]. It is clear from the previous considerations that Favre-averaged equations are formally simpler, but hide the complexity of the problem in the fewer modelling terms, which, for this reason, should be treated with more care. In the following, only models based on the first strategy will be discussed, but some references to the conditioned average quantities will be mentioned. In this introduction it is just pointed out the issues implicitly related to this kind of modelling approach. Three models will be discussed: the first one is the G-Equation model, which was first proposed by Williams [51] and then developed by other authors, in particular Peters [92]. The second one is known as the flame surface density model (FSD) [121] and has been developed by different groups for quite a long time. The third approach, which shares many common features with the first two, was proposed by Zimont [129] and Weller [124] independently and it is known in literature as Flame Speed Closure model or referring to the two authors

name (Weller's model). All these models have been introduced to study planar flame configurations (V-shape/Bunsen flames). Then, they were initially applied to internal combustion engines with minimal changes. This last aspect will be further discussed in the last section of this chapter.

4.4.2 G-Equation model

The G-Equation model is the application of the level set approach [3] to turbulent combustion problem. A scalar Field named $G(x,t)$ (in the early works it was named F) is used to represent a distance function from the average flame front position. Starting from equation 4.28, Peters [92] derived the following Favre-average evolution equation for G:

$$\frac{\partial \bar{\rho}\tilde{G}}{\partial t} + \nabla \cdot \left(\bar{\rho}\widetilde{\mathbf{U}}\tilde{G}\right) = (\bar{\rho}_u S_t)|\nabla \tilde{G}| - \bar{\rho}\widetilde{D}_t\kappa \tag{4.38}$$

where the curvature term κ is equal to $\nabla \cdot n$, with n the normal direction of the flame towards the unburnt gas region ($n = -\nabla\tilde{G}/|\nabla\tilde{G}|$). For convenience, the value $G(x,t) = 0$ is associated with the mean flame front position and the positive region of $G(x,t)$ points toward the fully burnt gas side. $\widetilde{D}_t$ is given by the employed turbulence model and the only remaining unknown term is S_t, which is the turbulent burning velocity. Peters provided also a modelling equation to compute these quantities; however also other correlations, like experimental ones, can be used, provided that they represent the motion of the averaged flame front, which is seldom the case. The position of the average flame front, for the previous definition of the progress variable, defines the iso-surface $\bar{c} = 0.5$. Actually, $G(x,t) = 0$ could represent any iso-surface, providing that S_t models the motion of that surface. For example, if the leading edge of the flame brush is chosen (for example associated with $\bar{c} = 0.05$), then $\widetilde{U}_{rms} \sim \overline{U}_{rms,u}$ for equation 4.37, which is more consistent with the measured one. The last modelling part is to associate every value of $G(x,t)$ with a corresponding value of $\bar{c}$. Peters proposed a transport equation for the variance of G, $\tilde{G''^2}(x,t)$ which is associated with the flame brush thickness by the relation $\Delta_t = \sqrt{\widetilde{G''^2}(x,t)}/|\nabla\tilde{G}|$. With these quantities it is possible to correlate the progress variable with the value assumed by G. For example from the analysis of experimental results taken by different authors shown in [63]:

$$\bar{c} = 0.5 + 0.5\, erf\left(\frac{G}{\sqrt{2}\sqrt{\tilde{G''^2}(x,t)}}\right) \tag{4.39}$$

Alternatively, a transport equation of the progress variable (see equation 4.40) can be solved, correlating the reaction term with the value of G as done, for example, in [80]. More details of G-Equation approach will be given in chapter 6.

4.4.3 Flame surface density model

A general average transport equation for the progress variable $\tilde{c}$ can be written as:

$$\frac{\partial \bar{\rho}\tilde{c}}{\partial t} + \nabla \cdot \left(\bar{\rho}\tilde{\mathbf{U}}\tilde{c}\right) + \nabla \cdot \left(\widetilde{\bar{\rho}u'c'}\right) = \widetilde{\dot{\omega}} \tag{4.40}$$

where $\widetilde{\bar{\rho}u'c'}$ is the turbulent flux term resulting by averaging procedure and $\widetilde{\dot{\omega}}$ is a generic source term. In some works the previous relation is derived from the energy conservation equation, assuming an adiabatic system and a constant heat capacity and equidiffusive mixture. c is identified as a non-dimensional temperature (θ in section 3.2.2). Even if this seems to be also a result of relation 4.31, it can led sometimes to misunderstand. For example, in some DNS works iso-temperature surfaces inside the structure of the flame, after averaging, are identified with $\bar{c}$, which in the context of BML analysis has a completely different physical meaning. In order to avoid such confusion, the derivation from [124] will be presented in the next section. This derivation is more coherent with flamelet concepts and BML analysis than the previous method. The flame surface density model describe $\widetilde{\dot{\omega}}$ as the product of the flame surface density Σ by the local consumption rate per unit of flame area $\rho_u \langle C_L \rangle$.

$$\widetilde{\dot{\omega}} = \rho_u \langle C_L \rangle \Sigma \tag{4.41}$$

The flame surface density $\Sigma(x,t)$ measures the probability of a surface being in the point at coordinate x at time t. Let δA be the area of a surface within the volume δV, then $\Sigma(x,t)$ is the expectation of $\delta A/\delta V$. A high flame surface density at a given location in the flow corresponds to a high turbulent reaction rate. An analytical transport equation of Σ has been derived in [97] using geometrical considerations. The final result is very similar to the stretch rate relation 3.44 and it is:

$$\frac{\partial \Sigma}{\partial t} + \nabla \cdot (\langle \mathbf{U} + S_L n \rangle_s \Sigma) = (\nabla \cdot \mathbf{U} - nn : \nabla \mathbf{U} - S_L \nabla \cdot n)\, \Sigma \tag{4.42}$$

where the operator $\langle \rangle_s$ is the surface mean, S_L is the propagation speed of the surface and $\vec{n}$ is the normal to the flame front pointing towards the fresh gases. The source term proportional to Σ on the right hand side is the stretch rate. Using Favre decomposition, equation 4.42 can be rewritten as:

$$\begin{aligned} \frac{\partial \Sigma}{\partial t} + \nabla \cdot \left(\widetilde{\mathbf{U}} \Sigma \right) + \nabla \cdot (\langle \mathbf{U}' \rangle_s \Sigma) &= \left(\nabla \cdot \widetilde{\mathbf{U}} - \langle nn \rangle_s : \nabla \widetilde{\mathbf{U}} \right) \Sigma \\ &+ \langle \nabla \cdot \mathbf{U}' - nn : \nabla \mathbf{U}' \rangle_s \Sigma \\ &- \nabla \left(\langle S_L n \rangle_s \Sigma \right) + \langle S_L \nabla \cdot n \rangle_s \Sigma \end{aligned} \tag{4.43}$$

The terms in this equation which need to be modelled are the turbulent flux (third term on the left hand side), the stretch rate associated with turbulent component of velocity (second term on the right hand side) and the last two terms on the right hand side of equation, which are related to kinematic restoration and curvature effects. Different closure models based on heuristic arguments have been proposed in literature. The final formulation assumes the following form:

$$\frac{\partial \Sigma}{\partial t} + \nabla \cdot \left(\widetilde{\mathbf{U}} \Sigma \right) = \nabla \cdot \left(\frac{\nu_t}{\sigma_\Sigma} \nabla \Sigma \right) + \kappa_m \Sigma + \kappa_t \Sigma - D \tag{4.44}$$

where gradient assumption has been employed to model the turbulent flux, κ_m represents the stretch rate associated with average velocity, κ_t indicates the stretch rate associated with turbulence and D is a destruction term which is introduced in order to eliminate flame surface when $\tilde{c} \to 1$. The propagation term $\nabla \left(\langle S_L n \rangle_s \Sigma \right)$ in this form

is neglected, but unless U is very high, it should not. In RANS simulation, also stretch associated with average velocity (κ_m) can be neglected, while for LES it is kept. The turbulent stretch rate term κ_t is taken to be proportional to the inverse integral scale turnover time $\tilde{\epsilon}/\tilde{k}$ and is corrected with an efficiency function $\Gamma(u'/S_L, l_t/\delta_L)$ which was derived from DNS computation of vortex flame interaction [78]. The term D is constructed in order to become big near $\tilde{c} \to 1$; usually this value is inversely proportional to $\tilde{c}(1-\tilde{c})$ or more simply $(1-\tilde{c})$. For more examples of closure models see [30]. Even if these papers are quite old, more recent works [21] still use the same closure models.

4.4.4 Flame speed closure model

This model was firstly developed based on empirical observation by Zimont [129]. Weller started from flame surface density theory and conditioned average technique to derive a model [124] whose final version is very close to the one previously proposed by Zimont. More recently Lipatnikov [62] started from equation 4.40 and derived a more general form of the Zimont's one. In particular Weller used the relation $\Sigma = \Xi|\nabla\bar{c}|$ and derived a transport equation for Ξ starting from 4.42. Ξ is called wrinkling factor (or wrinkle density) and is defined as the flame area per unit area resolved in the mean propagation direction (equation 4.53). Weller first defined an indicator function $I(x,t)$ such as it is 1 for points belonging to the unburnt gas zone and 0 for points belonging to the burnt zone; then he defined a zone volume fraction $\alpha(x,t)$ as the probability of a point(x,t) being in unburnt gas zone $\alpha = \overline{I(x,t)}$ where the over-bar denote the ensemble average. Then, using conditioned-averaging relations [28] for a generic properties Q:

$$\overline{I\nabla Q} = \nabla\overline{IQ} - \lim_{\delta V\to 0}\overline{\frac{1}{\delta V}\int_{S(x,t)} Qn(x,t)dS} \tag{4.45}$$

$$\langle Q\rangle_s = \frac{\lim_{\delta V\to 0}\overline{\frac{1}{\delta V}\int_{S(x,t)} Q(x,t)dS}}{\Sigma} \tag{4.46}$$

$$\overline{I\nabla Q} = \nabla\overline{\alpha Q} - \langle Qn\rangle_s\Sigma \tag{4.47}$$

$$\overline{I\nabla\cdot Q} = \nabla\cdot\overline{\alpha Q} - \langle Qn\rangle_s\Sigma \tag{4.48}$$

$$\overline{I\frac{\partial Q}{\partial t}} = \frac{\partial\alpha\overline{Q}}{\partial t} + \langle Q\mathbf{V_I}\cdot n\rangle_s\Sigma \tag{4.49}$$

Where $S(x,t)$ is the equation for the interface, n denotes the direction of the unit normal to the interface, pointing towards the unburnt zone, Σ is the same defined in the previous sub-section and $\mathbf{V_I}$ is the absolute velocity of the interface. Replacing $Q = 1$ into 4.49, remembering that the interface absolute velocity is the sum of fluid and propagation velocity $\mathbf{V_I} = \mathbf{U_I} + S_I$, and decomposing $\mathbf{U_I}n$ into surface average, it is obtained:

$$\frac{\partial\bar{\alpha}}{\partial t} + \langle\mathbf{U_I}\rangle_s\langle n\rangle_s\Sigma + \langle\mathbf{U_I'}n'\rangle_s\Sigma = -\langle S_I\rangle_s\Sigma \tag{4.50}$$

Using $Q = 1$ in equation 4.47:

$$\langle n\rangle_s\Sigma = \nabla\bar{\alpha} \tag{4.51}$$

from the last two relations, replacing $\alpha = 1 - \beta = 1 - \bar{c}$, which requires a change of sign, it is obtained:

$$\frac{\partial \bar{c}}{\partial t} + \langle \mathbf{U_I} \rangle_s \nabla \bar{c} + \langle \mathbf{U'_I} n' \rangle_s \Sigma = \langle S_I \rangle_s \Sigma \tag{4.52}$$

which starts to look like equation 4.40 written in non-conservative form. Defining Ξ as the ratio of the average flame area per unit volume $\langle A_f \rangle_s = \Sigma$ and the average flame area projected onto the mean propagation direction $\hat{n} = \widehat{\langle n \rangle}_s$ (normalized vector of the average surface normal direction), it is obtained:

$$\Xi = \frac{\Sigma}{\langle A_s \rangle_s} \tag{4.53}$$

$$\langle A_s \rangle_s = \lim_{\delta V \to 0} \overline{\frac{1}{\delta V} \int_{S(x,t)} \hat{n} \cdot n dS} = |\langle n \rangle_s| \Sigma \tag{4.54}$$

remembering equation 4.51:

$$\Xi = \frac{\Sigma}{|\nabla \bar{c}|} \tag{4.55}$$

$$\hat{n} = -\frac{\nabla \bar{c}}{|\nabla \bar{c}|} \tag{4.56}$$

the substitution of Σ in equation 4.52 with the wrinkling factor gives:

$$\frac{\partial \bar{c}}{\partial t} + \langle \mathbf{U_I} \rangle_s \nabla \bar{c} + \langle \mathbf{U'_I} n' \rangle_s \Xi |\nabla \bar{c}| = \langle S_I \rangle_s \Xi |\nabla \bar{c}| \tag{4.57}$$

Which can be written also as:

$$\frac{\partial \bar{c}}{\partial t} + \langle \mathbf{U_I} \rangle_s \nabla \bar{c} + \left(\langle S_I \rangle_s - \langle \mathbf{U'_I} n' \rangle_s \right) \Xi \hat{n} \nabla \bar{c} = 0 \tag{4.58}$$

Using Damkohler concept, the product $\langle S_I \rangle_s \Xi \hat{n}$ is the turbulent burning velocity. It is interesting to note that the term associated with the turbulent scalar flux could be included in the definition of turbulent burning velocity, as partially done by Peters, and that it depends on Ξ. Starting from Eqn. 4.55, Weller developed also a transport equation for the wrinkling factor, whose final form is:

$$\begin{aligned} \frac{\partial \Xi}{\partial t} + \langle V_I \rangle_s \nabla \Xi &= G \\ &+ \Xi \hat{n} \cdot \nabla \langle U_t \rangle_s \cdot \hat{n} - \frac{1}{\Xi} \hat{n} \cdot \nabla \langle V_I \rangle_s \cdot \hat{n} \\ &+ \Xi (\langle U_t \rangle_s - \langle V_I \rangle_s) \frac{\nabla |\nabla \bar{c}|}{|\nabla \bar{c}|} \end{aligned} \tag{4.59}$$

$V_I = \mathbf{U} + S_L n$, is the interface absolute velocity, while $U_t = \langle \mathbf{U_I} \rangle_s + (\langle S_I \rangle_s - \langle \mathbf{U'_I} n' \rangle_s) \cdot \Xi \hat{n}$ is overall propagation velocity. The first term G represents the contribution due to turbulence fluctuation and it is equal to:

$$G = -\Xi (\langle n' \cdot \nabla V_I \cdot n' \rangle_s + \langle n' \cdot \nabla V_I \rangle_s \cdot \langle n \rangle_s + \langle n \rangle_s \cdot \langle \nabla V_I \cdot n' \rangle_s) \tag{4.60}$$

The second term is associated with stretch generation, the third corrects the previous effects on the projected area. The last two terms are associated with cusps formation

at the trailing edge (increase of Ξ) of the flame while it tends to smooth the leading edge of the flame (decrees of Ξ). The surface average velocity can be modelled with the conditioned average value corrected by a surface correlation term, which depends on turbulence, using gradient assumption:

$$\langle \mathbf{U_I} \rangle_s = \overline{U_I} - \overline{D_I} \frac{\nabla \Xi}{\Xi} \tag{4.61}$$

$$\begin{aligned} \langle \mathbf{U'_I} n' \rangle_s \Sigma &= -\Sigma \overline{D_I} \nabla \cdot \langle n \rangle_s = -\Sigma \overline{D_I} \nabla \cdot \frac{\hat{n}}{\Xi} \\ &= \overline{D_I} \frac{\nabla \Xi}{\Xi} \nabla \bar{c} - \overline{D_I} (\nabla \cdot \hat{n}) \hat{n} \cdot \nabla \bar{c} \end{aligned} \tag{4.62}$$

Which, substituted in 4.52, gives:

$$\frac{\partial \bar{c}}{\partial t} + \left(\mathbf{U_I} + \langle S_I \rangle_s - \overline{D_I} \nabla \cdot \hat{n} \right) \nabla \bar{c} = 0 \tag{4.63}$$

It is noticed that equation 4.63 is formally identical to Eqn. 4.38 of the G-Equation model, but the variable $\bar{c}$ has a different meaning than G. Moreover the correlation between Favre-averaged quantites and interface properties is not straightforward. Equations 4.63 and 4.59 provide the equations needed to close the set of equations obtained with conditioned average technique. In the present work, Favre-average equations are used, and the unknown terms of the previous equations must be closed with relations which are function of Favre-averaged quantities. Applying the conditioned Favre-average to the mass conservation equation for the unburnt side of the flame and using the BML relations, it can be found:

$$\frac{\partial \bar{\rho} \tilde{b}}{\partial t} + \nabla \cdot (\bar{\rho} \widetilde{\mathbf{U}}_u \tilde{b}) = -\langle \rho_u S_{I,u} \rangle_s \Xi |\nabla \bar{b}| \tag{4.64}$$

Where $\tilde{b} = 1 - \tilde{c}$ is the regress variable. From BML relation 4.34.

$$\widetilde{\mathbf{U}}_u \sim \overline{\mathbf{U}}_u = \widetilde{\mathbf{U}} + (1 - \tilde{b})(\overline{\mathbf{U}}_u - \overline{\mathbf{U}}_b) \tag{4.65}$$

It is underlined that up to now the model has been mathematically derived using only conditioned average technique and BML assumption, which are coherent with flamelets regime description, while the following relation starts to introduce heuristic modelling assumption. Weller closed $\overline{\mathbf{U}}_u - \overline{\mathbf{U}}_b$ with a jump relation similar to the laminar flame case with the addition of a dispersion term:

$$\overline{\mathbf{U}}_u - \overline{\mathbf{U}}_b = \left(\frac{\overline{\rho}_u}{\overline{\rho}_b} - 1 \right) \langle S_{I,u} \rangle_s \Xi \hat{n} - \tilde{D}_t \frac{\nabla \tilde{b}}{\tilde{b}(1 - \tilde{b})} \tag{4.66}$$

The first term on the right hand side of 4.66 is self-explanatory, the second term is introduced to model the fact that Ξ is not constant through the flame brush, but it has its own distribution. As clearly stated in [124], the functional relation was assumed in order to obtain a gradient like term in the final progress variable equation. Introducing these two last relations in 4.64, making some algebraic operations (which modify $|\nabla \bar{b}|$

into $|\nabla\tilde{b}|$) and changing the regress variable with the progress variable, it is finally obtained:

$$\begin{aligned}\frac{\partial\bar{\rho}\tilde{c}}{\partial t}+\nabla\cdot(\bar{\rho}\widetilde{\mathbf{U}}\tilde{c})-\nabla\cdot(\widetilde{\nu_t}\nabla\tilde{c}) &= \langle\overline{\rho}_u S_{I,u}\rangle_s\Xi|\nabla\tilde{c}| \\ &+ \overline{\rho}_u(\tilde{c}-\bar{c})\nabla\cdot(\langle S_{I,u}\rangle_s\Xi\hat{n}) \\ &+ (\tilde{c}-\bar{c})\langle S_{I,u}\rangle_s\Xi\hat{n}\cdot\nabla\overline{\rho}_u \end{aligned} \tag{4.67}$$

The last term on the right hand side of the previous equation is negligible because $\nabla\overline{\rho}_u\sim 0$. The second term instead is not negligible a priori because Ξ can change a lot across the flame brush. Different modelling considerations have been developed for Eqn. 4.59. The final version of the Ξ equation which is implemented in OpenFOAM is described in [117]:

$$\begin{aligned}\frac{\partial\Xi}{\partial t}+\overline{\mathbf{U}}_s\nabla\Xi-\nabla\cdot(\widetilde{\nu_t}\nabla\tilde{\Xi}) &= G_W\Xi-R(\Xi-1) \\ &+ max[(\sigma_t-\sigma_u)]\Xi \end{aligned} \tag{4.68}$$

Where the most important terms are modelled as:

$$\overline{\mathbf{U_s}}=\widetilde{\mathbf{U}}+(\overline{\rho}_u/\overline{\rho}-1)\langle S_I\rangle_s\Xi\hat{n}-\frac{\tilde{D_t}\hat{n}}{|\nabla\tilde{c}|} \tag{4.69}$$

$$G_W=0.28/\tau_\eta \tag{4.70}$$

$$R=G_W\frac{\Xi_{eq}}{(\Xi_{eq}-1)} \tag{4.71}$$

For the remaining modelled quantities, see [117] (Eqn. 57 and 58). In addition to what it is written in the cited paper, it is underlined that in the passage from Eqn. 4.59 to Eqn. 4.68, the last term associated with cusps formation in 4.59 has been deleted for numerical issues encountered in 3D domain. This term is the main source of Ξ inhomogeneity across the flame brush; without it, the second term on the right hand side of Eqn. 4.67 becomes much less important and can be removed as well. As a consequence, the simplified Weller model is reduced to the Zimont model [129] (see Eqn. 4.73), with a turbulent burning velocity which practically increases exponentially in time (in homogeneous turbulence cases) until it reaches the equilibrium value, for which the turbulent velocity correlation by Gulder [41] was chosen (it is interesting to note that, apart from the value of an experimentally tuned constant, Gulder and Zimont turbulent velocity correlations are the same). Lipatnikov in [62], assuming self-similarity and frozen homogeneous turbulence, showed that a general balance equation of the type 4.72 can be reduced to an expression like the one of the simplified Weller model. He started from the general balance equation of the progress variable:

$$\frac{\partial\bar{\rho}\tilde{c}}{\partial t}+\nabla\cdot\left(\bar{\rho}\widetilde{\mathbf{U}}\tilde{c}\right)=\nabla\cdot(k(t)\bar{\rho}D_{t,\infty}\nabla\tilde{c})-\nu\nabla f+\omega(t)W \tag{4.72}$$

Where $f(\tilde{c},\sigma,N,\xi)\geq 0$ is an arbitrary bounded function which is equal to zero at $\tilde{c}=0$ and $\tilde{c}=1$, N and ξ are respectively a non-dimensional velocity and a spatial coordinate with respect to the characteristic time and length scale of the flame. f represents pressure-driven transport term (the one which is responsible of counter-gradient

diffusion). $W(\tilde{c}, \sigma, N, \xi) \geq 0$ represents a generic reaction rate function which shares the same properties of f. $k(t)$ and $\omega(t)$ are generic functions of time which tends to 1 as $t \to \infty$. Lipatnikov demonstrates that in 1D, Eqn. 4.72 corresponds to equation:

$$\frac{\partial \bar{\rho}\tilde{c}}{\partial t} + \nabla \cdot (\bar{\rho}\widetilde{\mathbf{U}}\tilde{c}) - \nabla \cdot (\bar{\rho} D_t \nabla \tilde{c}) = \rho_u S_t |\nabla \tilde{c}| \tag{4.73}$$

Where S_t is the turbulent burning speed and the turbulent diffusion coefficient is equal to $D_t = D_{t,\infty}(k(t) - (1+a)\delta_t + a\omega(t)\delta_t^2(t))$, with δ_t the ratio of flame brush thickness on the fully developed value and $0 \leq a < 1$ is a constant. Moreover $s(t) = \delta_t(t)\omega(t)$, where $s(t) = S_t/S_{t,\infty}$. Finally Lipatnikov demonstrated that the solution of Eqn. 4.73 together with the mass conservation equation is:

$$\bar{c} = 0.5 + 0.5 erf(\sqrt{\pi}\frac{x - x_f}{\Delta_t}) \tag{4.74}$$

Where $x_f = \int S_t dt$ is the mean flame position ($\bar{c} = 0.5$) and $\Delta_t^2 = \int D_t dt$. This progress variable profile agrees well with the experimental profiles measured on different basic flame configurations (flame-holder, V-Shaped and spherically expanding flames) as shown in Figure 4.3. These results will be used to process data in the next section.

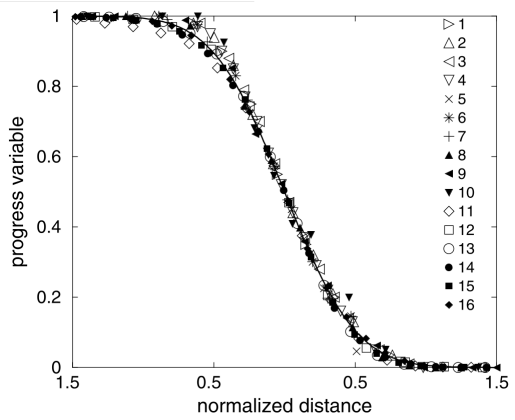

Figure 4.3: *Comparison of progress variable profile given by 4.74 with experimental data obtained by various authors for different configurations. The reverse value of the maximum gradient of $\bar{c}$ is used to estimate the flame brush thickness of the experimental data. The profiles are centered with respects to the position where $\bar{c} = 0.5$. Image is taken from [62], where more about the provenience of the experimental data can be found.*

This last result shows that the use of different closure expressions for the turbulent burning velocity/wrinkling factor as the one proposed in [92] does not change the structure of the solution of Eqn. 4.73. The Zimont/Weller model can be seen as an intermediate model between G-Equation and flame surface density. Anyway, the linear relation between the source term in the progress variable equation and the gradient of $\tilde{c}$ make this model more similar to the G-Equation model.

4.5 Comparison of RANS turbulent combustion models

In the previous section, the basic theory and ideas, from which the most employed models in literature are derived, were shown. As it could be expected, the models share

some analogies, for example Weller's model can be connected both to G-Equation (Eqns. 4.63 and 4.38) and to FSD model (Eqns. 4.67 and 4.51), but their different modelling strategies lead to final equations which behave quite differently. In this section, the models behaviour in basic configurations is compared to understand which of them is the most promising one for modelling combustion in SI engines from the first stages of flame development. In literature there are many examples of computation of the previous three models for engine applications (see [118], [6], [125]), both for RANS and LES simulations, but their results have been seldom compared. Moreover, in these works different expressions for the source terms in Σ equations or turbulent flame speed correlations were used. This makes the evaluation of the behaviour of these models difficult; the main idea that these articles suggest is that these models are essentially equivalent. From the author experience, this is not completely true and this section will try to show that, for RANS approaches, the numerical behaviour of FSC and G-Equation models makes them better suited that FSD for spark-ignition engine modelling. In particular they are better suited to be coupled with models whose aim is to simulate the initial stage of flame kernel development. The chosen configurations for the comparison are: a 1D planar configuration, which shows some basic properties of the model; a 2D cylindrical flame expansion, in order to compare the effect of geometry configuration on the results of the model and in particular the effect of stretch. Finally, as a summary, a very simple test case with an engine like configuration is shown. The subject of the comparison is the structure of the flame and some parameters which characterize the development of the flame. These are essentially the flame brush thickness and turbulent propagation speed. The focus of the comparison is to see which model is less subject to modifications when some parameters, which are not related to turbulence and flames properties (laminar flame speed and thickness), are changed; indeed these parameters should not alter a lot the flame behaviour. All these models were implemented in OpenFOAM, modifying the "XiFoam" solver [2], which is an implementation of the Weller's model. An important modification had to be applied to make the model coherent with BML analysis: in OpenFOAM conditioned average equations of unburnt gas enthalpy ($\bar{h}_u$) and Favre-average enthalpy ($\widetilde{h}$) are solved (their equations can be found in section 6.1). This is required because the properties of laminar flames (tabulated or obtained by experimental correlations) are based on the unburnt gas properties and not on the Favre-average quantities. With these two equations, it is possible to use expression 4.34 to obtain the conditioned average burnt gas enthalpy ($\bar{h}_b$). The standard code of OpenFOAM converts the progress variable into the Favre-average mass fractions of reaction products and of reactants employing relation 4.34. Then, these quantities are used to build a mixture composition which is used to derive the Favre-average temperature ($\widetilde{T}$) from the corresponding value of enthalpy $\widetilde{h}$. The problem is that, due to the non linear relation between enthalpy and temperature (c_p is obtained from JANAF coefficients), the computed $\widetilde{T}$ does not satisfy Eqn. 4.34 applied to temperatures. As density depends on temperature and not on enthalpy, the computed $\overline{\rho}$ is wrong and even relation 4.33 is no more satisfied. In other words, while relation 4.34 applied to temperature is always valid, its application to mass fractions is correct only for the simplified cases where the Lewis number is equal to one for all species and the specific heat capacity is constant. To correct this incongruence, the code was modified in order to compute $\widetilde{T}$ directly from the progress variable $\widetilde{c}$ through relation 4.34,

while the conditioned averaged temperatures of burnt and unburnt zones are obtained from the corresponding enthalpies.

4.5.1 Planar configuration

This configuration has been the subject of many studies and it is a basic test which can be used both for comparison and to assess the correct implementation of a model. For this configuration some analytical solutions are known, so that some of the results could just be theoretically provided. Furthermore, for this configuration G-Equation model behaves like the FSC model, so it is not showed. The case set-up is a duct closed on one side and open on the other side, as depicted in Figure 4.4. This configuration allows to study the transient behaviour of the flame and it also shares some properties with spherical expanding flames (the velocity increases ahead of the flame while it remains zero at burnt gas zone). The selected mesh size is uniform and equal to 0.5 mm, as, for higher resolution, the results were the same. All the selected numerical schemes are fully second order in space (Peclet number $\sim 1.6 < 2.0$) and time step is selected in order to have maximum Courant number which is less than 0.5. Three information characterize a RANS premixed combustion model: turbulent flame speed development, flame brush thickness and structure of the flame ($\bar{c}$ profile). For FSD model (Eqns. 4.40, 4.41 and 4.44), two of the many sub-models which describe the terms on the right hand side of equation 4.44 are selected: the CFM2-a and the CFM2-b (see Table 4.1). For FSC model the simplified Weller equation (with correspond to the Zimont model) is employed (Eqns. 4.73 and 4.68).

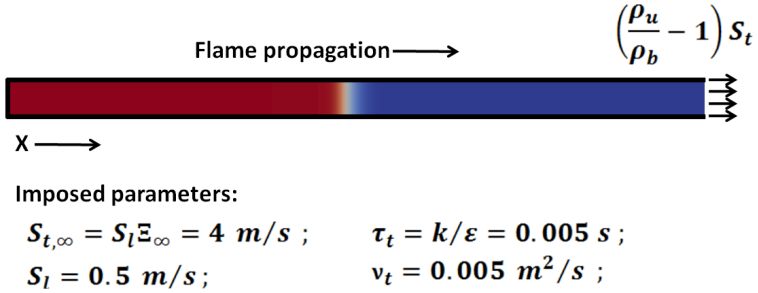

Figure 4.4: *Set-up of the 1D configuration test case. The duct is closed on one side in order to simulate an expansion process and open on the other side in order to preserve the pressure value.*

Symbols	Model CFM2-a	Model CFM2-b
k_m	0.0	0.0
k_t	$\alpha\Gamma_k \frac{\epsilon}{k}$	$\alpha\Gamma_k \frac{\epsilon}{k}$
D	$\beta \frac{S_L + C\sqrt{k}}{1-\tilde{c}} \Sigma^2$	$\beta \frac{S_L + C\sqrt{k}}{\tilde{c}(1-\tilde{c})} \Sigma^2$
$S_{t,\infty}$ from KPP-analysis	$\sqrt{\frac{6\alpha\Gamma_k C_\mu}{\sigma_\Sigma}} u_{rms}$	$\sqrt{\frac{6\alpha\Gamma_k C_\mu}{\sigma_\Sigma}} \left(1 + \beta(1 + C\frac{\sqrt{k}}{S_L})\right)^{-0.5} u_{rms}$

Table 4.1: *Source terms for Flame Surface Density models and corresponding turbulent flame consumption speeds.*

Turbulence parameters, laminar flame speed and constants of the models are imposed in order to obtain the same fully developed turbulent flame speed 4.4. While

for FSC model the expression of flame speed clearly compares in the progress variable equation, for the FSD model, the expressions obtained by Kolmogorov-Petrovsky-Piskounov (KPP) analysis [43] are employed. They are given in table 4.1 . The results of this approach are only valid for 1D configurations with constant density and frozen turbulence. As a consequence, two tests at constant and variable density are conducted. The parameters selected for the constant density case are kept also for the other test. To initialize the cases, the same initial $\bar{c}$ profile is imposed near the closed end of the duct. The selected profile is provided by Eqn. 4.74, which is already the solution of the FSC model. For FSD model such analytical profile does not exist and other profiles could be chosen. A linear profile was also selected in order to see how this initial condition could affect the transient result for FSD case. The initial Σ profile is provided by the following relation: $\Sigma = \Sigma_{max}\tilde{c}(1-\tilde{c})$.

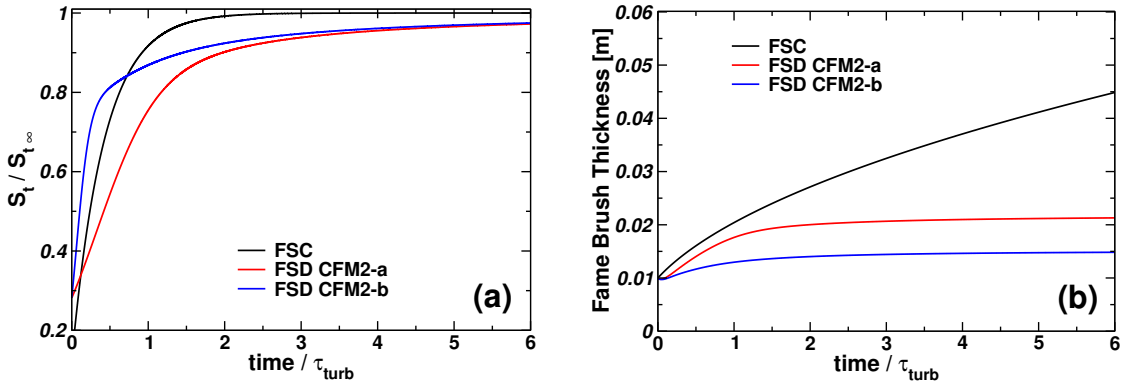

Figure 4.5: *Evolution of a planar turbulent flame for the constant density case. Figure (a) shows the non-dimensional turbulent flame speed. Figure (b) shows the turbulent flame brush thickness evolution. The parameters used to initialize the problem and to make the reported quantities non-dimensional are given in Figure 4.4.*

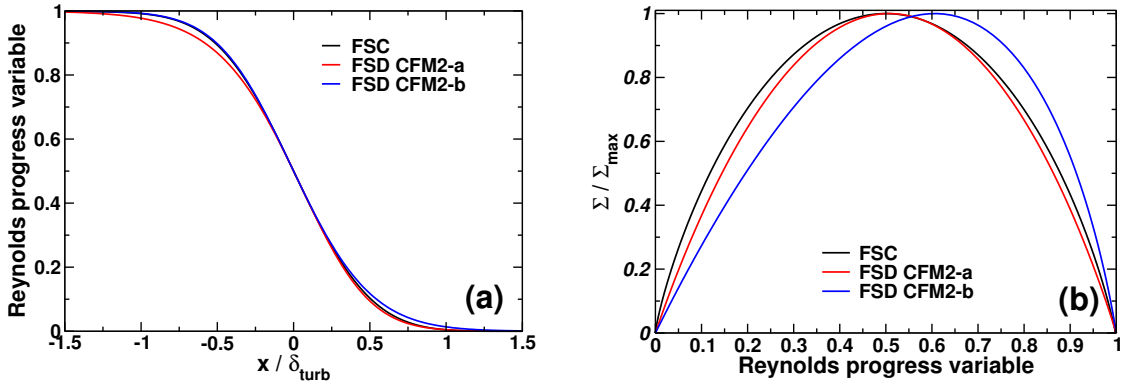

Figure 4.6: *Evolution of a planar turbulent flame for the constant density case. Figure (a) shows the Progress variable profile. Figure (b) shows the Dependence of Σ source term on the progress variable $\bar{c}$. The parameters used to initialize the problem are given in Figure 4.4.*

Figure 4.5 (a) shows the transient evolution of the turbulent consumption speed, which was computed integrating the source term of equations 4.73 and 4.40 over the whole domain and dividing the final result by the cross section area of the duct ($S_t = 1/A_{duct} \cdot \int \overline{\rho}\dot{\omega}dV$). The FSC model shows an exponential increase of consumption

speed with a characteristic time equal to (k/ε), which is related to the first two source terms of equation 4.68. The two CFM models show different trends and time responses to the transient phase. In particular, two phases can be identified: an initial short phase, in which the turbulent speed reaches about 80% of the final value, and a longer phase, in which the flame speed slowly reaches the fully developed turbulent flame speed. Figure 4.5 (b) shows the development of the flame brush computed as the inverse of the maximum gradient of $\bar{c}$ across the flame. It is seen that for the FSC model the flame brush increases indefinitely in time, even if the flame speed has reached the equilibrium value. Instead, the flame brush for the two CFM models reaches more or less a constant value. For FSD models, the developing time of the flame brush thickness is clearly associated with initial developing phase of the turbulent flame speed. Figure 4.6 (a) shows the structure of the flame at the end of transient of the flame speed for the three models. The profiles were obtained centering the point for which $\bar{c} = 0.5$ and normalizing the final results by the flame brush thickness. The FSC model shows the typical error function profile given by equation 4.74, which is symmetric with respect to the center of the flame. The results of FSD models, instead, are not symmetric but differ only a little from the profile given by the FSC model. This means that the experimental profile of this variable given in figure 4.3, with the related uncertainties, is not enough to draw some conclusions from them. The Figure 4.6 (b) shows the source term profiles of equations 4.73 and 4.40 across the flame brush. They are identified with Σ in both the equations, because at constant density $\bar{c} = \tilde{c}$ and relation 4.55 is satisfied. For FSC models Σ is a Gaussian distribution in space, as it is related to the derivative of $\bar{c}$ profile. The CFM2-a model shows a dependency which is not symmetric, but it is close to the relation $\bar{c}(1 - \bar{c})$. The CFM2-b model source term is clearly higher toward the leading edge of the flame than at the trailing edge. As can be noted from table 4.1, the two FSD models share three tuning parameters (α, β and C) which influence both the transient behaviour of the flame and its final structure. For the CFM2-a model only α influences the turbulent speed value, while for the CFM2-b model also the other two compare in the KPP relation (see the last raw of table 4.1). It is impossible to select a set of the three constants which guarantees the same final velocity with both formulations. As a consequence, in order to minimize the differences, two of the three parameters were kept constant, while α was changed in order to obtain the same equilibrium turbulent velocity. The final considerations which the author want to underline are not anyway influenced by this choice. Figure 4.7 shows the different transient responses for the three models with different initial imposed profiles. It can be noticed that the consumption speed of the FSC model is practically the same for both initial conditions, while the transient behaviour of the FSD models is strongly affected by this choice. This can be an important issue in spark-ignition engine simulation, especially if the initial stage of flame kernel development has to be modelled. In fact, even if an ideal sub-model was able to perfectly describe this phase, the improved accuracy provided by such a model would be lost when switching to the main combustion model.

Now the same test case with the same parameters (but only for error function profile initialization) is proposed for a variable density problem with temperature ratio of about 4 and 8, which are respectively typical values of SI engine and ambient condition cases. Figure 4.8 (a) shows the evolution of turbulent flame speed for the six cases considered. It can be noticed the FSC model keeps the same profile of the constant

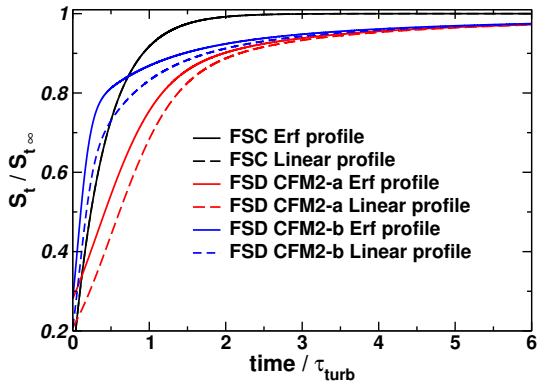

Figure 4.7: *Turbulent Flame speed development for different initializations of the progress variable.*

density cases. The little differences between the two cases are due to small pressure oscillations arising because of heat released during the flame initialization. Moreover, the pressure increases a bit across the flame due to momentum conservation, which is not considered in Lipatnikov analysis. These oscillations, which increase with the temperature ratio, produce some noise which is amplified when gradient quantities are computed. Both FSD models show more or less the same transient behaviour of the constant density case, but this time the equilibrium value increases with respect to the one predicted by KPP-analysis which, as already stated, is valid only for constant density flows. In particular this value increases with the temperature ratio. Looking at the corresponding thickening of the flame brush (Figure 4.8 (b)) and remembering that, for constant density case, the increase of velocity in time is related to the one of the flame thickness, it is concluded that the two effects are linked together (showing an opposite behaviour with respect to laminar flames). For the FSC model, as for the constant density case, these two effects are decoupled. Figure 4.9 (a) shows the $\bar{c}$ profile. The FSC model practically preserves the constant density profile (there is a little spread of $\bar{c}$, as the density ratio increases, which can be related to the pressure modification across the flame), while the profile changes more with the FSD models and the progress variable profile becomes flatter as the flame thickness increases. Figure 4.9 (b) shows the source term as function of $\bar{c}$; in line with relation 4.33, the source terms moves toward higher $\bar{c}$ as they depend on $\tilde{c}$.

In conclusion FSC model preserves its characteristic, as the turbulent flame parameters are kept constant, and it is less sensible to initial conditions, while the structure of the flame and the turbulent velocity of the FSD models are sensitive to the two parameters studied in this section. Because of the implicit relation which links these parameters to the flame evolution, FSD model is probably more subject to tuning constant dependency than the FSC model. The FSD model has more constants which can be tuned; KPP-analysis leads to a relation which, for different sets of constants, gives the same fully developed turbulent flame speed, so that there are some degrees of freedom in order to match some other properties of the flame. Anyway, the selected set of constants will probably be problem dependent and does not provide a clear way to find some general relations with measured physical quantities. One of the critics moved to the FSC model is that it is not able to predict a steady planar flame because of the continuous increase of the flame brush thickness. Weller argued that this is the result of the

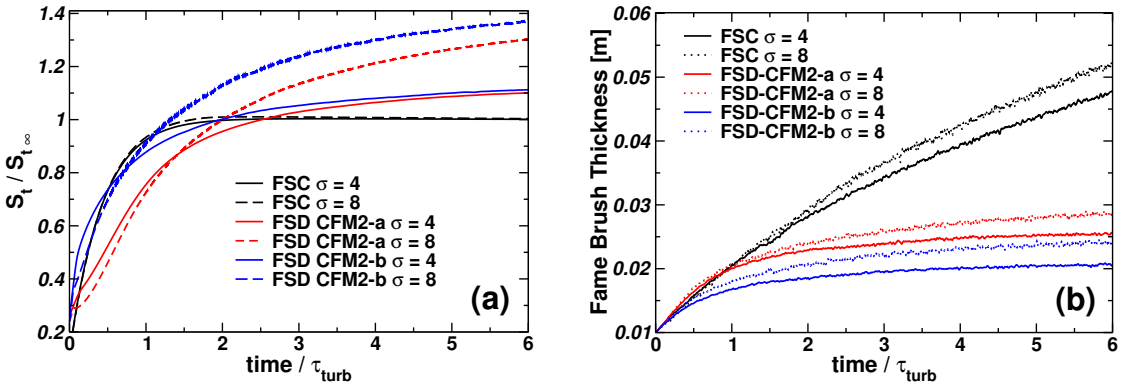

Figure 4.8: *Evolution of a planar turbulent flame for variable density cases. $\sigma = \rho_u/\rho_b$. Figure (a) shows the non-dimensional turbulent flame speed. Figure (b) shows the turbulent flame brush thickness evolution. The parameters used to initialize the problem and make the reported quantities non-dimensional are given in Figure 4.4.*

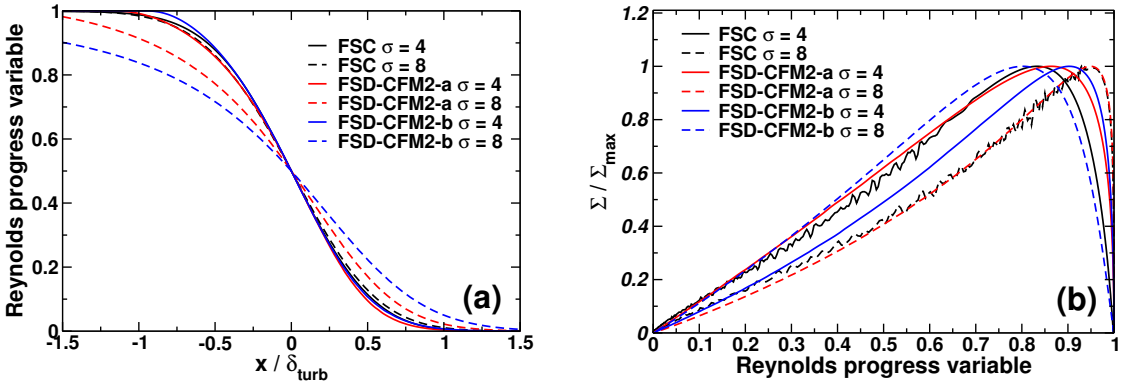

Figure 4.9: *Evolution of a planar turbulent flame for variable density cases. $\sigma = \rho_u/\rho_b$. Figure (a) shows the Progress variable profile. Figure (b) shows the Dependence of Σ source term on the progress variable $\tilde{c}$. The parameters used to initialize the problem are given in Figure 4.4.*

simplification of the cusps formation term in the Ξ equation (last term of 4.59), which is able to compensate the diffusion term. As shown in the previous section, Lipatnikov asserts in [62] that pressure driven transport term reduces D_t in time and, for very long development time, $D_t \to 0$, so that a finite flame brush thickness in achieved. Zimont, instead, suggests [122] the introduction of the following term on the right hand side of equation 4.67: $a\, u_{rms}(2\tilde{c} - 1)|\nabla\tilde{c}|$. This new source term does not alter the value of overall burning speed (the integral over the flame brush is zero in 1D), but set the value of the final flame brush thickness to be proportional to $a^{-1/2} l_t$, as proven in Figure 4.10. This term changes a bit the flame structure, as it shifts the source terms to the trailing edge of the flame, but not enough to be clearly different from the profile reported in Figure 4.3.

4.5.2 2D test case

In this section the same parameters and numerical set-up used in the previous test case are applied to a different geometry configuration, which is more in line with the one encountered in SI engines. This configuration is a 2D cylindrical expanding flame (Fig.

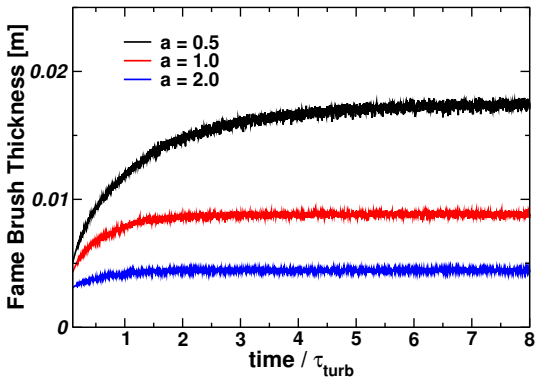

Figure 4.10: *Flame brush thickness after introduction of the term* $a\ u_{rms}(2\tilde{c}-1)|\nabla\tilde{c}|$ *in the progress variable equation. Flame brush development is shown for three values of the constant* a*.*

4.11). The main difference with the previous configuration is that this time the flame is subject to a decreasing stretch as the flame grows. The test case domain is a square which represents a quarter of the axis-symmetrical real configuration. The flame is ignited in one corner of the square; initial error function profile is imposed, but this time an important parameter which plays a role is the radius for which $\bar{c} = 0.5$. The initial flame brush thickness is selected to be 20% of the radius. Only the case with temperature ratio equal to 4 is discussed. Then some computations on a very simple engine configuration will be illustrated to conclude the test cases section.

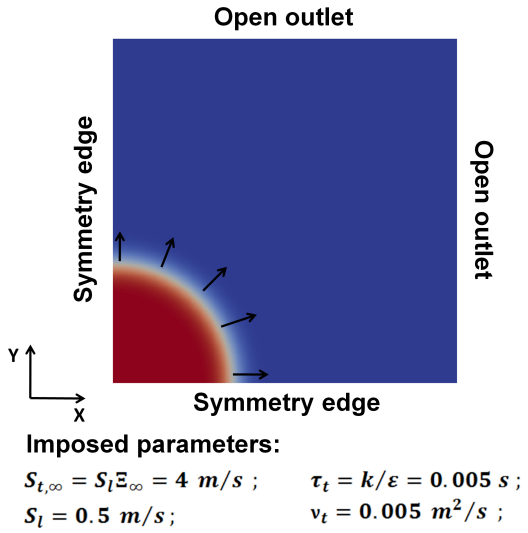

Figure 4.11: *Set-up of the 2D configuration test case.*

Figure 4.12 (a) shows the turbulent flame speed for the three models with initial radius equal to 1 cm, which is selected in order to guarantee high resolution level for the initial structure of the flame (the mesh size is 0.5 mm near ignition point). Because of the selected configuration, the surface of the flame increases with time and the computation of the turbulent flame speed requires the estimation of the average flame radius,

which is achieved by the following relation:

$$r = \frac{2}{\pi}A = \frac{2}{\pi}\int_V |\nabla \bar{c}| dV \tag{4.75}$$

$$S_t = \begin{cases} \frac{\int_V \rho_u S_t |\nabla \bar{c}| dV}{\int_V |\nabla \bar{c}| dV}, & For\ FSC\ model \\ \frac{\int_V \rho_u S_L \Sigma dV}{\int_V |\nabla \bar{c}| dV}, & For\ FSD\ model \end{cases} \tag{4.76}$$

Where A is the average flame front surface and the coefficient 2 takes into account that only a quarter of the real domain has been considered. The results of Figure 4.12 (a) are compared with the corresponding 1D results. Like laminar flames, stretch decreases the propagation speed of all the models. If equation 4.40 is rewritten using the gradient assumption in cylindrical coordinates system and only derivatives with respect to the radius are kept (because of symmetry), it is obtained:

$$\frac{\partial \bar{\rho}\tilde{c}}{\partial t} + \frac{\partial \bar{\rho}\tilde{\mathbf{U}}\tilde{c}}{\partial r} + \frac{\partial}{\partial r}\left(\bar{\rho} D_t \frac{\partial \tilde{c}}{\partial r}\right) = \widetilde{\dot{\omega}} - \frac{\bar{\rho} D_t}{r}\left|\frac{\partial \tilde{c}}{\partial r}\right| \tag{4.77}$$

Where the direction of increasing r is the same of the one of flame propagation, so that $\partial\tilde{c}/\partial r < 0 = -|\partial\tilde{c}/\partial r|$. Comparison of this result with equation 4.73 makes clear that the new term is a negative propagation velocity witch is proportional to the stretch rate and it is somehow the equivalent of the thermal-diffusion contribution of the Markstein number (first term in 3.48). The same effect appears in the flame surface density equation, but the radial profile of Σ is not monotonic, and this effect should sharp Σ profile in the middle. In fact, it also reduces the flame brush thickness with respect to the planar case, as illustrated in Figure 4.12 (b).

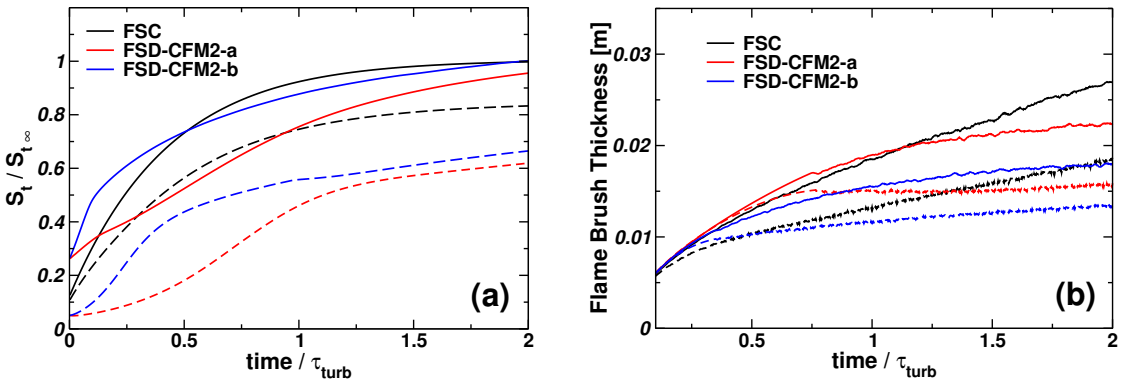

Figure 4.12: *Comparison of models results for the 1D planar and 2D cylindrical configurations with $\sigma = 4$. Turbulence properties can be found in Figure 4.11. Strain lines represent the planar case, dashed lines the cylindrical case. Figure (a) displays the turbulent flame speed. Figure (a) depicts the development of the flame brush thickness*

As for laminar flames, the reduction of velocity is stronger for higher ratio of flame brush thickness on average radius of the flame. Figure 4.13 shows this effect using FSC model and exploiting Zimont's modification (fig. 4.10) in order to change the flame brush thickness. The propagation velocity is fixed (about 4.7 m/s); the effective velocity is compared with the inverse of the radius, which is proportional to the stretch rate. It can be seen that, after an initial transient during which the flame adapts its

structure to the geometry, the combustion evolves with different trends towards the imposed velocity; in particular for higher flame brush thickness the flame speed reaches the planar flame value with lower rates.

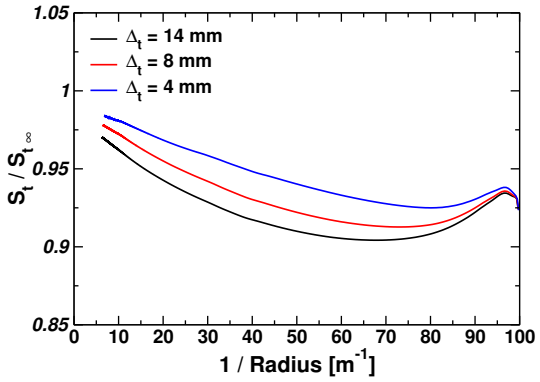

Figure 4.13: *Stretch effect on turbulent Flame speed evolution for different planar flame brush thicknesses* Δ_t.

If we look at a sequences of images of flame development, we can see a clear difference between the two models behaviours. In Figure 4.14 it is shown that the FSC model describes a flame which propagates in time while the flame brush increases its thickness. The structure of the flame is close to the one given by the planar profile and the flame initial profile rapidly rearranges to the stretched configuration. The FSD model has a longer adaptation time. As can be seen in Figure 4.15, initially the flame simply diffuses decreasing $\widetilde{c}$ near the ignition point. Then, when its thickness has grown enough, the flame starts to really propagate. If the transient behaviour and the modelling of initial stages are important, then FSC model is better. Considering that, at time 1.5 ms, the average flame radius is about 1.1 cm, potentially, in an engine simulation, the FSD model could predict an increasing flame brush thickness up to the cylinder walls. This would increase the pressure of the chamber but with a non-physical description of the flame growth.

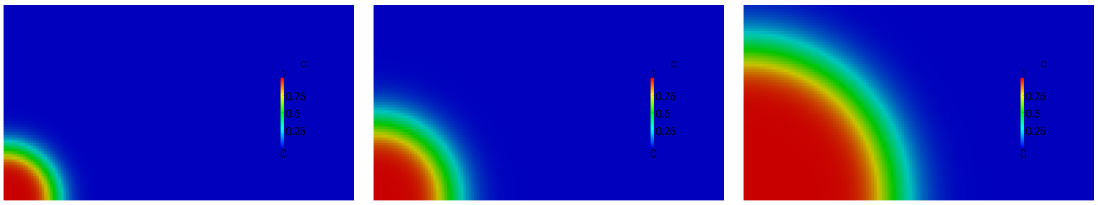

Figure 4.14: *Sequence of images which portrays the evolution of the flame for FSC model. The images show the progress variable profile for three time steps in succession (Time = 0.5 ms, 1.5 ms, 3.0 ms).*

In order to assess this last observation, a final test case is shown. A very simple engine configuration, known as "pancake engine" reported in [56], was used to test the model behaviour in an engine-like environment (hight pressure and temperature, no frozen turbulence). As shown in figure 4.16, the combustion chamber is disk-shaped with a nearly centrally located spark plug. As a consequence, the engine could be simulated by using an axis-symmetric mesh, represented by 2D wedge. Three experimental operating conditions were simulated for this engine (see table 4.2). The same set-up

Figure 4.15: *Sequence of images which portrays the evolution of the flame for FSD-CFM2-a model. The images show the progress variable profile for three time steps in succession (Time = 0.5 ms, 3.0 ms, 4.0 ms).*

proposed in [56] is used for these simulations. This configuration was selected because it is easy to be reproduced and fast to be computed.

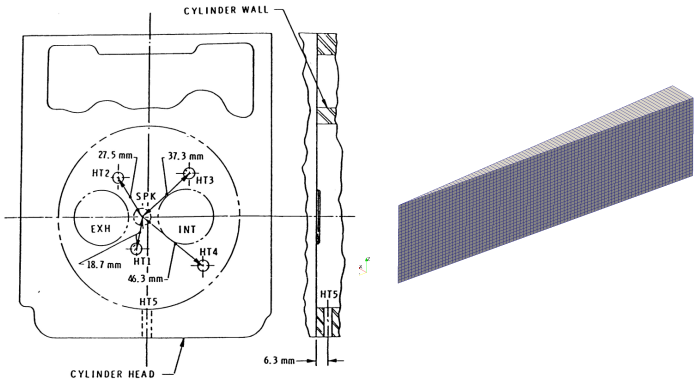

Figure 4.16: *Pancake engine configuration. Draft of the real geometry and of the mesh used in the simulations.*

Case	Volumetric Efficiency [%]	Overall Equivalence Ratio [-]	Engine Speed [rpm]	T (IVC) [K]	u_{rms} (IVC) [m/s]	l_t (IVC) [m]
1	40.0	0.87	1500	453	19.78	4.03
2	60.0	0.87	1500	429	19.78	4.03
3	40.0	0.87	1000	436	13.20	4.03

Table 4.2: *Simulated operating conditions for the selected engine. Further details can be found in [56]*

The models employed are modified versions of the previous solver adapted to run with LibICE moving mesh library [69]. In this case the CFM2-a version of flame surface density model and the G-Equation approach (more details of its implementation will be given in chapter 6) are compared. For the second model, the simplified Ξ equation 4.68 and relation 4.39 are used to compute the turbulent flame speed and to convert G scalar into the progress variable. As a consequence, the results obtained with G-Equation model and with FSC model are very similar. Therefore, only G-Equation results are shown. These models require a specific ignition treatments, as they have

no source term which describes ignition. In this configuration, numerical ignition is employed to initialize G-Field and Σ. For G-Equation model, the initial flame kernel grows linearly in time; the final radius and ramp time are given as input parameter (respectively 3.0 mm and 8 CAD). After the flame has reached this radius, the G-field equation is solved. For the FSD model, the same approach proposed in [9] is used. It involves the selection of an initial radius and delay time after which Σ is initialized by following this relation:

$$\Sigma = \frac{A_t}{V_0}\left(1 - erf\left(\frac{|r - r_0|}{2l}\right)\right) \tag{4.78}$$

where A_t is computed starting from the spherical surface obtained by the initial radius (about 1.5 mm) multiplied by the turbulent stretch term of Σ equation ($k_t = \alpha\Gamma_k\epsilon/k$), V_0 is a normalization volume on which the area is distributed and l is a diffusion length scale computed as $l = \sqrt{\nu_t(t - t_{ign})}$. As already stated, this is just a numerical initialization: no physical interpretation is given.

Figures 4.17 and 4.18 show the comparison of pressure and brunt mass fraction results for the case 1 of table 4.2, for which model constants were tuned. The peak pressure could not be captured because the engine suffers from quenching near the walls, an effect which the implemented models cannot predict. For these tests, the interest is focused on the behaviour of the flame of the two models to obtain the experimental data, more than the simple comparison of model results with experiment. Figure 4.19 shows the initial flame evolution for the G-Equation model. The flame shape has an initial imposed spherical geometry, which then moves toward the head of the cylinder, because of the mean flow. Then it starts to propagate to the whole engine. Figure 4.20 shows the same flame evolution for the FSD-CFM2-a model. Also in this case the initial shape of the flame is spherical, but it is lost in the following evolution. In particular it can be noticed that the flame does not propagate up to -9 CAD, but essentially it diffuses (The maximum progress variable at -9 CAD is about 0.97). Then the flame starts to propagate. The flame surface density shown in figure 4.21 underlines better this behaviour. In particular it can be noticed that at -9 CAD only a very small zone at the upper-left edge can be considered completely burned; all the remaining burnt volume belongs to the flame brush which practically covers one third of the total volume of the engine. This behaviour is not physically justified. At this time, only about 3% of the fuel mass is burnt, so that the pressure of the cylinder is not useful to analyze this phase.

For the sake of completeness, also the other two simulated points are shown in Figures 4.22, 4.23, 4.24 and 4.25, for which the model constants of the previous cases were kept equal. It can be noticed that the G-Equation model (or, more precisely, the Zimont/Gulder turbulent flame speed correlation, equation 4.84) seems to correctly respond to load changes (pressure changes), while the FSD model seems to scale better with different engine speeds (probably thanks to the INTFS Γ_k function [78], which appears in k_t, see table 4.1). Anyway the uncertainties related to the set-up of the model and the few information about the flame development do not allow to real support this last argument.

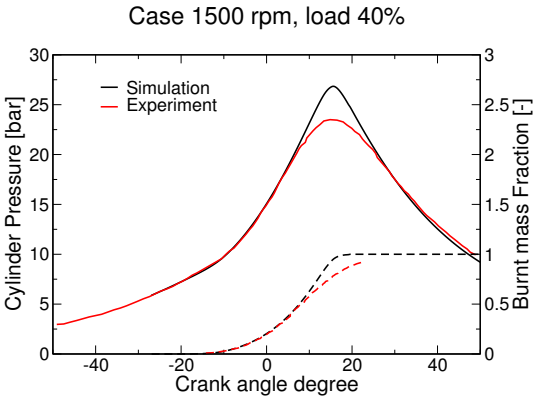

Figure 4.17: *Comparison between experiments and numerical results of G-Equation model of cylinder pressure and burnt mass fraction.*

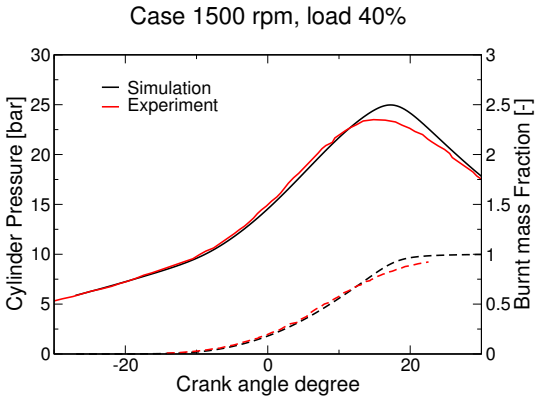

Figure 4.18: *Comparison between experiments and numerical results of FSD-CFM2-a model of cylinder pressure and burnt mass fraction.*

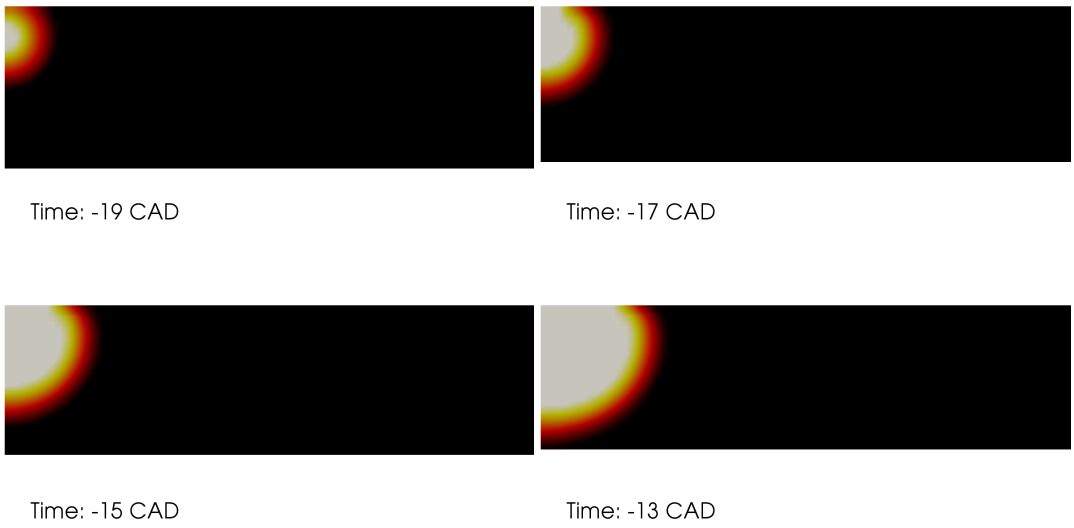

Figure 4.19: *Sequence of images which portray the initial evolution of the flame in pancake engine. Favre progress variable profile is shown for four Crank Angle Degrees before top dead centre.*

4.5.3 Summary of the comparison

In this section the behaviour of the three main models employed in literature has been tested in order to select the most promising one to simulate premixed combustion in SI engines. The results show that the flame surface density models are very influenced by the change of parameters which should not affect so much the flame behaviour and which are not directly controlled by the model. This seems to imply that this approach will probably rely much more on tuning constants than the other two models when different cases are studied. Moreover, as these constants are not directly associated with the main features that a RANS simulation can represent (average turbulent flame speed and flame brush thickness), information obtained by their tuning are not easy to be interpreted. Moreover, the transient behaviour of the FSD model is associated with an

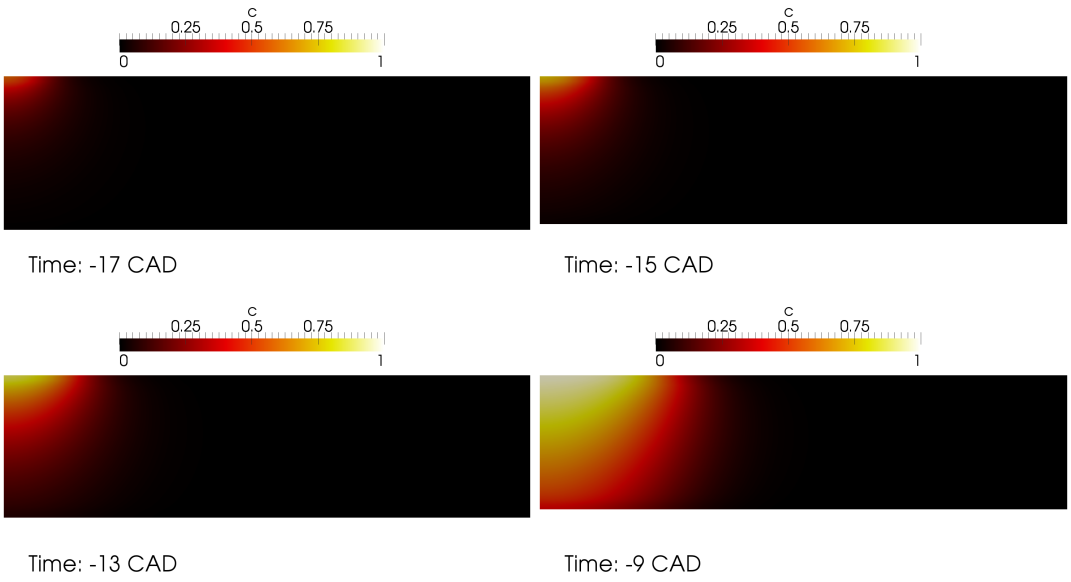

Figure 4.20: *Sequence of images which portray the initial evolution of the flame for FSD-CFM2-a model. Favre progress variable profile is shown for four Crank Angle Degrees before top dead centre.*

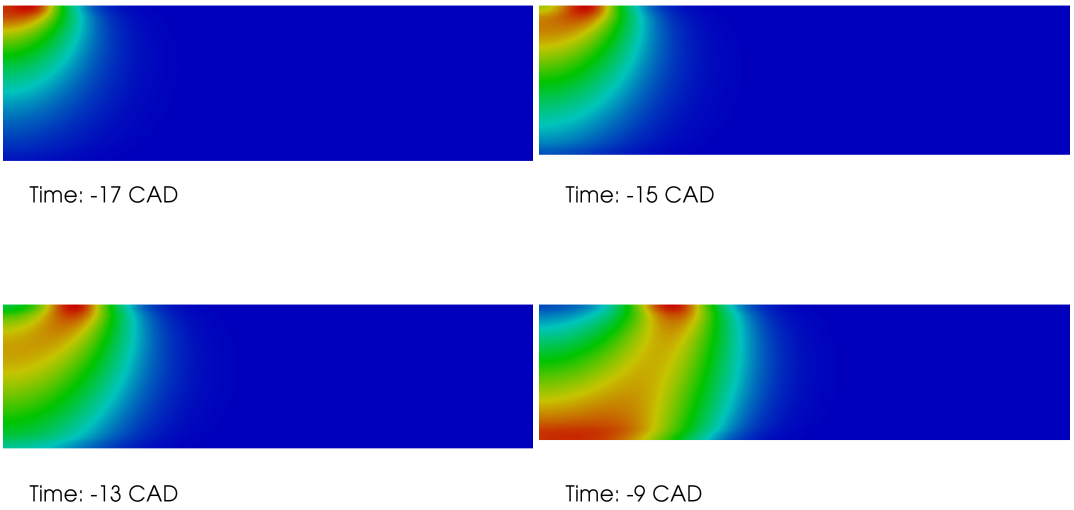

Figure 4.21: *Sequence of images which portray the initial evolution of flame surface density for FSD-CFM2-a model. The images correspond to those of Figure 4.20.*

initial increase of flame brush without propagation of the flame. When the thickness becomes close to its full developed value, then the flame starts to really propagate. This is due to the progress variable equation which retains a reaction-diffusion form. This feature probably (at least for RANS simulations) does not let many possibilities to simulate the initial stages of flame development. In particular, there is not a clear way to couple the results of dedicated sub-models employed to simulate this phase with the main model equations without losing the supposed higher accuracy provided by their

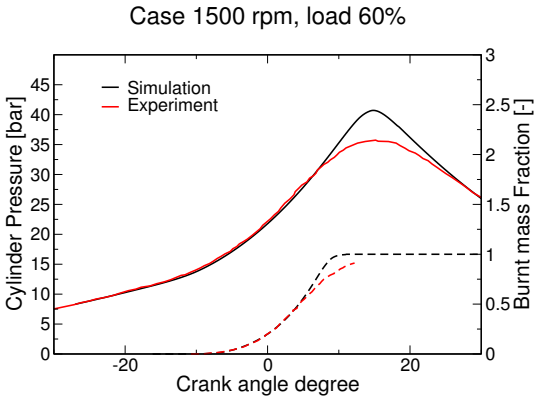

Figure 4.22: *Comparison between experiments and numerical results of G-Equation model of cylinder pressure and burnt mass fraction.*

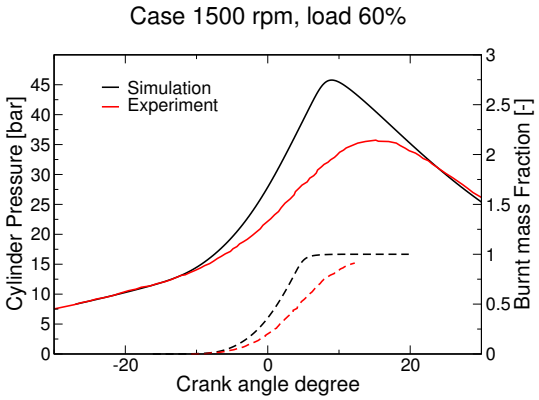

Figure 4.23: *Comparison between experiments and numerical results of FSD-CFM2-a model of cylinder pressure and burnt mass fraction.*

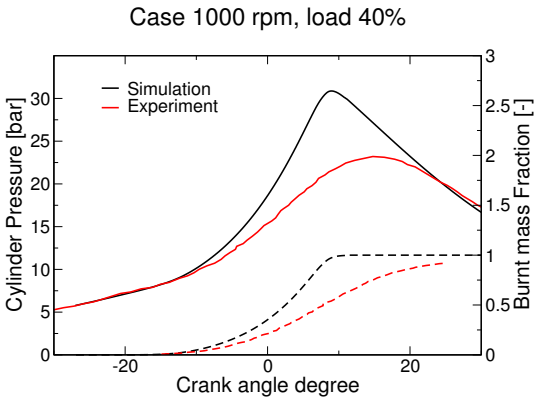

Figure 4.24: *Comparison between experiments and numerical results of G-Equation model of cylinder pressure and burnt mass fraction.*

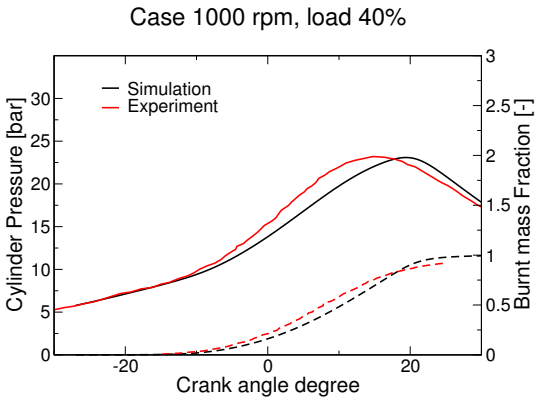

Figure 4.25: *Comparison between experiments and numerical results of FSD-CFM2-a model of cylinder pressure and burnt mass fraction.*

use. Even more, if we consider that in a real spark-ignition engine geometry the conditions are not so well defined as in these test cases (turbulence is inhomogeneous and the mesh quality can be much lower), the problem becomes more complex and harder to be handled. For FSC model, the flame brush thickness develops continuously but slowly in time. Its effect on the turbulent flame speed is quite weak. This is related to the propagative form assumed by the progress variable equation for this model. This form is more consistent with the concept of surface propagation, but it can also introduce a problem: at initial stages, if the flame brush grows faster than the propagation speed, the progress variable could travel back to the trailing edge. If this backward effect reaches a wall or the centre of an expanding sphere, then the flame will continue to propagate, but the maximum value reached by the progress variable will be always less than one and the flame could propagate and cover all the engine geometry without being able to completely burn the fuel. Even if this is unlikely to happen and can be avoided if a sufficient large initial flame radius is selected for ignition purposes, it anyway introduces a constraint which depends on the flow field and the mesh employed in a not obvious way. On the other hand, the FSD model allows the control of

the flame structure by means of the functions used to correlate the source terms of Σ equation with the progress variable and the tuning constants. This model is probably well suited to simulate statistically stationary cases, like Bunsen or V-shaped flames, for which many information about the structure of the flame are available and it is not important to simulate the initial transient of the flame. In fact the correlations used for the source terms of Σ are usually justified arguing that, at steady conditions (the sum of source terms equal to zero), Σ assumes a shape which agrees with experimental data ($\bar{c}(1-\bar{c})$). However, this clearly does not mean that the transient behaviour related to this description is correct. The FSC model is simpler: it does not allow to change the structure of the flame, which is anyway physically meaningful (see Figure 4.3), but it is able to decouple the propagation speed from flame structure. This makes easier the control of the flame evolution, which also means that it simplifies the analysis of the results. The flame brush thickness instead is still implicitly described in the progress variable equation and can be partially controlled by means of specific models of the turbulent diffusivity D_t (as proposed by Lipatnikov) or applying the modification suggested by Zimont (Figure 4.10). The G-Equation approach is somehow the simpler method; it just tracks the average flame radius position and it completely decouples flame brush evolution, propagation velocity and flame structure, which can be modelled by specific equations which do not interfere between them and offer the simpler way to control/understand the combustion process. Because of this decoupling, this approach is very flexible as it allows to use the correlations proposed by different authors for modelling single aspects of combustion. Finally, from a theoretical point of view, G-equation is more coherent with the concept of premixed flames seen as propagating surfaces wrinkled by turbulence instead of a combustion process controlled by turbulent mixing. As a consequence this last approach has been preferred to the others and will be further developed in the next chapters.

4.6 The turbulent flame speed

This section is focused on the main factor which influences the results of G-Equation combustion models: the turbulent flame speed. Many theoretical and experimental relations have been developed in time for the thin reaction zone and corrugated flamelets regimes. As pointed out in section 4.2, it is hard to clearly define the border line between these two regimes and engine working points are usually located across this line, so that both kinds of relations could be employed for practical purposes. Anyway from a theoretical point of view, the distinction between the two regimes can help to derive some relations, regarded as asymptotic limit results. Usually the parameters which appear in these relations are the root mean square velocity (u_{rms}) and the integral length scale (l_t) which, together with cascade energy concepts and fluid viscosity, are roughly able to describe all the turbulence scales. These are also the global quantities which are measured and that RANS two-equation models can estimate. The parameters, usually selected to describe the mixture combustion properties, are the unstretched laminar flame speed (S_L^0) and the flame thickness (δ_L), both with the diffusion and maximum temperature gradient definition (see Equations. 3.1, 3.3). As noticed in sections 3.3 and 3.4, also the Markstein number (Ma_b, which can be measured, or Ma_u, which can be derived from the first one comparing relations 3.49 and 3.48) should be included in

the description. Its influence on turbulent propagation speed is demonstrated, for example, in the experiments shown in [11], where some couples of air-propane mixtures (one lean and one rich) with the same laminar flame speed and density ratio show a different response to the same turbulence field. Moreover, for low turbulence levels, also intrinsic flame instabilities (which are characterized also by the density ratio σ) can play a role ([22], [115]). In the following, some relations derived for statistically steady planar flames will be reviewed; then some considerations about the unsteady case of spherical expanding flames, which is more significant for spark-ignition engine configuration, will be discussed.

4.6.1 Turbulent planar flames

This case is the corresponding case of laminar planar flame. The flame is statistically unstretched (some DNS computations show that the mean value of the stretch distribution is positive, but anyway close to zero) and experiments on duct geometries can be used to measure the flame propagation speed. In fact, for this configuration, considerations about mass conservation and flamelets regimes lead to the following simple relation:

$$\rho_u \mathbf{U} A_{duct} = \rho_u S_L^0 A_{turb} \tag{4.79}$$

Where $\mathbf{U}$ is the inlet velocity, A_{duct} is the cross-section area of the duct and A_{turb} is the flame area corrugated by turbulence eddies. The value of $\mathbf{U}$, for which the flame is fixed in laboratory coordinates system, gives the turbulent propagation speed: $\mathbf{U} = S_t = S_L^0 A_{turb}/A_{duct} = S_L^0 \Xi$. In general, it is not so easy to define when a turbulent flame is motionless and other experimental configurations like Bunsen and V-Shaped flames are usually preferred to estimate the turbulent propagation speed. These configurations require other relations than Eqn. 4.79. For planar turbulent flames, it is well accepted that the increase of turbulence intensity initially enhances the flame propagation speed; at higher values, this increment becomes less prominent (blending effect) and for even higher values the flame keeps the same propagation speed until quenching due to the induced stretch occurs. There are different theoretically derived expressions for Ξ; most of them share many aspects in their derivation, which is based on scales analysis. One of the first theoretically derived expressions was proposed by Damkohler in 1940. He considered two cases: the first one is for large turbulence scale ($l_t/\delta_l >> 1$, which is practically the corrugated flamelets regime), for which he assumed that the interaction between the wrinkled flame front and the turbulent flow field is purely kinematic. Using the geometrical analogy with a Bunsen flame, Damkohler related the increase of the flame surface area to the velocity fluctuation divided by the laminar burning speed:

$$\frac{S_t}{S_L^0} = \Xi \sim \frac{u_{rms}}{S_L^0} \tag{4.80}$$

The second case represents small scales turbulence $l_t/\delta_L \sim o(1)$ which can be associated with the thin reaction zone. For this case Damkohler assumed that chemical time scale τ_c of turbulent flame is the same of the corresponding laminar flame, while turbulence only increases heat exchange in the preheat reaction zone. From dimensional analysis:

$$\frac{S_t}{S_L^0} \sim \left(\frac{D_t/\tau_c}{D/\tau_c}\right)^{1/2} \rightarrow S_t \sim \frac{D_t}{D}^{1/2} \sim Da^{1/2} u_{rms} \tag{4.81}$$

Where $D_t \sim u_{rms} l_t$ is the turbulent diffusion coefficient and $D \sim \delta_L S_L$ is the laminar diffusion coefficient (δ_L is defined as a diffusion length). This second case is coherent with a mixing-controlled combustion process. For common values of turbulent Reynolds numbers ($Re_t \sim 4000$), the relation $l_t/\delta_L \sim o(1)$ implies low values of Damkohler number ($Da < 1$), which indicates that the flame is in the broken reaction zone. In this regime the flame quenches and the assumption that the chemical time scale is not altered by turbulence is at least arguable. Anyway, the previous argument can be applied to the smallest scales in the cascade concept, for which the corresponding turbulence intensity u_n is much lower than u_{rms} and then the Damkohler number can be much more than one. For example, Zimont in [129] derived his relation assuming to be in the thin reaction zone. In this regime, he argued that small eddies, penetrating the preheat zone, change the structure of the laminar flame increasing its thickness to δ_{nt} and reaction speed to u_{nt}, while eddies bigger than δ_{nt} corrugate the flame with purely kinematic interaction. He applied the same Damkohler assumptions to estimate u_{nt} and proposed the following relation for the turbulent propagation flame speed:

$$S_t = u_{nt} \frac{\Delta_t}{\lambda_f} \tag{4.82}$$

$$\frac{u_{nt}}{S_L^0} \sim \left(\frac{D_{nt}/\tau_c}{D/\tau_c} \right)^{1/2} \rightarrow S_t \sim Da^{-1/2} u_{rms} \tag{4.83}$$

where Δ_t/λ_f is a wrinkling coefficient Ξ for this "thickened flamelet", Δ_t is the dispersion of the random oscillation of thickened flamelets (essentially the brush thickness) and λ_f a microscale cut-off length. It is noticed that Eqn. 4.83 gives a different exponent than Eqn. 4.81 as $D_{nt} \neq D_t$. After some empirical and theoretical assumption, Zimont estimates λ_f and proposed the final relation:

$$S_t = A Da^{1/4} u_{rms} \tag{4.84}$$

where $A = 0.5$ was obtained from experimental analysis. For a critical discussion of this final result, see [61], appendix D. The same expression, with $A = 0.62$ was proposed by Gulder in [41]. In this case, the relation is only the result of extrapolation from experimental data. In this case S_t increases more weakly with Da than relation 4.81. Combining both Damkohler results in a quadratic expression for the turbulent flame surface area ratio and taking only the positive root result, Peters in [91] derived the following relation for the propagation speed of the mean flame position:

$$\frac{S_t}{S_L^0} = 1 - \frac{a_4 b_3^2}{2 b_1} \frac{l_t}{\delta_L} + \sqrt{\left(\frac{a_4 b_3^2}{2 b_1} \frac{u_{rms} l_t}{\delta_L S_L^0} \right)^2 + a_4 b_3^2 \frac{l_t}{\delta_L}} \tag{4.85}$$

which can be rewritten as:

$$\frac{S_t - S_L^0}{u_{rms}} = -\frac{a_4 b_3^2}{2 b_1} Da + \sqrt{\left(\frac{a_4 b_3^2}{2 b_1} Da \right)^2 + a_4 b_3^2 Da} \tag{4.86}$$

Which shows a Damkohler number dependence for low value close to $Da^{1/2}$, while for $Da >> 1$, the turbulent flame speed becomes Damkohler number independent ($S_t \sim b_1 u_{rms}$). The proposed modelling constants are summarized in table 6.1 in

chapter 6. Being this expression the result of the combination of the two asymptotic relations obtained by Damkohler, Peters stated that this relation should be valid for both corrugated and thin reaction zone regimes. All the previous relations only use δ_L and S_L to characterize the laminar flame behaviour. As previously pointed out, also the Markstein number should be included as a parameter in these relations. One of the few correlations which takes this aspect into account is proposed in [13]:

$$\frac{S_t}{u_{rms}} = 1.53 \left(\frac{S_L^0}{u_{rms}} \right)^{0.3} Da^{0.15} Le^{-0.3} \tag{4.87}$$

Where Ma_u is represented by the Lewis number. In other correlations, stretch effects are introduced as a correction of the laminar flame speed value by a term named stretch factor I_0 which multiplies S_L^0. In the author's opinion, the Markstein number should be considered when the relation between turbulence and flame scales is described. For example δ_L could be replaced with $Ma_u \delta_L$ or with $Pe_{cr} \delta_L$ because, as described in 3.4, asymptotic theory shows that for length scales lower that this quantity, a noise signal is damped out (Figure 3.8). Small turbulent scales, whose energy density is low, could be associated with this noise. As a consequence, the correct way to take this effect into account is to use this parameter directly when scaling relations are derived. This damping effect is confirmed for laminar flames when Darrieus-Landau instability develops, but is also seen in turbulent flames. For example the two Schlieren images taken from [116] and reported in Figure 4.26 and 4.27 represent two developing spherical flames for mixture with different value of Markstein number at the same turbulent flow field. In particular, Figure 4.26 shows a near equidiffusive flame (Methane $\phi = 0.9$) and Figure 4.27 shows a strong non equidiffusive flame (Hydrogen $\phi = 4.0$). The turbulent integral scale is the same for the two cases and also the turbulent Reynolds number. It can be noted that the smallest wrinkles of Figure 4.27 are well defined and bigger than those of Figure 4.26, even if the Kolmogorov scale is almost the same (it is even smaller for the hydrogen case). This indicates that thermo-diffusion effect represented by the Markstein number increases the value of the lower cut-off length for which turbulence wrinkle the flame. This effect can be related to the kinematic restoration mechanism identified by Peters. While Peters assumes as a first approximation a constant value for the laminar flame speed $S_L = S_L^0$, asymptotic theory shows that, if $Le_{eff} > 1$, positive stretches reduce local flame propagation while negative stretches enhance this value. As a consequence, small scale wrinkles, induced by low intense turbulence eddies, are associated with strong increase of local stretch and are immediately cancelled out by flame motion. As Peters introduced the Gibson scale ($l_G = (S_L^0/u_{rms})^3 l_t$) to describe kinematic restoration effect, a new scale, which depends also on the Markstein number, could be introduced to describe the same effect.

Many other expressions can be found in literature. Some of them can be obtained from KPP-analysis ([43]) of flame surface density models. Many others use fractal theory to derive relations like:

$$\frac{S_t}{S_L^0} = 1 + \left(\frac{l_0}{l_i} \right)^{D_f - 2} \tag{4.88}$$

Where D_f is the fractal dimension whose value varies between 2 (laminar case) and 7/3 (fully turbulent case) and is probably function of the ratio u_{rms}/S_L^0 or Re_t. l_0 is

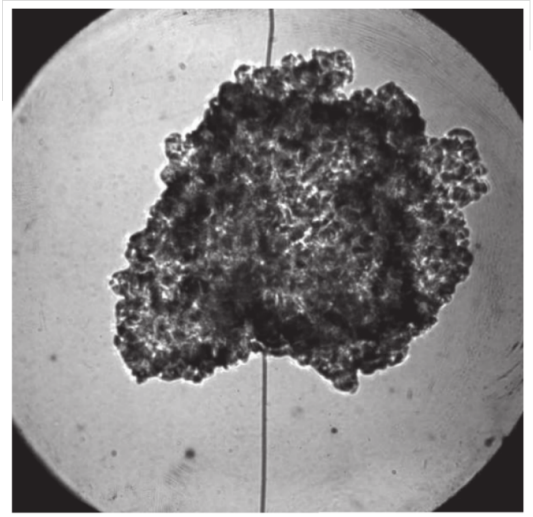

Figure 4.26: *Methane-air mixture, ϕ = 0.9, p = 5 atm, δ_L = 0.16 mm, $Ma_b\delta_L$ = 0.12 mm, $\bar{R}$ = 21.87 mm, l_t = 4 mm, Re_t = 210.*

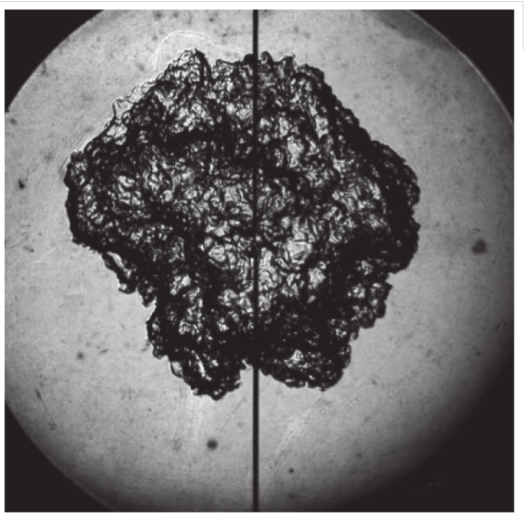

Figure 4.27: *hydrogen-air mixture, ϕ = 4.0, p = 5 atm, δ_L = 0.09 mm , $Ma_b\delta_L$ = 0.35 , $\bar{R}$ = 21.41 mm, l_t = 4, Re_t = 221.*

the outer cutoff scale, which is usually associated with the integral length scale. l_i is the inner cutoff scale and it can be associated with the Kolmogorov scale, which only accounts for the turbulence, or the Gibson scale, which accounts also the kinematic restoration effect. It could also be associated with the critical Peclet number, which would include both kinematic restoration and non-equidiffusion effects.

All these relations developed in time clearly demonstrate that more work has to be done, both to increase the accuracy of the available experimental data and to better define combustion regimes which are associated with different mechanism. It must be remembered that, in all experiments, turbulence properties are actually taken in the unburnt zone far from the flame. Modifications of turbulence properties induced by heat release, which are associated with σ and geometrical configuration, should be also taken into account. Many recent experimental works are paying much more attention to the description of the experimental tests, with the indication of some parameters which were not considered before. Maybe, when enough new data will be collected, it will be clearer if some of the previous relations are better then others to describe the experimental results. Alternatively, direct numerical simulations could be very helpful to resolve the problem, as they remove many of the uncertainties which characterize experimental data; they directly provide all the information needed to a comprehensive post-processing; they allow to decouple some of the many mechanisms which affect flame propagation (for example constant density combustion can be simulated, but not reproduced experimentally), making the analysis of the problem easier. Unfortunately, the collection of enough data by means of DNS is still far to be possible (usually in one paper only a single test is discussed). Hydrodynamic model provides a way to potentially overcome this issue.

4.6.2 Turbulent spherical expanding flames

In this section the global transient behaviour of turbulent propagation speed, which is typically encountered in SI engines, is discussed. Some modifications of the expressions analyzed in the previous section, which try to incorporate these new effects, are proposed. When a premixed mixture is ignited at the centre of a vessel, a flame kernel is formed and starts to develop. If the mean flow field is not so intense near the spark plug to distort the kernel, initially the flame assumes a laminar spherical shape [94]; then it starts to be wrinkled by the turbulent eddies, until it reaches a statistically steady condition. This transient phase is connected with different physical mechanisms:

- Not all the eddies which compose the turbulent spectrum are able to wrinkle the flame. In particular, defining δ as the ratio of the average radius of the flame on the length scale of a generic eddy, if $\delta < 1$, the vortex can corrugate the flame; if $\delta > 1$ the eddy convects the flame kernel like a particle. As the flame grows in size, it will be wrinkled by bigger and bigger vortexes.
- The corrugation of a laminar flame front takes some time before the wrinkled surface reaches a fully developed status. This is true also for planar flames.
- For lean mixture of fuels, whose Lewis number is bigger than one, the high stretch rate due to curvature tends to damp out the corrugation induced by small eddies. This could be the reason for which the flame keeps a laminar spherical shape in the first phase after ignition.
- For planar like flames, the average stretch is close to zero. In spherical expanding flames, this value is different from zero and decreases in time with the radius. Some global effects, like the one analyzed in section 4.5.2, are likely to appear.
- In spherical expanding flames, the increase of flow velocity due to the change of density across the flame is ahead of the flame. Its increase can be connected with the relation: $U_r = S_t(\rho_u/\rho_b - 1)$, where U_r it the component in the radial velocity direction. As a consequence, the induced velocity gradient could increase the turbulence intensity level of the unburnt. This affects the flame propagation speed, creating a loop for which the flame continuously accelerates in time. To the author's knowledge, this effect has not been systematically considered in experiments, for witch only turbulence properties without combustion are usually measured.

This topic is quite specific and it was not extensively studied as V-shaped or Bunsen flames. This is probably related also to the problems arising with experimental configurations used to investigate such unsteady processes. Bradley in [11] and more recently in [15], analyzed some issues related to the employed experimental measuring techniques and how to correlate the experiments with global average quantities. In particular, in order to compute the ensemble average of the flame radius, high-speed MIE scattering images should be taken, as they capture the flame density discontinuities in one cross-section of the flame, while Schlieren images capture the projection of the 3D flame on a plane. As a consequence, MIE scattering images allow to compute the radius of the sphere "so chosen that the volume of unburned gas inside is equal to the volume of the burned gas outside" [11]. The ensemble average of this radius

should correspond to the position of the flame front for which $\overline{c} = 0.5$ and its standard deviation to the flame brush thickness. The problem is that MIE scattering requires a planar laser sheet which, for big cross-sections, is quite demanding. The usually adopted Schlieren imaging technique will always estimate higher radii. The meaning of the radius obtained with such technique is not really clear, even if it has been sometimes identified (without a concrete explanation) with the leading edge of the flame ($\overline{c} = 0.05$). For these reasons Bradley in [11] correlated the radii obtained with the two techniques and he found a linear correlation. Anyway, this additional passage and the doubts about the generality of this correlation to other conditions (in particular different density ratio) will always increase the uncertainties related to the values estimated with Schlieren imaging technique. Apart from these difficulties, which make even harder to understand the physics of the problem from experiments, some way to model the effect previously listed have been proposed. Bradley in many of his group's works, see for example [14], proposed to compute an effective turbulence intensity which affects the flame. Its value is estimated by the integration of the turbulent spectrum shown in Figure 4.1. The results of this computation gives the ratio $u_{rms,eff}/u_{rms}$ as function of the ratio between the diameter of the flame and the integral length scale ($2r/l_t$). u_{rms} and l_t are quantities that are usually measured or which can be computed with RANS models. An example of results of this integration is shown in Figure 4.28. In this case the full turbulent intensity is only reached when the flame diameter has become equal to the combustion chamber geometrical length, which can be n-times the integral scale. This model can be used also in RANS simulations and it was tested by the author, but the integration process for every cell is computationally expensive and the definition of the maximum geometrical length is not so clear as in the experiments for which it was proposed. Moreover, the final result is significantly affected by large scale contribution (larger than the integral length scale), for which the spectrum dependency on wavenumber is more flux-dependent than the one in the inertial sub-range. As a consequence, a simpler and less expensive way to model this effect is to use the scaling relations presented in section 4.1 for the inertial sub-range, replacing l_n with the radius of the flame and using equation 4.15 to replace u_{rms} in the various expressions. Such problem does not exist in LES simulations, as the filter size is practically always smaller than the flame radius.

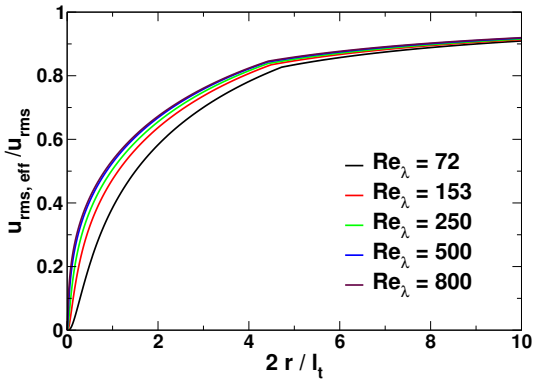

Figure 4.28: *Turbulence intensity ratio for increasing value of flame diameter normalized on the integral length scale for different Taylor Reynolds numbers.*

About the second point listed before, many evolution equations of turbulent flame speed were already proposed in this chapter. For example the Ξ equation in Weller's model which, as already shown, describes an exponential increase of the turbulent speed with a time constant equal to integral length turnover time $\tau_t = k/\varepsilon$. Lipatnikov in [61], starting from relation 4.82 of Zimont's model, made the turbulent diffusivity value D_t change with time, accordingly with Taylor's theory for mixing layers ($D_t/D_{t,\infty} = 1-exp(t/\tau_t)$). As a consequence, because of relation 4.82, also S_t evolves in time. In particular, using Eqn. 4.89 to express the flame brush increase in time, it can be obtained:

$$\Delta_t^2 = \int D_{t,\infty}(1 - exp(t/\tau_t))dt \tag{4.89}$$

$$\frac{S_t}{S_{t,\infty}} = \left(1 + \frac{\tau_t}{t}\left(exp\left(-\frac{t}{\tau_t}\right) - 1\right)\right)^{1/2} \tag{4.90}$$

where $S_{t,\infty}$ is the fully developed turbulent flame speed, corresponding to the fully developed turbulent diffusivity $D_{t,\infty}$. t is the time after ignition or the Lagrangian traveling time of the flame, seen as a particle moving from the ignition point (for example the flame holder rod in a V-Shaped flames) to the actual position. Arguments similar to the ones already exposed led Peters in [65] to update equation 4.85. Specifically, he proposed to substitute the integral length scale with the flame brush thickness, because of their proportionality ($\Delta_t = b_2 l_t$); then to compute the flame brush thickness through an appropriate transport equation (Eqn. 6.14 in chapter 6 which in homogeneous, frozen turbulent environment is simplified to $\Delta_t/\Delta_{t,\infty} = b_2\left(1 - exp(-c_s t/\tau t)\right)^{1/2}$). Finally to replace u_{rms} with $u_n = u_{rms}(\Delta_t/\Delta_{t,\infty})^{1/3}$ in equation 4.85 (the final solution is Eqn. 6.10 reported in chapter 6). Apart from the last model, which uses Δt instead of the flame radius, it is not clear if these models can already include the effect of the increasing range of turbulent wavelength affecting flame wrinkling. For example, Lipatnikov originally proposed his model for planar like flames configuration (V-Shaped), but then he also applied the same model to spherical expanding flames, without considering the average radius of the flame. Figure 4.29 shows a comparison of the transient behaviour predicted by the use of equations 4.68, 4.90 and 6.10. It is noted that only Peters model shows a weak dependence on the flame properties by means of the Damkohler number, while the others equations are only affected by turbulent characteristic time k/ε. Moreover Peters model shows the smaller transient time.

The third point of the list could be included, as proposed previously, by replacing the laminar flame thickness with the Markstein thickness or the critical Peclet number multiplied by the laminar flame thickness; an example in which this kind of scaling seems to work well is reported in [116], where extrapolation from experimental data provides an expression which is formally identical to Eqn. 4.81. In this case, the computation of the Damkohler number is different as u_{rms} is replaced with an effective value $u_{rms,eff}$, which increases with the average radius, l_{int} with the average radius of the flame R and the diffusion thickness δ_L with $Ma_b\delta_L$:

$$\begin{aligned} S_t &= Da^{1/2} u_{rms,eff} \\ Da &= \frac{S_L^0 R}{u_{rms,eff} Ma_b \delta_L} \end{aligned} \tag{4.91}$$

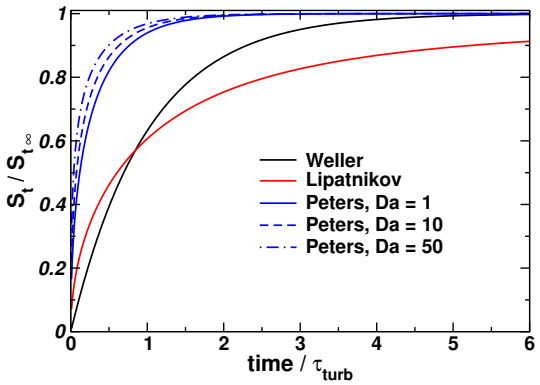

Figure 4.29: *Comparison of the transient behaviour of turbulent flame speed models proposed in [117], [63] and [65]. Turbulent flame speeds are scaled on the corresponding equilibrium value ($t \to \infty$). Time is scaled on the integral length turbulent turnover time $k/\epsilon = 0.005s$. For Peters model, various curves are reported for different Damkohler numbers.*

From what explained in 3.4, it could be argued that the flame should reach a certain radius before being wrinkled by turbulence. The critical length obtained by the Peclet number is probably higher than the one associated with the disturbances introduced by a turbulence field, whose amplitude is finite and not infinitesimal, but it could be proportional to that. Because also the Markstein number represents the same physical mechanism, these two parameters could be interchangeable.
The effect of the average stretch rate due to mean curvature is implicitly implemented in the models, as shown in the previous section (and explicitly in equation 4.38). More considerations about this issue can be found in [64]. It could be argued that, in these models, this effect is associated only with turbulent quantities and not with the Markstein number, which probably could play a role also on the big scales. Moreover, the average curvature is correlated with the mean flame radius and not with turbulent length scales, which corroborates the choice of the authors of [116] to replace the hydrodynamic length scale l_t directly with R.
Some considerations about the modification of turbulent field by premixed flames are discussed in [66]. In this work it is stated that this topic has been considered of secondary importance by scientific community. Moreover, it is underlined that the description of these effects requires the solution of conditioned equations on which, in the author's knowledge, only Lipatnikov is actually working. Multiphase flow solvers, hydrodynamic model and BML analysis could be used as a starting point to develop this kind of approach, which should also be applied within the LES context.
In general, there are many problems when the experimental data and computed results are compared to determine if a model is able to predict the transient behaviour of a premixed flame. First, the uncertainties related to the fully developed quantities are inherited in transient computation. Second, in some cases more model constants are introduced; finally suitable experimental data cannot be easily found. For example Bradley's group and more recently Law's group have made many experimental studies about turbulent spherically expanding flames at constant pressure. In [116], the author uses some experimental data of both groups in order to derive the already discussed scaling law (Eqn. 4.91). The problem is that the radius they measure is obtained by averaging Schlieren images, which cannot be clearly compared with any quantity ob-

tained by models. Moreover, even if this radius is associated with the leading edge of the flame, then it would be the result of two effects: flame propagation and flame brush thickness increase. On the other hand, if a closed vessel is used and pressure measurements are employed, then S_L, δ_L and turbulence smallest scales would change in time because of the pressure increase. As these quantities are not measured, the uncertainties related to their change will increase the overall errors of the measurement. MIE scattering technique could provide statistical information of many quantities, including flame brush thickness and average radius; the problem is that, in the author's knowledge, very few experiments are actually available with this technique [11]. A future alternative can be the post-processing of DNS simulations, which are still very expensive.

4.7 Concluding remarks

In this chapter many physical aspects related to premixed turbulent combustion were discussed. In particular, scales characterizing turbulence have been reviewed together with information which can be obtained by the different turbulence models. The discussion of cascade concept shows that, while combustion is a multiscale process, this is no more true for turbulence. The existence of time and spatial scales in premixed combustion gives a way to analyze the interaction between turbulence and flame by means of the combustion regime diagram. It was shown that for, the flamelets regime, the separation between turbulence and flame scales lets the problem to be treated as a multiscale process. Moreover, the hydrodynamic model was presented. This model is seen as convenient way to represent combustion in DNS simulations, which is also coherent with the others models. Then RANS models were introduced, underlining the differences between Conditioned and Favre equations and the relations between their quantities. For this last formulation of the problem, the main models employed in literature were reviewed; these are the flame surface density model, the flame closure model and the G-Equation model. Their behaviours were compared by means of simplified geometry. In particular it was noted that the flame surface density model is less suitable to describe combustion in transient conditions, as this aspect is implicitly described in the Σ equation, whose source terms were originally proposed to describe the steady-state structure of the flame. As a consequence, the transient behaviour is simply the result of an adjustment of the flame from the initial imposed profile to its equilibrium structure. The implicit description of turbulent flame propagation speed and flame brush thickness do not clearly give the user a way to control these quantities and the set of tuning constant is probably more case-sensitive. The opportunities provided by the better description of equilibrium flame structure are probably useless for transient simulation cases. On the other hand, the FSC model and even more the G-Equation model provide a way to decouple these effects and allow to use explicit sub-model to describe the single aspects of combustion process. As a consequence, these models are thought to be better suited for RANS simulation, where modelling has a strong impact on the results of simulations. Moreover, the propagative form of the progress variable equation is more coherent with flamelets regime than the reaction diffusion equation provided by flame surface density model. For LES simulations, transient related to the models is much shorter and FSD models are probably less subject to these problems. After this choice, discussion is moved to the sub-model of the turbulent propagation

speed. Some relations valid for statistically steady planar configuration in the corrugated flamelets and thin reaction zone regimes were reviewed. Then the attention was shifted to the transient behaviour typical of spherically expanding flames. Some issues and modelling strategies proposed in literature to deal with it were reviewed. For all the discussion, the author tried to distinguish modelling results from the physics of premixed combustion, underling the limits of some approaches and providing some suggestion/comments based on the results of asymptotic analysis. The common arguments proposed by different authors in modelling phase were underlined, but the limited availability of suitable experimental data did not allow the author to assess if the proposed modifications could be able to improve the accuracy of the already known correlations. Between the many relations, Zimont's and Peters's ones are probably the most used and validated. As a consequence, were implemented in the model described in chapter 6.

CHAPTER 5

modelling ignition process

In spark-ignition engines, ignition process is a very important phase. Unlike other industrial combustors like gas turbines, a non-negligible fraction of combustion time is spent for the formation of the flame. Timing is very important as an advance or delay of heat release of few crank angle degrees can significantly change the pressure development inside the cylinder and, as a consequence, the mechanical work extracted by the piston. Moreover, early combustion creates high pressure peaks, can overheat engine walls and promotes the conditions that lead to knock. Late combustion can cause the release in atmosphere of unburnt hydrocarbons and carbon monoxides and overheat the exhaust gas system. Ignition process is affected by some random effects, such as the local mixture composition, which can change because of internal exhaust gas recirculation, spark discharge process, which is characterized by some statistical properties, and the local flow motion, which can convect the flame kernel away from the spark plug, slowing down or enhancing combustion depending on the flame size. Due to these statistical effects, pressure history can change a lot from cycle to cycle, generating the well known cyclic dispersion problem. An high variability of working conditions associated with this phenomenon can reduce the engine lifetime and also the performance of other components of the system, like after-treatment or transmission devices. Cyclic dispersion is also an important reason for which lean mixtures are not employed for operating points at low loads. As a consequence, a better understanding of ignition process and early flame kernel phase can lead to the development of strategies which can reduce cyclic dispersion and improve the whole engine performance. Moreover all the combustion models introduced in the previous chapter require an ignition sub-model, as they have no source term which represents ignition. For these reasons, this chapter is focused on early combustion stages, in particular on spark discharge process which ignites the mixture and the sub-sequent flame kernel development. Some simplified

models proposed to describe these phases for RANS/LES applications are discussed. Some details about spark discharge theory are given, as, in combustion literature, this topic is usually little considered.

5.1 Spark discharge

Spark discharge is a process which converts a fluid into a plasma. Plasma is considered one of the four fundamental states of the matter; it is a fluid in which a non-negligible number of molecules or atoms are dissociated into ions and electrons. Plasmas are characterized by being globally neutral, but conductive fluids. In literature, plasmas are classified on the base of the ionization degree: there are the so called low ionization degree plasmas, for which only 1% of the molecules are dissociated, and fully ionized plasmas. Another common classification is between non-thermal and thermal plasmas. The first type is characterized by a non-equilibrium distribution of energy between different degrees of freedom, excited states and particles; the second one by thermodynamic equilibrium. Usually, low ionization degree plasmas are also non-thermal and are called cold plasmas, while fully ionized plasmas are associated with high temperature and thermodynamic equilibrium. For non-thermal plasmas, it is assumed that the energy distribution can be described by several temperatures such as the electron temperature (T_e), electronic excitation temperature (T_{elex}), vibrational temperature (T_{vib}), rotational temperature (T_{rot}) and translational temperature (T_{trans}); typically $T_e > T_{elex} > T_{vib} > T_{rot} = T_{trans}$. In spark-ignition engines both non-thermal and thermal plasmas can be generated. For the normally employed direct current system, various discharge regimes exist and are shown in Figure 5.1. This diagram is build by means of "discharge tube" [100], an experimental set-up working in steady conditions. All these regimes are encountered in spark-ignition engine. Even if for spark plug the discharge process is unsteady and far from the ideal conditions of discharge tubes, many measured current and voltage properties are well represented by this diagram. The goal of this theoretical part is to provide some information on the parameters which influence the phenomenon and some simplified correlations between these global parameters, in order to replace the solution of a more complex problem. In particular, the quantities investigated are voltage and current.

5.1.1 Dark discharge and breakdown regimes

Plasmas can be generated in two way: by increasing the temperature of a gas up to some thousands kelvins, for example with a laser, or by applying a strong external electromagnetic field. The second strategy is the one used in SI engines. For the standard spark plug shape (cylindrical electrodes), the electric field between the spark gap can be assumed homogeneous. At low voltages, the gas between the electrodes works like a perfect insulator. As the potential difference across the gap increases beyond a threshold value, a small current begins to flow. In the dark discharge regime (called with this name because no visible radiation is emitted and is represented by line C-E of Fig. 5.1), the high electric field starts to excite the free electrons, which are always present in air because of external ionizing sources like radiations (background ionization). These electrons move towards the anode and along their path they collide with heavy particles. As the voltage increases, the energy of the population of electrons is shifted to higher

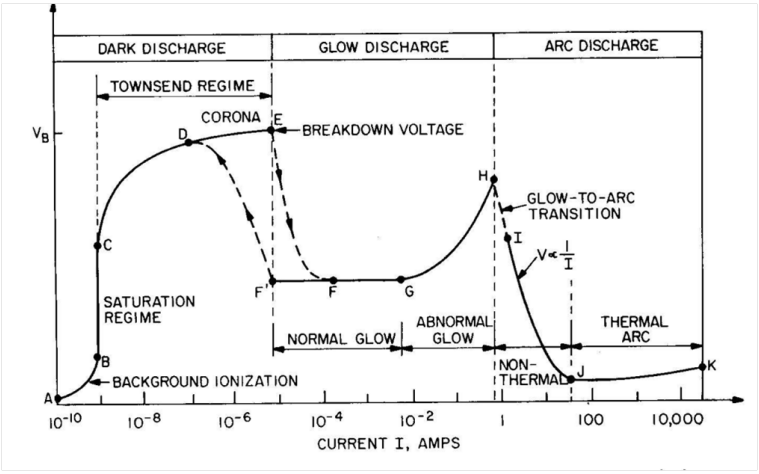

Figure 5.1: *Direct current discharge regimes.*

values and the probability that collision between electrons and heavy particles results in ionization and emission of new electrons also increases. This probability is affected mainly by three parameters: the nature of the gas which fills the electrode gap, as the activation energy for dissociation changes with the various molecules, the applied external voltage and the free mean path between collisions. Electrons are accelerated by the external electric field and acquire kinetic energy associated with a velocity oriented as the electric field (drift velocity v_d). Part of this energy, after a collision, becomes associated with a random velocity component (from the point of view of statistical mechanic, the energy associated with this last velocity is directly related to the temperature). Because the mass of electrons is very small in comparison with the one of heavy particles and collisions for low energy electrons can be considered elastic, most of the energy exchanged in the collision is kept by electrons. Long free mean paths let the electrons gain enough kinetic energy to promote ionization of heavy molecules. The effects of external field and free mean path can be summarized by the single parameter E/N, where E is the external electric field and N is the particle density (for ideal gases $N = p/(RT)$) which is related to the free mean path (as N decreases, the free mean path increases). Ions generated by ionization process move toward the cathode, while electrons move towards the anode and continue to collide and to create new charged particles, establishing a cascade mechanism. The consequence of this process is the increase of the current flowing in the external circuit applied to the spark plug. As the voltage increases, this current rises and a higher number of ions reaches the cathode. If only electrons produced by background ionization are considered, defining the saturation current density $J_{sat} = e \cdot d_{gap} \cdot S$, where $S = dn/dt$ is the number of electrons produced by background ionization per unit volume, e the electron charge and d_{gap} the gap between electrodes, the current density at increasing distance from the cathode x assumes an exponential form [100]:

$$J_e = \frac{J_{sat}}{\alpha \cdot d}(exp(\alpha \cdot x) - 1) \tag{5.1}$$

Where α is defined as the probability of ionizing collisions per unit length. It is known in literature as first Townsend ionization coefficient and it is an exponential function of

E/N:

$$\alpha = D \cdot N exp\left(-\frac{B}{E/N}\right) \tag{5.2}$$

Where B is a constant which depends on the ionization potential of the gas and D is another constant which still depends on the gas which fills the inter-electrodes volume: they can be both accurately measured. In order to preserve this process, a high external voltage across the gap is required. Its value can be estimated as the product $E \cdot d_{gap}$. When the ions produced by collisions reach the cathode surface, they are neutralized by the electrons flowing in the external circuit applied to the electrodes. Some of these ions together with the photons, also generated by collisions, can extract electrons from the cathode surface when they hit it. This electron creation mechanism is named secondary process to distinguish it from the production of electrons by collisions, which is called primary process. The total flux of electrons emitted by the cathode surface ($F_{e,c}$) is equal to the sum of the emissions due to ions ($F_{e,i}$) and photons ($F_{e,p}$):

$$F_{e,c} = F_{e,i} + F_{e,p} \tag{5.3}$$

Defining the secondary emission coefficient of the cathode γ as the ratio of flux of electron emitted by the cathode on the flux of incident ions ($F_{i,i}$):

$$\gamma = \frac{F_{e,i}}{F_{i,i}} \tag{5.4}$$

Using equation 5.1 and remembering that for charge conservation the flux of ions which hit the cathode surface must be equal to the difference of the flux of electrons on the anode ($F_{e,a} = F_{e,c} exp(\alpha d_{gap})$) and the flux of electrons emitted by the cathode, $F_{e,c}$ is equal to:

$$F_{e,c} = F_{e,p} \frac{exp(\alpha x)}{1 - \gamma(exp(\alpha x) - 1)} \tag{5.5}$$

$$\alpha \cdot d = ln(1/\gamma + 1) \tag{5.6}$$

Formally, when the denominator tends to zero, i.e. equation 5.6 is satisfied, the current rises to infinite and breakdown occurs (point E in Figure 5.1). Relation 5.6 is known as Townsend criterion and this breakdown process is said to be driven by the Townsend mechanism. For ideal gas and constant temperature environment (N can be replaced with p), this last relation can be rewritten in term of breakdown voltage, using relation 5.2 and $E = V/d$, as:

$$V_b = \frac{C \cdot p \cdot d}{ln\left(A \cdot p \cdot d / ln(1/\gamma + 1)\right)} \tag{5.7}$$

Where A and C correspond respectively to B and D and account the change from N to p. This relation is known in literature as Paschen's law [88]. From a physical point of view, this process requires that the voltage across the spark gap is increased to V_b (thousand of volts) and maintained constant for some time. A series of sub-sequent cascade processes previously described have to be fulfilled until the current has risen enough to make the process self-sustaining. At this point the high voltage across the electrodes is no more necessary and its magnitude decreases to lower values (hundreds of volts). Experiments showed that the Townsend theory was sometimes inconsistent

with observations. In particular it was found than for high values of the product $N \cdot d$, another mechanism, named streamer, controls the process. This concept was originally proposed in [67] and verified in more recent works. Streamer mechanism characterizes the cases for which the ratio of the free mean path on the inter-electrodes gap is much less than one. Briefly, one electron collides with many different molecules as it travels from the cathode to the anode and the avalanche ionization process can generate a great number of electrons, giving rise to a localized space charge which propagates in the discharge gap creating a thin conductive channel named streamer [101]. An extended explanation is given in the following. Assuming to have one background electron in the volume between the electrodes which starts to move and to collide with heavy particles; after some collisions and because of electrons diffusion, the electron density distribution can be expressed as:

$$n_e(x,r) = (4\pi D_e t)^{-3/2} exp\left(\frac{(x - v_d t)^2 + r^2}{4 D_e t} + \alpha v_d t\right) \tag{5.8}$$

$$r_a = \sqrt{4\pi D_e t} = \sqrt{\frac{4\pi D_e x_0}{\mu_e E}} \tag{5.9}$$

where t is the traveling time of the electrons from the cathode to the anode along the axis direction. $x_0 = v_d \cdot t$ is the position along this axis and the drift velocity v_d is equal to $\mu_e E$, where μ_e is the electron mobility. r_a is the avalanche diffusion radius in the transversal plane. Considering equation 5.8, the positive ions density is:

$$n_i = \int_0^t \alpha \cdot v_d \cdot n_e \; dt = \frac{\alpha}{\pi r_a^2} exp\left(\alpha x - \frac{r^2}{r_a^2}\right) \tag{5.10}$$

When the charge amplification factor $exp(\alpha x)$ is high, the production of a space charge with its own significant electric field takes place. Since the electrons are much faster than ions, they always run at the head of avalanche, leaving the ions behind (see the first three picture of Figure 5.2) and thus creating a dipole with the characteristic length $1/\alpha$ (mean distance for an electron before creating an ion). The local fields in front of the avalanche head add up and produce a field which is stronger than E. While in the zone between the centers of the space charges of opposite signs, the resultant field is weaker than E. When the avalanche reaches the anode, the electrons sink into the metal and only the positive space charge of the ionic trail remains in the gap. The total electric field is then due to the external one, the ionic trail and also the ionic charge image in the anode as depicted in picture four of Figure 5.2. The resulting electric field in the ionic trail near the anode is less than E. A strong primary avalanche amplifies the external electric field leading to formation of thin weakly ionized plasma channel (see pictures five and six in Figure 5.2), the so called streamer, which is in a non-thermal state with the gas temperature which is only a bit higher than the initial one. This description is valid for small spark gaps for which the streamer is created only after the avalanche has reached the anode and is called cathode-directed or positive streamer mechanism.

The avalanche-to-streamer transformation occurs when the local field of an avalanche becomes comparable with the external one, i.e. when the amplification αd_{gap} is big enough. For example, if it is assumed that all the electrode belong to a spherical volume of radius r_a, for the Gauss theorem, at the tip of the avalanche the electric field

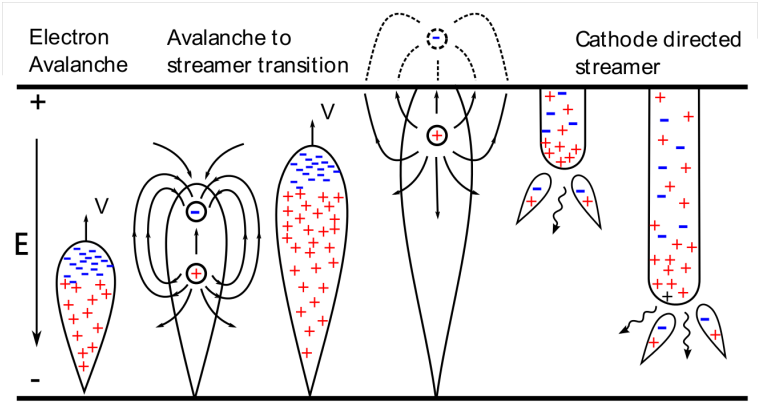

Figure 5.2: *Mechanism of formation of streamers: first electrons avalanche generates a dipole which enhances the local electric field ahead of the avalanche, speeding up collisions process and leaving behind a positive trail. When the electrons sink into the anode surface, a strong primary avalanche back to the cathode is generated.*

is:

$$E_a = \frac{e \cdot exp(\alpha x)}{4\pi\epsilon_0 r_a^2} \tag{5.11}$$

Where ϵ_0 is the vacuum permittivity. The substitution of r_a in 5.11, the relation $E_a = E$ and the substitution of x with the spark gap d, lead to:

$$\alpha \cdot d = F + ln(d/d_{ref}) \tag{5.12}$$

where F is a constant which depends on the gas and the selected reference spark gap d_{ref}; its value can be obtained by fitting experimental data: for example a suggested value is 17.7 with $d_{ref} = 1\,cm$. Equation 5.12 is known as the Raether's avalanche-streamer criterion [101]. It can be used to estimate the external voltage for which there is transition from Townsend to streamer mechanism and the breakdown voltage for this second condition. As for the Paschen's law, the main properties witch characterize the breakdown voltage are summarized in the single parameter $d_{gap} \cdot p/T$. Empirical expressions can be directly extrapolated from experimental data; for example in [89] it is underlined that for high pressure, Paschen's law like equation could not fit the experimental data and the following alternative relation is proposed:

$$V_b = 4.3 + 136\frac{p}{T} + 324\frac{p}{T} \cdot d \tag{5.13}$$

The main differenced between what was previously described and the actual conditions in spark-ignition engines is that, up to now, only quasi-steady state conditions have been considered. Such conditions are fulfilled only if the external circuit increases the voltage across the spark gap with a small rate, such that the voltage is kept practically constant for the duration of the physical processes involved in breakdown. Then a DC discharge is generated and the measured voltage is a deterministic quantity. If this is not true, then the process assumes the characteristics of a pulse discharge and the breakdown voltage becomes a stochastic quantity as, between the reach of the DC breakdown voltage and the end of the process, the electric field can significantly increase. In particular, looking at Figure 5.3 different delay times can be identified: t_s is

the statistical time (a period starting when the DC voltage breakdown is reached and lasting until the incidence of an initial electron, i.e., a free electron at an energetically favorable place to start the avalanche process), t_l is the avalanche time (starting with the appearance of the first avalanche and ending with the onset of full self-sustained discharge), and t_f is the formation time (needed for the formation of the thermal spark channel). The statistical nature of pulse breakdown is essentially due to t_s. For a detailed discussion about pulse breakdown voltage measurements and related statistical distributions, see references [86] and [85]. This aspect is simply mentioned to justify the fact that spark discharge in SI engines should be treated as a statistical process and that suitable measurement techniques should be employed to deal with it. Anyway, as the induced over-voltage tends to speed up the breakdown process, the actual voltage value usually remains close to the one of DC breakdown, which can be used as a good approximation of the real value.

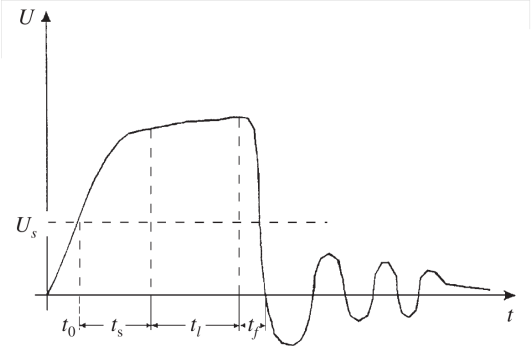

Figure 5.3: *Time dependence of pulse breakdown voltage in gases. U_s is the DC breakdown voltage*

5.1.2 Arc and glow discharge regimes

In this section the regimes characterizing the spark discharge after breakdown are discussed. The high pressure environment and over-voltage induced by the standard ignition devices, due to the external electrical circuit connected to the spark plug, generate a breakdown driven by the streamer mechanism. At the end of this phase, a thin conductive non-thermal plasma channel is created between the electrodes which sudden decreases the resistance seen by the external circuit. Then the energy accumulated on the electrodes surfaces of the spark plug, which behaves like a capacitor with a small capacitance, is rapidly discharged. In [70] it is stated that, after breakdown, this energy is high enough to produce a very high current flux which heats the spark channel and induces the development of an arc phase which lasts only few nanoseconds and is followed by the glow phase. A normal glow discharge (Fig. 5.1 line F-G) is a non-thermal plasma, as the temperature of electrons is much higher than the one of heavy particles which can remain close to the ambient value. The conductive column is quite thick and collisions are few, which is the reason why equilibrium condition is not reached. The current which can flow through the spark is small, usually less then 100 mA. The current flux is almost constant and the variation of the total current is supported by the modification of the cross-section of the conductive column. Arc discharge (Fig. 5.1 line I-K), on the contrary, is close to be an equilibrium plasma. The conductive channel

is thin and the current fluxes are much higher with respect to the glow discharge mode. As a consequence, collisions are much more frequent, the energy density is higher and the local gas temperature usually reaches some thousand degrees, promoting thermal ionization. The current supplied by arc discharge is higher than the one of glow phase and it has no upper limit value. Moreover the voltage across the spark gap is higher for the glow discharge. Typical examples of arc mode are lightnings and arcs produced by welders, while common examples of glow discharge are Neon lamps or plasma globes. The voltage across the spark gap is the sum of three contributions: the cathode sheath voltage fall, the positive column voltage and anode sheath voltage fall. Cathode and anode sheaths are the two regions very close to their respective electrodes where charge distribution is not uniform and, as a consequence, where the electric field changes in space. In the positive column the plasma is globally neutral and the voltage difference across it is proportional to the length of the column. At high pressure (ambient or higher), cathode and anode sheaths are very thin regions, so that the length of the positive column is practically equal to the spark gap distance. In the glow mode, the voltage fall at cathode region is close to the Paschen's law minimum and the channel naturally adapts itself to the current changes, lengthening or shortening this layer to keep the same voltage fall. This is why, with a fixed geometry, voltage-current profile is practically constant for a wide range of current intensities (Fig. 5.1 line F-G). Anode voltage fall is usually negligible with respect to cathode one. For low current the voltage starts to increase as the current decreases. An explanation of this effect can be found in [111], where an increase of rotational temperature of nitrogen with increasing current intensity is measured (see Fig. 5.4). Due to the very small relaxation time between rotational and translational degrees of freedom, these two temperatures are the same. As the Eulerian pressure is associated with the energy of translational degree of freedom, for the previous consideration, the rotational temperature can be used in the ideal gas law to estimate the particle density N. As a consequence, an increase of this temperature increases the ratio E/N and lower voltages are required to maintain the same discharge properties. From Fig. 5.4 it can be noted that the temperature reaches an asymptotic value as the current increases; so also the discharge voltage reaches a constant value for high electrical current.

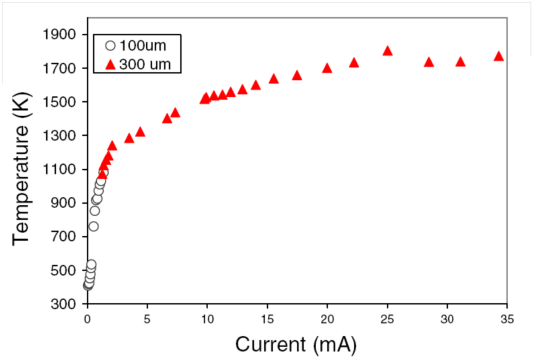

Figure 5.4: *Variation of rotational temperature with discharge current for normal glow discharge in air at atmospheric conditions at 100 and 300 μm electrode spacing. The image is taken from [111]*

These considerations explain the glow mode voltage relations proposed in [89] and

[52] which assume the form:

$$V_{glow} = constant + B \cdot i^{-a} \cdot p^{m} \cdot d_{gap} \tag{5.14}$$

where the constant value is essentially related to the cathode voltage fall which remains close to the Paschen's minimum. The linear dependence with d_{gap} is associated with the positive column. B, a, m > 0 are extrapolated empirical constants. a should be close to zero, as the relation between voltage and current holds only for small values of this last quantity. The absence of temperature dependence pointed out in [89] could be explained by Figure 5.4. As the gas temperature reaches the quite high value of 1300 K for very low currents, the contribution of the initial temperature could be canceled out by the current, at least in the range considered in [89] (300-600 K). As shown in figure 5.1, glow discharge has an upper limit current threshold which, when exceeded, triggers new physical mechanisms that lead to the transition to arc discharge (see line G-J in Figure 5.1). Between the many possibilities, the most accredited mechanism which causes this transition is cathode thermionic emission. As previously mentioned, photons and ions collisions on the cathode surface are able to knock out electrons. The efficiency of this process is indicated by means of the Townsend secondary emission coefficient γ, whose value for metal material is $\gamma \sim 10^{-2}$, which means that the process is very inefficient. This collision mechanism is required as, at room temperature, the conduction electrons of a metal have not sufficient thermal energy to leave the surface. If the metals are heated above the temperature of about 1500 K, the electrons will receive energy from the violent thermal lattice in vibration sufficient to cross the surface barrier and leave the metal. This process is known as thermionic emission. Richardson-Dushman equation [77] provides an expression for the saturation current density J_s which describes the current flow between the cathode and the anode due to thermionic emission:

$$J_s = \frac{4\pi m_e k^2}{h^3} T^2 exp\left(-\frac{W}{kT}\right) \tag{5.15}$$

Where T is the surface temperature, m_e the electron mass, k and h Boltzmann and Planck constants and W is the work function, which is the energy required to knock out an electron from a Fermi level and is a characteristic of a given material, but can be decreased by the electric field with a mechanism known as Schottky effect [53]. In general the increase of current over a threshold value induces the formation of local hot spots on the cathode surface which become thermionic emissions sources. Then the conductive column collapses into a thin structure where temperature increases and equilibrium conditions are reached. The transition current depends on material of the electrodes and their shape and does not depend on the external circuit characteristics, which, anyway, can trigger or not the mechanism. This current is a very difficult quantity to be estimated, but it can be measured. Thermionic emission reduces a lot the number of ions and photons required to knock out electrons from cathode surface and, for this reason, the cathode sheath voltage fall decreases a lot because it is no more sustained by local density charge. Because arc discharge is almost close to thermal equilibrium, the relation between arc column voltage and current became nearly ohmic ($J = \sigma E$). To summarize these last concepts, Figures 5.5 and 5.6 show voltage and current profile of a CDI ignition system (more details are provided in the next section) discharging in air at atmospheric pressure for various capacitor charging voltages. It

can be noticed that at about 275 mA there is a transition between glow and arc discharge. This passage is underlined by the sudden decrease of voltage. For the case with 125 Volt charge, the current rises well above the threshold value and the transition occurs only two times. For the case with 105 Volt charge, an incomplete transition continuously occurs as the current value does not clearly become more than the threshold value. Finally for the lower energy case, discharge works only in glow mode and the voltage remains practically constant until a low current of about 10 mA is reached at 1.75 ms; then there is a low voltage increase until discharge is completed and oscillations related to the external circuit are seen.

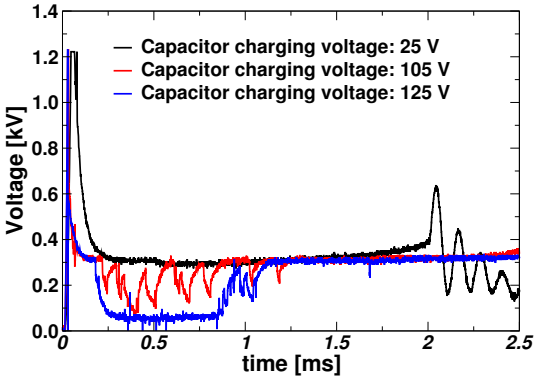

Figure 5.5: *CDI ignition system: spark gap voltage evolution for three capacitor charging voltages. Data were kindly provided by Dr. Kian Eisazadeh Far.*

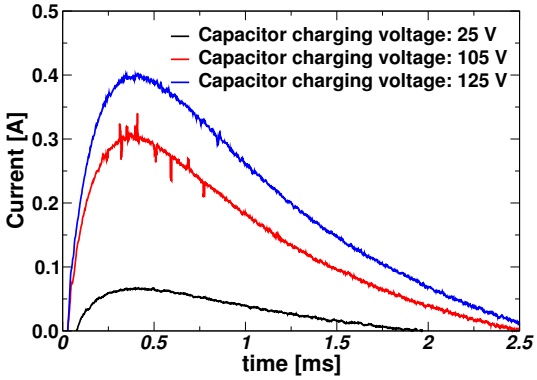

Figure 5.6: *CDI ignition system: discharge current evolution for three capacitor charging voltages. Data were kindly provided by Dr. Kian Eisazadeh Far.*

5.1.3 Ignition devices

In the previous section it was pointed out that the development of spark and the transition between different regimes is strictly connected with the external circuit, as it determines the current flowing in the plasma. In this section, a short description of the most employed ignition systems is provided. In the years many ignition devices have been designed in order to improve the classic one known as transistor controlled ignition (TCI), from capacitor discharge ignition (CDI) system [103], to laser-inducer spark ignition [76] or rail-plug ignition system [36]. Anyway, currently only TCI and CDI systems are produced on industrial scale and 90% of the car fleet employs TCI system. As a consequence only these two devices are discussed. The main difference between them is the electrical circuit, while the same spark plug can be used for both systems. Figures 5.7 and 5.8 show a typical circuit scheme for the two systems.

These systems have to provide a large voltage difference across the spark gap in order to trigger breakdown at hight pressure and they must do it quickly because of the high SI engines speed. The common electrical device which characterizes the two systems is a transformer which couples the primary circuit, connected to the battery, to the high voltage secondary circuit, connected to the spark plug. For the TCI system the voltage on the primary circuit side of the transformer remains close to the one of the battery and the coil ratio of the transformer is some hundreds. At rest, the primary circuit is closed and the battery charges the coil whose fully charged energy is $1/2 \cdot L \cdot i^2$,

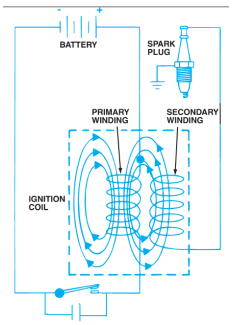

Figure 5.7: *Essential features of a transistor controlled ignition (TCI) circuit scheme*

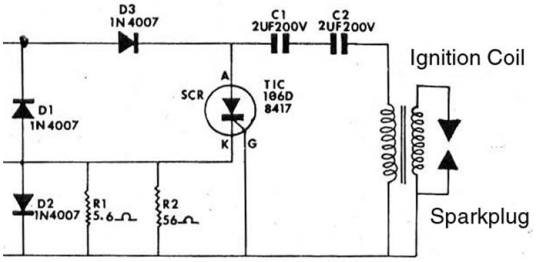

Figure 5.8: *Essential features of a capacitor discharge ignition (CDI) circuit scheme*

where L is the inductance of the coil. When discharge is required, a switch opens the primary circuit and the voltage across the coil increases due to the steep change of current which has to go to zero. The transformer multiplies this voltage which reaches the breakdown value. After the onset of the spark, the secondary circuit works like a RL circuit and releases a fraction of the coil energy into the gas inside the cylinder. Because of the high resistance of the secondary circuit wire, a small amount of the stored energy reaches the spark; 50-90% of it is lost in the process. The addition of other components on the secondary circuit (like a capacitor in parallel with the spark plug) can increase the efficiency of the circuit. In the years, most of the improving efforts were oriented to deal with this issue and the responsiveness of the system. An example of current profiles during charging and discharging phases compared with the numerical results of the basic electric circuit configuration discussed before, is shown in Figures 5.9 and 5.10, where circuit properties where tuned in order to obtain the experimental signal.

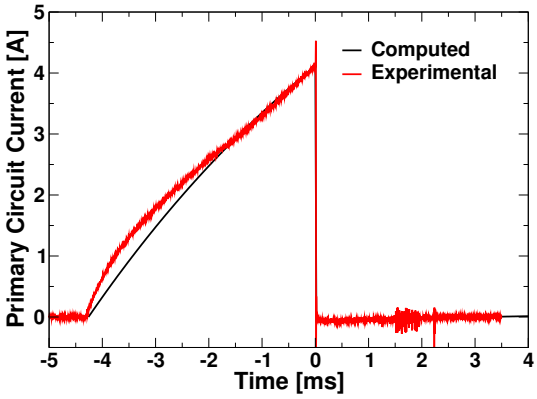

Figure 5.9: *Current profile of the primary circuit of a TCI ignition system*

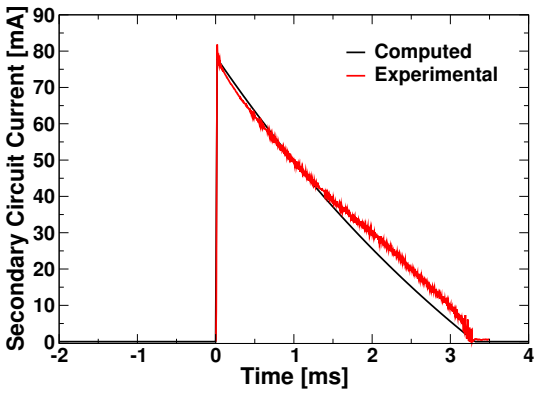

Figure 5.10: *Current profile of the secondary circuit of a TCI ignition system*

The TCI system provides low current to the spark plug; as a consequence the related discharge is the glow mode. Spark lifetime depends mostly on the inductance and resistance of the transformer and is of the order of few milliseconds, while typical voltage ramp rate is 10 kV/ms. The CDI system stores the energy on a series of capacitors on the primary circuit. As a consequence, the energy stored is $1/2 \cdot C \cdot V^2$; an additional control circuit on the primary side is used to impose the final voltage which is usually between 100-400 Volt. As a consequence the coil ratio of the transformer can be ten

time lower that the one of the TCI system and also the corresponding wire resistance decreases by a factor of 10. When ignition is triggered, the primary circuit is opened and the same effect described for the TCI system is obtained. The response of the resulting basic circuit looks like the ones of a RLC circuit which is a damped sinusoidal signal. Eventually only the first half-wave is kept and auxiliary circuits are used to stop the current flux in the opposite direction. The typical current output is of the order of the Ampere, thus the common discharge type associated with CDI system is the arc mode. The typical voltage ramp rate is about 100 kV/ms and the discharge time is of the order of hundreds microseconds.

5.2 Models for spark discharge

In SI engines, the plasma column connects two systems: the electrical circuit and the gas which fills the volume between the electrodes. The electrical circuit sees the spark plug as a load and requires its constitutive equation (relation between voltage and current) which depends on the geometry of the electrodes and other parameters which can be extracted by the fluid system. The relations presented in the previous section are enough to describe the time evolution of current and voltage. The only problem is to know the electrical circuit components and their properties, which can be provided by their manufacturer. Once these information are available, the numerical solution of the obtained system of equations, which are linear and only time dependent, is easy and no time consuming. On the contrary, the complete description of the processes involved in the fluid part of the system is complex and can be even more computationally expensive than a combustion problem. In general thermal and non-thermal plasmas require different approaches. Thermal plasmas are easier to be described as standard Navier-Stokes with some supplementary equations can be employed [39]. These additional relations are the four Maxwell equations which form a linear system (or weakly non linear if variable properties are considered). Their solution does not add any new issues with respect to the ones encountered in non reacting flows equations. Moreover some reasonable physical approximations can greatly simplify Maxwell equations and reduce their additional computational cost. This approach is possible because thermal plasmas can be considered as a reacting mixture which instantaneously reaches its equilibrium composition. As a consequence, it can be treated as a mixture like air with particular properties (see Figure 5.11) related to the change of composition which can be directly obtained by correlations, as the ones proposed in [26].

Non-thermal plasmas, instead, require a completely different approach as they are characterized by a non-equilibrium distribution of energy between the different degrees of freedom of the molecules. modelling techniques available in literature reformulate the problem in a more familiar fluid-dynamic context [112]. These models treat the plasma as a reactive mixture introducing new chemical species and reactions (like ions and excited nitrogen) and at least two temperatures, one for heavy particles and another one for electrons. Each of these temperatures is computed with its own energy equation. Simplified electron Boltzmann equation [42] can be solved to estimate the transport properties and reaction rate coefficients, which require, as inputs, the electrons temperature and the ratio E/N. When ignition is studied with this approach, a suitable chemical mechanism witch includes ions, electrons and excited species must be provided. As this topic is quite recent, there are more uncertainties related to these

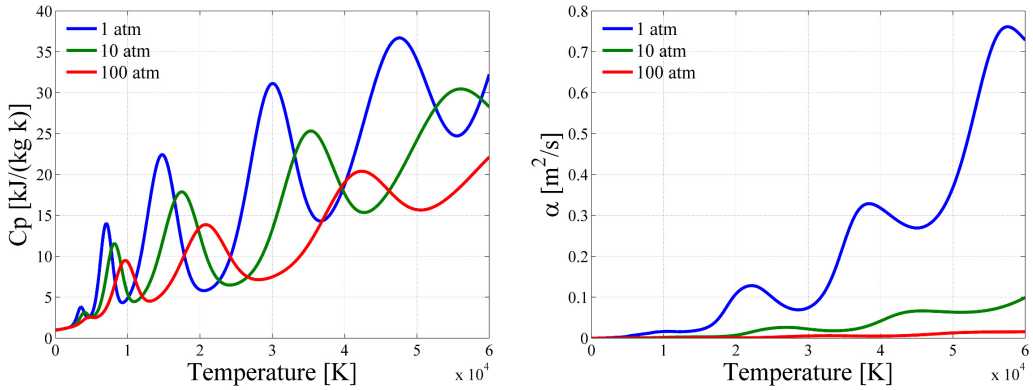

Figure 5.11: *Properties of a thermal air plasma: on the left specific heat at constant pressure, on the right thermal conductivity. Fitting relations are available in [26]*

chemical mechanisms than the ones employed to describe the same fuel in other situations (like auto-ignition in Diesel engines). Anyway examples of DNS simulations can already be found in literature [112]. The need of low computational time approaches, which are more suitable to the combustion models proposed in this work, requires some simplifications. As a consequence, only thermal plasmas are considered in the following. A discussion about this issue is postponed to the following sub-section.

5.2.1 Simplified models to describe spark discharge process

In this work, spark discharge is regarded as a sub-model to initialize combustion and to compute the early flame radius. As such, only very low computational time approaches have been testes/employed; specifically 0D and 1D models are considered. For their nature, these approaches need to include many simplifications, but, as only global parameters are required, the inaccurate description of some details is not a priori important if they do not influence the global result. Moreover detailed models require more information about initial and boundary conditions which are usually not available. Maly's works on spark ignition process have been considered a reference for engines community for a long time. A summary of his findings is presented in [70]. From the author's experience, it is quite hard to find other works on the same topic in engine literature. Anyway, in other research contexts, many works on spark discharge process were done and a deeper understanding of the governing mechanisms was achieved. Many of the previous considerations were taken by these alternative sources. In light of this, what is written in [70] is reviewed. Maly stated that, in the context of SI engines, discharge produced by ignition devices always follows these three phases in order: breakdown, arc phase and glow mode. As already explained, ignition devices generate a pulsed discharge; breakdown phase is accomplished by streamer mechanism, as the discharge occurs in high pressure environment and under high over-voltage conditions. Maly estimated temperature after breakdown around 60000 K and, as a corroboration of this, he stated that he had measured traces of N^{4+}. As can be seen in figure 5.12, where the recent data proposed in [26] are shown, effectively N^{4+} only appears at temperature higher than 45000 K. A more detailed definition of the statement "after breakdown" must be provided, as the conductive column generated by streamer is a non-thermal

plasma at room temperature. For what the author understood, this expression refers to the state of the gas after some nanoseconds, when the energy stored in the spark plug is discharged, and practically also includes what was defined as "arc phase". Then, the rise of temperature depends more on the spark plug properties than the external circuit characteristics.

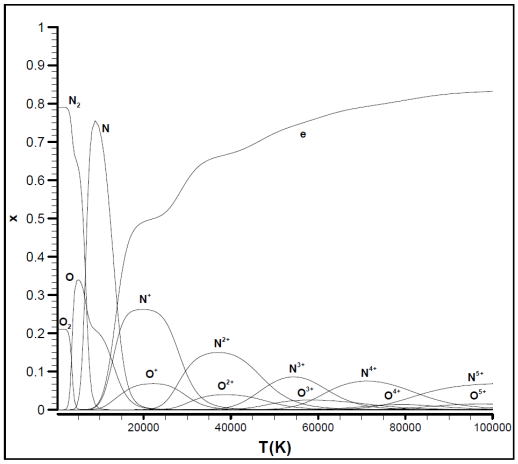

Figure 5.12: *Molar fraction of N_2 and O_2 species in air at atmospheric pressure, for increasing temperature*

In order to further verify this result and to provide more information at the end of breakdown phase, a 1D blast wave solver was implemented. An extended version of 1D equations in Lagrangian mass coordinate system presented in [95] and [109] is solved, both in spherical ($dm = \rho r dr$) and cylindrical coordinate ($dm = \rho h dr$) systems:

$$\frac{\partial r}{\partial t} = u \tag{5.16}$$

$$\frac{1}{\rho} = \frac{\partial r^2}{\partial m} \tag{5.17}$$

$$\frac{\partial u}{\partial t} = -r\frac{\partial (p+Y)}{\partial m} \tag{5.18}$$

$$\frac{\partial \epsilon}{\partial t} + (p+Y)\frac{\partial (1/\rho)}{\partial m} = \frac{1}{\rho}\frac{\partial}{\partial m}\left(\frac{r^2\lambda}{c_v}\frac{\partial \epsilon}{\partial m}\right) + Q \tag{5.19}$$

where 5.17, 5.18 and 5.19 are respectively the mass, momentum and energy (ϵ) conservation equations. Y is an artificial viscosity introduced to control numerical oscillation near the shock wave front and Q is the sum of energy source and sink terms. As the expected result is characterized by high temperatures, thermal equilibrium is assumed and the properties taken from [26] are used in the computation. As source term, the specific power provided by the spark plug is introduced, while as sink term, radiative losses are considered by means of the correlation of the net efficiency coefficient presented in [81]. The previous equations in addition with the equation of state $\epsilon = \epsilon(p, \rho)$ are solved explicitly in the following order: first, momentum equation is used to update the velocity, then mass conservation is solved to compute density and finally the energy and equation of state are iteratively solved in order to update both ϵ and p. The function

$\epsilon = \epsilon(p, \rho)$ and the other properties ($\lambda = \lambda(p, \rho)$, $T = T(p, \rho)$, etc...) are expressed in form of 2D table instead of employing directly the relations proposed in [26], which are quite time consuming. Using the information provided by Maly in [70], the energy discharged by the spark plug can be estimated as $E_{bd} = 1/2 \cdot C \cdot V_{bd}^2$, where $C = 10\,pF$ is a typical value of the capacity of the spark plug and $V_{bd} = 6kV$ is given as an estimation of breakdown voltage at ambient condition using Eqn. 5.13. The electrical circuit in this first stage (spark plugs and conductive channel) can be modelled as an RC circuit whose characteristic time can be estimate as $R \cdot C \sim 1\,ns$, where the suggested value of the channel resistance R after breakdown is 50 ohm. The power discharged in the system is simply estimated as $E_{bd}/(R \cdot C)$. The spark channel is modelled as a cylinder with the typical length of 1 mm (electrodes distance). The channel radius in which the breakdown energy is discharged is set to 0.04 mm as suggested in [70]. This quantity should be equal to the diameter of the streamer which reaches the anode and it could be estimated by means of Eqn. 5.9 using the spark gap length and appropriate average transport properties. The evolution of axis temperature and pressure are shown in Figure 5.13 for different breakdown energy. The power released is great enough to induce an increase of pressure which generates a strong shock wave. This one rapidly propagates away and the axis pressure decreases close to its initial value after about 2 μs. The temperature at axis position does not reach the temperature estimated by Maly for the typical energy discharge range of spark-ignition engine (0.3-1.0 mJ as stated in [70]), but the order of magnitude is the same. Anyway in [70] it is not mentioned the amount of energy deposited after breakdown to reach the estimated 60000 K. For example, referring to the same case, in [108] it is written that the energy necessary to reach 60000 K is about 30 mJ, which is much higher than the one employed in these computations. It is not clear however if this energy is the one effectively discharged in the fluid in the first few nanoseconds after breakdown or the total energy discharged for the whole duration of the discharge, which can last some milliseconds.

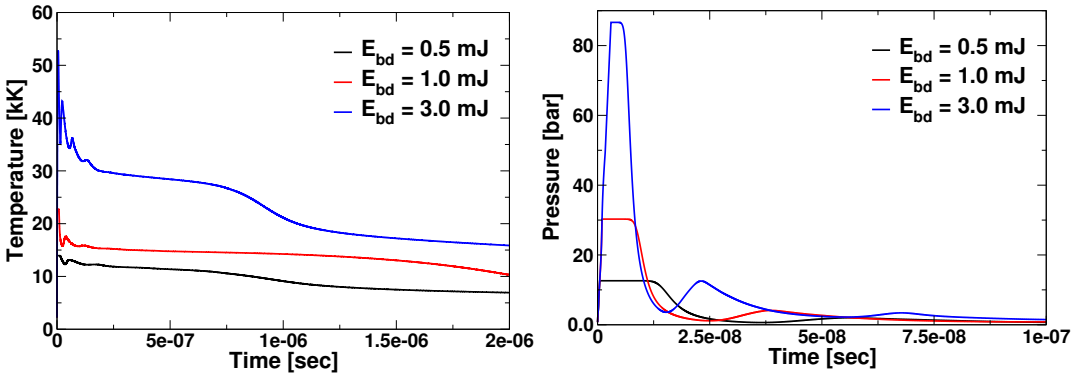

Figure 5.13: *Axis temperature and pressure evolution in the very fist stages after breakdown. The three cases are computed with different discharge energies.*

As pointed out by Maly, radiation losses do not seem to be important as the computations of temperature with and without the net efficiency coefficient are found to be practically the same. Figure 5.14 shows the temperature evolution at the very first stages after breakdown for breakdown energy of 0.5 mJ. It is noted that there is a sudden increase of temperature (like the step at 0.35 mm for the line at 0.25 μs) far from the axis, due to shock wave compression, and a smother increase closer to the axis, due

to thermal conduction. The maximum temperature quickly decreases, but it still keeps a high value at the end of the computation. As the shock wave goes far from the spark channel, the velocity field practically goes to zero and the subsequent evolution of temperature profile could be computed only with a heat conduction equation as proposed in [71]. The final temperature profile after 2 μs of this case could justify the subsequent development of an arc phase as the electrode should be heated to high temperature and thermionic emission could be generated. Anyway experimental evidence shows that, after this phase, the behaviour of the plasma is driven by the current value provided by the external circuit properties. As a consequence usually for a TCI system glow phase starts.

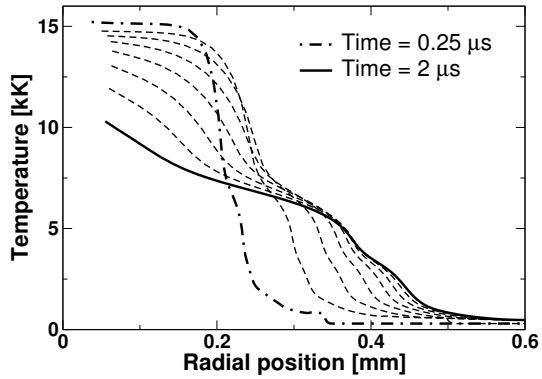

Figure 5.14: *Temperature profile evolutions after breakdown. Model results are plotted for every* $0.25\mu s$.

Because glow phase is associated with non-thermal plasma, some questions about how to model this stage without employing the very costly non-equilibrium treatment can arise. Maly could have provided a way to partially account these effects, as he proposed some efficiency functions which can be found in [70] and [71]. In particular, the product of the efficiency functions by the input power should give the effective power which heats the flow. For the glow phase, the proposed efficiency is lower than for the arc phase. If these efficiencies are obtained as a results of heavy particle temperature measurements and input power, than they could partially include non-thermal effects within. Moreover, as the translational temperature rises, relaxation times decrease and the distribution of energy between different degrees of freedom reaches equilibrium faster; so, in combustion problems, the influence of non-thermal effects should be lower than in discharge in pure air. The author has anyway some doubts about the generalization of the results obtained, as in some works like [128], these are confirmed, while in other papers like [82] the resulting discharge is clearly a non-thermal plasma. This is because the influence of the external circuit is very important as it determines the current rise after the conductive channel has been established. For this reason it is hard to compare the results obtained by different authors which usually employ similar, but different ignition devices. As a comment about this part, it is noted that Maly in [70] promoted the use of high discharge powers to form a high temperature thermal plasma. Nowadays, instead, many researchers are trying to exploit non-equilibrium plasmas in order to improve combustion efficiency and control, as they identified that high energy electrons can promote radicals production and ignite a mixture also at low temperatures. Steamers could be used to ignite big volumes as shown in 5.15 without the need of high

discharge power and the related issues concerning spark plug surface consumption.

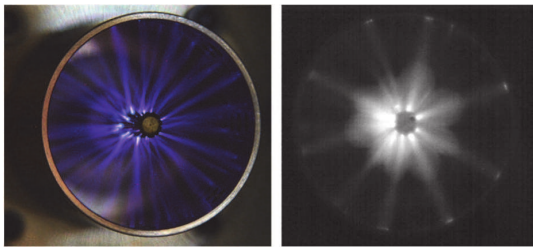

Figure 5.15: *Example of application of non-thermal plasma for combustion. On the left streamer discharge in air. On the right application of the igniter to the combustion of lean $C_2H_4 - air$ mixture.*

A simple 0D thermodynamic model was proposed in [108] to compute the diameter and temperature immediately after breakdown, when the shock wave has moved away from the spark channel. In this approach, the energy is supposed to be supplied instantaneously to a constant volume vessel which then expands with an adiabatic transformation from the obtained shock wave pressure to its initial value. More details are given in section 6.3.2, here it just noted that its results are in line with the ones showed for the 1D model and, as a consequence, can be used as an alternative way to describe the phase immediately after breakdown.

To model the following part of the discharge, a 1D heat conduction equation can be solved as suggested in [71] and confirmed by the computations with the blast wave solver. In [33] an interesting study on this phase is proposed. Data of the radius of high temperature sphere resulting from discharge in air for different energy input are shown (Figures 5.16 and 5.17) and a simple 0D thermodynamic approach, which provides remarkable results such as the ones shown in Fig. 5.18, is proposed. Therefore this model was implemented and tested.

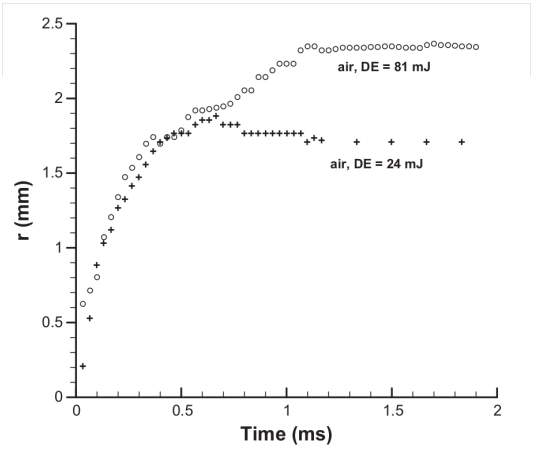

Figure 5.16: *Measured high temperature kernel radii for different discharge energies.*

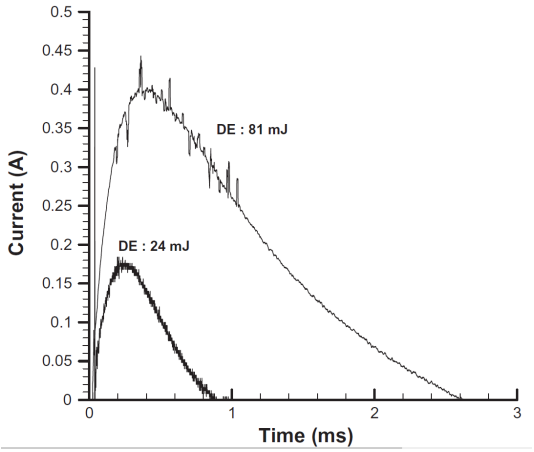

Figure 5.17: *Discharged current profile with different charge levels of the CDI system capacitor.*

The model assumes that, after breakdown, the system can be considered at constant pressure. Moreover, analysis of shadowgraph pictures leads the author of the article to

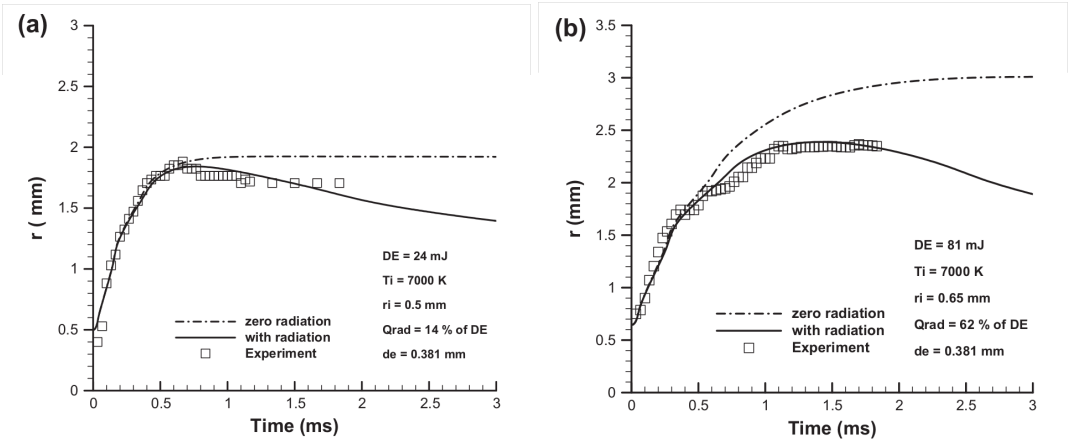

Figure 5.18: *Comparison of experimental and computed spark radii after breakdown. Figure (a) shows the case at lower discharge energy 24 mJ. Figure (b) shows the case at the higher discharge energy of 81 mJ. Images were taken from [33].*

conclude that, being the thermal boundary layer very thin, the system can be assumed as developing at constant mass. Thermal equilibrium hypothesis is justified by the high temperatures involved. As a consequence, energy and gas state equations are enough to describe the problem: the equations proposed in [33] are reformulated as:

$$m_0 c_p \frac{\partial T}{\partial t} = \dot{Q}_{spk} - \dot{Q}_{rad} - \dot{Q}_{fall} - \dot{Q}_w \tag{5.20}$$

$$V = \frac{m_0 \cdot R \cdot T}{n \cdot p} \tag{5.21}$$

$$r = \left(\frac{3V}{4\pi}\right)^{1/3} \tag{5.22}$$

where the volume V and the temperature T are the variable of the problems. m_0 is the initial hot mass after the shock wave has moved away from the spark channel. It is computed using the initials conditions which are partially considered as tuning variable. $\dot{Q}_{spk} = V \cdot I$, $\dot{Q}_{fall} = V_{fall} \cdot I$ are respectively the total spark energy deposited and the energy associated with the cathode and anode falls, which is supposed to be completely loss because of heat conduction at electrodes. I and V are measured, while V_{fall} is estimated to be 165 Volt. $\dot{Q}_{rad}$ is computed with net efficient coefficient data presented in [81] (NEC data are available up to 30000 K; as a first approximation, for higher temperatures, this value is kept constant in agreement with the trend of the data). The wall losses $\dot{Q}_w$ are neglected for the purpose of these simulations. In [33] it is also stated that they play a minor role and can be considered incorporated in the cathode and anode voltage fall losses. Finally, the number of particles n which appear in Eqn. 5.21 is a function of T and it is obtained using the data of [26], while p is constant and it is an input parameter. As can be clearly seen by equation 5.21, the volume increase is driven by the rise of temperature which is partially counteracted by the corresponding increase of the number of particles due to dissociation. As shown in [33], temperature has to reach very high values in order to obtain the experimental radius. Computation of case with 24 mJ input energy leads to the result displayed in picture 5.19. The same

initial temperature and radius proposed in [33] are used: the temperature is set to 7000 K and the initial radius is 0.5 mm as indicated also in Figure 5.18.

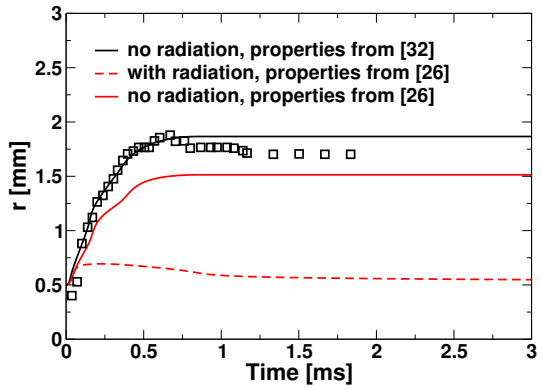

Figure 5.19: *High temperature sphere radius predicted by 0D model with and without radiation losses. Total discharge energy 24 mJ. Black line is the result computed with properties taken form [32]. Red lines are the results computed with properties taken form [26].*

The influence of radiation losses seems to be very important in this model and also the plasma properties. In particular, properties taken from [26] at high temperature are quantitatively different from the ones shown in [33]. A comparison of these properties can be seen in [32] (Figure 13). In particular in Figure 5.19, it is noticed that even with zero heat losses, the temperature computed using the data in [26] does not reach high enough values to give the experimental radius, while using the properties presented in [32], the computed radius reaches the experimental value only if radiation losses are negligible. The author of [33] states that most of the losses comes from radiation for the high energy case and from cathode and anode voltage fall for the low energy case. Because it was not clear how radiation losses were computed in [33] and the equations to be solved are simple enough to be revertible, to further verify the reported results and better understand the behaviour of the model, the computed radii shown in [33] as an input parameter in the model and heat losses are obtained as an output. Obviously the plasma properties obtained in [32] are used in conformity with the computation in [33]. Their values are shown in figure 5.20.

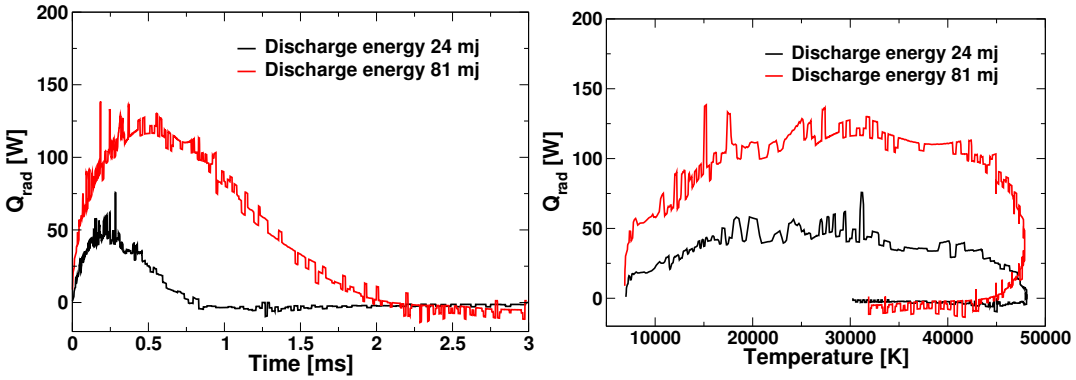

Figure 5.20: *Radiation heat losses obtained by the computed radii shown in [33]. Figure on the left shows the radiation losses in time, while the picture on the right shows the same losses as function of temperate*

The jumps of the values shown in figure 5.20 are due to the discontinuous input radius which was obtained from extrapolation of the data of Figure 5.18. The particular shape of the relation between radiation losses and temperature suggests that an analogous process as the one used for this verification was employed in [33] to estimate the radiation heat losses. Theoretically speaking, assuming that the model is able to describe the physics of the process, this methodology would provide a new way to indirectly measure radiation losses. For example, a common way to estimate radiation losses of thermal plasmas is to set-up an experiment 1D steady configuration for which temperature profile is measured. Then a 1D heat transfer equation is solved and radiation losses are tuned until the computed temperatures match the experimental data. The problem is that, in this case, the dependence of radiation heat losses with high temperature is unphysical. As a consequence, the results obtained by this model and reported in [33] are unfounded.

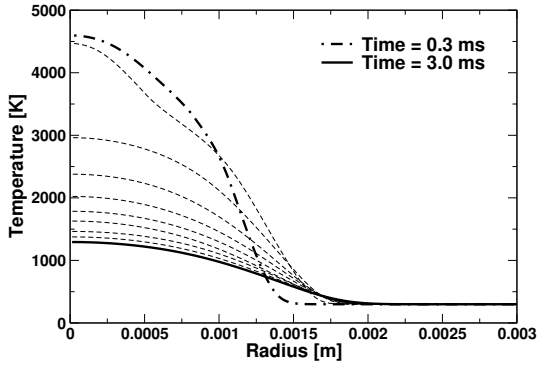

Figure 5.21: *Temperature profile evolution throughout glow phase. Model results are plotted for every 0.3 ms*

Temperature profiles computed with the 1D blast wave solver for the case where 24 mJ are discharged in air are shown in Figure 5.21. As there is no clear way to define the radius to be compared with the experiment, only results of temperature profiles are shown and a qualitative comparison is proposed. For glow discharge, constant current flux assumption is employed as suggested by the theory. The reported results give the idea that thermal diffusion plays an important role and the assumption adopted in [33] about the negligible thickness of the thermal layer is not justified. For the 1D computed case, 100 nanoseconds after breakdown axis temperature reaches a minimum value of about 3000 K (not shown in the figure) before starting to rise again, as the current provided by the electrical circuit increases. The maximum temperature does not exceed 5000 K (time 0.3 ms corresponds to the peak of power supplied by the spark as shown in figure 5.17). When the current is no more supplied, heat diffuses very slowly and the zone where the temperature starts to rise from the ambient value (which more or less corresponds to the measured radius, as shadow-graph technique measures the position of the peak of the second derivative of density), does not move as experiments suggest. This steady value of the radius obtained by the 1D computation is around 1.6 mm. The initial growth of the radius is affected by the increase of surface across which the current flows, as its flux is kept constant. The other case is not computed as it is not clear how to model the transition between glow and arc phase and in particular how to supply the input power. Theoretically speaking, the conductive channel should collapse

and current density and temperature should rapidly increase until the ohmic relation $J = \sigma \cdot E$ is established (σ is the electrical conductivity which can be computed like the other properties of thermal plasmas with the correlations proposed in [26]). In conclusion the results of 1D model are able to reach the experimental radius without the need of the very high and unrealistic temperature provided by the 0D approach.

5.3 Early flame kernel development

The results of the previous sections show that, after breakdown, a very hot channel with a diameter of the order of 1 mm is formed between the electrodes. The temperature is high enough to activate the reactions of the mixture. The high temperature region supplied by the electrical power further expands, but the reaction zone of the flame usually propagates faster and moves away from the spark. The history of flame kernel development is then controlled by the competition between heat provided by the spark channel and stretch effect. In section 3.3 the latest effect was analyzed by means of asymptotic theory and it was explained that stretch tends to reduce the temperature of the reaction zone which leads to a reduction of the propagation speed. The laminar flame speed exponentially depends on the reaction zone temperature, so that small changes of temperature produce a finite change of velocity. Analyzing expressions 3.42 and 3.62, it follows:

$$\left(\frac{S_L}{S_L^0}\right)^2 = exp\left(\frac{E_a}{RT} - \frac{E_a}{RT_{ad}}\right) \tag{5.23}$$

$$T = T_{ad} + T(0^+) \tag{5.24}$$

$$T(0^+) = \frac{1}{S_L^2}\left(\frac{1}{Su}\frac{dSu}{dt} - \frac{2\sigma\delta_L}{r}\right) I_D \tag{5.25}$$

where the temperature of the reaction zone is T and $T(0^+)$ is the perturbation term associated with stretch effect. The substitution of 5.24 into 5.23 and the linearization of the exponential term lead to relation 3.62. For positive values of I_D, which represents the Markstein number in this formulation, stretch reduces the flame speed. In the same way, heat conduction from the high temperature zone of the spark channel can rise the reaction zone temperature. Because $T(0^+) \sim 1/Ze$ is small, the flame speed can be influenced by spark energy deposition even if the flame front is far from the electrodes. Specifically, heat conduction can effectively counter stretch effects, as it avoids the reduction of the reaction zone temperature. When the flame front is close enough to the energy deposition zone, heat conduction can even increase the flame speed up to higher values than the one found for the unstretched case, as the reacting temperature can be higher than the adiabatic flame temperature. Being the relation strongly non-linear, all errors due to secondary effects, like heat losses due to cold electrodes or uncertainties in spark energy deposition process, are amplified. Moreover asymptotic relations are valid for $R/\delta_L >> 1$; the more this ratio decreases, the more important are the effects related to reaction mechanism which can be no more represented only by a global mechanism. Nevertheless, the physics which governs the process is quite clear. In [18] asymptotic methodology is applied to a simplified combustion case with the assumptions of constant density, constant thermal properties and for mixture far from

stoichiometry. The resulting simplified system requires only the solution of the non-dimensional temperature and deficient reactant equations which, in spherical coordinate system, are:

$$\frac{\partial \theta}{\partial t} = \frac{1}{r^2}\frac{\partial}{\partial r}\left(r^2 \frac{\partial \theta}{\partial r}\right) + \omega - H \cdot \theta \tag{5.26}$$

$$\frac{\partial Y_D}{\partial t} = \frac{1}{r^2 Le}\frac{\partial}{\partial r}\left(r^2 \frac{\partial Y_D}{\partial r}\right) - \omega \tag{5.27}$$

where:

$$\omega = \frac{1}{2Le} \cdot Y \cdot Ze^2 \cdot exp\left(\frac{Ze\sigma(\theta - 1)}{1 + (\sigma - 1)\theta}\right) \tag{5.28}$$

$$\theta = (\tilde{T} - T_u)/(T_{ad} - T_u) \tag{5.29}$$

$$Y_D = \tilde{Y_D}/Y_{D,u} \tag{5.30}$$

Energy deposition process is represented as a boundary condition at the centre of the sphere: $r^2 \partial T/\partial r|_{r=\epsilon} = -Q$ for $\epsilon \to 0$. H is a non-dimensional term which takes into account radiation losses and is considered a constant but it can assume different values on the two sides of the flames (burnt ad unburnt zones). The relation for the non-dimensional reaction term 5.28 can be obtained using the asymptotic value of the laminar flame speed 3.41, with constant density assumption and $n = n_d = 1$. An analytical solution can be derived if a quasi-steady assumption is employed, which implies that in the coordinate system attached to the moving flame front, time derivatives are negligible. Then the solution takes the form of a system of two non linear algebraic equations:

$$\Omega_Q + \Omega\theta_f = \left(\frac{1}{R^2 Le} exp\left(-S_L \cdot Le \cdot R\right)\right) / \left(\int_R^\infty \frac{exp\left(-S_L \cdot Le \cdot \tau\right)}{\tau^2} d\tau\right) \tag{5.31}$$

$$\Omega_Q + \Omega\theta_f = exp\left(\frac{Ze}{2}\frac{\sigma(\theta_f - 1)}{1 + (\sigma - 1)\theta_f}\right) \tag{5.32}$$

Where $\Omega = \Omega(H_u, H_b, S_L, R, \theta_f)$ and $\Omega_Q = \Omega_Q(Q, H_b, S_L, R)$ are quite intricate functions given in [18] (pp. 432, 442 respectively). Given the value of one variable, for example the flame front radial position R, then the other two variable S_L and T_f are unequivocally defined. The sum of Ω_Q and $\Omega\theta_f$ is the result of the superposition of effects which is valid because in the burnt zone the resulting differential equations are linear. It is noted that in [18] H is assumed to be constant on burnt and unburnt sides of the flame in order to make the problem linear and to obtain the asymptotic solution. Then, the same value for burnt and unburnt zone is used, while, for physical consistency, it should be $H_b \sim \sigma^3 H_u$, where $\sigma = T_{ad}/Tu \sim 6 - 7$. As a consequence, one of the conclusions of the paper, which states that radiation losses in unburnt zone are important for flame kernel growth, is probably misled by this unlucky choice of parameters. To obtain the analytical solutions it is assumed that the reaction zone is very thin $\delta_L/Ze \to 0$, while no such assumption is required for the ratio δ_L/R. This can provide some insight of the non linear relation between stretch and flame speed. Comparison of analytic results 5.31 and 5.32 and numerical solutions of the equations 5.26, 5.27 are given in Figure 5.22 for different power sources.

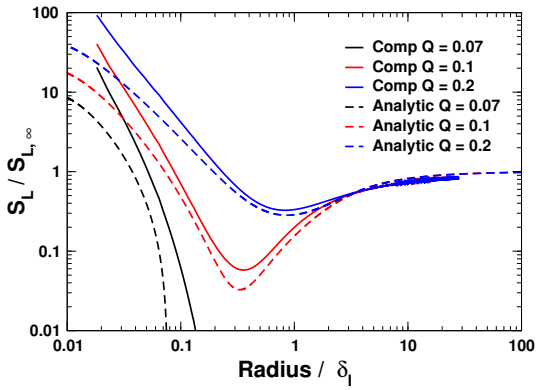

Figure 5.22: *Comparison of analytical results and numerical solutions of asymptotic equations 5.26 and 5.27 for various power sources*

The differences between the two results are connected to the unsteady terms neglected in the analytical solution, which are important only on the first stages of flame kernel development. As could be expected, the importance of ignition energy grows as the Lewis number of the mixture increases, for example with the same ignition energy at Lewis number equal to 1.0 and 1.3 (Figure 5.23) the minimum flame propagation speed changes from 0.3 to 0.02.

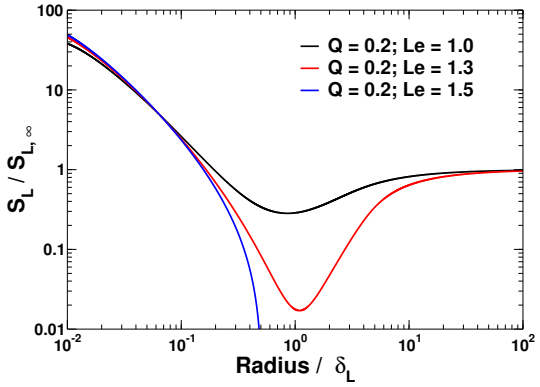

Figure 5.23: *Effect of Lewis number on flame kernel development*

The extension of the analytical solution to a variable density case could be achieved by applying superposition of effects and the jumping conditions across the flame front presented for example in [49]. In fact, on the burnt side of the flame, small spatial variation of temperature makes the assumption of constant properties and density plausible as a first approximation. As a consequence, the energy equation becomes linear. Anyway, as the validity of jumping conditions requires $\delta_L/R \rightarrow 0$, it is not a priori clear if this analytic solution could give more insight on the effect of energy deposition process, as the required flame radius should be big. For this reason, the author instead tried to numerically solve an extended version of equations 5.26 and 5.27. This extended version allows variable density and thermal properties $(\lambda/c_p) \propto (\tilde{T}/T_u)^{\beta+1}$, $D_{th} \propto (\tilde{T}/T_u)^{\beta}$ and a general mixture composition, but requires constant Lewis number, reaction exponent coefficient equal to one and low Mach number approximation.

The new set of equations is:

$$\frac{\partial \rho}{\partial t} + \frac{1}{r^N}\frac{\partial (r^N \rho u_r)}{\partial r} = 0 \tag{5.33}$$

$$\frac{\partial \theta}{\partial t} + \rho u_r \frac{\partial \theta}{\partial r} = \frac{1}{r^N}\frac{\partial}{\partial r}\left(r^N \left(\frac{1}{\rho}\right)^{\beta} \frac{\partial \theta}{\partial r}\right) + \omega - H \cdot \theta + Q_{spk} \tag{5.34}$$

$$\frac{\partial Y_D}{\partial t} + \rho u_r \frac{\partial Y_D}{\partial r} = \frac{1}{r^N Le_D}\frac{\partial}{\partial r}\left(r^N \left(\frac{1}{\rho}\right)^{\beta} \frac{\partial Y_D}{\partial r}\right) - \omega \tag{5.35}$$

$$\frac{\partial Y_E}{\partial t} + \rho u_r \frac{\partial Y_E}{\partial r} = \frac{1}{r^N Le_E}\frac{\partial}{\partial r}\left(r^N \left(\frac{1}{\rho}\right)^{\beta} \frac{\partial Y_E}{\partial r}\right) - \omega \ni \tag{5.36}$$

Where:

$$\omega = \frac{Ze^3}{2Le_D Le_E (z+2)} \Phi Y_D Y_E \rho^2 \sigma^{\beta-2} exp\left(\frac{Ze(T-1)}{\sigma + (1-\sigma)T}\right) \tag{5.37}$$

$$z = Ze\frac{\Phi - 1}{Le_E} \tag{5.38}$$

All the variables are non-dimensionalized with respect to their unburnt value except $Y_E = \widetilde{Y}_E / Y_{D,u}$. All the parameters which are not specified here can be found in section 3.2.3. Second order central difference implicit scheme in space and implicit Euler scheme in time are employed as in the simplified solution case. All the equations are solved separately using the solution of the previous time step for the other variables. Results of the comprehensive model for three cases are shown in Figure 5.24. The three cases represent mixtures of propane at different equivalent ratio, but the same environment condition. The density ratio varies between 3.5-4 as the unburnt gas temperature is about 600 K, which is close to typical engine operating conditions. All the parameters required to complete the set-up of the case (Lewis number, Zel'dovic number, etc..) were obtained by means of 1D computation with the mechanism proposed in [99] and are reported in table 7.6. One of the main difference with respect to the previous simplified case is that the stretch effect is stronger, as the burnt zone cools down much more both because the thermal conductivity is higher and because the hot mass is always lower than the mass to be heated. As a consequence, in the tested cases ignition by means of introduction of heat with a boundary condition is no more able to generate a propagating flame and the energy must be provided on a larger channel.

This model was originally thought as a way to better represent the non-linear effect of stretch on flame speed and as an approach to describe early flame kernel development in engine simulations by constructing tables which provide the flame speed as function of flame radius. Unfortunately the results of the model are not consistent. For example, in Figure 5.24 the non-dimensional flame propagation speeds do not tend to one for high radius values as in the simplified case. The reason of this behaviour is not actually clear, but the author thinks that the expression of the laminar flame 3.42 used to make the reaction rate ω non dimensional is too inaccurate to be applied for this numerical case. Alternatively, being the results very sensitive to small changes of some parameters, the problem could be numerical and could be solved with more accurate discretization schemes or strategies to increase the coupled solutions of the different equations.

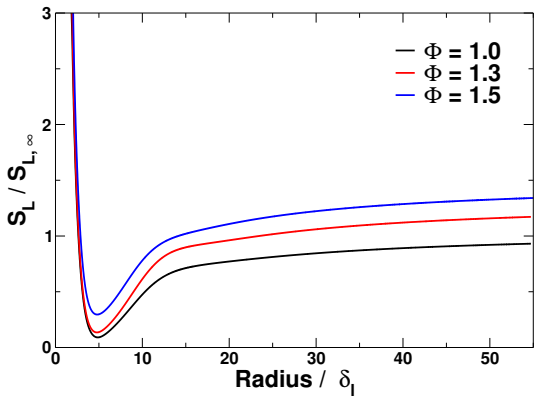

Figure 5.24: *Flame kernel grow for propane-air mixture at different equivalence ratio*

5.4 Concluding remarks

In this chapter information about spark discharge process and early flame kernel development were given. The aim of the description was mainly to give a general background about the problem in order to be able to evaluate if some of the simplified approaches proposed in literature are able to describe this process. It was found that, from the electrical point of view, the problem can be solved as the spark can be described by means of empirical correlations between voltage and current. These relations are found to be coherent with the known theory and, as such, they are quite reliable. Concerning the fluid-dynamic part, among the tested approaches, the 1D case seems to be able to reproduce some of the aspects described in literature and to provide realistic results, considering also the many unknowns of the problem. Regarding early flame kernel development, a 1D approach with the support of asymptotic theory was investigated. Unfortunately, while a simplified version of this approach was successfully implemented and tested, its extension to more realistic cases, which could provide some quantitative results, did not give coherent results. Further investigations are required in order to understand if the problem is conceptual (the laminar flame speed formulation used to compute the reaction rate is not coherent with this approach or too approximated) or simply numerical (different strategies to solve the system of equations and higher order schemes should be used).

CHAPTER 6

A comprehensive combustion model for spark-ignition engines

In the previous chapters, the physics of turbulent premixed combustion from ignition to a fully turbulent flame developed has been reviewed. In particular, the author tried to outline a logical sequence of steps to proceed from the lowest level of modelling (DNS with detailed chemistry) to the higher level (RANS without solving reactions). For each step, the main physical mechanisms involved were shown. It was analyzed what it is known from experiments and theory, and the models and related parameters proposed to describe these mechanisms. The author hopes that this description can help to clarify which aspects at every modelling level should be described (for example, in LES context the problem of flame development should not require specific sub-model like RANS), which aspects require more theoretical and experimental studies and what is lost in the modelling process (for example by the use Favre average equations in RANS instead of conditional average). The author is aware not to have covered every issues related to premixed combustion problem, as identification and study of these aspects have required the work of the whole combustion community over the last sixty years. Anyway he thinks that this description and the related reference articles, can provide enough information to have a clear idea of the state of the art and some suggestions for future developments. In this chapter, a model which takes into account most of the previous aspects is described. This model was originally developed for the flame surface density approach, then, for the problems shown in chapter 4, the model was readjusted for the G-Equation approach. Anyway, the main structure of the actual model is shared with the previous one and a summary of its description can be found for example in [68]. In the following, only the G-Equation version will be described. The model can be divided in two parts: the main part, in which the Eulerian transport equations for premixed combustion are solved, and a series of sub-models, which are

used to describe the early flame kernel development. This phase would require very fine mesh resolutions to be described by an Eulerian approach. These two parts are discussed in different sections.

6.1 Equations solved in the Eulerian domain

The equations solved by the main model are the Favre average version of reacting flows equations.

- Conservation of mass:

$$\frac{\partial \overline{\rho}}{\partial t} + \nabla \cdot \left(\overline{\rho} \widetilde{\mathbf{U}} \right) = 0 \tag{6.1}$$

- Conservation of momentum:

$$\begin{aligned} \frac{\partial \overline{\rho} \widetilde{\mathbf{U}}}{\partial t} + \nabla \cdot \left(\overline{\rho} \widetilde{\mathbf{U}} \widetilde{\mathbf{U}} \right) &= -\nabla \left(\overline{p} + \frac{2}{3} \left(\overline{\mu} + \overline{\mu}_t \right) \nabla \cdot \left(\widetilde{\mathbf{U}} \right) \right) + \\ &+ \nabla \cdot \left[\left(\overline{\mu} + \overline{\mu}_t \right) \left(\nabla \widetilde{\mathbf{U}} + \nabla \widetilde{\mathbf{U}}^T \right) \right] + \\ &- \frac{2}{3} \nabla \left(\overline{\rho} \widetilde{k} \right) \end{aligned} \tag{6.2}$$

- Conservation of Favre specific total enthalpy:

$$\frac{\partial \overline{\rho} \widetilde{h}_t}{\partial t} + \nabla \cdot \left(\overline{\rho} \widetilde{\mathbf{U}} \widetilde{h}_t \right) + \nabla \cdot \left[\left(\frac{\overline{\lambda}}{c_p} + \overline{\rho} \overline{\alpha}_t \right) \nabla \widetilde{h}_t \right] = \frac{\partial \overline{p}}{\partial t} \tag{6.3}$$

- Conservation of conditioned unburnt specific enthalpy:

$$\begin{aligned} \frac{\partial \overline{\rho} \widetilde{h}_u}{\partial t} + \nabla \cdot \left(\overline{\rho} \widetilde{\mathbf{U}} \widetilde{h}_u \right) + \nabla \cdot \left[\left(\frac{\overline{\lambda}_u}{c_{p,u}} + \overline{\rho} \overline{\alpha}_t \right) \nabla \widetilde{h}_u \right] &= \frac{\overline{\rho}}{\overline{\rho}_u} \frac{\partial \overline{p}}{\partial t} - \\ &- \frac{\overline{\rho}}{\overline{\rho}_u} \frac{D(\overline{\rho} \widetilde{K})}{Dt} \end{aligned} \tag{6.4}$$

With:

$$\overline{\mu}_t = C_\mu \frac{\overline{\rho} \widetilde{k}^2}{\widetilde{\epsilon}} \tag{6.5}$$

$$\overline{\alpha}_t = \frac{\overline{\mu_t}}{\overline{\rho} Pr_t} \tag{6.6}$$

$$\widetilde{K} = \frac{1}{2} \widetilde{\mathbf{U}} \cdot \widetilde{\mathbf{U}} \tag{6.7}$$

The two enthalpy equations are solved in order to compute T_u, T_b. From ideal gas law, it is possible to compute ρ_u, ρ_b. By means of the relation 4.31, the value of $\overline{\rho}$, which is used in all the others equations, is computed. The value of turbulent viscosity is obtained by one of the various two-equation k-epsilon models implemented in OpenFOAM which are not reported here, as they are formally identical to the non-reacting flows versions which can be found in many textbook like [98]. The previous equations are common to all the combustion models shown in chapter 4. For the G-Equation

model, equation 4.38 is also solved, where the turbulent flame speed can be selected between the various relations described in sections 4.6.1 and 4.6.2. For consistency with finite volume code OpenFOAM, equation 4.38 is rewritten in a conservative like form:

$$\frac{\partial \overline{\rho}\tilde{G}}{\partial t} + \nabla \cdot \left(\left(\overline{\rho}\widetilde{\mathbf{U}} + \overline{\rho}_u S_t \mathbf{n} \right) \tilde{G} \right) = \tilde{G} \nabla \cdot \left(\overline{\rho}_u S_t \mathbf{n} \right) - \widetilde{D}_{t,t} \kappa \tag{6.8}$$

$$\widetilde{D}_{t,t} = \sqrt{c_s c_\mu 2 S c_t \widetilde{k}} \Delta_t \tag{6.9}$$

$$\begin{aligned} \Xi &= -\frac{a_4 b_3^2}{2b_1} Da \left(\frac{\Delta_t}{\Delta_{t,\infty}} \right)^{5/3} \frac{u_{rms}}{S_L} + \\ &+ \sqrt{\left(\frac{a_4 b_3^2}{2b_1} Da \left(\frac{\Delta_t}{\Delta_{t,\infty}} \right)^{5/3} \right)^2 + a_4 b_3^2 Da \left(\frac{\Delta_t}{\Delta_{t,\infty}} \right)^2 \frac{u_{rms}}{S_L}} \end{aligned} \tag{6.10}$$

$$S_t = S_L (1 + \Xi) \tag{6.11}$$

Where $\mathbf{n} = -\nabla \widetilde{G} / |\nabla \widetilde{G}|$ is the normal vector pointing toward the unburnt gas region. The curvature term can be neglected as for the spatial scheme employed in a finite volume solver, second derivatives are subject to high errors for arbitrary shapes of the flames. Moreover its effect is negligible except for the initial stages of combustion, for which mesh size is not fine enough to give a correct value of curvature and sub-models are employed instead of the Eulerian equations. With the exception of $\mathbf{n}$, this formulation can be easily solved with implicit methods. The last important part is how to convert the distance function G into the progress variable $\widetilde{c}$. As already stated, two strategies can be adopted: the first one is to assume that the probability density function of finding the flame has a Gaussian shape as suggested in [126] and confirmed in [63]; then:

$$\bar{c} = 0.5 + 0.5 erf\left(\frac{\widetilde{G} - \widetilde{G}_0}{\sqrt{2\widetilde{G''^2}}} \right) \tag{6.12}$$

where the average flame position $\widetilde{G_0} = 0$ and $\widetilde{G''^2}$ is the variance. From the relation between the flame brush thickness and $\widetilde{G''^2}$ and, being $\widetilde{G}$ a distant function such that $|\nabla \widetilde{G}| = 1$, it is clear that:

$$\Delta_t = \frac{\sqrt{\widetilde{G''^2}}}{|\nabla \widetilde{G}|} = \sqrt{\widetilde{G''^2}} \tag{6.13}$$

The above relation is used only for dimensional consistence. As a consequence $\sqrt{\widetilde{G''^2}}$ in 6.12 can be replaced with Δ_t and other relations like the one proposed in [63] can be employed. To compute this quantity, the equation proposed by Peters in [92] is used:

$$\begin{aligned} \frac{\partial \overline{\rho}\widetilde{G''^2}}{\partial t} &+ \nabla \cdot \left(\left(\overline{\rho}\widetilde{\mathbf{U}} + \overline{\rho}_u S_t \mathbf{n} \right) \widetilde{G''^2} \right) - \nabla \cdot \left(\overline{\rho}\widetilde{D}_t \nabla \widetilde{G''^2} \right) = \\ &= \widetilde{G''^2} \nabla \cdot \left(\overline{\rho}_u S_t \mathbf{n} \right) + 2\overline{\mu}_t (\nabla \widetilde{G})^2 - \mathbf{n} \nabla \left(\overline{\rho}\widetilde{D}_t \mathbf{n} \nabla \widetilde{G''^2} \right) - c_s \overline{\rho}\widetilde{G''^2} \frac{\epsilon}{k} \end{aligned} \tag{6.14}$$

As before, the equation has been written in conservative like form. All the model constants are reported in table 6.1.

Symbols	Definition	Suggested Value
a_1	$l_t = a_1 \cdot u_{rms}/\epsilon$	0.37
a_2	$k = a_2 u_{rms}^2$	1.5
a_3	$\tau_t = k/\epsilon = a_3 l_t/u_{rms}$	$a_3 = a_1/a_2 = 4.05$
a_4	$D_t = a_4 l_t u_{rms}$	$a_4 = C_\mu/Pr_t \cdot a_2^2/a_1 = 0.78$
C_μ	$\nu_t = C_\mu k^2/\epsilon$	0.09
c_s	Constant in Eqn. 6.14	2.0
b_1	$S_t = b_1 \cdot u_{rms}$	2.0
b_2	$\Delta_t = b_2 \cdot l_t$	$2a_3a_4/c_s$
b_3	$S_t/S_L = b_3\sqrt{D_t/D}$	1.0

Table 6.1: *Constants value for Peters turbulent flame speed relation. For more details about their derivation, see ([92] pp. 132).*

Alternatively Lipatnikov model [63] can be used to express the turbulent flame speed and the flame thickness in function of local field properties and time after ignition:

$$\frac{\partial \bar{\rho}\widetilde{D}_t}{\partial t} + \nabla \cdot \left(\bar{\rho}\widetilde{\mathbf{U}}\widetilde{D}_t\right) - \nabla \cdot \left(\bar{\rho}\widetilde{D}_t \nabla \widetilde{D}_t\right) = \bar{\rho}(\widetilde{D}_{t,\infty} - \widetilde{D}_t)\frac{\epsilon}{k} \tag{6.15}$$

$$\frac{\partial \bar{\rho}\Delta_t^2}{\partial t} + \nabla \cdot \left(\bar{\rho}\widetilde{\mathbf{U}}\Delta_t^2\right) - \nabla \cdot \left(\bar{\rho}D_t \nabla \Delta_t^2\right) = 4\pi \widetilde{D}_t \tag{6.16}$$

$$\frac{S_t}{S_{t,\infty}} = \sqrt{1 + \left(\frac{\widetilde{D}_t}{\widetilde{D}_{t,\infty}}\right)/ln\left(1 - \frac{\widetilde{D}_t}{\widetilde{D}_{t,\infty}}\right)} \tag{6.17}$$

Where $D_{t,\infty} = \nu_t/Sc_t$, $S_t = ADa^{1/4}u_{rms}$ and the suggested value for A is 0.5. This model has the advantage of requiring less turning constants.

6.2 Numerical solution of Eulerian equations

In OpenFOAM, the previous system of partial differential equations is solved with an iterative implicit pressure-based sequential solution procedure. Specifically, the solution of unsteady RANS equations is performed by a procedure known as PIMPLE which is in between the SIMPLE (Semi-Implicit Method for Pressure-Linked Equations, [35]) and the PISO (Pressure-Implicit with Splitting of Operators [120]) algorithms. PISO was originally conceived as a predictor-corrector method to be used with a fixed number of passes through the equations on each time step. These stages are one outer iteration (momentum predictor) and two or more inner iterations (pressure/velocity corrector). PIMPLE algorithm allows the use of more outer iterations together with under-relaxation factors for each time step. This makes the algorithm looks like a SIMPLE which retains the correct time derivative terms. Both momentum predictor and pressure corrector require the solution of a sparse implicit linear system, which is the results of the discretization of the linearized form of the previous partial differential equations; instead the velocity corrector operation is explicit. This algorithm was originally proposed for problems where the only unknowns are velocity and pressure; equations of additional quantities are included in each pressure/velocity corrector step to maintain a tight coupling among the equations. At the end of the pressure/velocity corrections, equations requiring a lesser degree of coupling are solved (e.g., turbulence

model equations). The process is repeated as necessary, starting from the momentum predictor, until converged solution for the current time step or global iteration is obtained. Three levels of iterations are thus employed for each time step: an outer loop, an inner loop and the iterations required to solve the linear system resulting from implicit discretization of each equation. Every iteration of the outer loop corresponds to the momentum predictor step, while every iteration of the inner loop to the pressure/velocity corrector step. Because of under-relaxation factors, PIMPLE algorithm allows less restrictive constrains related to the Courant number, which can be more then one. Anyway, in order to correctly compute a transient stage, in general, not too many outer iterations should be employed and time step should be adjusted in order to satisfy convergence criteria for a small number of outer iterations. Among the many resolved quantities, G-Field requires particular care. The G-Equation is an application of Level-set approach originally developed by Osher in [83] to combustion problems. Its solution requires some attention as G-Field, for convenience, has to represent a signed distant function; a property which is not conserved when equation 6.8 is solved. To solve this issue, different procedures, known as reinitialization process, have been proposed. For example, one of these procedures involves the solution of the additional equation $G_t + S(G)(|\nabla G| - 1) = 0$ [90] until a steady state solution is obtained. Other techniques like the narrow band approach [3] or fast marching method [106] were proposed in order to reduce the computational time. These methods are usually proposed for finite difference solvers with structured grids and employ high order essentially non-oscillatory (ENO) [84] or weighted ENO [46] schemes. Unfortunately OpenFOAM is optimized for finite volume method and non-structured mesh, so that the implemented grid data structure is difficult to be used for schemes which require big computational molecules. Being this work a preliminary study on turbulent combustion models and considering that many other models do not require these particular approaches, it was decided to used as much as possible the already available code. As a consequence, the closest scheme which resembles ENO one, which is the linear upwind scheme, is used to solve the G-field equation. For reinitialization process, the procedure suggested in [90] does not always work with the available numerical schemes, so a direct way is employed. The following steps explain in details the employed procedure; the explanation is supported by Figure 6.1.

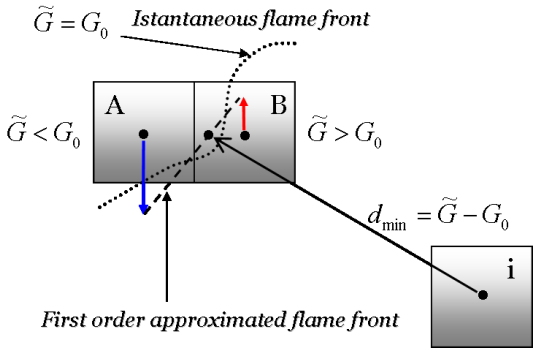

Figure 6.1: *Reinitialization procedure applied to G-Field*

- Equation 6.8 is solved. The updated value of the G-Field is named G^{up}.

- Localization of the mean flame front position: a list of points is created. A new point is added for every surface which connects two cells A and B for witch $G(A)^{up} \cdot G(B)^{up} < 0$. The point coordinates are computed by linear interpolation:

$$\overline{X} = \overline{X}_A + \frac{G^{up}(A)}{G^{up}(A) - G^{up}(B)}(\overline{X}_B - \overline{X}_A) \tag{6.18}$$

  Where $\overline{X}_A$ is the Cartesian position vector of the centre of cell A. For the generic quantity Φ which has to be set equal to the value found on the surface (like the flame brush thickness), a weighed linear interpolation is employed:

$$\Phi = \Phi_A \frac{G^{up}(A)}{G^{up}(A) - G^{up}(B)} + \Phi_B \left(1 - \frac{G^{up}(A)}{G^{up}(A) - G^{up}(B)}\right) \tag{6.19}$$

- For a selected cell of the domain, the minimum distance d from the list of points found in the previous step is computed; the final G value of the selected cell becomes:

$$\tilde{G} = H \cdot G^{up} + (1 - H) \cdot sign(G^{up}) \cdot d \tag{6.20}$$

  where

$$H = \frac{1 - tanh(3(d - \alpha\Delta X)/(\Delta X))}{1 - tanh(-(3\alpha\Delta X)/(\Delta X))} \tag{6.21}$$

  α is set to 3 and ΔX is an estimated cell size. In this way if $G^{up} \to 0$, $\tilde{G} = G^{up}$ and the higher order accuracy guaranteed by the second order spatial scheme employed to solve 6.8 is preserved.

- In order to reduce the computational time, only cells whose previous value of G is lower that 2 times the maximum flamebrush thickness are considered; in fact for the outer cells a correct value of $\tilde{G}$ is not essential.

This reinitialization method is quite expensive. The implementation of better performing procedures is postponed to future works. Some results which prove the validity of the implemented approach are presented in Figures 6.2 and 6.3.

Figure 6.2 shows the evolution of the iso-surface $G = 0$ of an expanding sphere with fixed expanding velocity of 4 m/s. For one case the centre of the sphere is fixed, for the other case all the points of the sphere move with a velocity of 8 m/s. The graph compares the theoretical radius with the one computed for the fixed expanding sphere and the moving one. The error increases with time, but its maximum value is only about 1.5 %. Euler implicit scheme in time is used; it is noted that accuracy is influenced by the combustion Courant number which is the same (about 0.3) for both computations. A second order scheme in time, with the same time step, decreases the maximum error to about 0.1 %. Figure 6.3 shows the same comparison in a more complex geometry with unstructured mesh. The same accuracy is obtained. The error increases if a complete tetrahedral mesh is employed as the sphere starts to be wrinkled because of mesh effects and the maximum error at the end of the computation rises to about 8%.

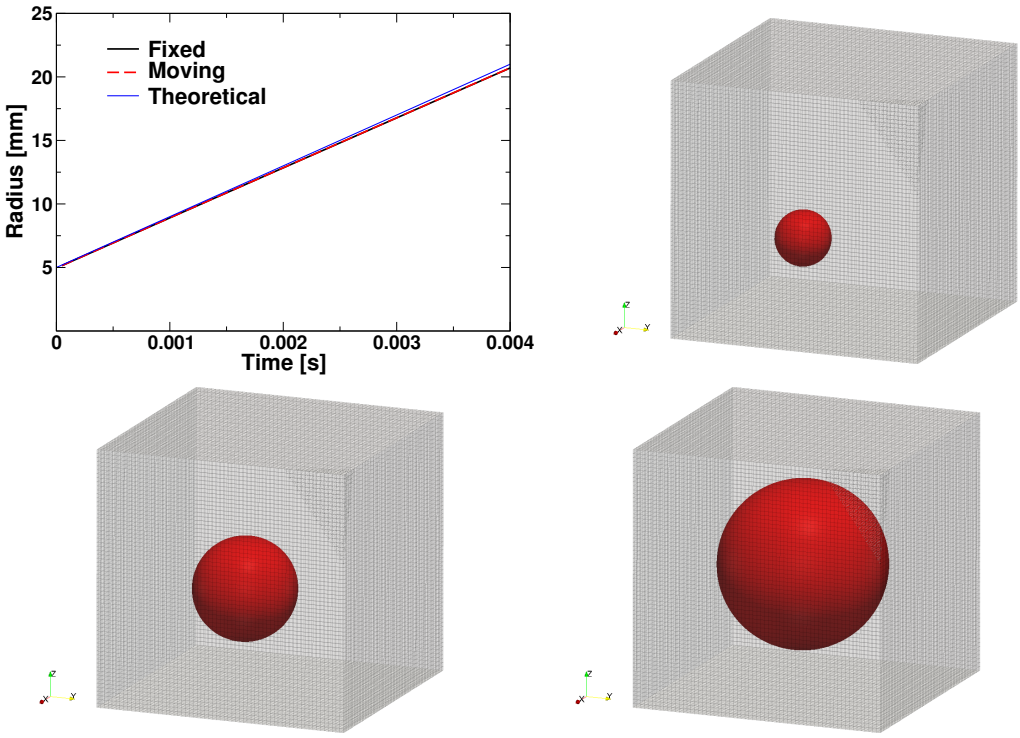

Figure 6.2: *G-Equation: comparison of computed and theoretical radius for a moving spherical expanding geometry in a fully structured mesh.*

6.3 Sub-models which describe initial stages of flame kernel

The last part of the model description concerns flame initialization and initial flame development. As the main model has no term which is able to describe ignition and because initially the flame is small with respect to mesh size, Eulerian equations are not able to correctly describe the problem. In many codes the physical description of this part is usually neglected and numerical initialization is prescribed as done in chapter 4. In the proposed model this initial combustion stage is modelled on the basis of some of physical mechanisms which were reviewed in the previous chapters, knowing that a trade-off between model complexity, computational effort and available information are to be considered. In literature similar approaches have been already proposed for example in [34], [29] and more recently in [25]. Some concepts taken from these articles are put together in the presented model. The main idea is to use a Lagrangian approach to describe the initial development of different flame kernels, seen as moving particles. After breakdown, the formed spark-channel is represented by a set of Lagrangian particles, that are initially placed along a line between the two electrodes. Each of these particles represents an ignition spot (see Figure 6.4), as it is assumed that after breakdown, as shown in section 5.2.1, the temperature value rises enough to always ignite the mixture. Eventually the flame could not be able to propagate because of the high stretch induced by turbulent motion. However, because of the many uncertainties related to the estimation of turbulent stretch and even more on stretch extinction value, actually this aspect is not taken into account. These flame kernels are convected by the mean flow and specific sub-models are used to describe their growth.

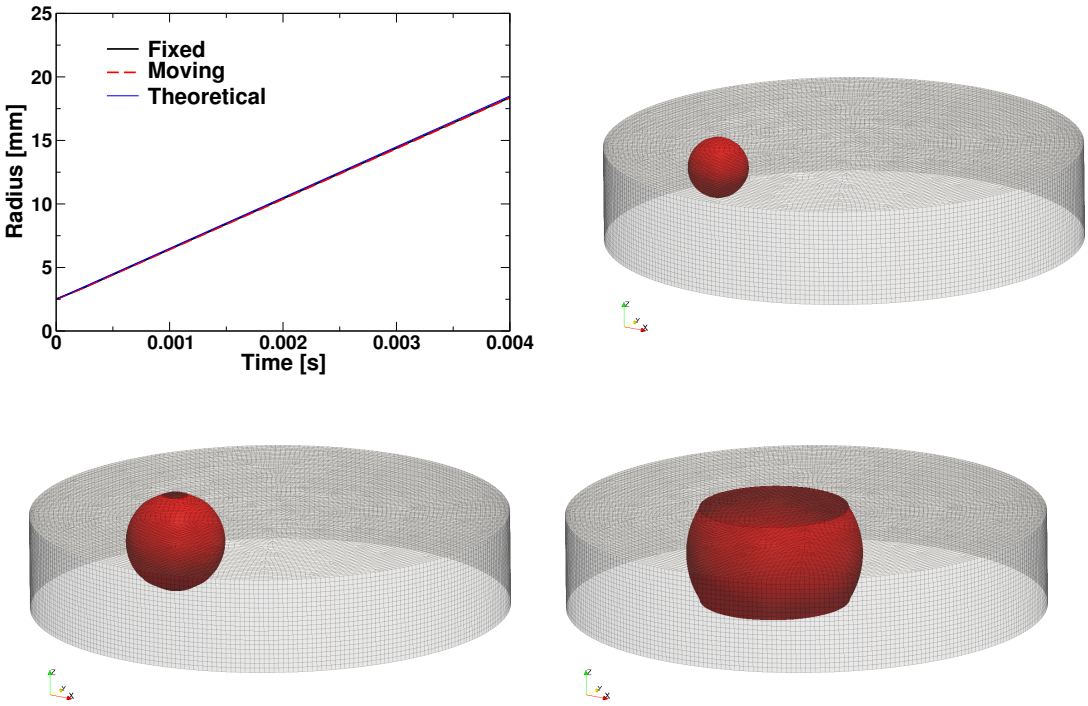

Figure 6.3: *G-Equation: comparison of computed and theoretical radius for a moving spherical expanding geometry in an unstructured mesh. The radius compared is computed at the traversal cross section in the middle of the cylinder*

6.3.1 Electrical circuit and spark energy deposition model

A detailed electrical circuit sub-model is employed to simulate spark discharge process and energy deposition in the fluid. In particular, the secondary circuit of a typical spark discharge system TCI 6.5 is described by means of the following equations:

$$\frac{\partial E_s}{\partial t} = -R_s i_s - V_{spk} i_s \tag{6.22}$$

$$E_s = \frac{1}{2} L_s i_s^2 = E_p = \frac{1}{2} L_p i_p^2 \tag{6.23}$$

$$V_{spk} = V_{fall} + 40.46 l_{spk} i_s^{-0.32} p^{0.51} \tag{6.24}$$

$$\frac{\partial E_s}{\partial t} = -R_s i_s - V_{spk} i_s \tag{6.25}$$

$$i_p = \frac{V_b}{R}\left(1 - exp\left(-\frac{t_{charge}}{R_i/L_p}\right)\right) \tag{6.26}$$

where E_s is the energy stored in the coil which can be given or computed with equation 6.26 if charge time is available. The properties of the electrical circuit can be estimated by means of experimental data of charge process and discharge in quiescent air, as shown for example in 5.10. Alternatively, if the electrical circuit is too different from the previous scheme, the current profile can be directly imposed, while the voltage across the spark gap V_{spk} is computed by means of the empirical relation 6.24 which

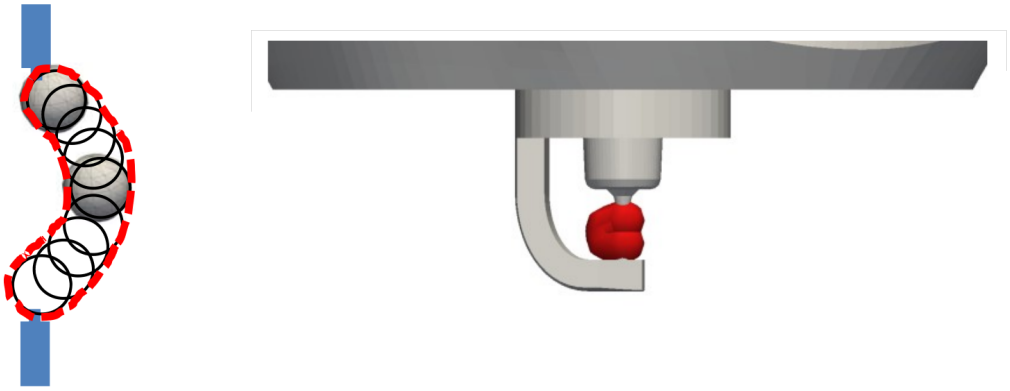

Figure 6.4: *Lagrangian approach concept. On the left a schematic view of a set of flame kernels after ignition, on the right an example of computation*

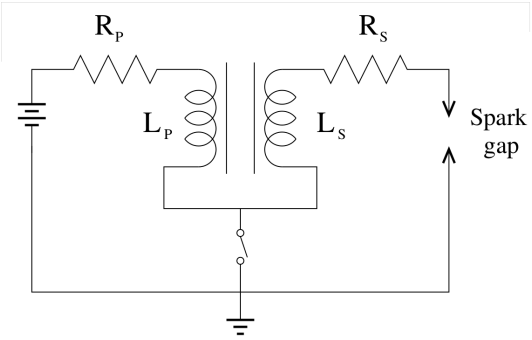

Figure 6.5: *Simplified scheme of a TCI system modelled in the solver*

was taken from [52]. As the spark channel is stretched, the voltage across the spark gap V_{spk} increases because of increasing length of the conductive channel l_{spk}. When it reaches a critical value, a new spark channel between the electrodes is formed (see Figure 6.6) and the voltage decreases to the initial value. In the model this effect is represented by the disposition of the set of flame kernels between the electrodes. This process is known as restrike and the critical voltage should scale as:

$$V_{rsk} = V_{rsk,0} \frac{d}{d_0} \frac{P}{P_0} \frac{T_0}{T} \tag{6.27}$$

where subscript 0 refers to a nominal value equal to about 1.3 kV at the nominal conditions $P_0 = 1bar$ and $T_0 = 298K$ and $d_0 = 1mm$, which is observed in some experimental data. In Figure 6.7, the restrike voltage of the lower velocity is about 1.3 while for the higher velocity it is 1.4. This could imply that also velocity influences the restrike voltage value for a mechanism probably similar to the one discussed at the end of section 5.1.1. The previous scaling law is obtained assuming that restrike will occur if $E/N = (E/N)_{cr}$. From experiments, it is clear that restrike voltage is lower than the breakdown value (it is about one tenth or lower). No experimental data are available to confirm the previous relation. Image 6.6, which is the measured voltage across the electrodes of a spark plug inside an engine, seems at least to confirm an increase of restrike voltage with pressure which could be partially compensated by the rise of

temperature. In the computations of next chapter, only the nominal value is used, in line with the experimental data available for that geometry.

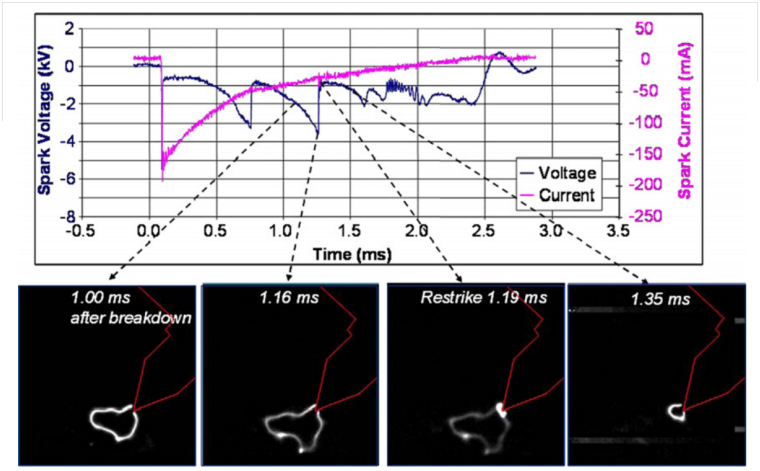

Figure 6.6: *Restrike phenomenology: on the top voltage and current profiles in time; on the bottom images of the spark during a restrike. After breakdown, a sudden change of voltage indicates that restrike has occurred. Images are taken from [24]*

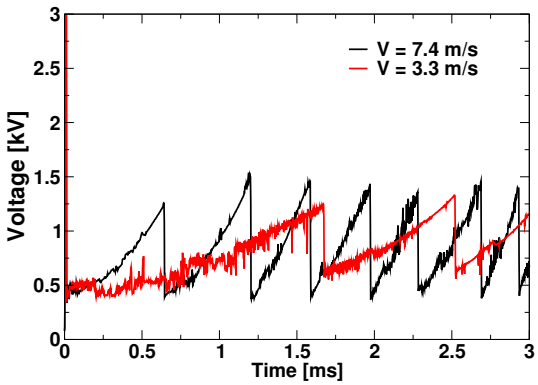

Figure 6.7: *Voltage evolution in time across the spark gap for different flow velocities at ambient pressure and temperature. Experimental data kindly provided by Chiba University.*

6.3.2 Flame kernel growth model

A similar approach to the one proposed in [71] is used to model the initial flame kernel development. Initially, because of breakdown process, the temperature rises a lot, while flame formation is not yet completed or it is subject to a very high stretch rate. Therefore thermal diffusion process is faster than flame propagation. As such, an heat diffusion equation is solved:

$$\frac{\partial T_{pl}}{\partial t} = \nabla(\alpha \nabla T_{pl}) + \frac{\eta_{eff} Q_{spk}}{\rho c_p Vol} \tag{6.28}$$

Due to the high temperature, the gas properties are computed from the tables obtained by the relations proposed in [26], while the heat exchange efficiency is taken

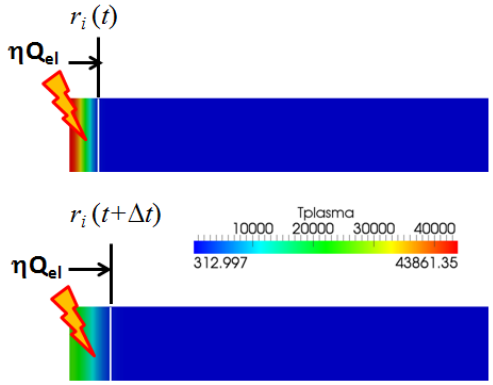

Figure 6.8: *1D thermal channel model: scheme of plasma velocity s_{pl} computation*

from [71]. A sub-cycling procedure ($\Delta t = 20ns$) is used to solve Eqn. 6.28. The temperature field is solved on a 1D grid representing a sector of the gas axis-symmetric region that surrounds the spark electrodes 6.8. The mesh height is set to be equal to the electrodes gap, while the radial length of the domain is set to 1.0 cm, which is significantly higher than the maximum diameter of the flame kernel that is reached during this phase. To solve the steep gradient, a grid size of about 10 μm is employed. The following initial and boundary conditions were imposed at spark time and after each restrike event:

$$T_{pl}(r) = (T_{ign} - T_u) \cdot exp\left(-\frac{\pi}{4.0}\left(\frac{r}{r_{ign}}\right)^6\right) + T_u \tag{6.29}$$

where T_u is the average temperature of the mixture at ignition time computed on the main mesh domain. The starting temperature and diameter (T_{ign} and r_{ign}) after breakdown are estimated with the approach exposed in [110], which describes the phase immediately after breakdown with a two steps 0D thermodynamic model. In the first step, it is assumed that the conductive channel in which the energy stored in the spark plug is discharged, behaves like a constant volume vessel. In the second step, the system is subject to isotropic expansion from the high pressure induced by the energy discharge process to the actual engine pressure. The relations which describe this process and give the final temperature and diameter are:

$$T_{ign} = T_u\left(\frac{1}{k}\left(\frac{T_{bd}}{T_u} - 1\right) + 1\right) \tag{6.30}$$

$$r_{ign} = \frac{k-1}{k} \cdot \frac{E_{bd}}{p\pi d_{gap}(\frac{T_{bd}}{T_u} - 1)} \tag{6.31}$$

$$E_{bd} = \frac{1}{2} \cdot C \cdot V_{bd}^2 \tag{6.32}$$

where T_{bd} is set to 40000 K, according to the computation of the previous chapter. $k = c_p/c_v$ is estimated with the average temperature computed with T_{ign} and T_{bd} after a first estimation of T_{ign} with the average value obtained from T_u. Breakdown energy is computed by means of relations 6.32 and 5.13. Alternatively, the 1D bast wave solver

described in section 5.2.1 can be used to compute the initial temperature profile after breakdown. This last model is not implemented in the current solver for computational time reasons. The initial kernel displacement velocity is computed as:

$$s_{pl} = \frac{r_k(t + \Delta t) - r_k(t)}{\Delta t} \tag{6.33}$$

where r_k corresponds to the position $T_{pl}(r_k) = T_{ad}$. To estimate the laminar flame speed subject to stretch, equation 3.66 is used. Only curvature contribution is considered as there is no clear way to estimate the stretch induced by turbulence. In order to take into account turbulence contribution to flame wrinkling, the same equations presented in the previous section are rewritten for the Lagrangian description. Spatial derivatives are neglected and partial derivatives in time become total derivatives. The resulting expression can be integrated in time giving the following algebraic expression:

$$G''^2 = \delta_L^2 exp\left(-c_s \frac{t - t_0}{\tau_t}\right) + b_2 \Delta_t^2 \left(1 - c_s \frac{t - t_0}{\tau_t}\right) \tag{6.34}$$

Equations 6.13, 6.10 and 6.11 are used to compute the total growth rate of the flame kernel:

$$\frac{\partial r}{\partial t} = s_{pl} + \frac{\rho_b}{\rho_u} S_L^0 I_0 (1 + \Xi) \tag{6.35}$$

If Lipatnikov model is chosen, then the algebraic expressions to compute the wrinkling factor are:

$$\Delta_t = \sqrt{4.0 \pi D_{t,\infty}} \sqrt{(t - t_0) - \tau_t \left(1 - exp\left(-\frac{t - t_0}{\tau_t}\right)\right)} \tag{6.36}$$

$$\Xi = A D a^{1/4} \frac{u_{rms}}{S_L} \sqrt{1 - \frac{\tau_t}{t - t_0}\left(1 - exp\left(-\frac{t - t_0}{\tau_t}\right)\right)} \tag{6.37}$$

All the variables related to the fields, which are resolved on the main mesh, are obtained averaging their values of all the cells in which the flame front is. $I_0 = S_L / S_L^0$ corresponds to Eqn. 3.66. Relation 6.35 mimics the flame kernel expansion behaviour for which the initial velocity is high, then it decreases reaching a minimum and then starts to increase again. s_{pl} is initially very high due to the high temperature gradient, then it quickly goes to zero, while $S_L^0 I_0$ increases with the radius and Ξ increases in time.

6.4 Coupling the Lagrangian model with the mesh domain

A summary diagram of the whole model is shown in figure 6.10. During the simulation Eulerian fields and Lagrangian particles are evolved with the same time step. The coupling between the two parts of the model implies the exchange of information in both direction: before the tracking algorithm is performed, the computed flow field data such as ambient density, turbulence quantities (k and ε), laminar flame speed and velocity field are passed to the Lagrangian part. Particles are convected by the mean flow while they grow in size because of the flame propagation speed and thermal expansion due to the heat transferred from electrical circuit to the gas phase. Such quantity is provided

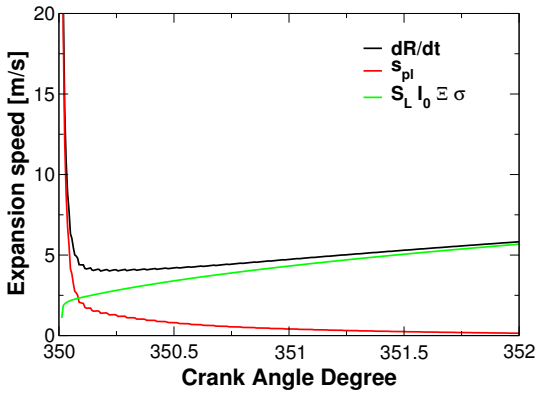

Figure 6.9: *Example of computed flame kernel velocity. The picture shows the separate contribution of flame speed related to expansion of ht channel and laminar flame speed development.*

by a suitable model that predicts the current and voltage evolution inside the secondary circuit. This sub-model requires the length of the spark channel, which is easily computed from the particles position. Once the tracking phase is performed, the G value is reconstructed by means of two G-Fields: one (G_{spk}) is associated with the Lagrangian particles, the other one (G_{field}) is related to the field solved by Eulerian equation 6.8. The first field is computed as follows: for each cell of the domain, the value of G is taken as the minimum distance from the flame front represented by the flame kernels. This quantity is computed as the magnitude of the distance between the cell centre and the kernel position plus its radius:

$$G_{spk} = |\overline{X}_{celli} - \overline{X}_{kernel}| + r_{kernel} \tag{6.38}$$

After this computation, the cells for with $G_{spk} = 0$ are found and the average values of k and ε are used to update turbulence properties, which are then used to computed Ξ and $\widetilde{G''^2}$ of the flame kernel. To move the particles, the interpolated velocity in the position of the centre of the flame kernel is used. At the same time, the quantities computed by the flame kernel sub-models like $\widetilde{G''^2}_{spk}$ are mapped on the cell for which $G_{spk} > G_{field}$. When restrike occurs or the flame kernel radius exceeds a selected value, G_{spk} is mapped on the G_{field} by selecting the maximum value between G_{spk} and G_{field}.

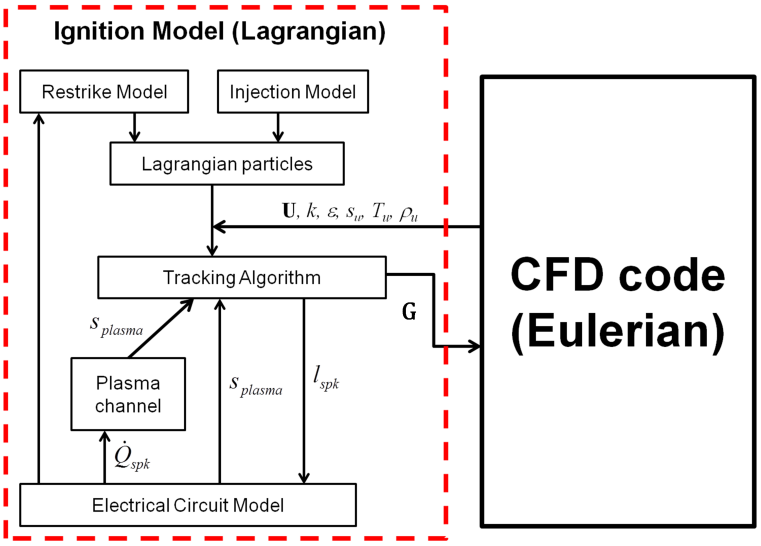

Figure 6.10: *Diagram patterns of the proposed model: interaction between sub-models, Lagrangian particles and Eulerian mesh*

CHAPTER 7

Combustion model validation

In this chapter an evaluation of the model behaviour is proposed, comparing its results with experimental data of an engine like environment. The selected test case is an experimental configuration which is well known in literature and it is presented in [45] and [71]. The choice of this configuration is mainly driven by the following reasons:

- This is one of the few engine like configurations which is expressly developed to study combustion. Experimental works on real engine configurations usually give fewer information about combustion process.
- The geometry is simple and described well enough to be correctly reproduced. The flow field at ignition time is practically unaffected by initial conditions, while, for real engines, the whole gas exchange process should be computed before compression with the related uncertainties.
- Many parameters which are usually fixed in real engine, can be changed in this configuration: mixture composition, ignition system and spark positions and, as usual, engine speed.
- Some data of the flow field are available and Schlieren images taken from two views can describe the geometry of the flame and allow the estimation of the burnt volume.
- Burnt volume can be used to describe the initial stages of flame development, as pressure variations are minimal in this stage. The description of this phase is one of the main features of the proposed model.
- The volume of the chamber is quite big and, for the combustion phase under investigation, pressure changes are quite small. As a consequence, the problem is a

bit simplified as many variables which influence combustion, like laminar flame speed and thickness, do not change significantly during combustion because of pressure rise.

On the other hand, this set of experiments has also some limits:

- The available experimental points for the single test are few and the uncertainties related to the estimation process are probably rather high, as average Schlieren images suffer the problems already discussed in section 4.6.2 and the geometry of the flame is quite complex so that the authors of the experiment had to make some assumptions in order to compute the burnt volume.
- No pressure traces are available which are very reliable measurements and could be helpful to verify average cylinder mass and temperature at ignition time.
- Engine speeds are low and, for some cases, also the turbulent Reynolds number. Both turbulence and combustion models are designed to describe a very high Reynolds number flow.

In the following the experimental apparatus and the available data are reported; then the numerical set-up and the imposed initial conditions are discussed. Results of the cold flow cases are shown and compared with the available experimental data. Finally a selection of the experimental cases is solved with the proposed combustion model and its results are presented.

7.1 Experimental configuration and test conditions

Herweg et al. in their works used a laboratory engine 7.1 which is designed to induce a strong swirl motion inside a cylindrical chamber where combustion occurs. By varying the piston speed and the spark position, i.e. in the centre of the chamber and in a peripheral zone, Herweg et al. investigated separately the effects of mean flow velocity and turbulence intensity on the development of the flame kernel. Thanks to optical access, provided by two large quartz windows at both cylinder ends and two circumferential windows, LDV measurements of velocities and turbulence intensity at the peripheral spark position together with high speed Schlieren filming were allowed. From the images of the flame taken from the two pair of orthogonal windows, Herweg et al. estimated the burned volume at different crank angles. They assumed that the flame cross section is ellipsoidal and used the images to estimate the axes dimensions of the section point by point. The main geometrical data are summarized in Table 7.1.

The experimental data provided in [45] cover 60 operating conditions including variation of engine speed and relative air/fuel ratio. Experiment were performed considering two different spar-plug positions (central and peripheral) and ignition systems (TCI and CDI). The complete list of the operating conditions is summarized in table 7.2

7.2 Case set-up

The main tool adopted to generate the mesh of the geometry is snappyHexMesh, a utility included in the opensource CFD toolbox OpenFOAM [2]. Its approach is based on the octree concept, where each cell is halved in the proximity of the boundaries,

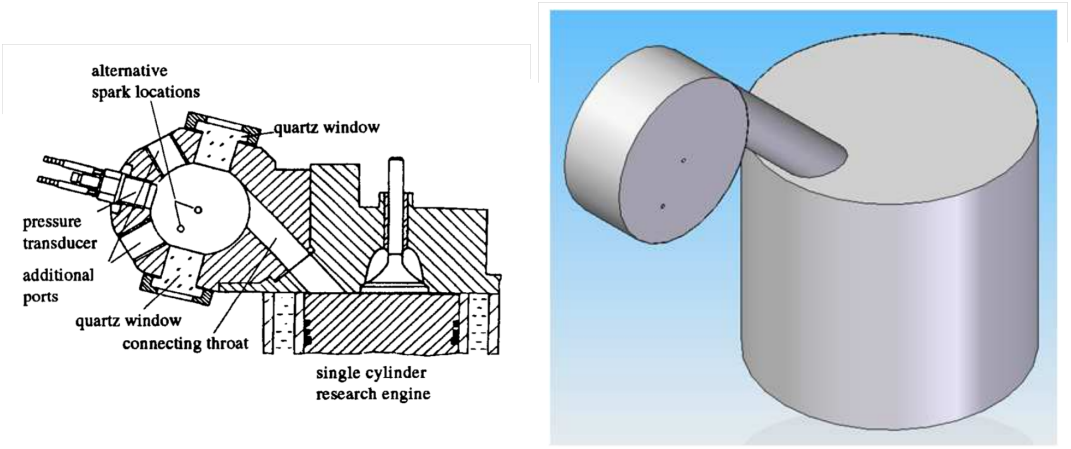

Figure 7.1: *Experimental engine configuration: on the left the original sketch taken from [45], on the right the geometry drawn by a CAD program*

Quantity	Value
Bore	73.0 mm
Stroke	67.0 mm
Connecting Rod Length	112.0 mm
Clearance heigth	1.0 mm
Compression ratio (from IVC to SA)	7.3
Side chamber diameter	45.0 mm
Side chamber clearance	19.0 mm
Connecting throat diameter	12.0 mm
Thin wire electrodes	1.0 mm
Spark gap	1.0 mm

Table 7.1: *Geometry data of the simulated side-chamber engine*

Ignition timing	350 CAD
IVC	192 CAD
Mixture inlet temperature	298 K
Pressure at ignition timing	5 bar
Fuel	propane
Engine speed range	300, 500, 750, 1000, 1250 rpm
Mixture air index	1.0, 1.3, 1.5
Ignition location	central, peripheral
Ignition system	TCI, CDI

Table 7.2: *Operating conditions tested in experiments*

refining the mesh up to the adequate level. As a starting point, a closed surface which defines the geometry domain must be provided together with an initial mesh composed by hexahedral elements, as shown in Figure7.2.

In a first stage, the initial block mesh is converted into a castellated mesh which approximates the shape of the geometry in a stair-step way. Then vertices are moved to the nearest boundaries by means of a smoothing algorithm (snapping phase). Therefore, the mesh generated adopting this strategy is predominantly hexahedral, with a small percentage of polyhedral elements near the boundaries. These three passages are

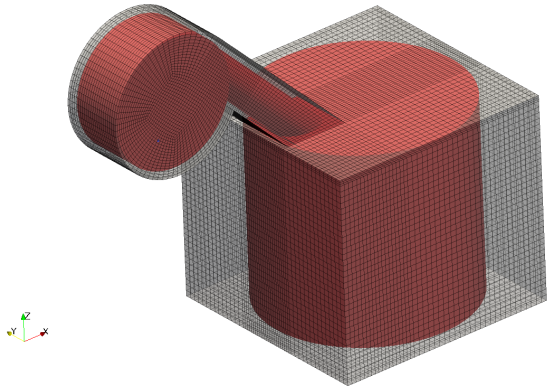

Figure 7.2: *Data needed to create a mesh with snappyHexMesh utility*

shown in Figure 7.3. The work to be done, in order to obtain a good mesh without an excessive number of cells, is to provide an initial block mesh which is already refined where more cells are needed, possibly with cell oriented in the direction of the flux (snappyHexMesh preserve the main features of the initial block mesh) and then select the parameters which control snappyHexMesh algorithm. Usually the creation of the initial block mesh and choice of snappy parameters require an iterative process in order to obtain the best final result.

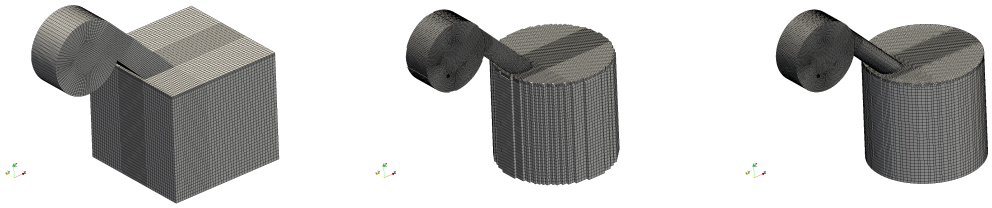

Figure 7.3: *The three stages (from left to right) to build a mesh with snappyHexMesh: fist stage, a block mesh must be provided; second stage castellated mesh is created; final stage the mesh is adapted to the real geometry*

An example of the final mesh obtained with this procedure for the configuration with centered electrode is shown in Figure 7.4. Two refinement levels are used near the electrodes position. Because the volume of the cylinder is greatly reduced during compression, 8 meshes are created to simulate this phase. This is done in order to reduce the number of cells and save computational time and also to avoid too big cell aspect ratio near the duct connecting the cylinder with the side chamber. During the cold flow computation the cells are compressed and no layer addition-removal technique is applied. When the mesh is changed, the various fields are mapped on the new mesh and the computation starts again. Only the cells within the cylinder are subject to compression and change from mesh to mesh. The total amount of cells at IVC is about 600000 while the mesh used to simulate combustion phase (from 348 to 372 CAD, where 360 CAD is the top dead center) has about 300000 cells.

The temperature at IVC is known and it is 298 K for all test cases, while the pressure is computed in order to obtain about 5 bar before ignition, as prescribed in the paper.

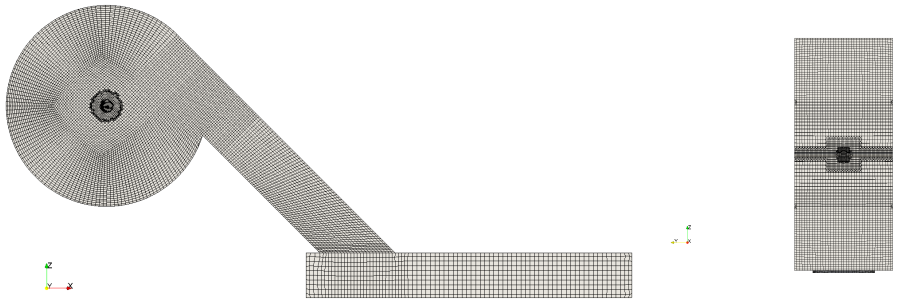

Figure 7.4: *Example of finite volume discretization domain used for computations: on the left a section taken in the middle of the whole engine is shown. On the right details of the mesh of the side chamber are shown, in particular the figure shows a section which pass through the center of the chamber and cut it in the direction traversal to the figure depicted on the left.*

Mixture composition depends on the selected test; for premixed combustion the most convenient way to define the mixture is to give the thermo-physical properties of the mixture, seen as a single component, without separating the various species. In particular, the weighed Janaf coefficients are provided for both the unburnt mixture and the burnt one. The composition of the burnt gas is computed with Flamemaster at spark time conditions and kept constant, as the change of unburnt temperature and pressure is low enough not to considerably change the fully burnt mixture composition. Considering that temperate and pressure change within a small range, for each of the three mixtures the laminar flame speed is provided by a 2D table which is obtained from 1D flame computations. Adiabatic conditions are imposed to all the geometry surfaces and the final average temperature at 350 CAD, which is the ignition time, is about 600 K. Initial velocity is set to zero in the whole domain, while turbulence properties are selected using standard relations which connect the integral length scale with the cylinder bore and the turbulence level with the engine speed. In this case the geometry is too different from an usual engine to behave like it and the last two initial conditions are questionable. Anyway it was found that because of unsteadiness of the problem and that the geometry strongly controls the flow evolution, different initial conditions do not practically change the final result. For one case, a complete cycle was computed in order to obtain more realistic initial velocity and turbulence conditions. At the end of the compression with these initial conditions, it was seen the final values of velocity and turbulent intensity inside the side chamber are practically identical to the case where homogeneous initial conditions are selected. This is a good property of this configuration as, in standard engines, the influence of turbulent and velocity fields at IVC are more important and their values are usually not provided by experimental data. In Figure 7.5 the pressure profile of a case without combustion is shown in order to assess that mesh changes and mapping procedure do not create any problem as no discontinuity is visible.

Regarding the electrical circuit of the spark plug, current and voltage profile obtained from figure 6a in [71] are used to estimate the main characteristic of the presumed TCI simplified system. The matching parameters are reported in table 7.3 and the matching current profile is shown in Figure 7.6. With these parameters the total

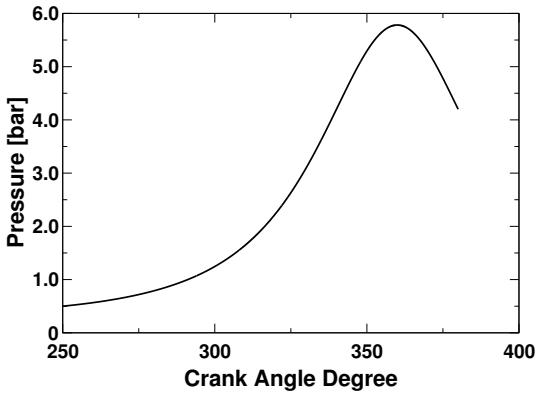

Figure 7.5: *Pressure development in compression phase*

discharge time should be in line with experiments even if the voltage fall across the spark gap will be a bit different from the experimental value. CDI system has not been considered in this work, as no equivalent circuit is implemented and because the experimental results for many cases are not able to detect any difference with the other ignition system.

Parameter	Value
L secondary circuit	24 H
R secondary circuit	7500 Ohm
Charged Energy	80 mj

Table 7.3: *Properties of mixture at different air-fuel equivalence ratio*

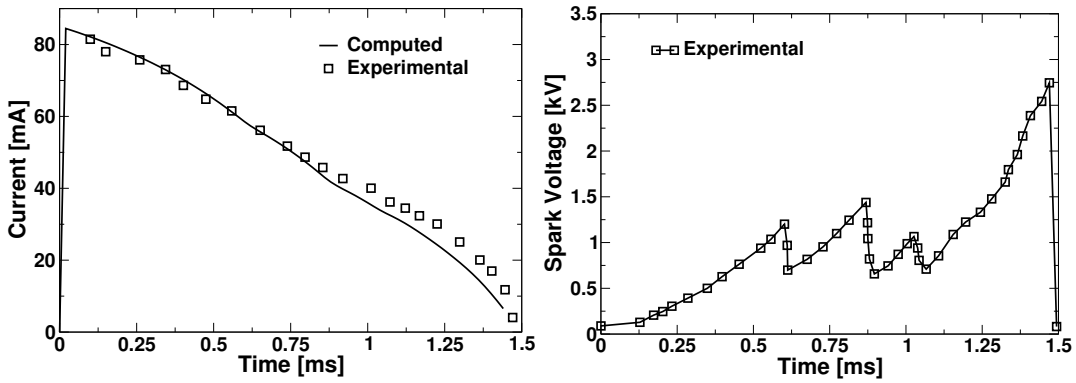

Figure 7.6: *Comparison between profile obtained by the simplified electrical system and experimental data extrapolated from [71] (Fig 6a): on the left current evolution in time after matching and on the right the experimental voltage across the spark gap*

The selected numerical schemes are full second order for the diffusive terms, second order with TVD for convection terms and implicit first order scheme in time.

7.3 Results at non combusting conditions

In this section, results of cold flow computations are shown in order to describe the properties of the flow field before the start of combustion. Because the results prac-

tically scale linearly with engine speed, for some figures only the case at 1000 rpm is considered. During the compression phase, the cylinder pushes the flow inside the duct which is tangentially connected to the side chamber and creates a strong swirl motion which is not completely centered as the duct section is big enough to prevent an axisymmetric behaviour of the flow. Initially the flow behaves like a jet flow as the velocity field inside the chamber is close to zero. As the compression phase goes on, the high velocity jet travels around all the chamber and starts to interact with the flow coming from the duct (see the left picture of Figure 7.7). Initially the flow coming from the duct has a higher momentum than the flow coming from the bottom of the chamber; as a consequence the last flow is deviated and the motion in the chamber remains non symmetric. As the piston comes close to the cylinder head, the velocity intensity of the flow coming from the duct quickly decreases and the outgoing jet is deviated by the flow inside the chamber. The structure of the motion becomes more axisymmetric and behaves like a cylindrical rotating body. Anyway, the center of rotation never reaches the geometrical center of the chamber.

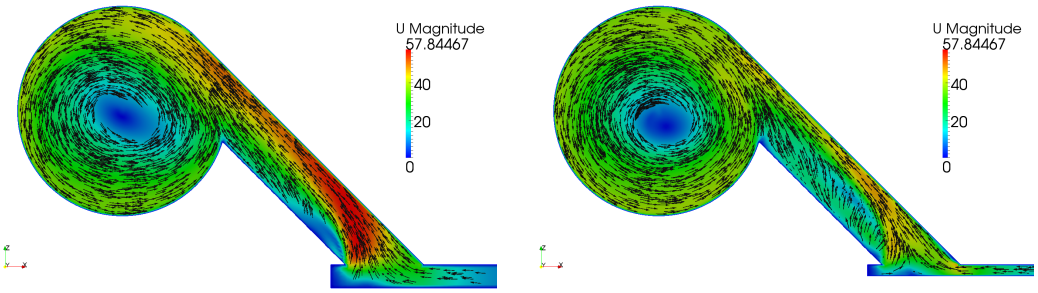

Figure 7.7: *Swirl motion inside the side chamber at 335(left) and 345(right) CAD*

Radial profiles of non-dimensional velocity magnitude and turbulent intensities for three engine speeds at ignition time (350 CAD) are shown in Figure 7.8. The line on which the values were taken starts from the center of the chamber and arrives to the outer surface along the direction which connects the central and peripheral electrodes positions (see Figure 7.1). It can be seen that the velocity in the center of the chamber, where the electrodes are located, is different from zero and the zone which is close to the swirl center is around 2 mm below (the radius of the chamber is 22.25 mm). Velocity is practically directed tangentially and its magnitude continues to increase up to the outer zone of the chamber before decreasing just in the cells close to the wall. Velocity scales almost linearly with engine speed. The turbulence intensity is much more uniform over the whole radial direction; this is related to the radial velocity gradient which does not change a lot with the radius and turbulent diffusion.

Figure 7.9 shows the comparison of computed and experimental average velocity and turbulence intensities for different crank angle degrees at the peripheral spark position. It can be noticed that the average velocity agrees well with the simulation results, even if the initial conditions are far from being the real one. In particular the increasing rate is in line with experiments. Experimental data seem to be more scattered with respect to the change of engine speeds, while, as could be expected, the computed values are more in line with scaling theory. The turbulence level is over-predicted by about 50%, even if the trends are similar (practically constant in time). Different turbulence

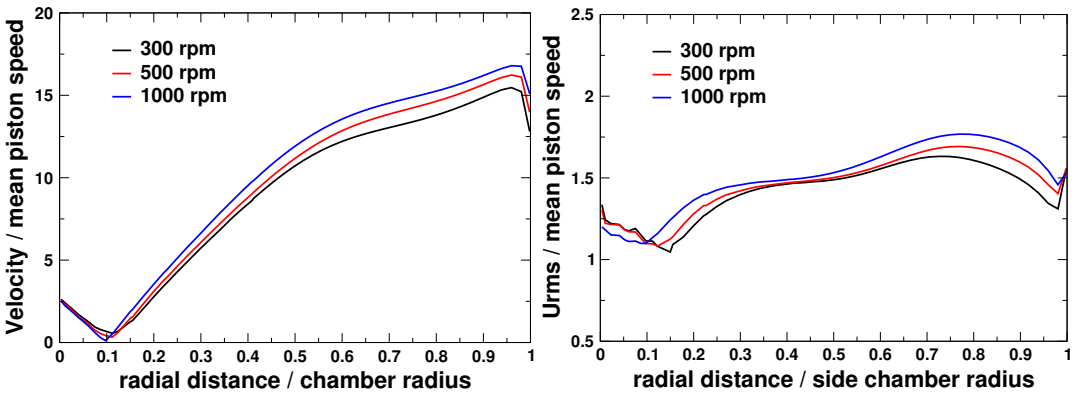

Figure 7.8: *Radial profile of non-dimensional velocity and turbulent intensities within the side chamber*

models were tested (RNG, Realizable k-epsilon, standard k-epsilon) in order to see if the results are heavily influenced by the selected model. It was found that the results of these models were very close to the ones of standard k-epsilon model with a bit lower turbulent intensity in line with what is usually reported. In Figure 7.7, it can be noticed that in the zone where the duct is connected with the cylinder, there is a strong velocity gradient and the flow entering in the duct is detached from the lower wall. This is the main source zone of turbulent intensity which is convected into the chamber without decaying enough. Some tests were carried out increasing the mesh refinement of the zone and adding some layers, but still no relevant changes of the turbulence properties inside the chamber were observed.

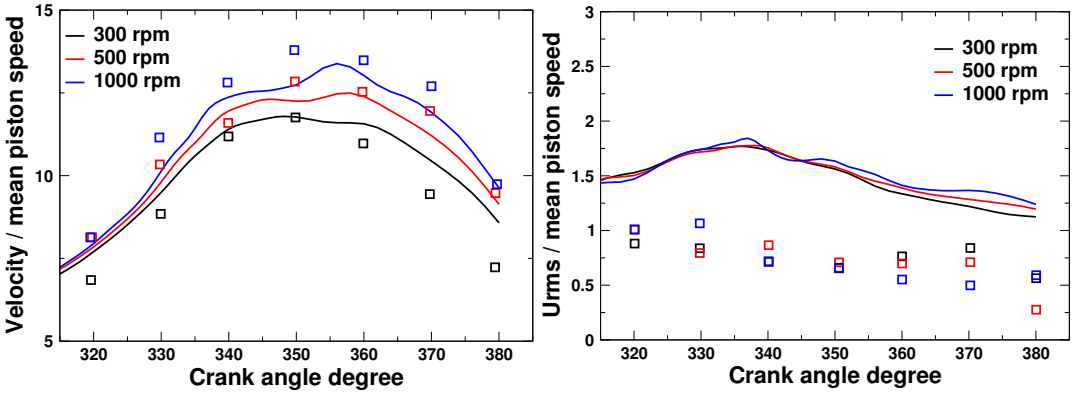

Figure 7.9: *Comparison of computed and LDV measurements at peripheral spark position for three engine speeds*

The main effect of the presence of electrodes is the change of the integral length scale. Figure 7.10 shows the value assumed by this length computed as $l_t = 0.37 \cdot k^{3/2}/\varepsilon$ in the central cross section of the side chamber with electrodes positioned at the center and at the peripheral position. The presence of electrodes, with the small gap distance between them, greatly reduces the integral length scale, while, as shown in Figure 7.8, the turbulence intensity is more uniform and does not change a lot between the spark gap. The value scales in the right way with the corresponding geometrical length (the duct diameter and the electrode gap which is only 1 mm). Anyway the validity of turbulence models in such a narrow zone between walls is questionable. Without

electrodes the integral length scale is uniform in the center of the channel and equal to about 3 mm. Figure 7.11 shows the radial variation (on the same points of figure 7.8) of the integral length scale for the case with central spark position for different engine speeds. It can be noticed that the value of this quantity correctly does not change a lot with different engine speeds, while it changes with the radius as the reference geometrical length scale changes.

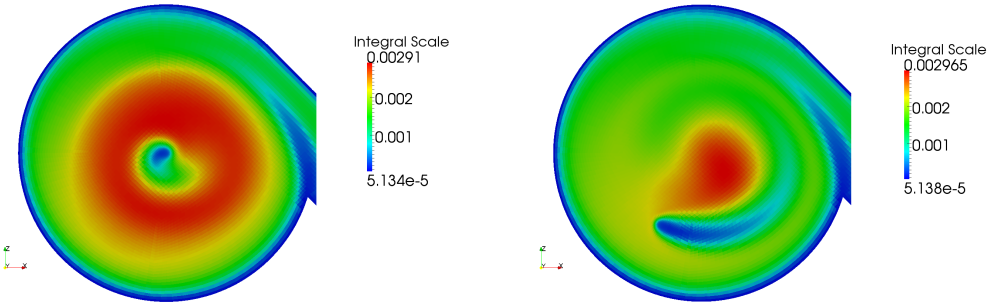

Figure 7.10: *Integral length scale at the middle section of the side chamber at 350 CAD for 1000 rpm engine speed. On the left central spark plug position, on the right peripheral spark plug position.*

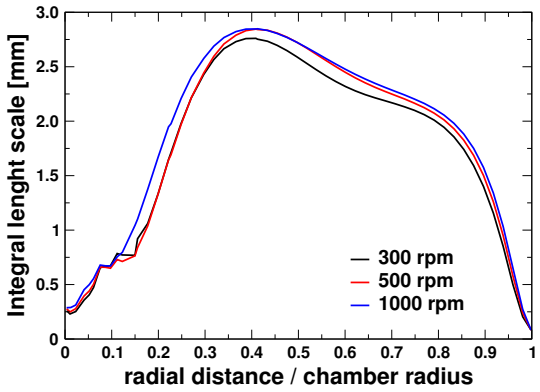

Figure 7.11: *Radial profile of integral length scale within the side chamber at 350 CAD for different engine speeds.*

7.4 Combustion data analysis

In [45] and [71] experimental data of estimated burned volume are reported. In particular, for each test case, the time for which the burnt volume has reached a threshold value (respectively 0.1, 0.2, 0.3, 0.4, 0.5 and 1.0 cm^3) is shown. It is reported that this value is obtained from the average of 50 runs. Moreover in [71] some data related to the turbulent propagation speed are reported. Considering the complexity of the flame geometry, especially in the peripheral spark cases, there is no obvious way to derive velocity from the burnt volume and no indication is given in the paper. As a consequence, only data related to the burnt volume are investigated. The data published in [71] for the central spark position, all engine speeds and air index ratios are presented in Figure 7.12. In this work, only experimental data with TCI ignition system are considered.

Because of the simpler flame shape, data corresponding to central spark position are

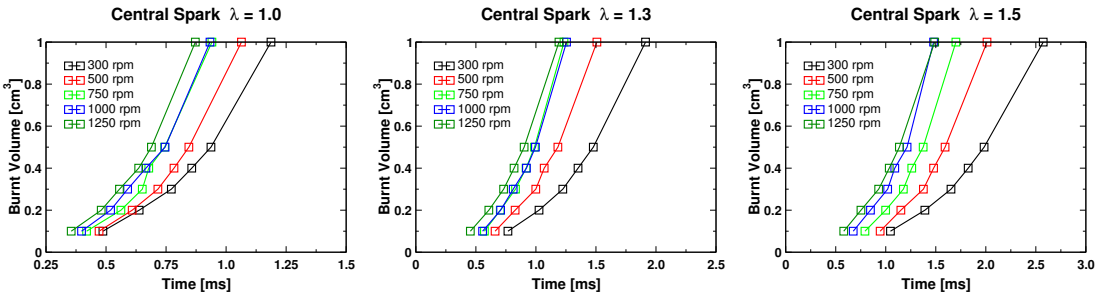

Figure 7.12: *Burnt volume as function of time after ignition for central spark position cases*

considered more accurate than the one associated with the peripheral spark zone. It can be noticed that for the case with stoichiometry mixture, burning speed increases, as expected, with the engine speed as the turbulence level increases, while the integral length scale remains the same. Only the case at 750 rpm does not agree with these trends, as it practically overlaps the case at 1000 rpm both at 1.0 and 1.3 air-fuel equivalence ratio. As a consequence in the following computation this case is not considered. Table 7.4 shows more in detail the effect of the change of mixture composition. The percentages shown are the time needed for the flame to burnt $1cm^3$ with respect to the corresponding time at stoichiometric mixture which is taken as a reference. It can be noticed that while this time obviously increase with leaner mixture, in general the percentage of the delay is reduced for higher engine speeds.

Quantity	$\lambda = 1.0$	$\lambda = 1.3$	$\lambda = 1.5$
300 rpm	100 %	161.2 %	216.9 %
500 rpm	100 %	141.7 %	189.1 %
750 rpm	100 %	131.2 %	180.8 %
1000 rpm	100 %	134.5 %	158.4 %
1250 rpm	100 %	136.6 %	170.7 %

Table 7.4

Figure 7.13 shows the experimental data related to the peripheral spark positions. This case is quite different from the previous one, as the spark plug works like a flame-holder. In fact, as the flame is convected away from the electrodes, the incoming fresh mixture is subject to ignition by means of the spark channel which, because of restrike, does not move very far from the electrodes. As a consequence, the flame can growth faster than the corresponding central spark position case. For this reason, while the total discharge time is quite irrelevant in the central position case, this is less true in the peripheral spark position case, as a longer discharge could potentially ignite a greater volume than a shorter one. Finally, as the velocity is higher at peripheral spark position, the induced stretch rate could increase; this is true only if velocity gradients are important in the tangential direction with respect of the flame front, otherwise it just convects the flame. Table 7.5 compares the time needed for the flame to burn a volume equal to $1cm^3$ with respect to the same time for the stoichiometric mixture at central spark position, which is taken as a reference. It can be noticed that, because of the flame holder effect, this time is reduced with respect of the central spark case for all the tests. In particular at high engine speeds, even the leaner condition is faster than the

stoichiometric mixture at the central spark position. Probably, for these cases, the uncertainties related to the measuring technique are higher than in the previous tests and the nature of the error should induce a systematic overestimation of the burnt volume. Anyway, the very different delay times, which decrease as the mean velocity increases, confirm that flame burns faster in the peripheral spark position cases and that the flame holder effect is not inhibited by the probably higher stretch rates.

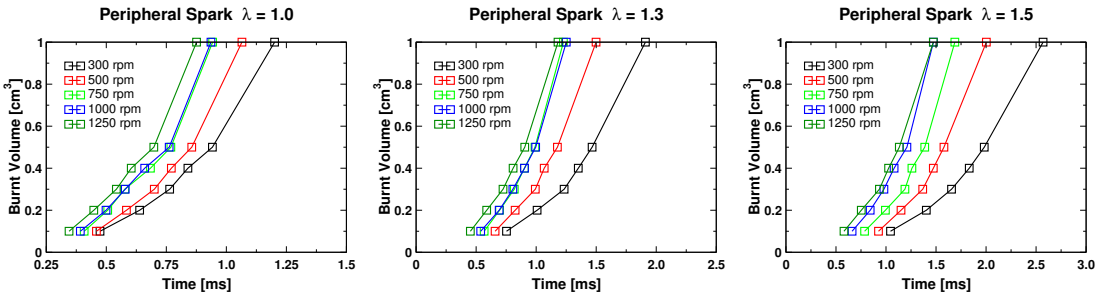

Figure 7.13: *Burnt volume as function of time after ignition for peripheral spark position cases*

Quantity	$\lambda = 1.0$	$\lambda = 1.3$	$\lambda = 1.5$
300 rpm	83.8 %	124.5 %	136.8 %
500 rpm	81.8 %	108.7 %	133.0 %
750 rpm	76.0 %	97.8 %	114.5 %
1000 rpm	66.7 %	82.2 %	95.8 %
1250 rpm	60.2 %	74.4 %	96.7 %

Table 7.5: *Experimental time delay of the peripheral spark position cases with respects to the corresponding stoichiometric mixture case with electrodes placed in the centre of the chamber.*

In order to further understand these behaviours, table 7.6 shows the properties of the three mixtures at 5.0 bar and 600 K which are about the conditions at ignition time. The data are obtained with Flamemaster, using the chemical scheme provided in [99] and the relations defined in chapter 3. It can be noted that the diffusion thickness is very small with respect to the integral length scale far from walls, which is about 3 mm, and justified the use of flamelets approach. For lean mixtures, Markstein numbers are considerably higher than the stoichiometric case because of the Lewis number associated with propane. The critical radius, beyond which flame instabilities can develop, follows the same trend. In particular, the estimated values for lean mixtures are much higher than the integral length scale, while, for the stoichiometric case, it is a bit lower. This could indicate that flame instabilities can play a role for this last case, while, for the others two, the corrugation of the surface induced by turbulence prevents the flame to reach the conditions for which intrinsic instabilities can develop.

The laminar flames data together with flow information obtained by cold flow computation allow to build a Borghi diagram which can be used to see what is the combustion regime which characterizes these operational points. In Figures 7.14 and 7.15, operating points for various radial positions at 350 CAD are plotted for different test cases characterized by the central spark position. The line $Ka_\delta = 1 \rightarrow Ka \sim 81$ is obtained by using a Zel'dovic number equal to 9.0. In particular 7.14 shows the data for a stoichiometric mixture at different engine speeds. The points between the electrodes,

Quantity	$\lambda = 1.0$	$\lambda = 1.3$	$\lambda = 1.5$
Temperature	600 K	600 K	600 K
Pressure	5.0 bar	5.0 bar	5.0 bar
Laminar flame speed	0.754 m/s	0.536 m/s	0.374 m/s
Laminar flame thickness	0.08 mm	0.11 mm	0.14 mm
Diffusion thickness	0.015 mm	0.023 mm	0.033 mm
Density ratio	4.22	3.78	3.50
Zel'dovich number	9.20	9.02	8.97
Effective Lewis number	1.07	1.69	1.76
Markstein number (burnt side)	1.21	3.82	4.15
Critical radius	2.38 mm	7.64 mm	11.58 mm

Table 7.6: *Properties of mixture at different air-fuel equivalence ratio*

for which the integral length scale is low, are placed on the left of the diagram, near the laminar region. As the radial distance increases, the points move towards right. The points of a single case are aligned around the same y-coordinate, as the turbulent intensity is quite homogeneous. As engine speed increases, the points move towards the broken reaction zone as the turbulence intensity changes, while the integral length scale remains practically the same. In Figure 7.15, the points for cases with the same engine speed (1250 rpm), but different air-fuel equivalence ratio are shown. As the mixture composition becomes leaner, the laminar flame speed is reduced, while the diffusion length increases; as a consequence the points move towards the broken reaction zone both because of the increase of y-coordinate and the decrease of the x-coordinate values. At 1250 rpm corresponds the highest turbulence intensity, as a consequence all the other points are below the line at 1250 rpm and 1.5 air-fuel equivalence ratio, which is far from the broken reaction zone. It can be noticed that the points are placed in the thin and corrugated reaction zone, but if the laminar flame thickness associated with the maximum gradient is used, most of them would move into the thin reaction zone regime.

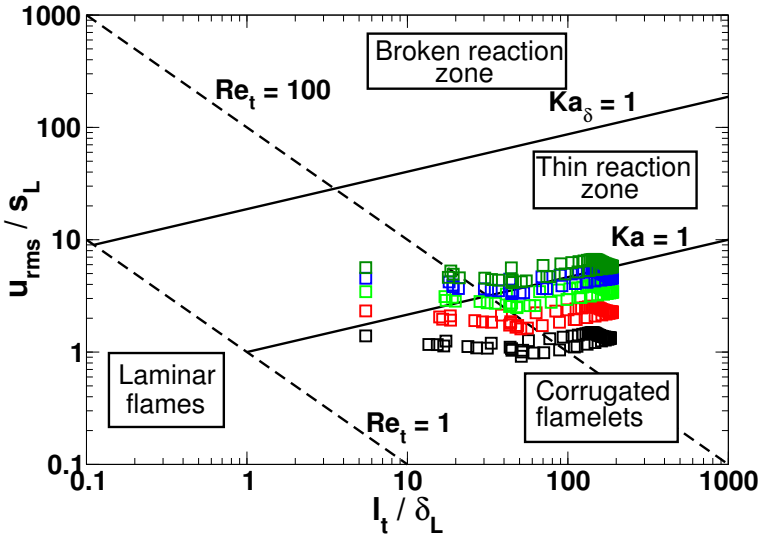

Figure 7.14: *Position in Borghi diagram of test points for different engine speeds at stoichiometric condition. The colors indicate the same engine speeds of figure 7.12*

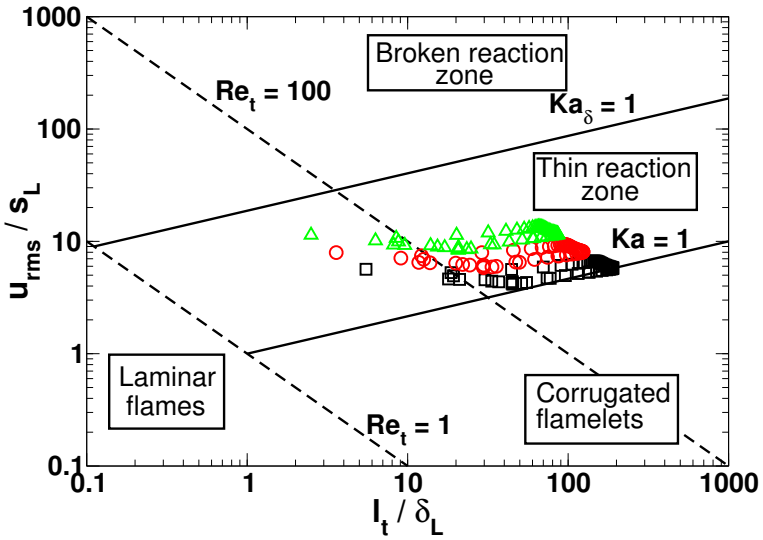

Figure 7.15: *Position in Borghi diagram of test points at 1250 rpm for different air-fuel equivalence ratios. Symbols correspond to: black-square* $\lambda = 1.0$*, red-circle* $\lambda = 1.3$ *and green-triangle* $\lambda = 1.5$

7.5 Combustion model results

In this section, the results of the combustion model are compared with the available experimental data. Only the selection of points displayed in table 7.7 is considered. In particular, the case 750 rpm is avoided as the experimental data are very close and some times also faster then the case at 1000 rpm. Moreover higher engine speeds are preferred as they are more relevant for real engine applications and also because the resulting Reynolds number is higher, which is more in line with the assumptions of the model. In other works which employ Peters relations [65] for the turbulent propagation speed, c_s is selected as tuning parameter. This constant controls the transient evolution of the flame (see Eqn. 6.34). In this configuration, because of the low value of integral length scale near the spark plug, the transient time of the turbulent flame speed is very fast. As a consequence, the constant b_3 is selected as tuning parameter which is related to the equilibrium propagation velocity value for low Damkohler numbers. The equilibrium flame brush thickness is also quite small in some regions and, to avoid numerical problems related to a steep change of fluid density, a minimum flame thickness is imposed. The case for which the constant is tuned is the one with central spark position, stoichiometric mixture and engine speed of 1000 rpm. The selected value is $b_3 = 0.56$, which is lower than the suggested one.

Figure 7.16 shows the results of the computation for the cases with electrodes placed in the centre of the chamber and stoichiometric mixture composition. The computed values correctly follow the experimental data for the four selected engine speeds. This indicates that the uncertainties related to the turbulence intensity estimation can be at least partially corrected by means of the selected tuning constant. The same set-up is used to compute variable mixture composition cases with the same engine speed. Figure 7.17 displays the results for six cases for two engine speeds and the three experimental mixture compositions. It is observed that the results of the model for lean mixtures are always delayed with respects to the experimental data. Moreover, it is

Engine speed	air-fuel equivalence ratio	Spark position
300 rpm	1.0	Central
500 rpm	1.0	Central
1000 rpm	1.0	Central
1000 rpm	1.3	Central
1000 rpm	1.5	Central
1250 rpm	1.0	Central
1250 rpm	1.3	Central
1250 rpm	1.5	Central
300 rpm	1.0	Peripheral
500 rpm	1.0	Peripheral
1000 rpm	1.0	Peripheral
1000 rpm	1.3	Peripheral
1000 rpm	1.5	Peripheral
1250 rpm	1.0	Peripheral
1250 rpm	1.3	Peripheral
1250 rpm	1.5	Peripheral

Table 7.7: *Considered test cases conditions for comparison and model evaluation.*

interesting to notice that the results for the 1250 rpm case are better than for the cases with 1000 rpm for which b_3 is specifically tuned. In [71] there are some indications about the uncertainties related to the measurements which increase with leaner mixtures; for a burnt volume of $1cm^3$ the reported value is about 16%. The data shown in [71] refer only to the 500 rpm case; as turbulence intensity and flame wrinkling increase with engine speed, probably also the uncertainties related to the measurement increase. The maximum discrepancy between computed and predicted results is about 20%, which is not far from the uncertainties associated to the measurements. Anyway, as the error is systematic, it can be related to model deficiencies or wrong input parameters. When mixture composition is changed, mainly three parameters are modified: the density ratio, the Markstein number and the laminar flame speed. Among them, the density ratio predicted by the adopted chemical mechanism is the most correct one. From some tests, it was found that a reasonable reduction of Markstein number does not considerably modify the result. As a consequence, the only parameter which could explain the systematic delay is the underestimation of the laminar flame speed given by the chemical mechanism. In order to verify this last consideration, in Figure 7.18, a comparison between the laminar flame speed predicted by the chemical mechanism and some experimental data is proposed. The reported environment conditions are at ambient temperature and 3 pressure levels. It can be noticed that the chemical mechanism predictions match the experimental data for ambient conditions around stoichiometry. As the mixture composition moves from stoichiometry, the differences become more important and the predicted values are always underestimated. For example for a mixture with equivalent ratio equal to 0.7 at 5 bar the predicted laminar flame speed is about 20% lower than the experimental data, while for 10 bar it is 10% lower. Due the absence of experimental data for higher temperatures, it can be only indirectly concluded that the laminar flame speeds are effectively underrated, but the underestimation cannot be clearly quantified.

Figure 7.19 gives some information about the shape of the flame for the central spark condition cases. It can be seen that the flame assumes a cylindrical shape, as the spark

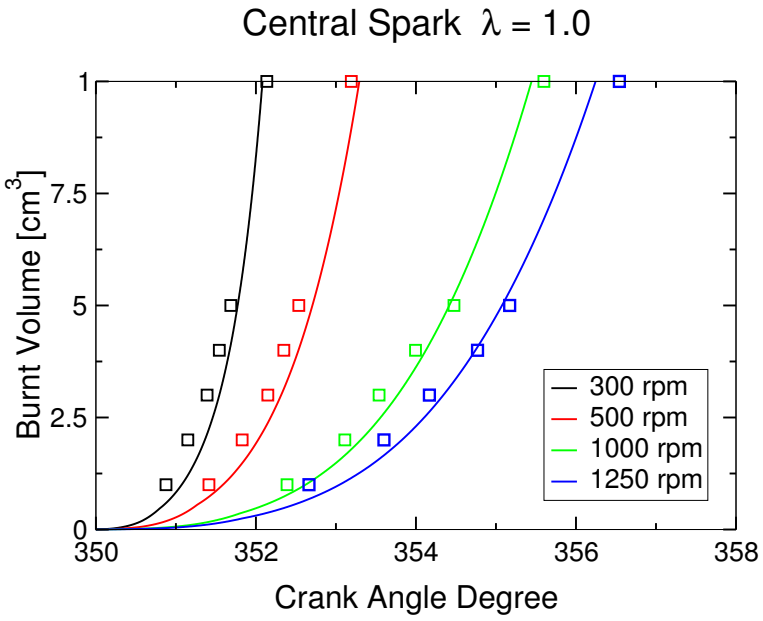

Figure 7.16: *Comparison of experimental and computed burnt volume for different engine speeds.*

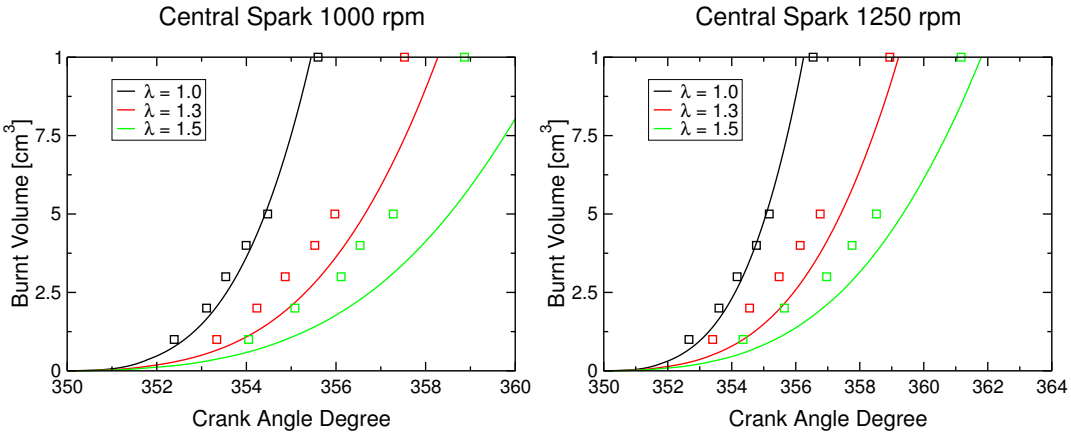

Figure 7.17: *Comparison of experimental and computed burnt volume for different mixture compositions. Two engine speeds are shown: 1000 rpm on the left, 1250 rpm on the right.*

channel is longer than the initial radius. The flame seems to grow a bit faster along the chamber axis direction and keeps this shape. Figure 7.20 shows the progress variable field at the central cross section of the side chamber. It can be noticed that the flame is slowly convected below the electrodes towards the centre of the swirl vortex. The flame brush thickness slowly increases in time as the integral length scale is small near the electrodes; only as the flame grows and reaches zones where the integral length value is bigger, the flame brush increases further and becomes thicker than the imposed initial value.

For the peripheral cases, the local high velocity stretches the spark channel, increases its length and voltage fall, until restrike condition is fulfilled and a new spark channel is created. This is well represented by the computed voltage across the electrodes shown in Figure 7.21, where two cases at the same engine speed but different

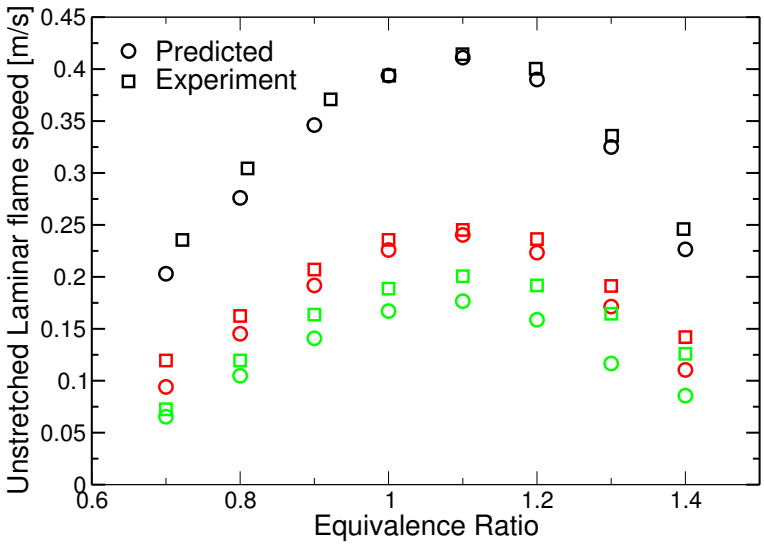

Figure 7.18: *Comparison of experimental and computed laminar flame speed with the mechanism proposed in [99]. All the data are taken at ambient temperature (298 K), but different pressures. Black symbols corresponds to 1 atm, red symbols to 5 bar and green symbols to 10 bar. Experimental data at ambient pressure are taken from [99], while higher pressure data are taken from [48].*

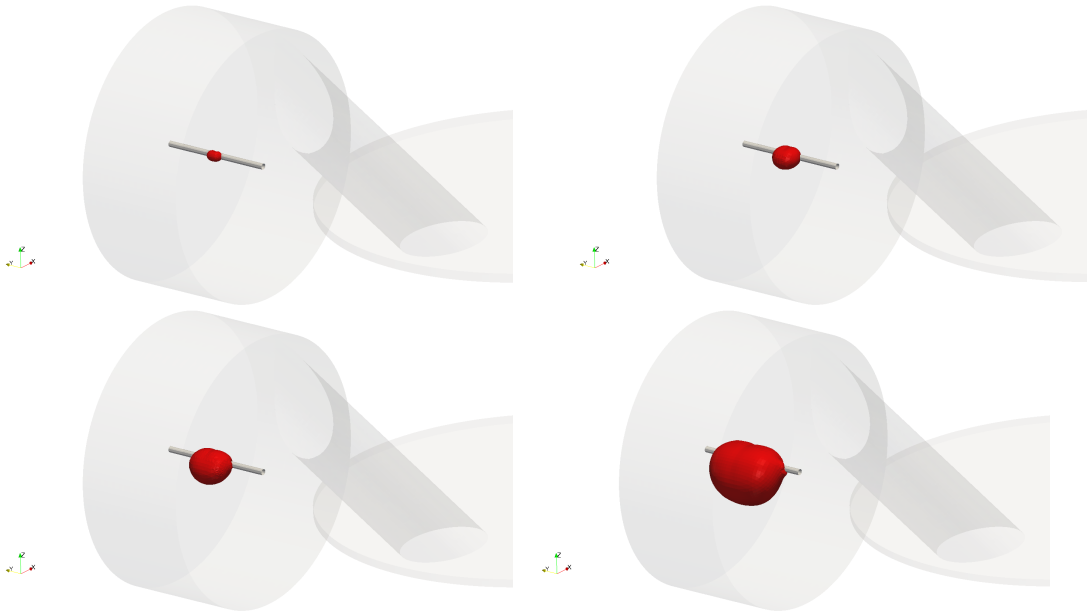

Figure 7.19: *Average flame position ($G = 0$) for the 1000 rpm case at stoichiometric condition with electrodes located in the centre of the chamber for four crank angle degrees: 351, 352, 353 and 355.*

electrodes positions are compared. It can be noticed that for the central spark plug position, only few restrikes occur while for the peripheral case this effect is continuously reproduced. In Figure 7.22 the results of the computation for the peripheral electrodes position and stoichiometric mixture cases are compared with the corresponding experimental data. The same value of the constant b_3 of central cases is kept. Results are less accurate than the central spark case, but in general are quite good, especially for low values of burnt volume. As the time increases, the model tends to predict faster

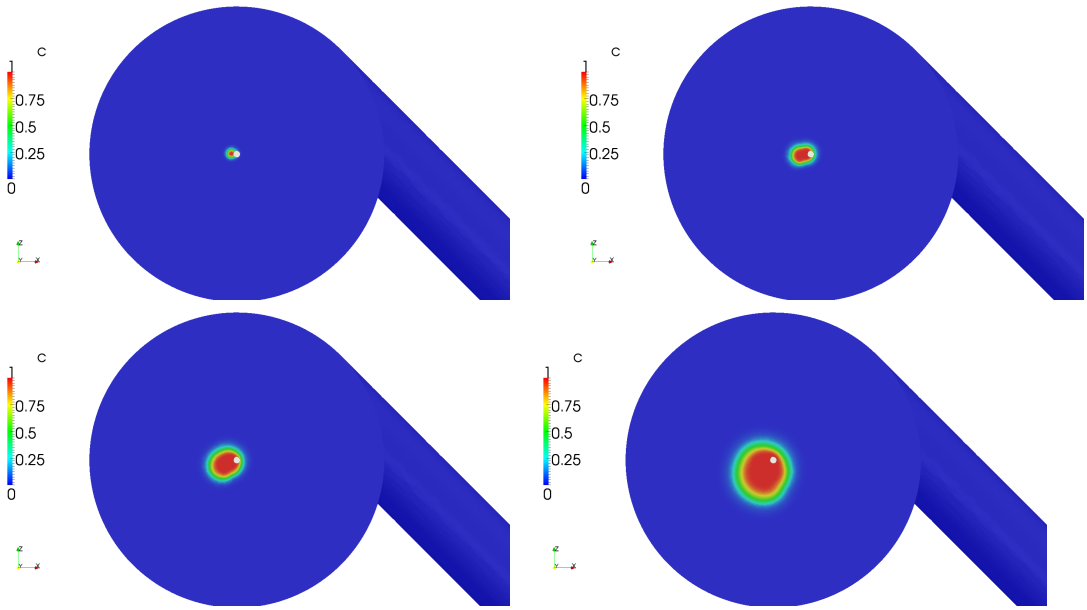

Figure 7.20: *Favre progress variable fields for the 1000 rpm case at stoichiometric condition with electrodes located in the centre of the chamber for four crank angle degrees: 351, 352, 353 and 355.*

burning rates. For the 1250 rpm case, experimental data are very close to the 1000 rpm case at initial stage, while, clearly, the computed results scale more linearly with engine speeds.

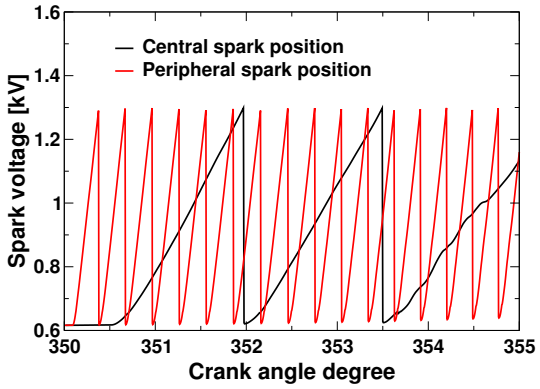

Figure 7.21: *Comparison of the computed spark voltage between the electrodes for central and peripheral spark positions at 1000 rpm.*

Figure 7.23 shows that electrodes work like flame holders. In fact, the high restrike frequency creates new spark channels which continue to ignite the incoming mixture. This effect is the main cause of the faster burning rate with respect to the central spark position case. In fact, turbulence properties do not change a lot with respect to the other configuration (see Figures 7.10 and 7.8), while the mean flow is about 6 times faster. The flame shape is quite complex as it is elongated by the flow, while it is expanding in all the outward directions. The spark channel assumes an arc form with its ends attached to the electrodes and its centre moved away from the spark gap zone by the high velocity of the flow. As a consequence, the zone near the electrodes in the central

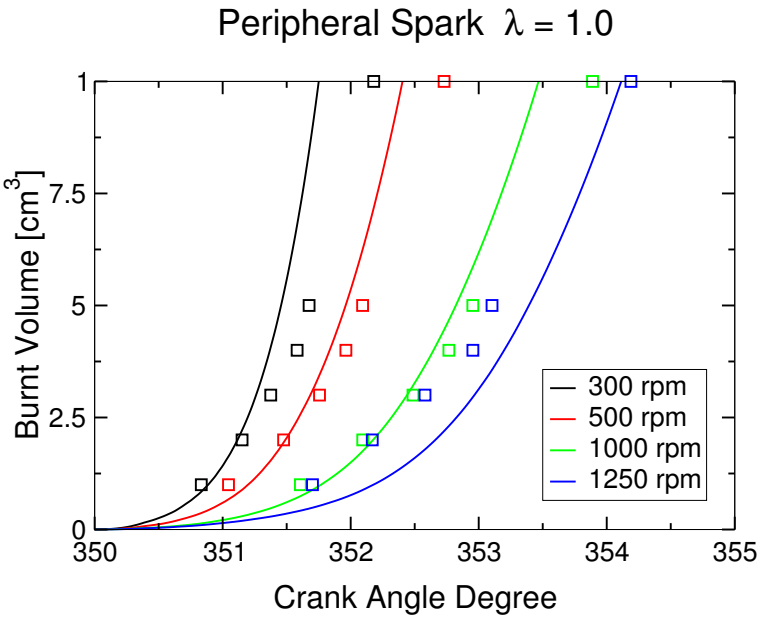

Figure 7.22: *Comparison of experimental and computed burnt volume for different engine speeds. Electrodes are located in the peripheral zone.*

cross section of the side chamber is far from the average flame position and the progress variable is lower than one, as depicted in Figure 7.24.

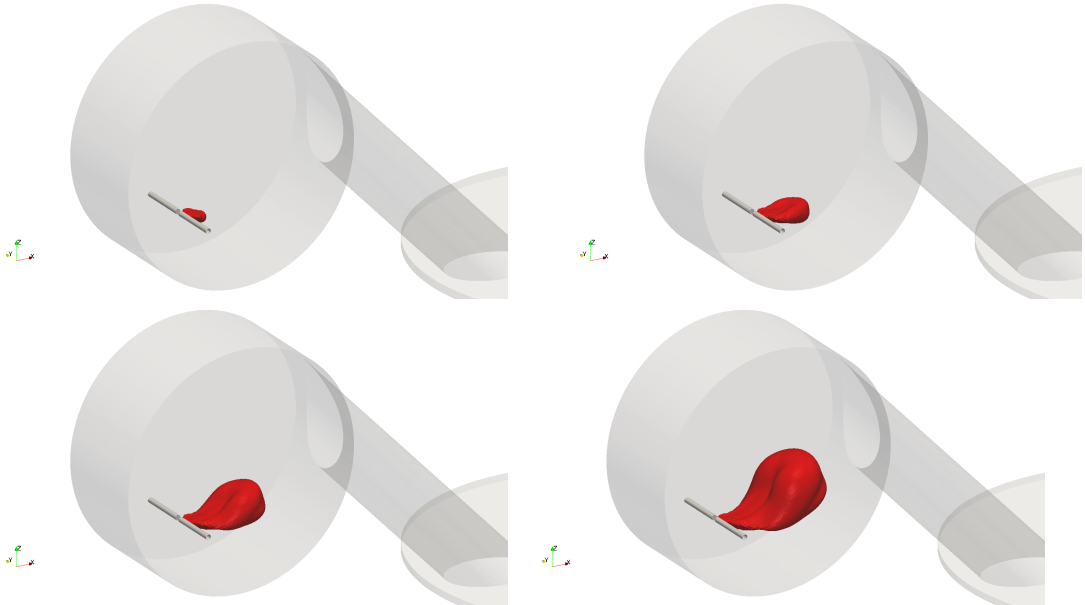

Figure 7.23: *Average flame position ($G = 0$) for the 1000 rpm case at stoichiometric condition with electrodes located in the peripheral zone for four crank angle degrees: 351, 352, 353 and 354.*

As an example of comparison between cases with different mixture compositions for the peripheral spark position configuration, Figure 7.25 shows model's results for 1000 and 1250 rpm engine speeds. The computed values are clearly delayed with respect to the experimental data, more than for the central spark position cases. Experimental

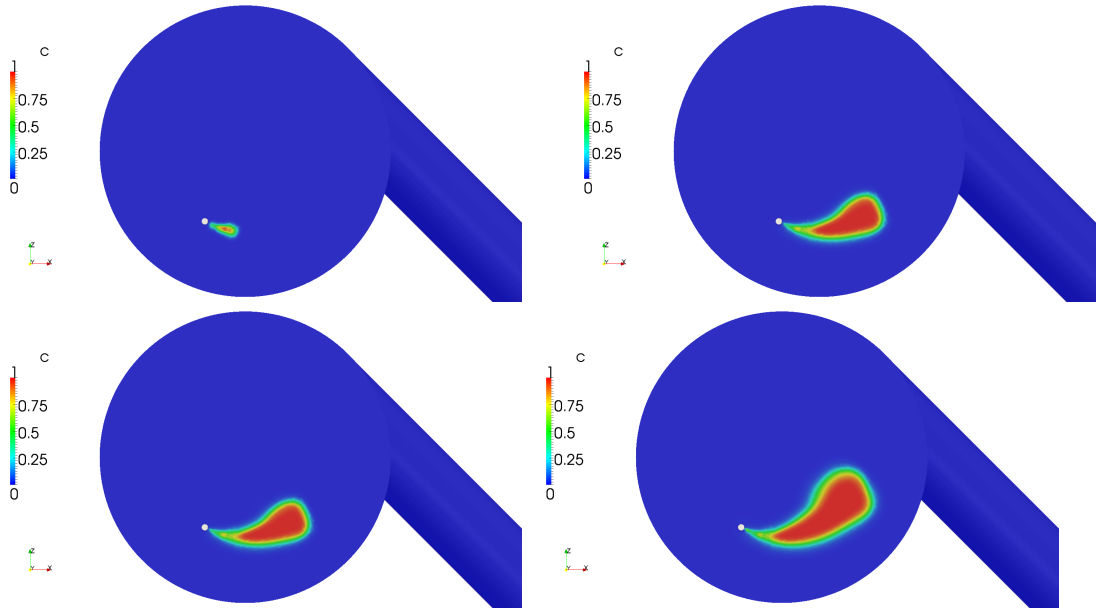

Figure 7.24: *Favre progress variable fields for the 1000 rpm case at stoichiometric condition with electrodes located in the peripheral zone for four crank angle degrees: 351, 352, 353 and 354.*

data of these three cases are very close, as if mixture properties were not affecting flame propagation in the peripheral spark position cases. Because of the relatively low turbulent intensities and computed Damkohler numbers, this behaviour has no a clear physical interpretation. It is also noticed that, for the lean mixtures, the computed results at 1000 rpm and 1250 rpm are close with respect to the crank angle. This means that, as the propagation speed decreases, the flame holder effect is enhanced, as the ignited volume is proportional to the mean flow velocity. This concept is depicted in Figure 7.26: while the length of the flame is essentially the same in the direction of the flow motion, for leaner cases the flame is much thinner. The propagation of the flame is then much more related to elongation effect which is essentially affected by the mean flow velocity. Table 7.8 shows the computed delay time for the twelve cases related to the two engine speeds 1000 and 1250 rpm. The delay times are represented normalizing the time needed to reach $1cm^3$ with the one of the corresponding stoichiometric central spark position case. This manipulation helps to understand how the different parameters which characterize these configurations affect the model predictions. All the peripheral cases are faster than the corresponding central position cases. For increasing air-fuel equivalence ratio, the difference between the two spark positions cases with respect to the delay time slightly increments. This effect is magnified by the engine speed. These trends are in line with the experimental data (see Table 7.5) for which this effect is more significant for lean mixtures.

To conclude the evaluation of the model, in the last test the properties of the electrical circuit are changed in order to reduce the discharge time and electrical energy deposited in the fluid. Specifically, the resistance of the secondary circuit is increased to about ten times the previous one to keep the same initial current value. In this way the transmission efficiency of the circuit is reduced from about 10% to 1%. Computations are performed with the engine speed of 1000 rpm and a stoichiometric mixture

Quantity	Engine speed	$\lambda = 1.0$	$\lambda = 1.3$	$\lambda = 1.5$
Central spark position	1000 rpm	100.0 %	151.8 %	198.7 %
Peripheral spark position	1000 rpm	66.6 %	118.3 %	160.5 %
Central spark position	1250 rpm	100.0 %	147.5 %	188.8 %
Peripheral spark position	1250 rpm	64.5 %	108.8 %	138.5 %

Table 7.8: *Computed time after ignition needed to burn a volume of 1 cm^3. The values are given as a percentage with respect to the corresponding stoichiometric mixture with electrodes placed in the centre of the chamber.*

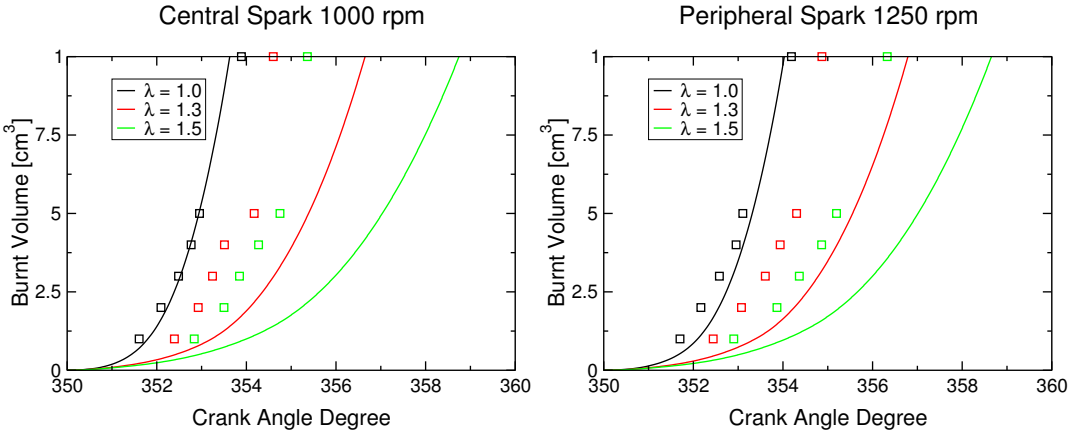

Figure 7.25: *Peripheral spark location: comparison of experimental and computed burnt volume for different mixture compositions. The two graphs represent respectively the 1000 rpm cases on the left and 1250 rpm cases on the right*

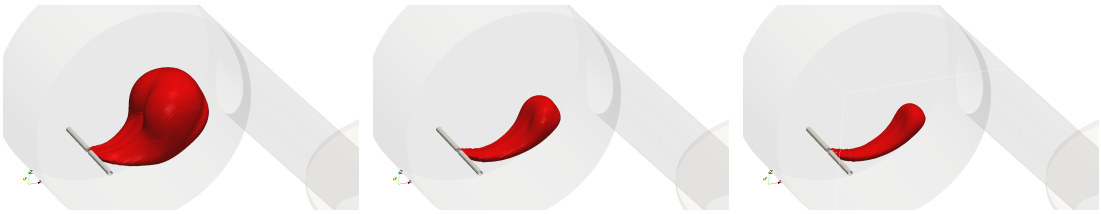

Figure 7.26: *Average flame position ($G = 0$) for the 1250 rpm, peripheral spark position case with different mixture compositions: images are shown with increasing air-fuel equivalence ratio (1.0, 1.3 and 1.5) from left to right at 355 CAD.*

for both the central and peripheral spark zone positions. The two cases are indicated as long and short discharge. Figure 7.27 (a) compares the current profiles of the selected cases. The position of the electrodes does not influence a lot the discharge process for two reasons: the voltage fall across the spark gap is much lower than the one of the secondary circuit wire and because, even if the restrike frequency is higher for the peripheral spark case, the average voltage is quite the same. Figure 7.27 (b) compares the burnt volumes of the four cases. For both configurations, the decrease of the power discharged in the fluid reduces the initial flame propagation velocity. Analyzing the time needed by the two cases to reach the same burnt volume, for the central spark position case, the delay between short and long discharge initially increases up to 0.19 CAD at 354 CAD, than it remains constant. For the peripheral spark position case, the delay increases continuously. The difference becomes greater when the discharge ends

as the electrodes do not anymore act as flame holders as shown in Figure 7.28. This last effect is also reported [45] when the experimental data with the TCI ignition system are compared with those with the CDI electrical circuit.

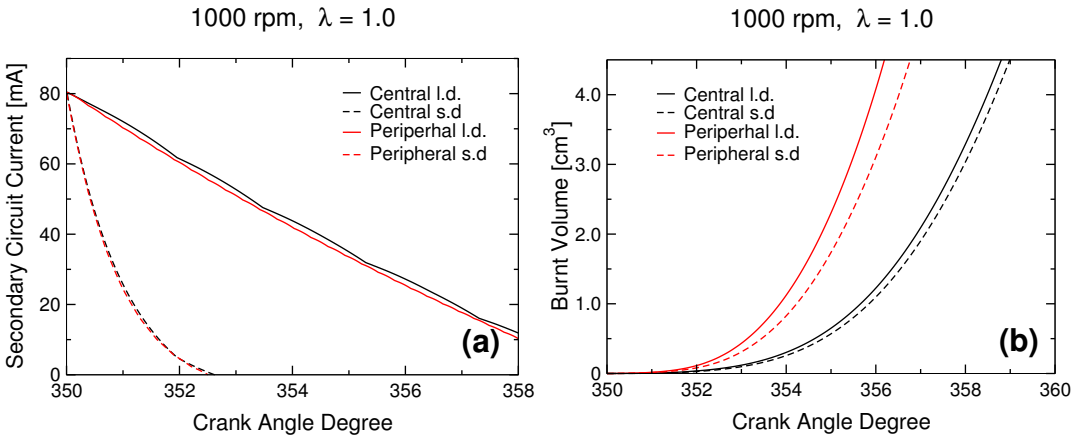

Figure 7.27: *Effect of different discharged powers: figure a) shows the discharge current profiles; figure b) shows the burnt volume evolution; l.d indicates long discharge case, while s.d means short discharge.*

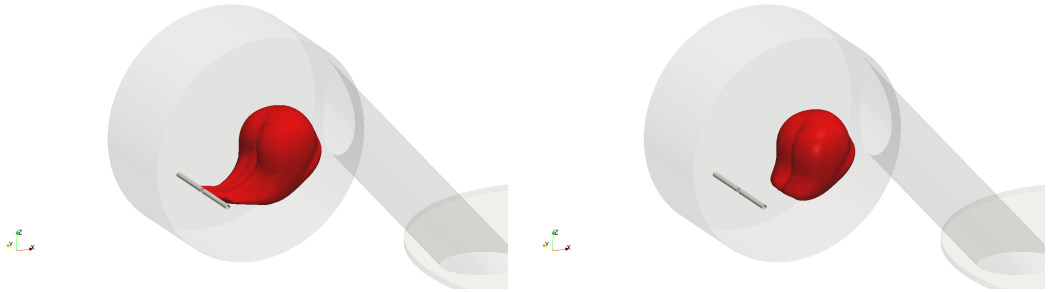

Figure 7.28: *Differences between a long and short discharge for the peripheral spark case: average flame position ($G = 0$) for the long discharge case on the left and the short discharge case on the right at 355 CAD.*

7.6 Summary

In this chapter the behaviour of the proposed comprehensive model was evaluated with the help of experimental data of a particular laboratory engine configuration with optical access. The model is able to reproduce the results of the experiments for the stoichiometric mixture composition for different engine speeds using the same constants. In particular it is able to represent the effect of mean flow contribution when the spark plug is positioned in the peripheral zone. For lean mixtures the results are less good as the laminar flame speeds predicted by the chemical mechanism are probably underestimated. Also the uncertainties of the experimental values are higher with these mixtures as reported in [71]. Anyway, the main features and trends of the experiments are correctly predicted. In particular, the higher burning rate for the peripheral spark position cases, which is more prominent for lean mixtures and high engine speeds.

The effect of different charging times/electrical circuits is also taken into account. The flame initially burns faster if higher electrical power is discharged, but the gain in time is quite limited for the central spark position case. For the peripheral case, the flame holder effect increases the difference between the various electrical circuits, probably even more if lean mixtures are considered. The flame shape and development are realistic since the first stages, with a fully burnt core and a flame brush thickness which increases in time, even if, in this configuration, it remains quite thin. Further validation is required, in particular with configurations for which more experimental data for a single set-up are available and more information about initial conditions are measured. These first results are encouraging, but more work has to be done especially to increase the computational efficiency of the model. As this is done, an extension of the approach to stratified combustion can be considered.

CHAPTER 8

Summary and conclusions

In the present work a detailed analysis about modelling premixed combustion in spark-ignition engines is proposed. The arguments of the discussion are supported by information taken from literature and by numerical simulations performed by the author, which required the implementation of appropriate solvers. As a result of this analysis, a new combustion solver was implemented within the OpenFOAM framework. This model describes premixed combustion since the very early stages of flame development. The work can be summarized in the following points:

- In the first part of the work it is shown how to exploit the multiscale physics of premixed flames to simplify a very complex and numerical demanding problem, which requires the solution of many reactions, into a problem where the flame is represented by a moving surface. This representation is designed to describe the kinematic behaviour of the flame and, as a consequence, the heat release rate in internal combustion engine simulations. The jumping relations across the flame surface and the equation which describe the dependence of flame propagation velocity on flow field represent the chemical properties of the reacting mixture. Asymptotic approach gives a rigorous way to find such relations and global parameters. It also clearly identifies the limits for which such equations are valid. The provided relations, because of their simple nature, are able to identify the physical mechanisms governing many of the effects which have been experimentally found. As a consequence, they also give some clues about what has to be modelled and how to do it. A list of global parameters (Zel'dovich number, effective Lewis number, Markstein number, critical Peclet number, unstretched laminar flame speed, laminar flame thickness) with the associated mechanisms and asymptotic relations are provided. This set of parameters defines the reacting behaviour of a mixture. For some of them, experimental results and empirical correlations

are available in literature. For many others, experimental uncertainties are very important (like for the Markstein number); the provided asymptotic relations in conjunction with 1D steady computations of reacting flows with detailed reaction mechanisms (for which free open-source solvers are available) can be used to complete the list.

- Once the flame properties have been identified, the discussion has been moved to turbulent combustion modelling. In particular, the typical quantities which are encountered in high level models (RANS and LES) have been clearly defined with their correct physical meaning, in order to avoid misunderstanding or wrong interpretation of DNS and experimental data. These quantities are the Favre, Reynolds and conditional average which are related by the well known BML relations. Unfortunately, for unsteady problems there are not many works in literature where DNS or experimental data can be really elaborated in order to obtain these quantities as it would require the repetition of the same experiment or computation for various times, which is quite expensive. Then models applied to turbulent combustion in the context of RANS and LES approaches have been reviewed. In particular, distinction between Favre and conditional average equations is underlined. The modelling limits of the first approach, which is practically the only one actually employed, are specified. A comparison among the most used models in literature has been proposed to understand which of them is more suitable to describe flame propagation in unsteady situation in the context of RANS approach. It is concluded that G-Equation and Flame speed closure model (or Zimont/Weller's model) due to their propagative form are able to decouple the flame structure from the turbulent flame speed value. This is an important property for a RANS model as the information available are useful only to define the fully developed flames. To model the unsteady behaviour of flames like the ones encountered in spark-ignition engines, suitable sub-models or transport equations must be provided. These relations would be very hard to be coupled with a flame surface density approach. The transient behaviour of this model is connected with a reaction-diffusion mechanism and depends a lot on initial conditions. Flame surface density models are eventually more suitable for LES simulations or statistically steady cases than unsteady RANS. Correlations and properties of the turbulent flame speeds are then proposed.

- To close the discussion about the aspects that a combustion model for SI engine simulations should deal with, spark ignition process and early flame kernel development are analyzed. Basic notions related to spark discharge theory are discussed together with ignition system devices, as the behaviour of the spark channel is heavily influenced by the connected electrical circuit. The aim this part was to identify the main parameters and mechanisms which influence spark discharge to provide some information about the kind of relations which can be used to compute quantities like breakdown voltage or the dependence between discharge voltage and current. These relations are needed if the energy discharged in the fluid has to be computed. Unfortunately there are not many published experimental works on these topics and a theoretical background is important in order to understand if relations found for different conditions can be directly imported

in spark-ignition engines environment. The obtained information are used in a 1D blast wave solver developed to estimate flow conditions after breakdown. Results of the model essentially confirm the findings presented by Maly in [70] with some differences. From 1D computations it is clear that breakdown is always able to ignite a mixture which is not eventually able to further expand because of stretch effect. Laminar flame kernel growth is governed by the competition between heat transfer form the hot plasma channel to the flame front position and the high stretch which characterizes small radius kernels. Asymptotic approach for a simplified case (mixture far from stoichiometry at constant density and properties) is used to show this effect and the non-linear relation between stretch and flame speed. An attempt to extend this approach to a more realistic case (variable density, general equivalent ratio and variable thermal properties) is made, but the results are not coherent with expectation. As a consequence, it cannot be used to extended, as originally planned, the validity of asymptotic relations. Further studies are needed in order to understand if the problem is related to numerical errors or because the asymptotic relation 3.42, used to write the equations in non-dimensional form, is too inaccurate for the case object of the study.

- Finally all the previous concepts are used to develop a combustion model based on G-Equation approach. The model take into account spark discharge process and early flame propagation by means of a Lagrangian description of the spark channel. A set of particles is introduced in the geometrical domain and each of them represents the geometrical centre of a flame. These kernels expand with a velocity computed with various sub-models which take into account spark energy deposition, curvature stretch effect and the turbulent properties of the flow. When restrike occurs, the previous set of flame kernels is converted into G-field of the main domain and the flame further develops by means of an Eulerian description. The model is tested against the experimental data provided in [71]. By the comparison it is concluded that the model is able to represents many features of the experimental case. In particular it is able to reproduce the interaction between the mean flow and the spark channel, which is an aspect usually neglected in many models. Moreover, the effect of discharged energy and mixture composition are investigated. It is found that the experimental trends are qualitatively correctly reproduced. For stoichiometric mixture the results are quantitatively good, while for lean mixtures the predictions are less accurate. Uncertainties related to the adopted value of the laminar flame speed is probably the main reasons for this lower accuracy. Globally, the results are promising, but further validations with better defined experimental tests are necessary.

Since this work started from scratch, it will be subject to many future developments, for example:

- many aspects discussed in the thesis are general topics of research by the whole combustion community and require deeper theoretical understanding and more rigorous/quantitative approach in modelling phase. In some parts of the work, suggestions are proposed to improve combustion models. The limited availability of suitable experimental data did not allow to clearly prove their validity.

- The implemented combustion model requires further development, especially in terms of computation speed. There are many works in literature which provide ways to get faster solution of G-Equation field, but their implementation in OpenFOAM requires quite a lot of changes in the mesh data structure. Moreover most of these approaches are developed for simplified domain (structured meshes) and must be extended to more general mesh types.
- G-Equation approach can be extended to stratified flames which seem to be the actual target of engine producers. Anyway, as the complexity and uncertainties related to these models are probably higher than for homogeneous mixture cases, a deeper insight on premixed combustion process and models behaviour should be achieved before starting to study this kind of combustion.
- Asymptotic theory together with hydrodynamic model can provide a deeper insight on turbulence flame interaction process. As the hydrodynamic model uses G-equation approach, the implemented model could be used also for this kind of simulations.

Bibliography

[1] FlameMaster documentation. *Avaiable from: http://www.itv.rwth-aachen.de/en/downloads/flamemaster/.*

[2] OpenFOAM documentation. *Avaiable from: http://foam.sourceforge.net/docs/cpp/.*

[3] D. Adalsteinsson and J.A. Sethian. A fast level set method for propagating interfaces. *Journal of Computational Physics*, 118:269–277, 1995.

[4] R. Addabbo. *The structure and stability of expanding and converging near-stoichiometric flames*. 2001.

[5] G.E. Andrews and D. Bradley. Determination of burning velocities: A critical review. *Combustion and Flame*, 18:133–153, 1972.

[6] O. Vermorel ans S. Richard, O. Colin, C. Angelberger, A. Benkenida, and D. Veynante. Towards the understanding of cyclic variability in a spark ignited engine using multi-cycle LES. *Combustion and Flame*, 156:1525–1541, 2009.

[7] J. Bechtold and M. Matalon. On the burning velocity of stretched flames. *Combustion and Flame*, 127:1906–1913, 2001.

[8] R. Borghi. *Recent Advances in the Aerospace Science, pages 117-138*. Plenum, New York, 1985.

[9] P. Boudier, S. Henriot, T. Poinsot, and T. Baritaud. A Model for Turbulent Flame Ignition and Propagation in Spark Ignition Engines. *24th Symposium (International) on Combustion*, 1992.

[10] D. Bradley, P. Gaskell, and X. Gu. Burning velocities, Markstein lengths, and flame quenching for spherical methane-air flames: a computational study. *Combustion and Flame*, 104(1):176–198, 1996.

[11] D. Bradley, M.Z. Haq, R.A. Hicks, T. Kitagawa, M. Lawes, C.G.W. Sheppard, and R. Woolley. Turbulent burning velocity, burned gas distribution, and associated flame surface definition. *Combustion and Flame*, 133:415–430, 2003.

[12] D. Bradley, R.A. Hicks, M. Lawes, C.G.W. Sheppard, and R. Woolley. The measurement of laminar burning velocities and Markstein numbers for iso-octane-air and iso-octane-n-heptane-air mixtures at elevated temperatures and pressure in an explosion bomb. *Combustion and Flame*, 115:126–144, 1998.

[13] D. Bradley, A.K.C. Lau, and M Lawes. Flame stretch as a determinant of turbulent burning velocity. *Phil. Trans. Soc. Lond.*, 338:359–387, 1992.

[14] D. Bradley, M. Lawes, and M.S. Mansour. Flame surface densities during spherical turbulent flame explosions. *Proceedings of the Combustion Institute*, 32(1):1587–1593, 2009.

[15] D. Bradley, M. Lawes, and M.S. Mansour. The problem of turbulent burning velocity. *Flow Turbulence Combustion*, 87:191–204, 2011.

[16] K.N.C. Bray, P.A. Libby, and J.B Moss. Unified modeling approach for premixed turbulent combustion-Part I: General formulation. *Combustion and Flame*, 61(1):87–102, 1985.

[17] N. Chakraborty and A.N. Lipatnikov. Conditional velocity statistcs for high and low Damkohler number turbulent premixed combustion in the context of Reynolds Average Navier-Stokes simulations. *Proceedings of the Combustion Institute*, 34:1333–1345, 2013.

[18] Z. Chen and Y. Ju. Theoretical analysis of the evolution from ignition kernel to flame ball and planar flame. *Combustion Theory and Modelling*, 11(3):427–453, 2007.

[19] S.H. Chung and C.K. Law. An integral analysis of the structure of stretched premixed flames. *Combustion and Flame*, 72:325–336, 1988.

[20] P. Clavin and F. Williams. Effects of molecular diffusion and of thermal expansion on the structure and dynamics of premixed flames in turbulent flows of large scale and low intensity. *Journal of fluid mechanics*, 116:251–282, 1982.

[21] O. Colin and K. Truffin. A spark ignition model for large eddy simulation based on FSD transport equation. *Proceeding of the Combustion Institute*, 33:3097–3104, 2011.

[22] F. Creta and M. Matalon. Propagation of wrinkled turbulent flames in the context of hydrodynamic theory. *Journal of Fluid Mechanics*, 680:225–264, 2011.

[23] Bradley D and Harper C.M. The development of instabilities in laminar explosion flames. *Combustion and Flame*, 99:562–572, 1994.

[24] R.N. Dahms, M.C. Drake, T.D. Fansler, T.W. Kuo, and N. Peters. Understanding ignition processes in spray-guided gasoline engines using high-speed imaging and the extended spark-ignition model SparkCIMM. Part A: Spark channel processes and the turbulent flame front propagation. *Combustion and Flame*, 158:2229–2244, 2011.

[25] R.N. Dahms, M.C. Drake, T.D. Fansler, T.W. Kuo, and N. Peters. Understanding ignition processes in spray-guided gasoline engines using high-speed imaging and the extended spark-ignition model SparkCIMM. Part B: Importance of molecular fuel properties in early flame front propagation. *Combustion and Flame*, 158:2245–2260, 2011.

[26] A. D'Angola, G. Colonna, C. Gorse, and M. Capitelli. Thermodynamic and Transport Properties in Equilibrium Air Plasmas in a Wide Pressure and Temperature Range. *The European Phisycal Journal D*, 58:47–62, 2008.

[27] G. Darrieus. Propagation d'un Front de Flamme: Assai de Theorie des Vitesses Anomales de Deflagration par developpement Spontane de la Turbulence. *International conference of applied mechanics, 6th, Paris*, 1946.

[28] C. Dopazo. On conditioned averages for intermittent turbulent flows. *Journal of Fluid Mechanics*, 81(3):433–438, 1977.

[29] J.M. Duclos and O. Colin. Arc and Kernel Tracking Ignition Model for 3D Spark-Ignition engine calculations. *Proceedings of COMODIA 2001 conference*, 2001.

[30] J.M. Duclos, D. Veynante, and T. Poinsot. A comparison of flamelet models for premixed turbulent combustion. *Combustion and Flame*, 95:101–117, 1993.

[31] M. Van Dyke. *Perturbation Methods in Fluid Mechanics*. Parabolic Press, 1975.

[32] K. Eisazadeh-Far, H. Metghalchi, and J.C. Keck. Thermodynamic Properties of Ionized Gases at High Temperatures. *Journal of Energy Resources Technology*, 133(2), 2011.

[33] K. Eisazadeh-Far, F. Parsinejad, H. Metghalchi, and J.C. Keck. On flame kernel formation and propagation in premixed gases. *Combustion and flame*, 157:2211–2221, 2010.

[34] S. Falfari and G. Bianchi. Development of an Ignition Model for S.I. Engines Simulation. *SAE Technical Paper*, (2007-01-0148), 2007.

[35] J.H. Ferziger and M. Perić. *Computational methods for fluid dynamics*. Springer, 1997.

[36] H. Gao, O.A. Ezekoye, M.J. Hall, and R.D. Matthews. A New Ignition for Large-Bore Natural Gas Engine Railplug Design Improvement and Optimization. *SAE Technical Paper Series*, (2005-01-0249), 2005.

[37] S. Gashi, J. Hult, K.W. Jenkins, N. Chakraborty, S. Cant, and C.F. Kaminski. Curvature and wrinkling of premixed flame kernels: comparisons of OH PLIF and DNS data. *Proceedings of the Combustion Institute*, 30:809–817, 2005.

[38] G.K. Giannakopoulos, A. Gatzoulis A, C.E. Frouzakis, M. Matalon, and A.G. Tomboulides. Consistent definition of "Flame Dispacement Speed" and "Markstein Length" for premixed flame propagation. *Combustion and Flame*, accepted, not yet published, 2014.

[39] A. Gleizes, J.J. Gonzalez, and P. Freton. Thermal plasma modelling. *Journal of Physics D: Applyed Physics*, 38:153–183, 2005.

[40] D. Goodwin. Cantera: An object-oriented software toolkit for chemical kinetics, thermodynamics, and transport processes. *Available: http://code.google.com/p/cantera*, 2009.

[41] O.L. Gulder. Turbulent premixed flame propagation models for different combustion regimes. *Twenty-Third Symposium (International) on Combustion*, pages 163–169, 1994.

[42] G.J.M. Hagelaar and L.C. Pitchford. Solving the Boltzmann equation to obtain electron transport coefficients and rate coefficients for fluid models. *Plasma Sources Science and Technologies*, 14:722–733, 2005.

[43] B. Hakberg and A.D. Gosman. Analytical determination of turbulent flame speed from combustion models. *Twentieth Symposium (International) on Combustion*, pages 225–232, 1984.

[44] F. Halter, T. Tahtouh, and C. Mounaim-Rousselle. Nonlinear effects of stretch on the flame front propagation. *Combustion and Flame*, 157:1825–1832, 2010.

[45] R. Herweg, Ph. Begleris, A. Zettlitz, and G.F.W. Ziegler. Flow Field Effects on Flame Kernel Formation in a Spark-Ignition Engine. *SAE Technical Paper*, (881639), 1988.

[46] G.S. Jiang and D. Peng. Weighted ENO schemes for Hamilton-Jacobi equations. *SIAM Journal on Scientific Computing*, 21(6):2126–2143, 1999.

[47] R. Kee, J. Grcar, S. Miller, and J. Miller. Premix: A fortran Program For Modeling Steady Laminar One-dimensional Premixed Flames. *Techinal report*, SAND85-8240, 1985.

[48] A.P. Kelley. *Dynamics of Expanding Flames*. UMI dissertation publishing, 2011.

[49] A.P. Kelley, J.K. Bechtold, and C.K. Law. Premixed flame propagation in a confining vessel with weak pressure rise. *Journal of Fluid Mechanics*, 691:26–51, 2012.

[50] P. Kelley, A.J. Smallbone, D.L. Zhu, and C.K. Law. Laminar Flame Speeds of C5 to C8 n-Alkanes at Elevated Pressures: Experimental Determination, Fuel Similarity, and Stretch Sensitivity. *Proceedings of the combustion institute*, 33:963–970, 2011.

[51] A.R. Kerstein, W.T. Ashurst, and F.A. William. Field equations for interface propagation in an usteady homogeneous flowfield. *Physsical Review A*, 37:2728–2731, 1988.

[52] J. Kim and K. Anderson. Spark Anemometry of Bulk Gas Velocity at the Plug Gap of a Firing Engine. *SAE Technical Paper Series*, (952459), 1995.

[53] M.E. Kiziroglou, X. Li, A.A. Zhukov, P.A.J. De Groot, and C.H. De Groot. Thermionic field emission at electrodeposited Ni-Si Schottky barriers. *Solid-State Electronics*, 52(7):1032–1038, 2008.

[54] H. Kolera-Gokula and T. Echekki. Direct numerical simulation of premixed flame kernel-vortex interactions in hydrogen-air mixtures. *Combustion and Flame*, 146:155–167, 2006.

[55] A.N. Kolmogorov. Local Structure of Turbulence in Incompressible Viscous Fluid for Very Large Reynolds Number. *Doklady AN. SSSR*, 30:299–303, 1941.

[56] T.W. Kuo and R.D. Reitz. Computation of premixed-charge cumbustion in pancake and pent-roof engines. *SAE Technical Paper*, (890670), 1989.

[57] L.D. Landau. On the Theory of Slow Combustion. *Acta Physicochimica URSS*, 73:77–85, 1944.

[58] C.K. Law. Combustion at a crossroads: Status and prospects. *Proceedings of the Combustion Institute*, 31:1–29, 2007.

[59] C.K Law, G. Jomass, and J.K. Bechtold. Cellular instabilities of expanding hydrogen/propane spherical flames at elevated pressure: theory and experiment. *Proceedings of the Combustion Institute*, 30:159–167, 2005.

[60] A.N. Lipatnikov. Conditional average balance equations for modeling premixed turbulent combustion in flamelet regime. *Combustion and Flame*, 152:529–547, 2008.

[61] A.N. Lipatnikov and J. Chomiak. Turbulent flame speed and thickness: phenomenology, evaluation and application in multi-dimensional simulations. *Progress in energy and combustion science*, 28:1–74, 2002.

[62] A.N. Lipatnikov and J. Chomiak. A theoretical study of premixed turbulent flame development. *Proceeding of the Combustion Institute*, 30:843–850, 2005.

[63] A.N. Lipatnikov and J. Chomiak. Modeling of turbulent scalar transport in expanding spherical flames. *SAE Technical Paper*, (2005-01-2109), 2005.

[64] A.N. Lipatnikov and J. Chomiak. Global stretch effects in premixed turbulent combustion. *Proceding of the Combustion Institute*, 31:1361–1368, 2007.

[65] A.N. Lipatnikov and J. Chomiak. On unsteady premixed turbulent burning velocity prediction in internal combustion engines. *Proceeding of the Combustion Institute*, 31:3051–3058, 2007.

[66] A.N. Lipatnikov and J. Chomiak. Effects of premixed flames on turbulence and turbulent scalar transport. *Progress in energy and combustion science*, 36:1–102, 2010.

[67] L.B. Loeb and A.F. Kip. Electrical discharge in air at Atmospheric Pressure: The Nature of the positive and Negative Point-to-Plane Coronas and the Mechanism of Spark Prpagation. *Journal of Applied Physics*, 10(3):142, 1939.

[68] T. Lucchini, L. Cornolti, G. Montenegro, G. D'Errico, M. Fiocco, A. Teraji, and T. Shiraishi. A Comprehensive Model to Predict the Initial Stage of Combustion in SI Engines. *SAE Technical Paper*, (2013-01-1087), 2013.

[69] T. Lucchini, G. D'Errico, H. Jasak, and Z. Tukovic. Automatic Mesh Motion With Topological Changes fro Engine Simulations. *SAE Technical Paper*, (2007-01-0170), 2007.

[70] R. Maly. *Road Vehicles Powered by Spark Ignition Engines. Spark Ignition: Its Physics and Effect on the Internal Combustion Engine*. J.C. Hilliard and G.S. Springer, 1984.

[71] R. Maly and R. Herweg. A Fundamental Model for Flame Kernel Formation in SI Engines. *SAE Technical Paper*, (922243), 1992.

[72] G.H. Markstein. *Nonsteady flame propagation*. Pergamon Press, 1964.

[73] M. Matalon and J.K. Bechtold. Spherically expanding flames. *Proceedings of the 1987 ASME/JSME Thermal Engineering Joint Conference*, 1:95–101, 1987.

[74] M. Matalon, C. Cui, and J.K. Bechtold. Hydrodynamic theory of premixed flames: effects of stoichiometry, variable transport coefficients and arbitrary reaction orders. *Journal of fluid mechanics*, 487:179–210, 2003.

[75] M. Matalon and B.J. Matrowsky. Flames as gasdynamic discontinuities. *Journal of fluid mechanics*, 124:239–259, 1982.

[76] M.H McMillian, S. Woodruff, S. Richardson, and D. McIntyre. Laser Spark Ignition: Laser Development and Engine Test. *Proceeding of the ASMEE ICE Division*, ICEF2004-917, 2004.

[77] A.C. Melissinos. *Experiments in Modern Physics*. Academic Press, 1973.

[78] C. Meneveau and T. Poinsot. Stretching and quenching of flamelets in premixed turbulent combustion. *Combustion and Flame*, 86:311–332, 1991.

[79] Y. V. Moshe. Moore's law and the sand-heap paradox. *Communication of the ACM*, 57:5–5, 2014.

[80] V. Moureau, B. Fiorina, and H. Pitsch. A level set formulation for premixed combustion LES considering the turbulent flame structure. *Combustion and Flame*, 156:801–812, 2009.

[81] Y. Naghizadeh-Kashani, Y. Cressault, and A. Gleizes. Net emission coefficient of air thermal plasmas. *Journal of Physics D: Applyed Physics*, 35:2925–2934, 2002.

[82] R. Ono, M. Nifuku, S. Fujiwara, and S. Horiguchi. Gas temperature of capacitance spark discharge in air. *Journal of Applied Physics*, 97, 2005.

[83] S.J. Osher and J.A. Sethian. Fronts Propagating with Curvature-Dependent Speed: Alogorithms Base On Hamilton-Jacobi Formulations. *Journal of Computational Physics*, 79:12–49, 1988.

[84] S.J. Osher and C.W. Shu. High-order essentially nonsocillatory schemes for Hamilton-Jacobi equations. *SIAM Journal of Numerical Analysis*, 28(4):907–922, 1991.

[85] P. Osmokrovic, G. Ilic, and C. Dolicanin. Determination of Pulse Tolerable Voltage in Gas Insulated Systems. *Japanese journal of Applied Physics*, 47(12):8928–8934, 2008.

[86] P. Osmokrovic, T. Zivic, B. Loncar, and A. Vasic. The validity of the general similarity law for electrical breakdown of gases. *Plasma Source Science and Tecnologies*, 15:703–713, 2006.

[87] O. Park, P.S. Veloo, N. Liu, and F.N. Egolfopoulos. Combustion characteristics of alternative gaseous fuels. *Proceedings of the Combustion Institute*, 33:887–894, 2011.

[88] F. Paschen. Ueber die zum Funkenubergabg in Luft, Wasserstoff und Kohlensaure bei verschiedenen Drucken erforderliche potential differenz. *Annalen der Physik*, 273(5):69–96, 1889.

[89] N. Pashley, R. Stone, and G. Roberts. Ignition System Measurement Techniques and Correlations for Breakdown and Arc Voltages and Currents. *SAE Technical Paper Series*, (2000-01-0245), 2000.

[90] D. Peng, B. Merriman, S.J. Osher, Ho. Zhao, and M. Kang. A PDE-Based Fast Local Level Set Method. *Journal of Computational Physics*, 155:410–438, 1999.

[91] N. Peters. The turbulent burning velocity for large-scale and small-scale turbulence. *Journal of fluid mechanics*, 384:107–132, 1999.

[92] N. Peters. *Turbulent Combustion*. Cambridge University Press, 2000.

[93] N. Peters and F.A. Williams. The asymptotic structure of stoichiometric methane-air flames. *Combustion and Flame*, 68(2):185–207, 1987.

[94] S. Pischinger and J.B. Hwywood. . *SAE Technical Paper Series*, (880518), 1988.

[95] M.N. Plooster. Shock Waves from Line Sources. Numerical Solution and Experimental Measurements. *The physics of fluids*, 13(11):2665–2675, 1970.

[96] T. Poinsot and D. Veynante. *Theoretical and numerical combustion*. R.T. Edwards, 2005.

[97] S.B. Pope. The evolution of surfaces in turbulence. *Internation Journal of Engineering Science*, 26(5):445–469, 1988.

[98] S.B. Pope. *Turbulent Flows*. Cambridge University Press, 2000.

[99] Z. Qin, V. Lissianski, H. Yang, W.C. Gradiner, S.G. Davis, and H. Wang. Combustion chemistry of propane: a case study of detailed reaction mechanism optimization. *Proceedings of the Combustion Institute*, 28:1663–1669, 2000.

[100] Y.P. Raizer. *Gas Discharge Physics*. Springer, 1991.

[101] H. Reather. *Electron Avalanches and Breakdown in Gases*. Butterwhorts, 1964.

[102] L. Richardson. *Weather Prediction by Numerical Process*. Cambridge University Press, Cambridge, 1922.

[103] G.J. Rohwein and L.S. Camilli. Automotive Ignition Transfer Efficiency. *SAE Technical Paper Series*, (02FFL-204), 2002.

[104] P.D. Ronney and G.I. Sivashinsky. A theoretical study of propagation and extinction of non-steady spherical flame fronts. *SIAM Journal on Applied Mathematics*, 49(4):1029–1046, 1989.

[105] K. Seshadri and N. Peters. The inner structure of methane-air flames. *Combustion and Flame*, 81(2):96–118, 1990.

[106] J.A. Sethian. A fast marching level set method for monotonically advancing fronts. *Proceeding of the National Academy of Science of USA*, 93:1591–1595, 1996.

[107] I.G. Shepherd, J.B. Moss, and K.N.C. Bray. Turbulent transport in a confined premixed flame. *19th Symposium (International) on Combustion*, pages 423–431, 1982.

[108] E. Sher, J. Ben-Ya'ish, and T. Kravchik. On the Birth of Spark Channels. *Combustion and flame*, 89:186–194, 1992.

[109] M.N. Shneider. Turbulent decay of after-spark channels. *PHYSICS OF PLASMAS*, 13(073501), 2006.

[110] J. Song and M. Sunwoo. A Modeling and Experimental Study of Initial Flame Kernel Development and Propagation in SI Engines. *SAE Technical Paper*, (2000-01-0960), 2000.

[111] D. Staack. *Characterization and Stabilization of Atmospheric Pressure DC Microplasmas and their Application to Thin Film Deposition*. Academic Press, 2008.

[112] A. Starikovskiy and N. Aleksandrov. Plasma-assisted ignition and combustion. *Progress in Energy and Combustion Science*, 39:61–110, 2013.

[113] C.J. Sun, C.J. Sung, L. He, and C.K. Law. Dynamics of Weakly Stretched Flames: Quantitative Description and Extraction of Global Flame Parameters. *Combustion and Flame*, 118(No. 1):108–128, 1999.

[114] C.J. Sung and C.K. Law. Structural sensitivity response and extinction of diffusion and premixed flames in oscillating counterflow. *Combustion and Flame*, 123(3):375–388, 2000.

[115] C. Swetaprovo, V. Akkernam, and C.K. Law. Spectral formulation of turbulent flame speed with consideration of hydrodynamic instability. *Physical review E*, 84(026322), 2011.

[116] C. Swetaprovo, F. Wu, and C.K. Law. Scaling of turbulent flame speed for expanding flames with Markstein diffusion considerations. *Physical review E*, 88(033005), 2013.

[117] G. Tabor and H.G. Weller. Large Eddy Simulation of Premixed Turbulent Combustion Using Flame Surface Wrinkling Model. *Flow, Turbulence and Combustion*, 72:1–28, 2004.

[118] Z. Tan and R.D. Reitz. An ignition and combustion model based on the level-set method for spark ignition engine multidimensional modeling. *Combustion and Flame*, 145:1–15, 2006.

[119] E. Varea, V. Modica, A. Vandel, and B. Renou. Measurement of laminar burning velocity and Markstein length relative to fresh gases using a new postprocessing procedure: Application to laminar spherical flames for methane, ethanol and isooctane/air mixtures. *Combustion and Flame*, 159:577–590, 2012.

[120] H.K. Versteeg and W. Malalasekera. *An introduction to computational fluid dynamics*. Longman Scientific and Technical, 1995.

[121] D. Veynante and L. Vervisch. Turbulent combustion modeling. *Progress in energy and combustion science*, 28:193–266, 2002.

[122] Zimont V.L. Private communication.

[123] J. Warnatz, U. Maas, and R.W. Dibble. *Combustion*. Springer, 2006.

[124] H.G. Weller. The development of a new flame area combustion model using conditional averaging. *Thermo-Fluids Section internal report TF/9307*, 1993.

[125] H.G. Weller, S. Uslu, A.D. Gosman, and R. Maly. Prediction of Combustion in Homogeneous-Charge Spark-Ignition Engines. *International Symposium COMODIA 94, The Japan Society of Mechanical Engineers*, pages 743–750, 1994.

[126] M. Wirth, P. Keller, and N. Peters. A Flamelet Model for Premixed Turbulent Combustion in SI-Engines. *SAE Technical Paper*, (932646), 1993.

[127] F. Wu, W.Liang, Z. Chen, Y. Ju, and Chung K. Law. Uncertainty of extrapolation of laminar flame speed from expanding spherical flames. *Proceedings of the Combustion Institute*, 2014.

[128] C. Zaepffel, D. Hong, and J.M. Bauchire. Experimental study of an electrical discharge used in reactive media ignition. *Journal of Applied Physics D*, 40:1052–1058, 2007.

[129] V.L. Zimont. Theory of turbulent combustion of a Homogeneus fuel mixture at hight Reynolds number. *Combustion, Explosion and Shock Waves*, 15:303–311, 1979.